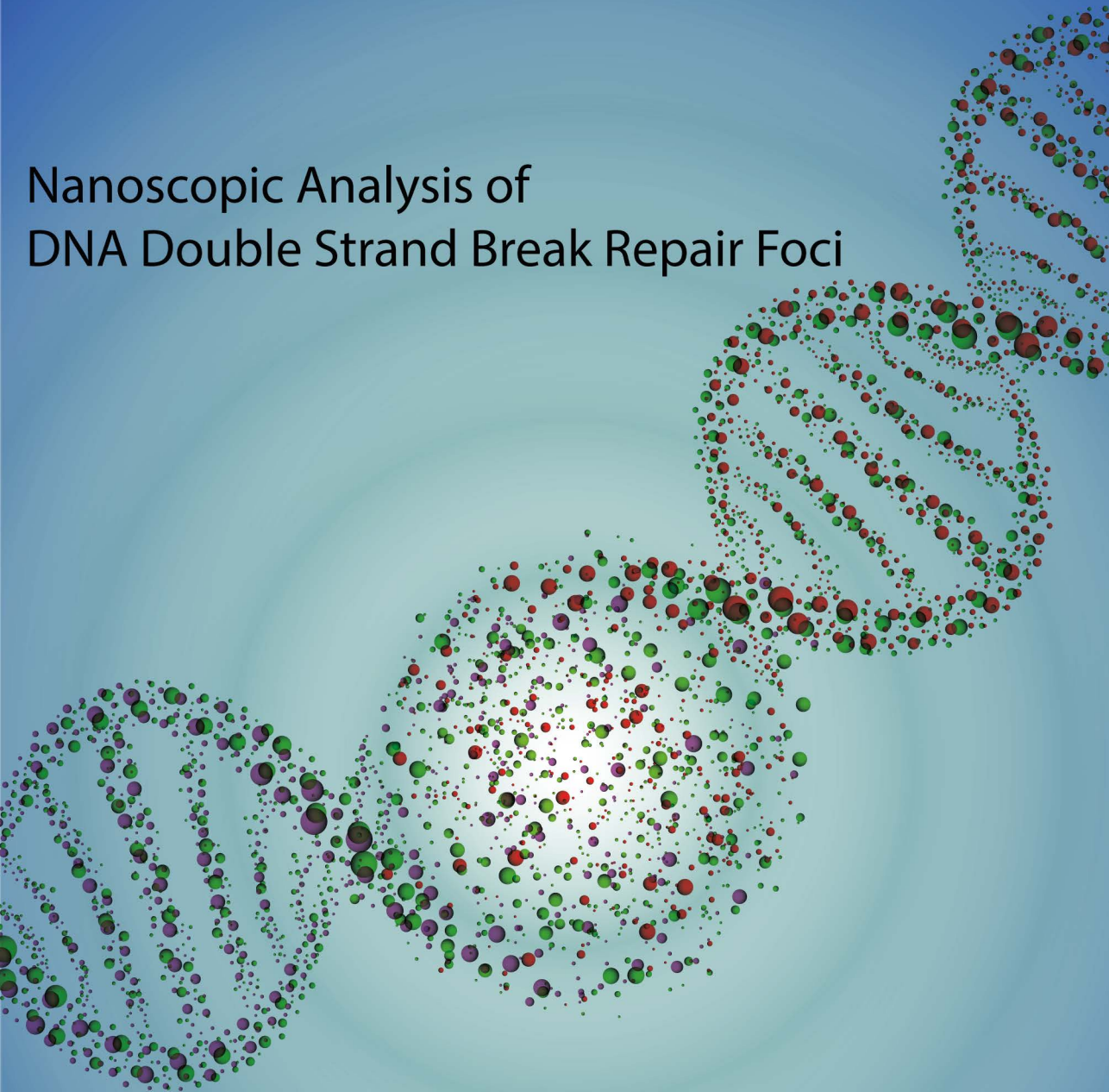


# Nanoscopic Analysis of DNA Double Strand Break Repair Foci



Maarten W. Paul

# **Nanoscopic Analysis of DNA Double Strand Break Repair Foci**

## **Colofon**

ISBN: 978-94-6295-580-6

Cover design: Maarten W. Paul  
Lay-out: Maarten W. Paul  
Printed by: Proefschriftmaken.nl || Uitgeverij BOXPress

The studies presented in this thesis were mainly performed at the department of Pathology of the Erasmus University Medical Center, Rotterdam, The Netherlands

Copyright 2017 © Maarten W. Paul

All rights reserved. No part of this thesis may be reproduced, stored in a retrieval system, or transmitted in any form or by any means, without prior written permission of the author.

# Nanoscopic Analysis of DNA Double Strand Break Repair Foci

Nanoscopische analyse van DNA dubbelstrengsbreuk reparatie foci

## Proefschrift

ter verkrijging van de graad van doctor aan de  
Erasmus Universiteit Rotterdam  
op gezag van de rector magnificus

Prof.dr. H.A.P. Pols

en volgens besluit van het College voor Promoties.

De openbare verdediging zal plaatsvinden op  
dinsdag 4 april 2017 om 11.30 uur.

door

**Martinus Willem Paul**  
geboren te Leidschendam

## **Promotiecommissie**

**Promotor:** Prof.dr. A.B. Houtsmuller

**Overige leden:** Prof.dr.ir. E.J.G. Peterman  
Dr. W.M. Baarends  
Dr. J. Essers

# Contents

<b>Chapter I</b>	General Introduction	9
	Scope of this thesis	33
<b>Chapter II</b>	Single Molecule Localization in R (SMoLR), a versatile software package for visualization and analysis of single molecule localization data in R	41
<b>Chapter III</b>	Super resolution imaging of RAD51 and DMC1 in DNA repair foci reveals dynamic distribution patterns in meiotic prophase	67
<b>Chapter IV</b>	Architectural plasticity of human BRCA2-RAD51 complexes in DNA break repair	93
<b>Chapter V</b>	Nanoscale organization of RAD54 revealed by super resolution microscopy	117
<b>Appendix</b>	Summary	140
	Samenvatting	142
	Curriculum Vitae	144
	List of publications	145
	PhD portfolio	146
	Dankwoord	148





**Chapter I**  
General Introduction



## DNA Repair

The genetic information of a cell is encoded in the DNA, the genome, which in eukaryotes resides in the cell nucleus. For proper functioning of a cell it is essential that information encoded in the genome is properly maintained, genetic information is not lost or changed and accurately replicated before cell division. However the integrity of the genome is continuously challenged by damage to the DNA and repair of those lesions is crucial for the cell to survive (Hoeijmakers, 2001). DNA damage can be inflicted by external as well as internal agents. External sources of DNA damage can be several types of radiation (UV, ionizing radiation), but also chemicals that induce modifications to the DNA structure. Reactive Oxygen Species (ROS) and oxidative stress are sources of internal sources of DNA damage (Figure 1).

The presence of unresolved DNA lesions can lead to complications during replication and can result in mutations and chromosomal rearrangements. Eventually this may lead to the development of cancer but also can accelerate aging (de Boer, 2002). To prevent the accumulation of DNA damage, multiple pathways are

in place to detect and repair DNA damage. Several types of DNA damage can occur which can be divided in damage to the single strand, DNA double strand breaks and interstrand cross-links (Figure 1). Pathways that repair damage in single strands are Base Excision Repair (BER), Nucleotide Excision Repair (NER), and Mismatch Repair (MMR). Double strand breaks are predominantly repaired by two different mechanisms, Non-Homologous End Joining (NHEJ) and Homologous Recombination (HR). Finally, interstrand cross-links (ICL) can be repaired by a combination of proteins involved in NER and DSB repair.

Below BER, NER, MMR and ICL will be briefly discussed, while mechanisms of DSB repair will be described in more detail, since the nanoscopic studies described in this thesis are focussed on the molecular mechanisms underlying the repair of double strand breaks, either those that accidentally occur in somatic cells (Chapter 4 and 5), or those that are induced in a regulated manner by the cell during meiosis (Chapter 3).

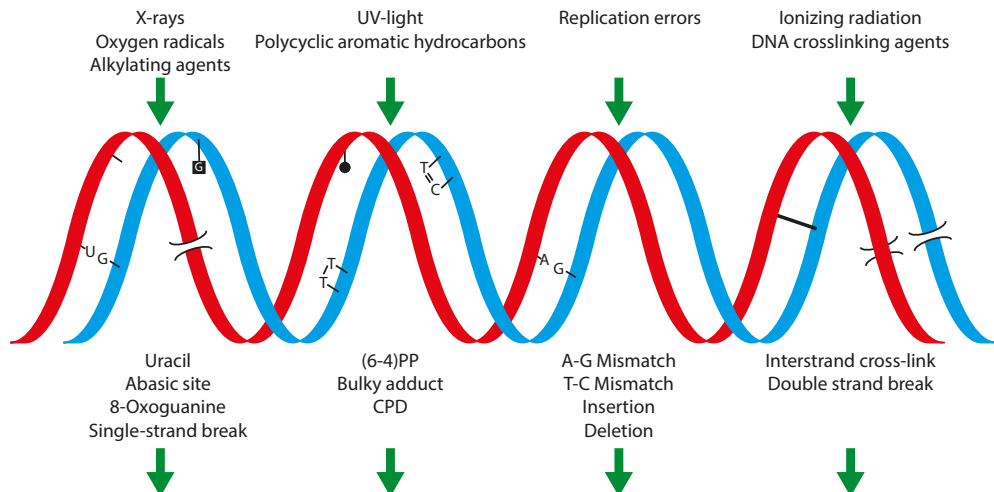


**Figure 1 The DNA Damage Response** The integrity of the DNA inside a cell is challenged by several damaging agents (above), which can lead to different types of DNA damage (below). A broad range of DNA Repair pathways is in place to repair these DNA damage. Small chemical modifications to the DNA molecule are repaired through Base Excision Repair, while bulky lesions induced by for example UV light are paired through Nucleotide Excision Repair. Mismatches introduced during replication are detected and repaired by Mismatch repair. Finally, DNA lesions involving both strands of the DNA molecule, for example crosslinks and double strand breaks are repaired by Interstrand Crosslink Repair (ICL) and Double Strand Break Repair pathways. Figure based on Hoeijmakers, 2001.

## Mismatch Repair

During DNA replication in S-phase, occasionally an incorrect base is incorporated. Such a mismatch can result in the incorporation of mutations in the replicated DNA strand. The pathway responsible for detection and resolution of these errors is referred to as mismatch repair (MMR). The mechanisms of the MMR pathway are highly conserved between prokaryotes and eukaryotes. Mismatches are recognized during replication by homologues of the MutS proteins in *E. coli*, which in humans is present as a heterodimer of MSH2 and MSH6 (Iaccarino et al., 1996) (Figure 2).

It is essential to replace the DNA mismatch in the newly synthesized strand and not in the parental strand, which is regulated through the mechanism of strand specificity. In *E. coli* strand specificity is determined by recognition of methylation of GATC-sequences which are only present in the parental strand. Binding of the mismatch sensor MutS to the mismatch results in an ATP dependent conformational change of MutS and subsequent recruitment of MutL results in displacement of the complex to the nearest methylated GATC site (Allen, 1997; Lahue et al., 1987). Subsequently MutH can introduce a nick at the unmethylated strand. In humans and other prokaryotes, the mechanism of strand discrimination is not fully understood, one of the possibilities is the use of earlier formed nicks at the nascent strand of the lagging strand at the replication fork (Nick McElhinny et al., 2010). However, this does not explain how the strand can be discriminated at the leading strand. The eventually recognized nascent DNA strand then gets nicked and is resected by EXO1 and resulting ssDNA recruits RPA. Subsequently the PCNA sliding clamp together with polymerase  $\delta$  then fills the gap. The nick that is left in the DNA strand can then be ligated by DNA ligase I (Kolodner and Marsischky, 1999).

## Base Excision Repair

Base Excision Repair (BER) detects and repairs small DNA lesions that do not directly interfere with DNA structure. These types of lesions occur by oxidation, deamination or alkylation of the DNA bases. The proteins involved

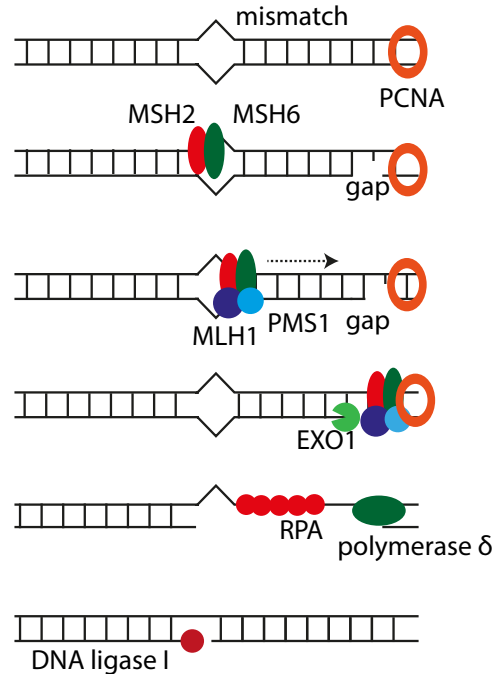


**Figure 2 Mismatch repair.** During replication mismatches between nucleotides can occur due to wrong incorporation of a nucleotide. The MSH2/MSH6 heterodimer can recognize these mismatches. Recruitment of MLH1/PMS1 forms a stable complex that recognizes a nearby ssDNA gap. Subsequently EXO1 can resect the ssDNA and RPA is recruited. Polymerase  $\delta$  can polymerase the DNA from the ssDNA towards the mismatch with mediation of PCNA followed by ligation of the DNA Strand by DNA ligase I. Figure based on Martin and Scharff, 2002.

in the detection of these lesions are DNA glycosylases (Lindahl, 1974). Several glycosylases are present in prokaryotes and eukaryotes which can detect different types of base pair damage (Krokan et al., 1997). The DNA glycosylases can detect damaged nucleotides and remove the nucleotide from the DNA helix. They do so by flipping the base out of the DNA double helix and cleaving the N-glycososidic bond leaving an abasic (AP) site (Figure 3).

This AP site is then recognized by AP endonucleases, like AP endonuclease 1 (APE1) which is highly active in mammalian cells (Friedberg and Meira, 2006). The removal of the AP site results in a single nucleotide gap. Following Short Patch Repair the gap can be filled by DNA Polymerase  $\beta$  (Pol $\beta$ ) and subsequently ligated by DNA ligase III $\alpha$ . When Pol $\beta$  is unable to fill the gap, Long

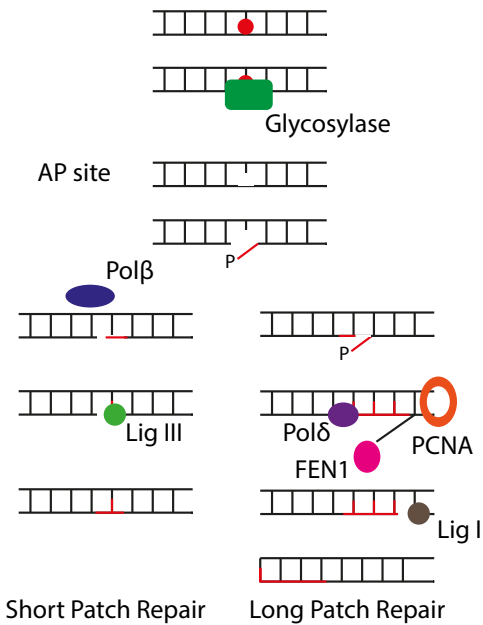


**Figure 3 Base Excision Repair.** Modifications to single bases of the DNA molecule are repaired by Base Excision Repair. The lesions are detected by Glycosylase proteins which convert the damaged base to an abasic (AP) site, which is subsequently converted to a single nucleotide gap. Following short patch repair Pol $\beta$  can fill the gap and LigIII can then seal the nick. In long patch repair, multiple nucleotides are displaced by polymerase  $\delta$  and these nucleotides are removed by FEN1. The double strand can then be restored by LigI. Adapted from: Christmann et al., 2003.

Patch repair takes place and proliferating cell nuclear antigen (PCNA) is recruited (Matsumoto et al., 1994) along with replication factor C (RFC) (Luckow et al., 1994). These proteins use the strand displacement activity of polymerase  $\delta$  to replace a couple of nucleotides. These displaced nucleotides are then removed by Flap endonuclease 1 (FEN1). Subsequently the nick can be ligated by DNA ligase I (LigI) (Dianova et al., 2001).

### Nucleotide Excision Repair

Lesions that results in the distortion of the DNA helix, for example 6-4 photoproducts and cyclobutane pyrimidine dimers (CPDs) are repaired through Nucleotide Excision Repair (NER). These types of lesions are predominately, formed by UV-C irradiation. DNA damage is detected by the NER machinery through two

different mechanisms, transcription coupled repair (TC-NER) and global genome repair (GG-NER) (Bohr, 1985; Mellon et al., 1987) (Figure 4). In TC-NER a lesion in the actively transcribed strand of a gene, is detected by the stalling of RNA polymerase II (RNA polII) when the polymerase encounters damage. Stalling of RNA polII results in the accumulation of the TC-NER specific factors, Cockayne Syndrome Group A and B (CSA and CSB), and USP7 together with UVSSA onto the damage (Fousteri et al., 2006; Nakazawa et al., 2012; Schwertman et al., 2012). Lesions outside active genes (or, sometimes lesions not yet detected during transcription) are detected by the damage sensor Xeroderma pigmentosum group C (XPC) which forms a complex with RAD23B and Centrin-2 (Masutani et al., 1994; Nishi et al., 2005). The XPC complex binds to distorted DNA structures and facilitates core NER proteins to process the lesion. The UV-DDB complex consisting of DNA damage-binding protein 1 (DDB1) and DDB2 mediates binding of XPC to the lesion (Moser et al., 2005).

After detection either by TC-NER or GG-NER, the so-called core NER proteins together form the NER repair complex. To enable access of other proteins to the DNA lesion, Transcription factor II H (TFIIH) complex unwinds the DNA helix using helicases XPB and XPD (Flores et al., 1992; Schaeffer et al., 1994). At the same time the TFIIH complex together with XPA verify the presence of a lesion and stabilise the structure. Subsequently the DNA strand containing the damaged nucleotides is excised by endonucleases XPG at the 3' side of the lesion while ERCC1-XPF complex takes care for excision at the 5' side (de Laat, 1998). The ssDNA of the undamaged DNA strand is covered and protected by Replication Protein A (RPA) (He et al., 1995). DNA polymerases together with PCNA can subsequently fill the single strand gap. Ligation by DNA ligase III finally fully restores the DNA double helix (Moser et al., 2007).

### Interstrand Crosslink Repair

Two DNA strands can become covalently crosslinked, which is very problematic for proper replication and transcription of the DNA. This

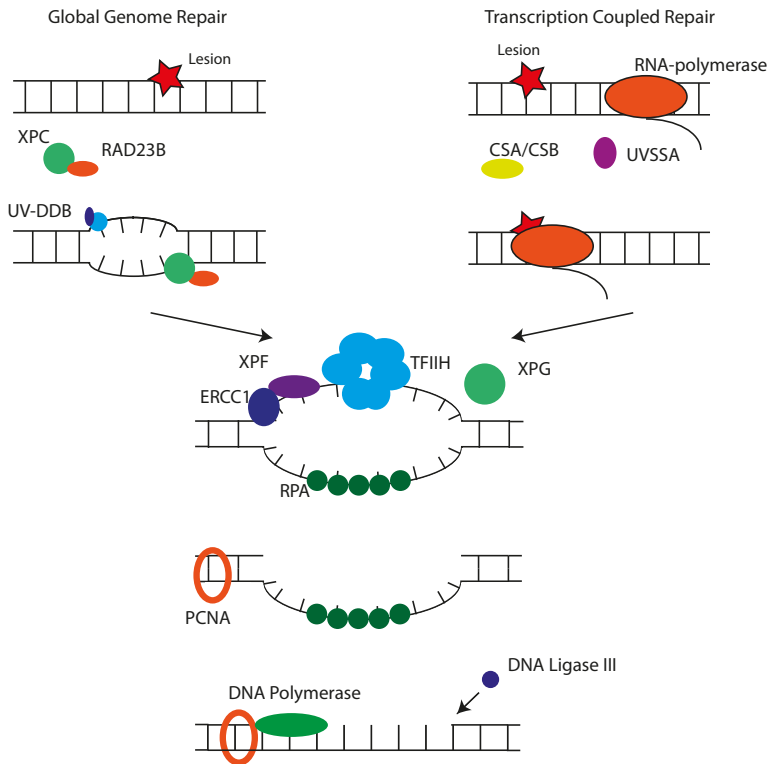


**Figure 4 Nucleotide Excision Repair.** Bulky DNA lesions can either be repaired through GG-NER or TC-NER. The XPC-RAD23 complex scans the chromatin for lesions. Upon binding of the XPC-RAD23B complex core NER factors can bind to the lesion. In TC-NER lesions in the transcribed strands of genes are detected by stalling of RNA PolII which result in the recruitment of CSA/CSB and UVSSA. The TFIIH transcription complex opens up the lesion which enables binding of XPF/ERCC1 and XPG to excise the damaged strand while the other strand of ssDNA is protected by RPA. DNA polymerases can fill the ssDNA gap which is then ligated by DNA Ligase III. Figure adapted from Foustari and Mullenders, 2008; Marteiijn et al., 2014.

explains the efficiency in cancer treatment of chemotherapeutic drugs as mitomycin C and cisplatin which induce these interstrand crosslinks (ICL) and thereby targets fast replicating cancer cells (Deans and West, 2011). For removal of the interstrand crosslink a complex pathway is required which involves the incision and restoration by DNA synthesis of both DNA strands. Interestingly, repair of interstrand crosslinks requires various repair factors involved in several other DNA repair pathways. During G1 of the cell cycle ICLs can be detected during transcription by stalling of RNA polymerase and are repaired by NER machinery (Sarkar et al., 2006). The repair of ICL during transcription is most relevant for slowly or non-replicating cells. Probably certain ICLs, which distort helix structure can also

be detected by GG-NER by recognition by XPC (Muniandy et al., 2010). As with replication dependent repair the crosslink can be 'unhooked' by nucleases (e.g. XPF-ERCC1) and subsequently Translesion polymerases (TLS) can bypass the lesion (Kuraoka, 2000; Sarkar et al., 2006).

During replication in S-phase, crosslinks will be encountered by stalling of the replication fork. This results in activation of proteins of the Fanconi anemia pathway. Fanconi anemia is a rare genetic disease which is caused by mutations in any of the proteins involved in this pathway, resulting in impaired bone marrow function, and high risks for different types of cancer. The FA proteins are essential for replication dependent repair, but appear not to be involved in replication independent repair. A complex

of FANCM, FAA24 and MHF1/2 recognize the crosslink. FANCM subsequently recruits the FA-core complex to the stalled replication fork. The FA-core complex is a large complex consisting of eight proteins (FANCA, -B, -C, -E, -F, -G, -L and -M) (Medhurst, 2006).

The recruitment of the core complex or more precisely the ubiquitylation of FANCD2, enables the recruitment of endonucleases like XPF-ERCC1, also involved in NER, and MUS81-EME1 and SLX1-SLX4, which also resolve recombination intermediates during homologous recombination (Sengerová et al., 2011). These nucleases excise the crosslink leading to a DNA double strand break. Translesion synthesis polymerases Pol  $\zeta$  and REV1 are subsequently used to bypass the damaged nucleotide. To restore the replication fork strand invasion can take place by RAD51 which is supported by other proteins involved in homologous recombination (Long et al., 2011).

### Double Strand Break Repair

DNA Double Strand Breaks (DSBs) obviously are a serious threat to the genome since breakage of both strands of the DNA helix can, for instance, result in chromosomal rearrangements. These can potentially lead to mutations, aberrant expression levels or fusion of genes that when expressed may disrupt transcriptional programs or other cellular function (Kanaar et al., 1998). DSBs occur as a result of ionizing radiation or by DNA modifying chemicals such as bleomycin which can cleave double-stranded DNA, but indirectly also replication inhibitors such as hydroxyurea and crosslinking agents like Mitomycin C and cisplatin can result in the formation DSBs. Furthermore, DSBs can be formed due to failure of repair of ssDNA lesions by the SSB pathways.

DSBs can be independently detected by both the Mre11, Rad50, Nbs1 (MRN) complex and the Ku70/80 heterodimer (Clerici et al., 2008; de Jager et al., 2001) (Figure 5). The way DSBs are recognized and repaired is dependent on the cell cycle. While Ku70/80 is involved in Non-Homologous End Joining (NHEJ) in G0 and G1, the MRN complex promotes Homologous Recombination (HR) in S and G2 phase. Upon recruitment of MRN the interaction between Nbs1 and Ser/Thr protein kinase ATM induces

auto-phosphorylation of ATM (Lee, 2004, 2005). Activated ATM subsequently phosphorylates several proteins involved in the DSB Repair pathway. The phosphorylation of histone H2AX at Ser139 by ATM is one of the hallmarks of DSB induction (Burma et al., 2001). Independently the recruitment of Ku70/80 can activate the protein kinase DNA-PKcs which is also involved in the phosphorylation of H2AX (An et al., 2010; Stiff, 2004). H2AX, is present in nucleosomes throughout the genome and upon activation of the DNA DSB Repair response, are phosphorylated H2AX ( $\gamma$ H2AX) at and in the vicinity of the DSBs. The phosphorylation of H2AX can spread several kilobases away from the DSB, and has been reported to be actually be more enriched further away from the break (Iacovoni et al., 2010; Rogakou et al., 1998). The phosphorylation of H2AX promotes the recruitment of MDC1 which binds directly to phosphorylated H2AX through its BRCT domain (Stucki et al., 2005). Further phosphorylation of MDC1 provides a binding platform for the E3 ubiquitin ligase RNF8 along with the E2 conjugating enzyme UBC13 (Plans et al., 2006).

This signalling cascade leads to the recruitment of several DNA response proteins of which 53BP1 and BRCA1 are essential in the choice by which pathway the DSB will be repaired, either Non-homologous End Joining (NHEJ) or Homologous Recombination (HR) (Shibata et al., 2011; Shrivastav et al., 2008). While HR, uses a donor template for repair, and is considered error free, NHEJ is prone to errors during repair. It is interestingly to note that DSBs are also induced in cells during specific cellular processes; in VD-J recombination in immune cells and in chromosome synapsis and crossover formation during meiosis. In VD-J recombination the potentially mutagenic properties of the NHEJ pathway are employed to create the variable sequence regions of antibodies. In meiosis, as will be discussed later in this introduction, the DNA strand interactions during HR are exploited for exchange of genetic information through chromosome crossover and to align the maternal and paternal homologous chromosomes so that they can be properly segregated during meiotic division.

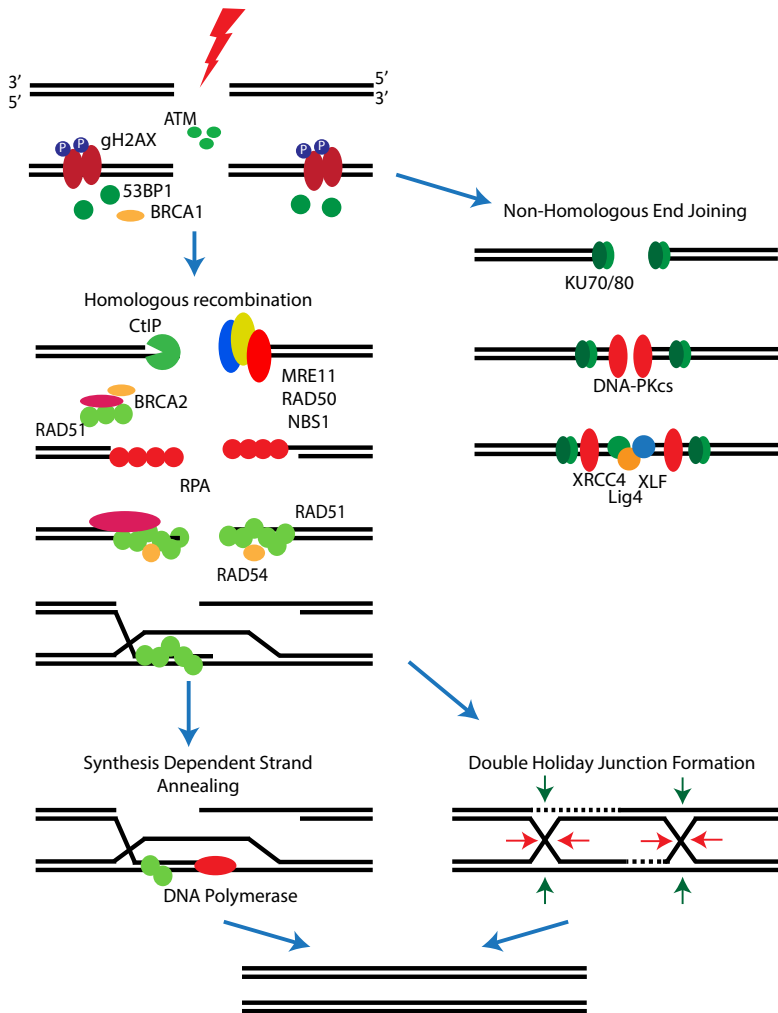


**Figure 5 Mechanisms of Double Strand Break Repair.** The detection of the DSB by the MRN complex induces the phosphorylation of the histone H2AX through activation of ATM. Depending on several factors as chromatin environment and cell cycle the DSB can be repaired by HR or NHEJ. In NHEJ 53BP1 promotes NHEJ. In NHEJ the hetero dimer Ku70/80 binds to the ends of the DSB and recruits DNA-PKcs. After the ends are properly processes the ligase complex consisting of XRCC4, XLF and LIG4 can ligate the two ends together. BRCA1 stimulates Homologous recombination by promotion of resection of the dsDNA. The ssDNA is protected by coating by RPA. The interaction of BRCA1 with BRCA2 through PALB2 facilitates the displacement of RPA and loading of RAD51 by BRCA2 onto the ssDNA. Several proteins, e.g. RAD54, are involved to mediate RAD51 in the process of homology search and strand invasion. RAD54 is also involved in removing RAD51 from the hetero duplex DNA. Subsequently by polymerization of the missing DNA the gap can be closed following the SDSA pathway. However, it is also possible that the second end of the break is captured and a double holiday junction is formed, which can be dissolved or resolved by different proteins, which lead to either Non-crossover or crossover products.

Although the exact mechanisms are not fully understood, evidence has been provided that the choice between HR and NHEJ repair is regulated through several proteins. While 53BP1 promotes repair through NHEJ, BRCA1 is essential for repair through HR (Chapman et al.,

2012a). It has been shown that BRCA1 promotes resection of the DNA, essential for HR, but at the same time resection needs to be prevented for NHEJ. Cells lacking functional BRCA1 are impaired in HR, however, additional loss of 53BP1 restores HR, suggesting the close interplay

between the two pathways (Bouwman et al., 2010). The pathway choice is highly dependent on cell cycle stage. Since HR requires the presence of the sister chromatid as a template, HR is mainly active during S/G2, while NHEJ is active during the entire cell cycle. Another aspect that affects pathway choice is the complexity of the DSB, where simple breaks can easily be ligated through NHEJ, and more complex breaks require more extensive end processing by the HR machinery.

### Non-Homologous End-Joining

During the G0 and G1 cell cycle phase NHEJ is the most prominent repair pathway. Upon detection of the DSB, the Ku70/Ku80 heterodimer binds to the broken ends of the DNA double strand (Britton et al., 2013; Walker et al., 2001). Binding of the Ku heterodimer enables the recruitment of DNA-PKcs which is stabilizing the two DNA ends (Gottlieb and Jackson, 1993). Subsequently DNA Ligase IV binds together with XRCC4 and XLF followed by displacement of DNA-PKcs (Hammel et al., 2010). Most DSBs have DNA ends which contain chemical modifications which need to be removed before the ends can be ligated together. Different nucleases are used to process the DNA ends while DNA polymerase is used to fill 3' overhanging ssDNA. If both ends of the break are compatible the ends can be ligated by the Ligase IV complex (Wilson et al., 1997).

Since NHEJ is also the pathway required for VD/J recombination, mutations in proteins essential for NHEJ can give rise to immune deficiencies, due to failure in the generation of antibodies (Nussenzweig et al., 1996; Taccioli et al., 1993). In VD/J recombination two DSBs are introduced by recombination-activating gene 1 (RAG1) and RAG2 and used to generate unique DNA sequences coding for the variable regions of antibodies, which is essential for the adaptive immune system (Grawunder et al., 1998).

### Homologous Recombination

Repair through Homologous Recombination requires 5 to 3' resection of the dsDNA ends, which is initiated by the MRN complex (Gravel et al., 2008). CtIP, upon interaction with the

MRN complex is recruited in a complex with BRCA1 and completes initial resection up to a couple of hundred base pairs (Sartori et al., 2007). Further resection is performed by several complexes, of which Exo1 and Dna2 have shown to be major players (Nimonkar et al., 2011). In mammalian cells BLM helicase activity is also important, since loss of this protein result in a reduced resection rate (Gravel et al., 2008). The resected ssDNA is rapidly covered by the Replication Protein A (RPA) heterotrimer to protect the ssDNA from degradation (Wang and Haber, 2004).

In yeast and mammalian cells, end resection can proceed up to several kilobases from the DSB (Zhou et al., 2013; Zierhut and Diffley, 2008). In most cases the recombinase RAD51 (bacterial RecA) replaces RPA on the resected ssDNA, forming nucleoprotein filaments wrapped in a helical way around the ssDNA. In yeast the replacement of RPA by RAD51 requires the activity of RAD52 (Hays et al., 1998), while in mammalian cells this function is likely executed by BRCA2 (Davies et al., 2001). The RAD51-DNA filament then plays a role in the search for the homologous DNA template that is required for error free repair of the DSB. When the homologous sequence in the sister chromatid is found, strand invasion can take place. After strand invasion of the RAD51 coated ssDNA a so-called D-loop structure is formed, in which one of the strand of the invaded dsDNA molecule is displaced, while the other strand pairs with the invading strand (Wyman and Kanaar, 2006). This is followed by DNA synthesis at the invaded strand by polymerases (Figure 5). After polymerization of the DNA required to restore the DNA sequence, the D-loop can be resolved and the extended DNA molecule is annealed to the DNA on the other strand, a process referred to as synthesis-dependent strand annealing (SDSA). Alternatively, the formed D-loop can migrate along the DNA molecule and the DNA on the other end of the break can be captured forming a double holiday junction (dHJ). The dHJ is then dissolved by a complex of BLM, TOPOIII and RMI1/2 in which case no crossover between the chromatids occurs, or it can be resolved by specific resolvases, for example MUS81-EME1

and GEN1. In some cases, depending on how these resolvases resolve the dHJ, this can lead to crossover (Matos and West, 2014).

Repetitive DNA sequences can also be repaired by an alternative pathway, called Single Strand Annealing (SSA) repair which uses the flanking homologous sequences around the DSB. In this situation, homologous sequences on the same broken DNA molecule can due to resection anneal and resolve the DSB by removal of the overhanging nucleotides using proteins involved in MMR. SSA is RAD51 independent and is induced by resection of repeats. RAD52 is suggested to be involved in SSA in both yeast and mammalian cells (Ochs et al., 2016; Singleton et al., 2002; Symington, 2002). SSA is a mutagenic repair pathway since it leads to loss of DNA nucleotides and is not favourable in case the DNA contains genetic information, however in some genomic regions this could be an alternative solution to repair through HR.

### **RAD51**

RAD51 is one of the core players in HR repair. It is involved in both homology search and subsequent strand invasion. RAD51 is, like its bacterial homolog RecA, a 43 kDa protein and contains peptide motifs responsible for its ATPase function (so called Walker A and B motifs). The ATPase activity of RAD51 was shown to be required for the dynamic organization of the filaments formed on ssDNA since filaments formed by ATPase deficient RAD51 (K191R) are impaired in strand invasion capacity (Fung et al., 2006).

In vitro incubation of both purified RecA and RAD51 with DNA substrates results in the formation of right-handed helical filaments which can be visualized by electron microscopy (Stasiak and Di Capua, 1982; Sung and Robberson, 1995). RAD51 bound DNA is underwound, both ssDNA as well as dsDNA, and the measured length of RAD51 DNA shows an extension of the DNA about 1.5 times that of B-form DNA, the common conformation of helical DNA (Benson et al., 1994). RAD51 bind 3 nucleotides per monomer and the helical pitch of RAD51 DNA is about 10 nm per turn and contains 19-20 nucleotides (Bell et al., 2012; Sheridan et al., 2008).

Single molecule experiments with fluorescently labelled RecA have shown that nucleation of filament formation can happen at different places along the DNA substrate, which then is followed by growth of the filament until a complete filament is formed (Galletto et al., 2006). Furthermore, although RAD51 can form filaments on both single stranded as well as double stranded DNA, ssDNA is the more favourable substrate (Candelli et al., 2014).

An important question is how the RAD51 filament is involved in homology search. To find the homologous DNA sequence to which the filament can pair, the large 3D volume of the genome needs to be explored. For RecA it has been shown by single molecule experiments that the length and the rigidity of the filaments is aiding in homology search, because it enables to probe the target DNA along the filament (Forget and Kowalczykowski, 2012). More recently it was shown for RAD51 by different single-molecule experiments that sets of approximately eight RAD51 monomers present in filaments can be used to probe the DNA sequence for homology (Lee et al., 2015). Although in vitro RAD51 is able to perform strand invasion by itself, in vivo RAD51 function is supported by several mediator proteins (Zelensky et al., 2014). In many organisms, several paralogs of RAD51 (RAD51B, RAD51C, RAD51D, XRCC2, and XRCC3) have been found of which some appear essential for proper homologous recombination. Those paralogs do not have recombination activity by themselves but are able to stimulate RAD51 recombination activity, by mechanisms which are not entirely clear (Masson et al., 2001; Yonetani, 2005). Some recent work has shown that RAD51 paralogs stabilize RAD51 filament and regulate the disassembly of the filament when necessary (Jensen et al., 2013; Taylor et al., 2015).

### **BRCA2**

BRCA2 is a large protein of about 384 kDa and consists of several domains with different functions. The N-terminal domain contains the interaction site with PALB2 (Partner and Localizer of BRCA2), through which BRCA2 interacts with BRCA1 (Oliver et al., 2009). An important



domain of BRCA2 contains the so-called BRC repeats which are essential for physical interaction with RAD51 (Bork et al., 1996). The BRC domain is one of the regions of BRCA2 which is highly conserved among species. Interestingly, BRC repeats 1 to 4 have high affinity with free RAD51 protein, while repeats 5 to 8 have preference for RAD51 bound to ssDNA (Carreira and Kowalczykowski, 2011). RAD51 not only binds to BRCA2 through the BRC repeats (Davies and Pellegrini, 2007), but also to an additional RAD51 binding site in the C terminal domain. The C-terminal part of BRCA2 also harbours the DNA-binding domain (DBD). The size of BRCA2 made it challenging to obtain a protein structure by x-ray crystallography, but, recently the structure of BRCA2 has been visualised by EM tomography (Shahid et al., 2014), revealing the positions in the BRCA2 dimer where RAD51 can bind. The C-terminal domain of BRCA2 has shown to be important in stabilization of replication forks in a HR independent way (Schlacher et al., 2011).

As mentioned above, BRCA2 is required for displacement of RPA for RAD51 at the ssDNA overhangs and this is also demonstrated by the fact that focus formation of RAD51 is dependent on BRCA2 (Yuan et al., 1999). For BRCA2 itself, recruitment to the DSB is dependent on the presence of BRCA1. BRCA1 and BRCA2 can form a complex through their interaction with PALB2 (Sy et al., 2009). Studying the dynamics of BRCA2 by single particle tracking has revealed that RAD51 interacts with BRCA2 while diffusing through the nucleus (Reuter et al., 2014).

BRCA2 was identified as a tumour suppressor gene, and is similar to BRCA1, when mutated, an important risk factor in hereditary breast and ovarian cancer (King, 2003). Most patients carry a heterozygous mutation of BRCA2, which upon loss of the functional copy of the gene, called loss of heterozygosity, leads to cells that only express a truncated form of BRCA2. In humans the nuclear localization signal for BRCA2 is present near the end of the protein, which explains why BRCA2 with mutations which resulting in truncated forms of BRCA2 are often not localized in the nucleus, impairing the process of HR (Spain et al., 1999). Patients with cancers with

mutated BRCA2, or a possible other defect in HR can profit from treatment with PARP inhibitors. Inhibition of PARP results in the conversion from single strand breaks to double strand breaks, which cannot be repaired by the cancer cells which are deficient in homologous recombination, thereby resulting in genome instability and cell death (Bryant et al., 2005; Farmer et al., 2005). The mechanism in which two genetic events are required for cell death is called synthetic lethality. Additionally, it has been found that BRCA2 is degraded in response to hyperthermia treatment (Krawczyk et al., 2011). A treatment of a tumor by local hyperthermia in combination with radiotherapy or PARP inhibitors can therefore improve the sensitization of the cancer cells to DNA damage by synthetically make them homologous recombination deficient.

#### **RAD54**

Another important mediator protein for RAD51 during homologous recombination is the ATPase RAD54. Human RAD54 is about 84 kDa in size and is a protein of the family of SWI2/SNF2 helicases. RAD54 is able to translocate itself along the DNA using ATP hydrolysis (Amítani et al., 2006).

RAD54 is involved in several steps in the process of homology search and strand invasion during homologous recombination and loss of RAD54 results in reduced homologous recombination proficiency (Wesoly et al., 2006). RAD54 is directly interacting with RAD51 nucleoprotein filaments (Mazin et al., 2000; Solinger et al., 2001). Through these interactions RAD54 has been shown to be involved in stabilizing the RAD51 ssDNA filament on the one hand (Mazin et al., 2003), while on the other hand it can disassemble RAD51 filaments on dsDNA (Solinger et al., 2002). It has therefore been suggested that RAD54 is involved in regulating the removal of RAD51 on dsDNA (Masonet et al., 2015). RAD54 is able to stimulate D-loop formation by RAD51 an essential step in homologous recombination (Petukhova et al., 1998). Furthermore by the interaction with RAD51, RAD54 is able to displace nucleosomes in the chromatin (Alexeev et al., 2003). After strand invasion, RAD54 is also

important in removal of the RAD51 from the dsDNA. RAD54 suggestively also has functions in homologous recombination independent of RAD51. In vitro RAD54 can bind to double Holiday Junctions and is able to perform DNA branch migration which requires its ATPase function. Furthermore, RAD54 directly interacts with dHJ resolvase Mus81 and stimulates Mus81-MMS4 nuclease activity at dHJs (Matulova et al., 2009).

### Double Strand Break Foci

Induction of DSBs results in the accumulation of several DNA DSB Repair proteins to the lesion. The accumulation of these proteins, generally named DSB foci, or DSB related foci, can be visualized by fluorescence microscopy using antibodies or by stably or transiently expressing the protein of interest to a fluorescent or photoactivatable protein (Figure 6). Besides the accumulation of proteins in foci, local post-translational modifications can be detected by specific antibodies. This makes DSB foci a very

interesting subject to study DSB repair by microscopy.

To study mechanisms of DSB repair and focus formation, DSBs can be induced in several ways. Commonly cells are exposed to ionizing radiation, for example by using gamma irradiation from a radioactive source. Breaks can also be introduced by a source aimed at a small region within the cell nucleus. A frequently used method is the induction of damage by sensitizing the DNA by incorporation of the thymidine analog BrdU in combination with 405 nm laser light to create a strip of DNA damage through the nucleus. Other alternatives are a UV laser or a multiphoton laser. However, these techniques have the disadvantage that many other types of DNA damage are induced (Dinant et al., 2007). A more specific method for local induction of DSBs is the use of a source emitting alpha particles (Stap et al., 2008), in which single alpha particles create a track of DSBs in the nucleus (Figure 6B). Furthermore, DSBs can be

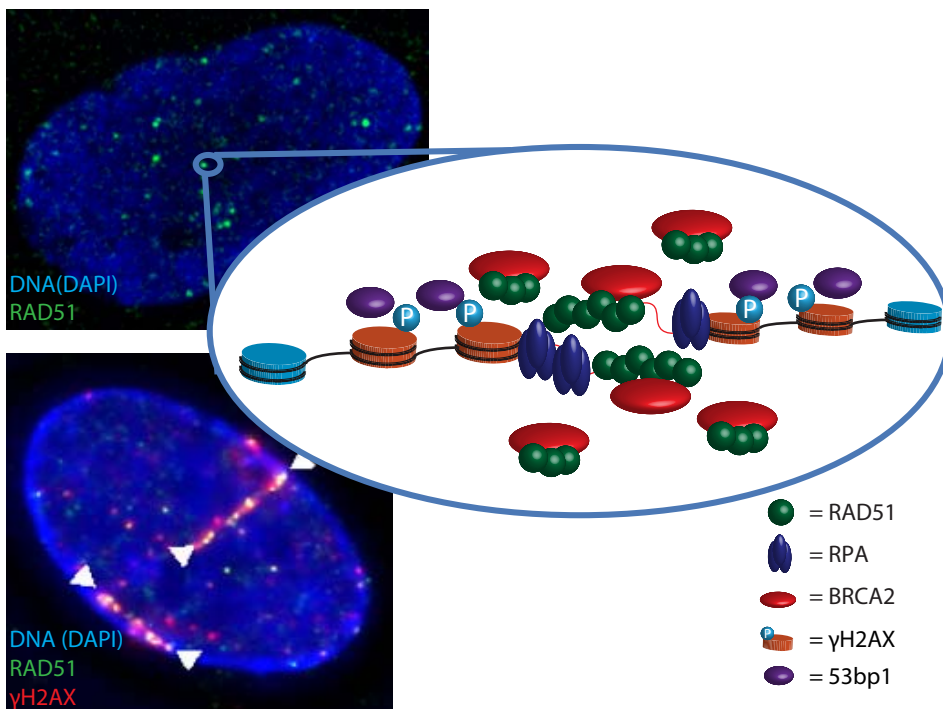


**Figure 6 Double Strand Break Foci.** A) Cell treated with ionizing radiation. Formation of RAD51 foci. Cartoon depicting a suggestive look at the internal distribution of a DSB focus. B) Using an alpha particle source DSBs can be locally induced along a track. Image from Krawczyk et al., 2011.

induced by DNA restriction enzymes. This can be achieved by introducing a unique restriction site in the genome, for example the I-SceI site, but also rare natural occurring restriction sites can be used (Iacovoni et al., 2010). With the recent advances in genome editing technologies using the bacterial host defence mechanism, CRISPR-Cas9, DSBs can also be introduced at specific sequences by directing the Cas9 protein to the genomic site of interest by gRNAs.

One of the hallmarks of DSB induction, phosphorylated H2AX ( $\gamma$ H2AX), is widely used to visualise DSBs and can be detected by antibodies right after the induction of DSBs. In line with their biological function, proteins involved in early steps of DSB repair e.g. MDC1 and proteins from the MRN complex can also be detected rapidly after induction of the DSBs. Also, phosphorylated ATM (S1981), which is essential

for the phosphorylation of several important DSB factors readily accumulates at DSBs (Suzuki et al., 2006). A bit later after damage induction also 53BP1 and BRCA1, which likely play a role in pathway choice between HR and NHEJ, are visible in foci (Bekker-Jensen et al., 2005). Interestingly, several NHEJ factors do not accumulate at DSBs to such an extent that they can be visualised as DSB foci. For example, Ku70/80 and DNA-PKcs does not form visible foci (Bekker-Jensen et al., 2006).

Besides BRCA1, also other HR factors, like PALB2 and BRCA2 accumulate in sufficient numbers at DSBs to be visualized as DSB foci. Furthermore, RAD51 forms DSB foci, but after induction of DNA damage it takes some time for RAD51 to appear in foci. Interestingly MRN and RAD51 only partly co-localize in foci, which can be explained by the fact that RAD51 is required

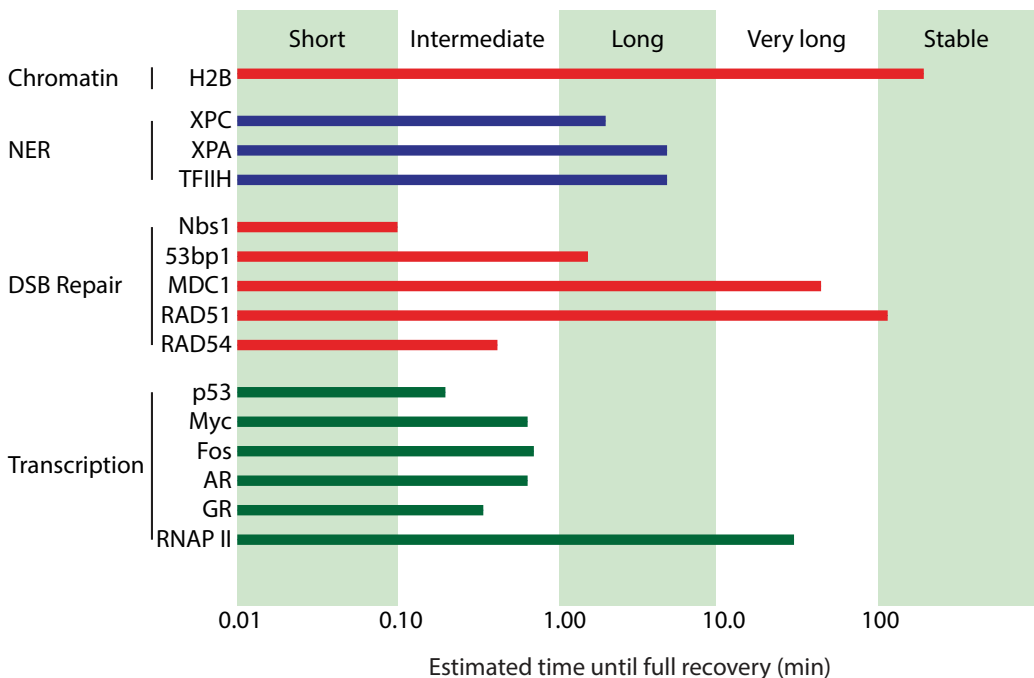


**Figure 7 Binding times of DNA binding proteins.** FRAP is an important method to assess the binding kinetics of DNA interacting proteins with the chromatin. The average residence times of protein on the DNA can be estimated from the recovery rate of a protein after photobleaching. The residence time of different proteins can differ over several decades from milliseconds to minutes or even hours. Very long stable interactions can be found at protein part of the chromatin e.g. histones while transcription factors have much shorter transient interactions. Proteins involved in DNA Repair e.g. NER or DSB Repair show frequently longer binding times than transcription factors. Figure adapted from van Royen et al., 2011.

later down the pathway, while MRN is required for initial resection. RAD51 remains at the focus for several hours, with the number of foci decreasing when DNA repair is performed (Agarwal et al., 2011; van Veelen et al., 2005). Although most factors disappear as accumulations after some time, it has for now been difficult to assess the rate of repair based on the composition of foci since there is so much variation and it is not always clear how the disappearance of foci correlate with the moment repair is completed.

Nonetheless analysis of RAD51 foci formation is often even used as a read out for proficiency of cells to perform HR (Bhattacharyya et al., 2000; Yuan et al., 1999). Although the accumulation of RAD51 might be explained by the formation of filaments with resected ssDNA (Raderschall et al., 1999) for some other proteins the mechanism and function of in DSB focus formation is still unclear. It has been proposed that focus formation reflects compartmentalization inside the nucleus, isolating the DSB from the rest of the DNA during repair (Bekker-Jensen and Mailand, 2010). The formation of biopolymer networks such as poly(ADP-ribose) (PAR) at the DSB might induce liquid demixing and thereby facilitates the local accumulation of proteins at the DSB (Altmeyer et al., 2015). Also, the large number of other post-translational modifications of proteins associated with induction of DSBs could be important for regulation of focus formation.

### ***Functional imaging of DSB Repair Proteins***

To study the dynamics of DNA-protein complexes in living cells a well-established technique to apply is Fluorescence Recovery After Photobleaching (FRAP). In FRAP, using a fluorescently labelled protein, the recovery of fluorescence after photobleaching a region in the cell is analyzed. In this way one can determine the kinetics of the fluorescent labelled protein. During the acquisition time of a FRAP experiment the chromatin can be considered immobile, while the interactions of the protein with the DNA can be studied and, for example, residence times of protein complexes on the DNA can be quantified (van Royen et al., 2011). It is interesting to observe that DNA Repair proteins

have relatively long residence times at the DNA, while for example transcription factors show much shorter binding (Figure 7). FRAP experiments on GFP tagged RAD51 have shown that it is almost stably bound at the foci (Essers et al., 2002) with a large immobile fraction, while others DSB proteins show very different dynamics at the foci. 53BP1 is present with a quite large immobile fraction at foci, where its immobilization requires interaction with MDC1 (Mok and Henderson, 2012). In contrast, RAD54 has much shorter residence times, in the order of seconds. However, also RAD54 forms bright DSB foci with tens to hundreds of molecules localized per focus, indicating very high on and off rates to and from the foci (Agarwal et al., 2011). Interestingly, in cells expressing mutant RAD54 unable to hydrolyse ATP, the mutant molecules in part are tightly bound to the focus, suggesting that these proteins are immobilized because they cannot perform their (ATP-hydrolysing) function.

Also, some attempts have been made to quantify the number of the different proteins inside the focus, either by using FCS or using internal fluorescent intensity standards. Interestingly, MDC1 and 53BP1 supposedly are present with thousands of molecules in a focus while for RAD54 the number is estimated to be several hundred (Agarwal et al., 2011; Mok and Henderson, 2012). However, these estimates are based on fluorescence imaging, and clear standards for this are not established, challenging comparison between different reports.

### ***Resolving the internal organization of DSB foci***

The internal protein distribution within DSB foci is difficult to assess with conventional fluorescence microscopy, although it is possible to discriminate proteins at the core of the DSB (like RAD51), or in the periphery (chromatin associated proteins like  $\gamma$ H2AX and 53BP1) (Bekker-Jensen et al., 2006). Using a combination of light microscopy and immunogold labelling it was shown that  $\gamma$ H2AX and Mre11 are forming separate compartments at the sites of damage (Dellaire et al., 2009). Super resolution microscopy now has opened the possibilities to study the internal organization of the foci. For

example, it has been shown using Structured Illumination microscopy that in foci that are repaired by HR BRCA1 is localized at the centre of the focus and 53BP1 is excluded from the core of the focus (Chapman et al., 2012b). Furthermore it was observed, by specific protein extraction protocols and using single molecule localization microscopy, that the NHEJ factors Ku70/80 localize near the two ends of the DSB while proteins as XRCC4 and XLF form elongated structures coating the DNA (Britton et al., 2013; Reid et al., 2015).

The internal organization of foci, especially the relative localization of different repair factors can be very useful to understand the underlying repair mechanisms even further as the different examples throughout this thesis are showing.

### **Double strand Break Repair and Homologous Recombination during Meiosis**

The fusion of paternal and maternal cells during sexual reproduction requires the formation of cells that only contain a single copy of every chromosome. The somatic cells that are the precursors of the germ cells need to go through two cell divisions. In the first meiotic division, the cells go from diploid to haploid, with either a paternal or maternal pair of every chromosome. In the second meiotic division, the chromatids are separated giving rise to four daughter cells from one precursor cell. During the meiotic divisions, proper segregation of the chromatids to the germ cells is both essential and challenging.

In prophase of the first meiotic division, homologous paternal and maternal chromosomes should first be paired in order to make sure that each daughter cell receives exactly one copy of each of the chromosomes. For pairing to take place the chromosomes need to find their homologous counterpart, which in higher eukaryotes takes several days to weeks to complete (Figure 8) (Bennett, 1977). To facilitate homologous chromosome pairing, DSBs are induced in a controlled manner by the nuclease Spo11 (Keeney et al., 1997). During meiosis, NHEJ is repressed making sure that the induced breaks

are repaired through homologous recombination, which only can take place if a homologous template is found (Joyce et al., 2012). By inducing multiple double strand breaks along the chromosomes, the simultaneous homology search and subsequent repair activity, as well as the formation of the synaptonemal complex leads to pairing of the homologous chromosomes. Similar to homologous recombination in somatic cells, homology search and repair in meiosis is accompanied by the accumulation of recombinases like RAD51 in DSB foci, with the important difference that in meiosis, DMC1 (a RAD51 paralogue) is present and localises at the DSB foci (see below).

The induction of DSBs and repair is tightly regulated in meiosis. Most breaks are directed to be repaired by the homologous chromosome, however only a subset of these lead to a crossover event. The number of crossover events per cell is actually quite constant. The fate of individual DSBs is determined by a complex mechanism, in which the relative position of DSBs in the nucleus appears to be essential (Wang et al., 2015). Precise analysis in yeast identified specific regions, named hotspots, where DSBs are more frequently found (Cao et al., 1990). Also in mouse, hotspots are found, but these are more difficult to identify than in yeast because the mouse genome is much larger while only a few crossovers per chromosome occur. Furthermore it is difficult to obtain a synchronous population of meiotic mouse cells (Petes, 2001; Qin et al., 2004).

In meiosis the homologous chromosome is preferentially used as a homologous template and recombination the sister chromatid is suppressed, in yeast it is estimated that twofold more interhomolog than intersister recombination is taking place (Schwacha and Kleckner, 1997). Homologous recombination between the homologous chromosomes is essential since it physically connects the chromosomes which is required for proper segregation of the chromosomes (Sung and Klein, 2006). However, it is to note that strand invasion at the homologous chromosome not necessarily leads to a crossover since repair can also take place via SDSA and even a double holiday junction a

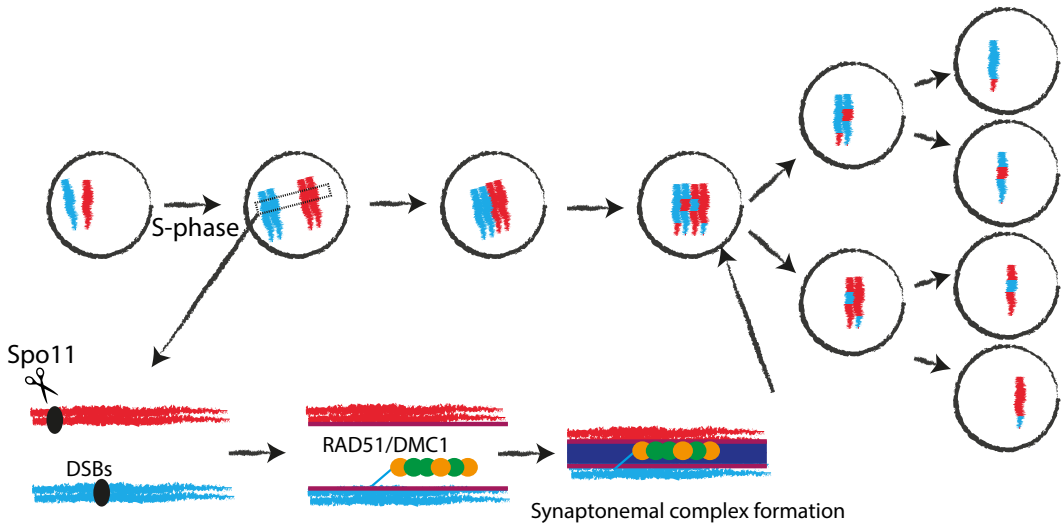


**Figure 8 DSB Repair during meiosis.** During meiosis, a single diploid cell is used to form four haploid cells. First the DNA is replicated. Subsequently an essential step is the alignment of the homologous chromosomes. This is mediated by induction of DSBs by the Spo11 endonuclease. Subsequently, repair of DSBs through HR, by recombinases RAD51 and meiosis specific recombinase DMC1 along with the formation of the synaptonemal complex results in paired chromosomes in which some of the genetic information is exchanged through crossover. After these processes are finished the cell divides twice to produce four daughter cells.

double holiday junction not necessarily leads to formation of a crossover. Formation of crossovers between the chromosomes generates rearrangements of different alleles along homologous chromosomes, which results in increased genomic diversity in the offspring. Furthermore, for proper alignment of the chromosomes during the first meiotic metaphase it is required to have at least one crossover per chromosome pair.

Along with the induction and repair of DSBs the pairing of the homologous chromosomes is stabilized by a proteinaceous scaffold named the synaptonemal complex (SC). The processing of the DSBs and SC formation are dependent on each other. On the one hand mutants lacking SC proteins which do not form a complete SC have elevated numbers of unrepaired breaks at later stages of meiosis, on the other hand cells that do not induce DSB, e.g. by knocking out Spo11, do not reach fully synapsed SCs (Baudat et al., 2000). As revealed by immunogold electron microscopy the synaptonemal complex consists of a central element (CE) and two lateral elements (Hamer et al., 2008). The spatial separation of the lateral elements of about 200 nm was

recently confirmed by super resolution using SIM (Qiao et al., 2012) and dSTORM (Schücker et al., 2015).

### **DMC1**

As already mentioned above, in many organisms a key difference between meiotic homologous recombination compared to homologous recombination somatic cells is the expression of and the localization to DSBs of a meiosis specific recombinase, DMC1 (a RAD51 paralog) to the DSBs. DMC1 is only expressed during meiosis and was first discovered in yeast. Although it structurally resembles RAD51, the amino acid similarity is only 26% (Bishop 1992). It has also been found that BRCA2, which is required for RAD51 filament formation, has certain BRC repeats which can also interact with DMC1 (Thorslund et al., 2007). In vitro studies with both RAD51 and DMC1 have shown very similar properties of the proteins; both RAD51 and DMC1 forms right-handed filaments on resected ssDNA and are involved in strand invasion and promote D-loop formation (Hong, 2001; Sehorn et al., 2004). Genetic studies showed that both proteins are required for faithful

homologous recombination in meiosis (Hong et al., 2013), however interestingly in yeast and *A. thaliana* it was shown that the catalytic function of RAD51 is not required during meiosis (Cloud et al., 2012; Da Ines et al., 2013). For several organisms it was shown by fluorescence microscopy that RAD51 and DMC1 co-localize at the DSB foci. Careful analysis in *A. thaliana* showed the presence of pairs of RAD51 and DMC1 foci (Kurzbaue et al., 2012). Biochemical studies which compared the interactions of RAD51 and DMC1 nucleoprotein filaments have shown that homology recognition for DMC1 has tolerance for mismatches in the repair template. This can have important implications for meiosis since repair through the homologous chromosomes requires tolerance for small difference in the sequence between the invading strand and template (Lee et al., 2015). With the advancements of super resolution microscopy, in yeast multiple RAD51 and DMC1 accumulations were observed within individual DSB foci (Brown et al., 2015). The super-resolved organization of mouse meiotic RAD51/DMC1 foci will be further discussed in this thesis in Chapter 3.

## Light microscopy

At the beginning of the 17<sup>th</sup> century the Dutch scientists Zacharias Jansen and Cornelis Drebbel were probably the first who designed and build a compound microscope. However, it was Antoni van Leeuwenhoek (1632-1723) who built a microscope with more than 200x magnification and high resolving power. This gave enough resolution to observe, for the first time, living microorganisms under a microscope, a discovery that had an enormous impact on science, and therefore on humanity, comparable with the discovery and unravelling of the genetic code in DNA. The development of phase contrast by Zernike (1941) and differential interference contrast (DIC) by Normarski further enhanced microscopy as an essential technique for biologists. With the possibilities of staining specific cellular structures with fluorescent dyes fluorescence microscopy became a popular technique. It became, for example, possible to stain DNA using DAPI as well as to use dyes to

specifically stain the plasma membrane. Using immunofluorescence with antibodies labelled with fluorescent dyes it not only became possible to visualize certain cellular structures but also the localization of specific proteins in a cell.

In fluorescence microscopy, the emission of light from fluorescent molecules after excitation with light of the appropriate wavelength shorter than the emitted light, can be visualised. This is possible since fluorescent molecules are lifted from their ground state to an excited state by absorbing a photon of the right wavelength. The excited fluorescent molecule can return to the ground state by the emission of a photon, which is called fluorescence. Since some of the absorbed energy is lost through other ways, the emitted photon will have less energy and thus have a longer wavelength. This makes it possible to separate the fluorescence emission from the excitation light using chromatic filters.

The resolution of a light microscope is limited by the diffraction of the light. This was already theoretically described by Ernst Abbe in the 19<sup>th</sup> century, and is now known as Abbe's law:  $d = \lambda / (2n \cdot \sin \theta)$ , where  $\lambda$  is the wavelength and  $n \cdot \sin \theta$  is the numerical aperture (NA), which describes the capacity of a microscope objective to capture light. Using optical microscopes with light with a wavelength within the visible spectrum this results in a resolution limit of about 200 to 250 nm. This implies that structural information below this resolution is lost in a light microscope image. Using an optical microscope light emitted from a point source (for example a fluorescent molecule) will be detected as a blurred spot. The distribution of the light from a point source is described by the point spread function (PSF). The PSF is formed by the diffraction of the light waves and from an x-y perspective looks as a central peak with rings surrounding this peak. When two point sources are closer together than the size of their PSFs their signals will overlap and this makes it in principle impossible to distinguish them, hence the limited resolution. However, as is done in super resolution microscopy, the resolution can be increased by spatially controlling excitation and emission of the fluorescent molecules used (see below).

## Confocal microscopy

For fluorescence microscopy it is essential to block the excitation light from the detector. With an epi-fluorescence microscope the same objective detecting the emission light is also used to illuminate the specimen. Moreover, the reflecting excitation light reflected by the object glass and cover slip are blocked by emission filters. This combined approach effectively prevents excitation light from reaching the ocular of the microscope as well as the detector or camera (Figure 9A). However, epi-fluorescence microscopy is limited by the presence of fluorescence from fluorescent molecules which are not in the focal plane. This out-of-focus fluorescence leads to an increased background signal (referred to as out-of-focus blur) which obscures or even overshines the in-focus objects in the specimen. The confocal microscope was developed to avoid this problem by introducing a pinhole in front of the detector in the light path blocking out-of-focus light (Figure 9B). This idea was patented by Marvin Minsky already in 1957. However, only the later availability of scanning lasers, sensitive detectors and computers to store the point-by-point detected fluorescence signal allowed the full development of the confocal laser scanning microscope (Brakenhoff et al., 1985). In the modern confocal microscope a scanner consisting of two mirrors is used to scan the sample point by point (one mirror) and line by line (the other mirror). A 2-D image can then be reconstructed and displayed on the computer screen. A 3-D image can be reconstructed in a similar way by acquiring a stack of 2-D images at different z-depth in the sample. The fact that the laser is scanned along the sample to form an image can also be used to locally administer light to a region of the field of view. This is for instance used in Fluorescence Recovery After Photobleaching (FRAP) to bleach the fluorescence in a small region in the cell. The recovery of fluorescence in time can be used to study the diffusion and binding of proteins in the living cell (Ellenberg et al., 1997; Houtsmuller et al., 1999).

## Total Internal Reflection Microscopy

Another approach to reduce background

fluorescence and improve axial resolution is Total Internal Reflection Microscopy (TIRF). With TIRF only a thin layer above the coverslip is illuminated by using the properties of the refractive mismatch between the glass and the water in the sample (Figure 9C). If light is applied at a so called critical angle, dependent on the numerical aperture of the objective, all light will be reflected on the glass-water interface. Nonetheless, due to electromagnetic phenomena (described in the well-known Maxwell equations) a so-called evanescent wave, of which the intensity exponentially declines, is present at the glass water surface (at the water side), effectively only exciting fluorescent molecules in a thin layer of ~200 nm above the coverslip (Axelrod, 1981).

Although TIRF microscopy enables imaging processes going on near the coverslip, so essentially those in the plasma membrane or very close to it, it is not possible to image deeper in the sample. To image at larger depth it is possible to reduce the reflection angle of the laser, so that the sample is illuminated by a sheet of light traversing through the specimen at an angle. This technique, called highly inclined and laminated optical sheet (HILO) concentrates the excitation light to a limited volume within the specimen and thereby reduces background (Tokunaga et al., 2008) (Figure 9D). However, the created light sheet is not parallel to the imaging plane and therefore results in excitation inhomogeneity in the image. Recently, also technology has been developed to create a thin lateral light sheet (Chen et al., 2014) (Figure 9E) or to enable imaging at multiple z-planes at the same time (Abrahamsson et al., 2012).

## Super resolution microscopy

Obviously, it has long been assumed that there is no way to achieve with a fluorescence microscope, a resolution below the limit defined by Abbe's law. However, already in 1978, a first description of a system that effectively brings the resolution of the light microscope below this diffraction limit was published (Cremer and Cremer, 1978), but a practical implementation of this so-called 4Pi microscope came much later (Hell and Stelzer, 1992). The 4Pi



microscopy improves the resolution along the optical axis (axial or z-resolution) by using two opposing objectives (Figure 9F). Due to interference of the emission light from both objectives the detection volume is reduced below that of the diffraction limited spot, thereby effectively increasing the axial resolution by a factor of approximately two, because molecules outside the volume (which is smaller than the diffraction limited spot) are not detected, and thus do not contribute to the emitted signal. Interestingly, this also has a beneficial effect on the lateral separation of objects (a “borrowed resolution increase”, Stephan Hell, personal communication, Houtsmuller) in the image plane, when these extend in depth through several image planes. After 4Pi microscopy, several other super resolution microscopy techniques emerged,

of which Stimulated Emission Depletion (STED), Structured Illumination (SIM) and Single Molecule Localization Microscopy (SMLM) are used the most frequently (Schermelleh et al., 2010) (Figure 9). All these techniques have in common that they circumvent, not break, Abbe’s law, using methods to either spatially or temporally separate the fluorescence emission signal of a sample.

### Stimulated Emission Depletion (STED)

The STED microscope reduces the size of the excitation volume of the laser by depleting the fluorescent capacity of molecules in the “outer layers” of the excitation spot (Klar and Hell, 1999). This is achieved, by applying a high intensity donut shaped laser beam, with a hole in the middle that is smaller than the diameter

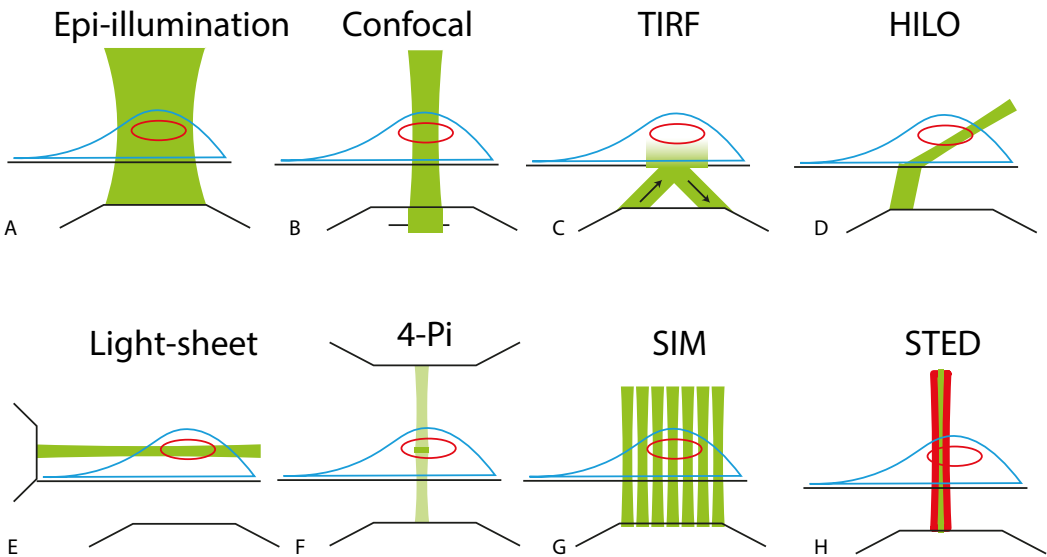


**Figure 9 Different types of illumination of a fluorescence microscope. A)** With Epi-illumination the sample is illuminated and detection is at the same side of the sample to reduce the amount of excitation light which is detected. **B)** Confocal microscopy reduces detection of out-of-focus fluorescence by a pinhole in both the excitation as detection path. Confocal microscopy is mostly done by laser scanning to create an image. **C)** A way to reduce the excitation volume is TIRF microscopy which illuminates the sample from an angle which result in excitation of only a thin layer above the coverslip. **D)** When the laser is applied at a slightly smaller angle a light sheet is formed which can illuminate deeper into the sample. **E)** Light-sheet microscopy uses an objective for excitation which creates a light sheet illuminating the sample, while the fluorescence is detected with another objective at a 90-degree angle. **F)** In 4-Pi microscopy the fluorescence is detected with two objectives on opposite sides of the sample. The interference of the light of the two objectives reduces the size of the PSF in the lateral direction. **G)** In SIM, the sample is illuminated with a pattern created with a grid in the excitation path. This grid can be shifted and rotated creating a set of images that together can be used to extract super resolution information from the images. **H)** STED is a super resolution technique which uses donut-shaped depletion beam which reduces the effective excitation volume, thereby this result in a super resolution image.

of the diffraction limited spot (Figure 9H). This depletion laser induces stimulated emission of the fluorescent molecules. Stimulated emission, is a process in which an excited molecule is stimulated to release a photon which does not allow the fluorescent molecule to relax to the ground state and thereby blocks their ability to fluoresce. Since reducing the excitation further and further requires higher excitation powers, the maximum lateral resolution that can be acquired by STED is about 30 nm (Figure 10). Just as with confocal and 4Pi microscopy the image is acquired by scanning the sample using scanning mirrors. The axial resolution in the standard STED setup is still diffraction-limited however by using different shapes of the depletion beam also the height of the excitation volume now can be reduced resulting also in a higher axial resolution (Harke et al., 2008). With RESOLFT (Reversible Saturable Optical Fluorescence Transition) microscopy also other mechanisms are used to switch the fluorescence off in the donut shaped beam (Hell et al., 2004). It is for example possible to use reversible photo switchable dyes or fluorescent proteins which can be turned off with light from one wavelength while the light in the middle of the excitation beam activates and excites the fluorescent molecules (Grotjohann et al., 2011).

### **Structured Illumination Microscopy (SIM)**

SIM uses yet another approach for improvement of the spatial resolution (Figure 9G). By modulating the excitation light using an interfering grid in the light path a specific excitation pattern can be created which projects a known fluorescence pattern on the sample. In a single SIM image only part of the sample is illuminated. Subsequently the grid pattern is translated and rotated multiple times. Taking them together, the individual images provide extra information about where the fluorescent molecules are located, and hence a higher resolution is achieved (Figure 10). This series of images is combined in one super resolution image using an algorithm that uses the information of the known position of the grid in the acquired images. The algorithm actually uses the fact that interference of the grid projected on the sample

results in shifting of high spatial frequency information to a lower frequency which can be extracted using Fourier Transformation (Gustafsson, 2000). In 3D-SIM also an axial interference pattern is applied which is also increasing the axial resolution. For SIM the maximum theoretical resolution increase is two times. Therefore, a maximum lateral resolution of about 100-150 nm can be obtained. Since the resolution is increased in all three dimensions with SIM eight times smaller volume can be resolved (Schermelleh et al., 2010).

### **Single molecule localization microscopy (SMLM)**

Instead of modifying the excitation light pattern, like with SIM and STED, another very powerful approach has been developed, termed single molecule localization microscopy (SMLM), which is based on two basic principles. The first principle is that the emission light of a single fluorescent molecule can be detected in a fluorescence microscope irrespective of the size of the molecule (the light source) (Moerner, 1996). Although the fluorescent molecule itself can be just about a nanometer in size the optical properties of the microscope expand the light of the fluorescent molecule in a way determined by the Optical Transfer Function to form a diffraction limited spot described by the Point Spread Function. The photon density of the Point Spread Function can be approached by a Gaussian distribution. The exact location of a molecule can then be determined on the basis of this 2-Gaussian, by fitting the spot to a calculated 2D Gaussian distribution. The center of the best fitting Gaussian then is the best estimate of the location of the fluorescent molecule, and the width of the fitted Gaussian gives the accuracy of this estimate. In this way, the location of the molecule can be determined at high accuracy, dependent on the number of detected photons (Figure 10).

The second principle of SMLM is that the location of individual molecules can only be determined as described in a dense sample by making sure that individual molecules are excited at different times, so that only a few molecules, that are further apart than the diameter

of the diffraction limited spot are emitting photons during recording an image.

This is practically implemented by either using spuriously photo activation and bleaching of fluorescent proteins (Photoactivated localization microscopy (PALM) (Betzig et al., 2006)) or by inducing stochastic blinking of organic dyes (Stochastic Optical Reconstruction Microscopy (Heilemann et al., 2008; Rust et al., 2006)). These activation or blinking events are recorded in a video using a camera. Subsequently software is used to detect and localize the molecules in the individual frames of the video. Eventually all the localizations make up the reconstructed super resolution image, see also Chapter II).

The resolution in SMLM depends on different factors (Rieger and Stallinga, 2014). The spatial resolution is dependent on the localization precision of the single molecules but in the same time the labeling density needs to be sufficiently high to resolve the underlying structure. The localization precision is mainly dependent on the number of photons that can be detected for a single molecule. The localization precision scales with the square root of the number of photons, but also factors such as the pixel size and background variation are important (Thompson et al., 2002). Generally speaking, the labeling density has to meet the Nyquist criterion to reach a certain resolution to resolve the underlying pattern (Huang et al., 2009). This means that one needs to have a sampling interval more than two (2.3) times smaller than the defined resolution (Shroff et al., 2008). However, when studying the localization of individual proteins in the cell the actual resolution of the entire image often is less relevant and the efficiency of detecting the molecules and the localization precision are most important.

The lateral resolution of SMLM is until now the highest among the different super resolution techniques. However, the axial resolution in SMLM is more difficult to define and is dependent on how far away from the focal plane one can still detect localizations. To obtain a higher axial resolution the information on the z-position of the localized molecules can be estimated by creating a point spread function that deforms depending on the z-position of the

molecule. This can be done by applying an astigmatic lens in the light path, which elongates the point spread function in vertical and horizontal direction above and below the focal plane respectively (Huang et al., 2008).

### ***Single Molecule Tracking in Living Cells***

Although most SMLM is performed in fixed cells, there are possibilities to use living cells for single molecule localization. Since the acquisition time for an SMLM image is relatively long, this is mainly interesting for structures that are relatively stable. Another application of localization microscopy in living cells is single molecule tracking. Since this also requires individual molecules that are spatially separated, controlled photoactivation can be used to detect only a subset of the molecules at a time. This methodology is described as single particle tracking PALM (sptPALM) (Manley et al., 2008). In single molecule tracking moving particles are localized by Gaussian fitting and subsequently followed in time by linking the localization events. The displacements of the molecules can be used to calculate the mean square displacement of the molecules. The mean square displacement for particles undergoing Brownian motion can be used to estimate the diffusion coefficient. However, particle tracking can also be used to quantify binding and dissociation kinetics (e.g. binding of a protein to the DNA) of molecules in cells. By tracking the individual dynamic behaviour of individual molecules (diffusion constant, binding kinetics) can be estimated and subsequently used to infer the dynamics of whole the population of molecules. Single particle tracking also enables detecting sub-populations of molecules that exhibit a certain type of mobility. Since the acquisition speed of a camera is limited there is a maximum speed that can be detected by single particle tracking. On the other hand, the dynamics of molecules that move with a speed below the localization precision is also impossible to assess. Normally particle tracking enables to study dynamics in the sub second range. Single particle tracking can be complemented with other established methods to study protein dynamics as Fluorescence Recovery After Photobleaching (FRAP),

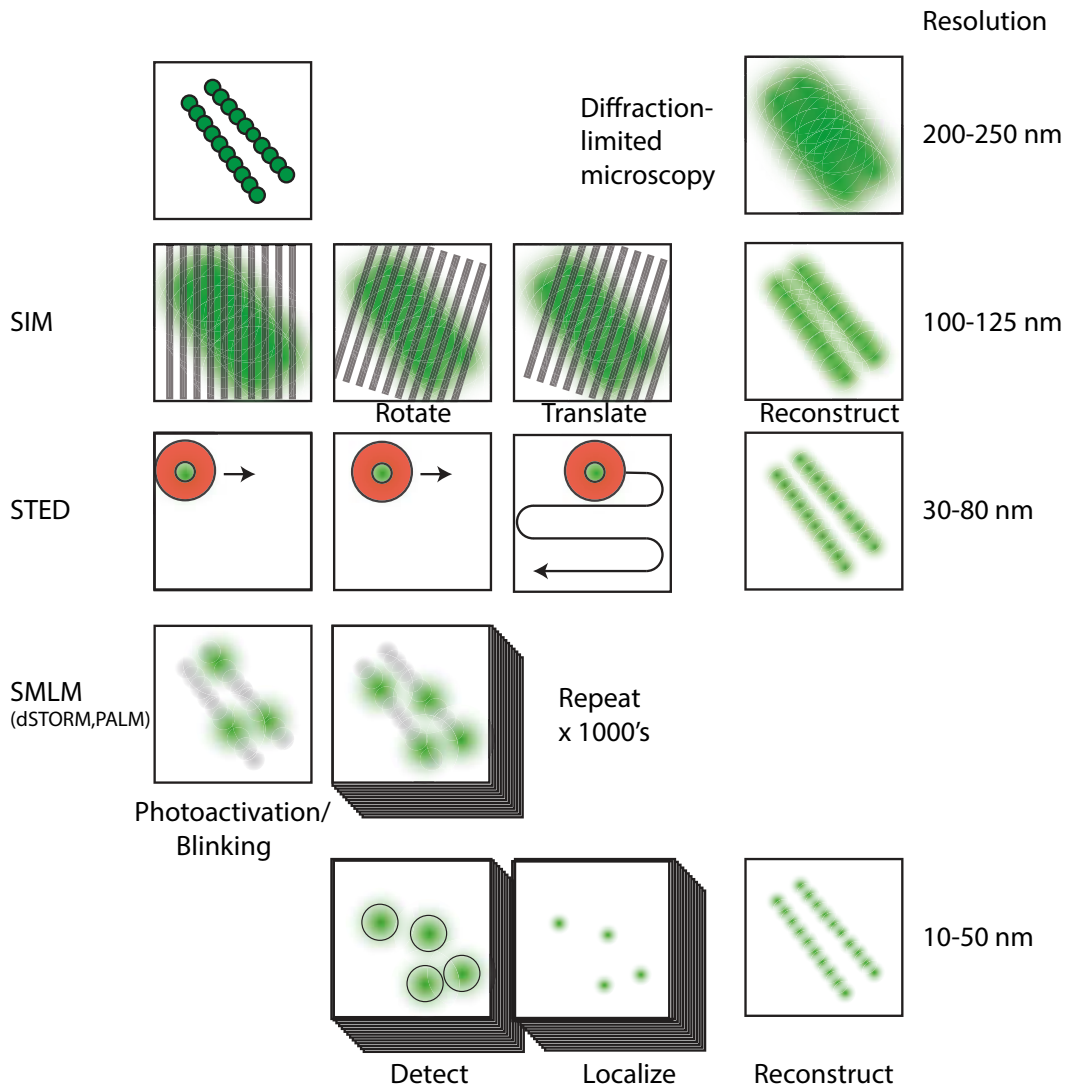


**Figure 10 Super resolution microscopy techniques.** The lateral resolution of diffraction limited microscopy is insufficient to resolve the two parallel structures. Structured illumination microscopy (**SIM**) has an increased lateral resolution by obtaining additional spatial information using a grid in the excitation path. Stimulated emission depletion (**STED**) microscopy reduces the excitation volume by depleting the fluorescence surrounding the excitation beam. Scanning over the sample results in an image with super resolution information. Single molecule localization microscopy (**SMLM**) techniques use stochastic blinking or photo activation to detect the fluorescence of individual molecules. By repeating this process many times for all the molecules in the sample a map can be reconstructed with position of the individual molecules.

which is able to give information at longer time ranges or by Fluorescence Correlation Spectroscopy (FCS) to study very fast dynamics (Reuter et al., 2014; Van Royen et al., 2014).

### Fluorescent proteins

The discovery of the Green Fluorescent Protein (GFP) isolated from the jellyfish *Aequorea*

*victoria* revolutionized fluorescence microscopy in living cells. GFP is a barrel-shaped protein in which, after proper folding, a fluorescent moiety is formed inside the barrel, through an autocatalytic reaction of some amino acids. Since no specific cellular machinery is required for this, the protein can be expressed in its fluorescent form in any cell type. The gene encoding for GFP

can be fused to any gene encoding for a protein of interest, which then can be studied with any type of fluorescence microscopy. Obviously, it is necessary to first verify whether the function of the protein is not affected by the presence of the bulky tag. Wild type GFP from *A. victoria* has a near UV excitation spectrum, but an optimized version EGFP, has a red-shifted excitation spectrum and increased photo stability. This variant therefore made it much easier to use using existing microscopes. Several other GFP variants have been engineered that are fluorescent at different wavelengths (BFP, CFP, YFP). Additionally other fluorescent proteins were discovered for example dsRed, from the coral *Discosoma* genus, which was optimized to mCherry (Shaner et al., 2004). All together a large range of fluorescent proteins are currently available ranging the entire visible light spectrum.

Another group of FPs are the photoactivatable fluorescent proteins (PA-FPs). One of the first PA-FPs that was developed is Photoactivatable GFP (PA-GFP), a variant of wildtype GFP that was engineered so that it only becomes fluorescent after activation by illumination of light with a wavelength of about 400 nm (Patterson and Lippincott-Schwartz, 2002). Later, also other photoactivatable proteins were developed for example a photoactivatable variant of mCherry, PA-mCherry (Subach et al., 2009). The photoactivation of those proteins induces a conformational change of the chromophore leading to an increase in the fluorescence of that molecule. Besides PA-FPs, which can be switched on by light, also variants exist of which excitation and emission wave lengths can be changed, the so-called photoconvertible proteins. Those proteins exhibit a shift in excitation and emission spectrum after irradiation with 400 nm laser light, similar to the photoactivatable proteins. Recent examples are mEos2 and mMaple3 (Wang et al., 2014; Zhang et al., 2012). Additionally fluorescent proteins are available that can be reversibly switched between two fluorescent states, for instance Dronpa which is switched off by 488 nm illumination and reactivated by 405 nm illumination up to 100 times (Eisenstein, 2005).

Using PA-FPs it is possible to photoactivate

a subpopulation of the fluorescent proteins under the microscope which makes it possible to follow proteins in time activated in a specific region of the sample. With the development of super resolution microscopy techniques the photoactivatable properties of the PA-FPs also turned out to be very useful to temporally separate the fluorescence of individual molecules as is done in Photo activated localization microscopy (PALM) (see below and Betzig et al., 2006).

## Labelling and Nanoscopy

Especially STED and SMLM techniques require specific fluorescent dyes which are optimised for the imaging technique. For instance, STED requires dyes which enable stimulated emission without photobleaching, which is not the case for regular fluorescent proteins. Therefore, certain specific organic dyes are mostly used in STED. For SMLM dyes are required that enable observing the individual dyes at different time points with a high photon yield. Especially when using photoswitchable fluorescent proteins, the number of photons that are detected is limited which reduces the localization precision. For photoswitchable proteins photoswitching performance is also important. It is, for example, known that the frequently used photoswitchable protein mEos2 shows blinking over longer time scales, which might result in artefacts and overcounting in the final image (Annibale and Scarselli, 2010).

Alternatively, chemical dyes, which are often brighter than FPs, can be used for SMLM using the stochastic blinking of those dyes between a fluorescent and dark state, which is named Stochastic Optical Reconstruction Microscopy (STORM). Originally this was achieved by using antibodies labelled with a pair of different fluorescent dyes (Rust et al., 2006). One of the dyes was used as reporter dye which could be switched to a dark state by a laser and reactivated by exciting an activator dye with laser light of a different wavelength. The reporter dye is able to return from the dark state by energy transfer from the activator dye to the reporter dye. By using activator dyes with a different excitation spectrum it is possible to perform multi-colour STORM (Bates et al., 2012). A disadvantage is

that this might give rise to cross talk when doing multi-color imaging and it requires antibodies labelled with multiple dyes that are close enough for energy transfer.

Another approach, direct STORM (dSTORM), uses the photochemical properties of the dye together with a specific imaging buffer to create stochastic blinking of the fluorophores. The advantage of this technique is that no dye pair is required. Although many studies have shown that many organic dyes can be used for dSTORM (Dempsey et al., 2011; van de Linde et al., 2011), there is large variation in the performance of the different dyes. This can be explained by the fact that some organic dyes are more resistant to bleaching and have a more stable dark state, which makes them more suitable for dSTORM. The imaging buffer in dSTORM mostly consists of an oxygen scavenger (e.g. glucose oxidase) and reducing agents (such as  $\beta$ -mercaptoethanol and 2-Mercaptoethylamine), they both prevent irreversible bleaching of the dyes and in the same time they stabilize the dark state of the fluorescent molecules. Another SMLM approach is PAINT (point accumulation and imaging of nanoscale topography), which uses dyes that upon reversible binding to their substrate become fluorescent. By recording the binding and dissociation of the molecules by fluorescence the molecules can be localized (Sharonov and Hochstrasser, 2006).

SMLM can also be applied to living cells, especially for single particle tracking. Approaches with antibodies labelled with organic dyes are typically not compatible with living cells since antibodies cannot cross the cell membrane, but antibodies have been used to study the dynamics of membrane receptors (Dahan, 2003). One of the options is the use of photoconvertible proteins such as mEos2, but they have a limited photostability, which makes it challenging to follow the individual proteins long enough.


Alternative methods have been developed that enable direct labelling of proteins with organic dyes in living cells. This can be achieved by introducing non-natural amino acids to the protein of interest which then can be labelled with organic dyes using click chemistry or alternatively by genetic tagging of proteins of

interest with a tag with a reactive group (Xue et al., 2015). Examples of those tags are SNAP or Halo-tag (Juillerat et al., 2003; Los et al., 2008). The cells can be labeled in vivo with a cell permeable dye, for example TMR. Recently new cell-permeable fluorogenic dyes, which become more fluorescent upon binding, were published which is a great step forward in live cell single molecule localization imaging (Grimm et al., 2015; Lukinavičius et al., 2013).

## Concluding remarks

Super resolution microscopy is a fast developing field, where novel approaches and technical improvements rapidly expand the number of potential applications. The power of microscopy in biology, general speaking, is that it enables researchers to directly observe cellular processes in individual cells, which is especially interesting in living cells. The promise of an improved resolution by super resolution microscopy is therefore, of course, very stimulating for biologists. It will help them to study the process of interest with improved spatial detail. However, the increase in resolution does bring up new questions about what the observed nanoscale structures in these high-resolution images really mean and to what extent this is relevant or significant for the function of proteins inside these structures.

Additionally, the observations made by super resolution frequently reveals protein organizations people never have seen before which makes it difficult to link them directly to underlying biological mechanisms. In structures with a quite well defined structure such as nuclear pores, super resolution has been very effective in confirming previously known nanoscale structure, however describing nanoscale protein organization in which the spatial localization of the proteins is not so clearly defined is far more challenging. Nonetheless it is very important to define the organization of these proteins in different cellular structures, to eventually match the imaging data together and to come up with new molecular mechanisms on how nanoscale organization of proteins relates to their function. In the field of DNA repair, for



instance, it would be very revealing if we could better understand how the spatial localization of the several repair proteins regulate the repair of the DNA lesions. In this thesis analyses were performed on the single molecule localization of different DNA repair proteins in different model systems. Often, we tried to look at different time points after damage to get insight how the localization of the proteins supports their function. For the future further exploration, especially in living cells, would make it possible to follow the nanoscale localization of DNA Repair proteins surrounding the DSBs in real time. With the recent advances in ultrathin light sheet microscopy, the further development of new fluorescent probes that can be used in living cells and even faster imaging it is only a matter of time before we will be able to follow such biological processes in living cells at the single molecule level.

## Scope of this thesis

The project of this thesis was executed within the STW 'Nanoscopy' program, which includes several physics and biology research groups from TU Delft, Vrije Universiteit Amsterdam, Universiteit Utrecht and Universiteit van Amsterdam, focusing on development and application of a wide range of nanoscopic methods. The goal of the project was to investigate new ways to apply super resolution microscopy in biomedical research. The vast developments in super resolution microscopy techniques require substantial efforts to investigate how to apply the wide variety of nanoscopic techniques currently emerging to address important biological questions. One of these relevant questions is how DNA repair proteins are organized at the sites of DNA damage to facilitate proper repair of DNA lesions. DNA repair pathways are essential mechanisms for a cell to survive and require a wide range of different proteins with different functions to be in the right place at the right time. During DNA Double Strand Break repair through Homologous Recombination, proteins accumulate on the sites of damage, in so-called foci, which can be visualized by fluorescence microscopy using fluorescently tagged proteins. The spatial organization of proteins at the sites of damage however, is difficult to visualize using normal fluorescence microscopy since the resolution of a light microscope is limited. To reveal the nanoscale organization of proteins the improved spatial resolution of novel super resolution microscopy technique become of hand. In this thesis, we investigated the nanoscale organization of several DNA Repair proteins by developing and applying novel super resolution assays, in particular single molecule localization microscopy. In **Chapter I** the mechanisms of DNA Repair are discussed together with the recent developments in (super) resolution microscopy.

In **Chapter II** a software package is presented that was specifically developed to analyze single molecule localization data of, for example, cells with Double Strand Break foci. In the chapter is described how to extract structural and spatial information from this data. For this purpose, we developed a software package which provides a streamlined approach to process and quantify

specific features of the super-resolved images. This enables quantitative analysis of nanoscale structures and relate the protein organization to the biological functions of the proteins in study.

We applied these analysis methods in **Chapter III** to study the spatial organization of two recombinases, RAD51 and DMC1, involved in meiotic Homologous Recombination using single molecule localization microscopy in meiotic cells. This analysis revealed how both recombinases, suggestively having different functions in meiosis, are localized at DNA Double Strand Breaks. We were able to follow the changes in relative nanoscale cluster organization of DMC1 and RAD51 at different stages of meiosis. Furthermore, we used rotational analysis to visualize how the relative distances between the DMC1 and RAD51 protein clusters were changing during progression of meiosis and validate these structural dynamics using simulations.

In **Chapter IV**, scanning force microscopy was used to study how individual BRCA2 proteins form different complex configurations which change upon interaction of BRCA2 with RAD51 and DNA. The structural organization of these complexes clarify the molecular mechanisms whereby BRCA2 delivers RAD51 to sites of damage in cells. To address the question whether the delivery of RAD51 results in separation of RAD51 and BRCA2 at the sites of damage we used single molecule localization microscopy. This analysis enables us to quantify the relative localization of RAD51, BRCA2 and RPA in DNA Double Strand Break Foci.

In **Chapter V**, we aimed to visualize the localization and dynamics of the ATPase RAD54 which is closely involved in regulating the function of RAD51 during the DNA repair process. Using super resolution microscopy, we were able to analyze the effect of ATPase activity of RAD54 on the nanoscale localization of RAD54 and RAD51 in cells. In the ATPase mutant cells we detected very elongated RAD51 foci, on which patches of closely associated RAD54 could be detected. The RAD54 molecules in the mutant were immobilized on the RAD51 foci, which we could show by tracking individual RAD54 molecules in living cells. Finally, we used local photoactivation of individual foci to follow the local dynamics of the fraction of immobile RAD54 molecules within individual foci in time.



## References

- Abrahamsson, S., Chen, J., Hajj, B., Stallinga, S., Katsov, A.Y., Wisniewski, J., Mizuguchi, G., Soule, P., Mueller, F., Darzacq, C.D., et al. (2012). Fast multicolor 3D imaging using aberration-corrected multifocus microscopy. *Nat. Methods* *10*, 60–63.
- Agarwal, S., van Cappellen, W.A., Guenole, A., Eppink, B., Linsen, S.E.V., Meijering, E., Houtsmuller, A., Kanaar, R., and Essers, J. (2011). ATP-dependent and independent functions of Rad54 in genome maintenance. *J. Cell Biol.* *192*, 735–750.
- Alexeev, A., Mazin, A., and Kowalczykowski, S.C. (2003). Rad54 protein possesses chromatin-remodeling activity stimulated by the Rad51-ssDNA nucleoprotein filament. *Nat. Struct. Biol.* *10*, 182–186.
- Allen, D.J. (1997). MutS mediates heteroduplex loop formation by a translocation mechanism. *EMBO J.* *16*, 4467–4476.
- Altmeyer, M., Neelsen, K.J., Teloni, F., Pozdnyakova, I., Pellegrino, S., Gröfte, M., Rask, M.-B.D., Streicher, W., Jungmichel, S., Nielsen, M.L., et al. (2015). Liquid demixing of intrinsically disordered proteins is seeded by poly(ADP-ribose). *Nat. Commun.* *6*, 8088.
- Amitani, I., Baskin, R.J., and Kowalczykowski, S.C. (2006). Visualization of Rad54, a Chromatin Remodeling Protein, Translocating on Single DNA Molecules. *Mol. Cell* *23*, 143–148.
- An, J., Huang, Y.-C., Xu, Q.-Z., Zhou, L.-J., Shang, Z.-F., Huang, B., Wang, Y., Liu, X.-D., Wu, D.-C., and Zhou, P.-K. (2010). DNA-PKcs plays a dominant role in the regulation of H2AX phosphorylation in response to DNA damage and cell cycle progression. *BMC Mol. Biol.* *11*, 18.
- Annibale, P., and Scarselli, M. (2010). Photoactivatable fluorescent protein mEos2 displays repeated photoactivation after a long-lived dark state in the red photoconverted form. *J. Phys. ...* *1*, 1506–1510.
- Axelrod, D. (1981). Cell-substrate contacts illuminated by total internal reflection fluorescence. *J. Cell Biol.* *89*, 141–145.
- Bates, M., Dempsey, G.T., Chen, K.H., and Zhuang, X. (2012). Multicolor super-resolution fluorescence imaging via multi-parameter fluorophore detection. *ChemPhysChem* *13*, 99–107.
- Baudat, F., Manova, K., Yuen, J.P., Jasin, M., and Keeney, S. (2000). Chromosome synapsis defects and sexually dimorphic meiotic progression in mice lacking Spo11. *Mol. Cell* *6*, 989–998.
- Bekker-Jensen, S., and Mailand, N. (2010). Assembly and function of DNA double-strand break repair foci in mammalian cells. *DNA Repair (Amst)* *9*, 1219–1228.
- Bekker-Jensen, S., Lukas, C., Melander, F., Bartek, J., and Lukas, J. (2005). Dynamic assembly and sustained retention of 53BP1 at the sites of DNA damage are controlled by Mdc1/NFBD1. *J. Cell Biol.* *170*, 201–211.
- Bekker-Jensen, S., Lukas, C., Kitagawa, R., Melander, F., Kastan, M.B., Bartek, J., and Lukas, J. (2006). Spatial organization of the mammalian genome surveillance machinery in response to DNA strand breaks. *J. Cell Biol.* *173*, 195–206.
- Bell, J.C., Plank, J.L., Dombrowski, C.C., and Kowalczykowski, S.C. (2012). Direct imaging of RecA nucleation and growth on single molecules of SSB-coated ssDNA. *Nature* *491*, 274–278.
- Bennett, M.D. (1977). The time and duration of meiosis. *Philos. Trans. R. Soc. Lond. B. Biol. Sci.* *277*, 201–226.
- Benson, F.E., Stasiak, A., and West, S.C. (1994). Purification and characterization of the human Rad51 protein, an analogue of *E. coli* RecA. *EMBO J.* *13*, 5764–5771.
- Betzig, E., Patterson, G.H., Sougrat, R., Lindwasser, O.W., Olenych, S., Bonifacino, J.S., Davidson, M.W., Lippincott-Schwartz, J., and Hess, H.F. (2006). Imaging Intracellular Fluorescent Proteins at Nanometer Resolution. *Science* *313*, 1642–1645.
- Bhattacharyya, A., Ear, U.S., Koller, B.H., Weichselbaum, R.R., and Bishop, D.K. (2000). The Breast Cancer Susceptibility Gene BRCA1 Is Required for Subnuclear Assembly of Rad51 and Survival following Treatment with the DNA Cross-linking Agent Cisplatin. *J. Biol. Chem.* *275*, 23899–23903.
- de Boer, J. (2002). Premature Aging in Mice Deficient in DNA Repair and Transcription. *Science* *296*, 1276–1279.
- Bohr, V. (1985). DNA repair in an active gene: Removal of pyrimidine dimers from the DHFR gene of CHO cells is much more efficient than in the genome overall. *Cell* *40*, 359–369.
- Bork, P., Blomberg, N., and Nilges, M. (1996). Internal repeats in the BRCA2 protein sequence. *Nat. Genet.* *13*, 22–23.
- Bouwman, P., Aly, A., Escandell, J.M., Pieterse, M., Bartkova, J., van der Gulden, H., Hiddingh, S., Thanasoula, M., Kulkarni, A., Yang, Q., et al. (2010). 53BP1 loss rescues BRCA1 deficiency and is associated with triple-negative and BRCA-mutated breast cancers. *Nat. Struct. Mol. Biol.* *17*, 688–695.
- Brakenhoff, G.J., van der Voort, H.T.M., van Spronsen, E.A., Linnemans, W.A.M., and Nanninga, N. (1985). Three-dimensional chromatin distribution in neuroblastoma nuclei shown by confocal scanning laser microscopy. *Nature* *317*, 748–749.
- Britton, S., Coates, J., and Jackson, S.P. (2013). A new method for high-resolution imaging of Ku foci to decipher mechanisms of DNA double-strand break repair. *J. Cell Biol.* *202*, 579–595.
- Brown, M.S., Grubb, J., Zhang, A., Rust, M.J., and Bishop, D.K. (2015). Small Rad51 and Dmc1 Complexes Often Co-occupy Both Ends of a Meiotic DNA Double Strand Break. *PLOS Genet.* *11*, e1005653.
- Bryant, H.E., Schultz, N., Thomas, H.D., Parker, K.M., Flower, D., Lopez, E., Kyle, S., Meuth, M., Curtin, N.J., and Helleday, T. (2005). Specific killing of BRCA2-deficient tumours with inhibitors of poly(ADP-ribose) polymerase. *Nature* *434*, 913–917.
- Burma, S., Chen, B.P., Murphy, M., Kurimasa, A., and Chen, D.J. (2001). ATM phosphorylates histone H2AX in response to DNA double-strand breaks. *J. Biol. Chem.* *276*, 42462–42467.
- Candelli, A., Holthausen, J.T., Depken, M., Brouwer, I., Franker, M. a. M., Marchetti, M., Heller, I., Bernard, S., Garcin, E.B., Modesti, M., et al. (2014). Visualization and quantification of nascent RAD51 filament formation at single-monomer resolution. *Proc. Natl. Acad. Sci.* *111*, 15090–15095.
- Cao, L., Alani, E., and Kleckner, N. (1990). A pathway for generation and processing of double-strand breaks during meiotic recombination in *S. cerevisiae*. *Cell* *61*, 1089–1101.
- Carreira, A., and Kowalczykowski, S.C. (2011). Two classes of BRC repeats in BRCA2 promote RAD51 nucleoprotein filament function by distinct mechanisms. *Proc. Natl. Acad. Sci.* *108*, 10448–10453.
- Chapman, J.R., Taylor, M.R.G.G., and Boulton, S.J. (2012a). Playing the End Game: DNA Double-Strand Break Repair Pathway Choice. *Mol. Cell* *47*, 497–510.

- Chapman, J.R., Sossick, A.J., Boulton, S.J., and Jackson, S.P. (2012b). BRCA1-associated exclusion of 53BP1 from DNA damage sites underlies temporal control of DNA repair. *J. Cell Sci.* 125, 3529–3534.
- Chen, B.-C., Legant, W.R., Wang, K., Shao, L., Milkie, D.E., Davidson, M.W., Janetopoulos, C., Wu, X.S., Hammer, J.A., Liu, Z., et al. (2014). Lattice light-sheet microscopy: Imaging molecules to embryos at high spatiotemporal resolution. *Science* 346, 1257998–1257998.
- Clerici, M., Mantiero, D., Guerini, I., Lucchini, G., and Longhese, M.P. (2008). The Yku70–Yku80 complex contributes to regulate double-strand break processing and checkpoint activation during the cell cycle. *EMBO Rep.* 9, 810–818.
- Cloud, V., Chan, Y.-L.L., Grubb, J., Budke, B., and Bishop, D.K. (2012). Rad51 is an accessory factor for Dmc1-mediated joint molecule formation during meiosis. *Science* 337, 1222–1225.
- Cremer, C., and Cremer, T. (1978). Considerations on a laser-scanning-microscope with high resolution and depth of field. *Microsc. Acta* 81, 31–44.
- Dahan, M. (2003). Diffusion Dynamics of Glycine Receptors Revealed by Single-Quantum Dot Tracking. *Science* 302, 442–445.
- Davies, O.R., and Pellegrini, L. (2007). Interaction with the BRCA2 C terminus protects RAD51–DNA filaments from disassembly by BRC repeats. *Nat. Struct. Mol. Biol.* 14, 475.
- Davies, A.A., Masson, J.-Y., McIlwraith, M.J., Stasiak, A.Z., Stasiak, A., Venkitaraman, A.R., and West, S.C. (2001). Role of BRCA2 in Control of the RAD51 Recombination and DNA Repair Protein. *Mol. Cell* 7, 273–282.
- Deans, A.J., and West, S.C. (2011). DNA interstrand crosslink repair and cancer. *Nat. Rev. Cancer* 11, 467–480.
- Dellaire, G., Kepkay, R., and Bazett-Jones, D.P. (2009). High resolution imaging of changes in the structure and spatial organization of chromatin, ??-H2A.X and the MRN complex within etoposide-induced DNA repair foci. *Cell Cycle* 8, 3750–3769.
- Dempsey, G.T., Vaughan, J.C., Chen, K.H., Bates, M., and Zhuang, X. (2011). Evaluation of fluorophores for optimal performance in localization-based super-resolution imaging. *Nat. Methods* 8, 1027–1036.
- Dianova, I.I., Bohr, V.A., and Dianov, G.L. (2001). Interaction of Human AP Endonuclease 1 with Flap Endonuclease 1 and Proliferating Cell Nuclear Antigen Involved in Long-Patch Base Excision Repair. *Biochemistry* 40, 12639–12644.
- Dinant, C., Jager, M. de, Essers, J., Cappellen, W.A. van, Kanaar, R., Houtsmuller, A.B., Vermeulen, W., de Jager, M., and van Cappellen, W.A. (2007). Activation of multiple DNA repair pathways by subnuclear damage induction methods. *J. Cell Sci.* 120, 2731–2740.
- Eisenstein, M. (2005). New fluorescent protein includes handy on-off switch. *Nat. Methods* 2, 8–9.
- Ellenberg, J., Siggia, E.D., Moreira, J.E., Smith, C.L., Presley, J.F., Worman, H.J., and Lippincott-Schwartz, J. (1997). Nuclear Membrane Dynamics and Reassembly in Living Cells: Targeting of an Inner Nuclear Membrane Protein in Interphase and Mitosis. *J. Cell Biol.* 138, 1193–1206.
- Essers, J., Houtsmuller, A.B., Veelen, L. van, Paulusma, C., Nigg, A.L., Pastink, A., Vermeulen, W., Hoeijmakers, J.H.J., and Kanaar, R. (2002). Nuclear dynamics of RAD52 group homologous recombination proteins in response to DNA damage. *EMBO J.* 21, 2030–2037.
- Farmer, H., McCabe, N., Lord, C.J., Tutt, A.N.J., Johnson, D.A., Richardson, T.B., Santarosa, M., Dillon, K.J., Hickson, I., Knights, C., et al. (2005). Targeting the DNA repair defect in BRCA mutant cells as a therapeutic strategy. *Nature* 434, 917–921.
- Flores, O., Lu, H., and Reinberg, D. (1992). Factors involved in specific transcription by mammalian RNA polymerase II. Identification and characterization of factor IIH. *J. Biol. Chem.* 267, 2786–2793.
- Forget, A.L., and Kowalczykowski, S.C. (2012). Single-molecule imaging of DNA pairing by RecA reveals a three-dimensional homology search. *Nature* 482, 423–427.
- Fousteri, M., Vermeulen, W., van Zeeland, A.A., and Mulenders, L.H.F. (2006). Cockayne syndrome A and B proteins differentially regulate recruitment of chromatin remodeling and repair factors to stalled RNA polymerase II in vivo. *Mol. Cell* 23, 471–482.
- Friedberg, E.C., and Meira, L.B. (2006). Database of mouse strains carrying targeted mutations in genes affecting biological responses to DNA damage Version 7. *DNA Repair (Amst.)* 5, 189–209.
- Fung, C.W., Fortin, G.S., Peterson, S.E., and Symington, L.S. (2006). The rad51-K191R ATPase-Defective Mutant Is Impaired for Presynaptic Filament Formation. *Mol. Cell Biol.* 26, 9544–9554.
- Galletto, R., Amitani, I., Baskin, R.J., and Kowalczykowski, S.C. (2006). Direct observation of individual RecA filaments assembling on single DNA molecules. *Nature* 443, 875–878.
- Gottlieb, T.M., and Jackson, S.P. (1993). The DNA-dependent protein kinase: Requirement for DNA ends and association with Ku antigen. *Cell* 72, 131–142.
- Gravel, S., Chapman, J.R., Magill, C., and Jackson, S.P. (2008). DNA helicases Sgs1 and BLM promote DNA double-strand break resection. *Genes Dev.* 22, 2767–2772.
- Grawunder, U., Zimmer, D., Fugmann, S., Schwarz, K., and Lieber, M.R. (1998). DNA ligase IV is essential for V(D)J recombination and DNA double-strand break repair in human precursor lymphocytes. *Mol. Cell* 2, 477–484.
- Grimm, J.B., English, B.P., Chen, J., Slaughter, J.P., Zhang, Z., Revyakin, A., Patel, R., Macklin, J.J., Normanno, D., Singer, R.H., et al. (2015). A general method to improve fluorophores for live-cell and single-molecule microscopy. *Nat. Methods* 12, 244–250.
- Grotjohann, T., Testa, I., Leutenegger, M., Bock, H., Urban, N.T., Lavoie-Cardinal, F., Willig, K.I., Eggeling, C., Jakobs, S., and Hell, S.W. (2011). Diffraction-unlimited all-optical imaging and writing with a photochromic GFP. *Nature* 478, 204–208.
- Gustafsson, M.G. (2000). Surpassing the lateral resolution limit by a factor of two using structured illumination microscopy. *J. Microsc.* 198, 82–87.
- Hamer, G., Wang, H., Bolcun-Filas, E., Cooke, H.J., Benavente, R., and Hoog, C. (2008). Progression of meiotic recombination requires structural maturation of the central element of the synaptonemal complex. *J. Cell Sci.* 121, 2445–2451.
- Hammel, M., Yu, Y., Fang, S., Lees-Miller, S.P., and Tainer, J.A. (2010). XLF Regulates Filament Architecture of the XRCC4-Ligase IV Complex. *Structure* 18, 1431–1442.
- Harke, B., Ullal, C.K., Keller, J., and Hell, S.W. (2008). Three-Dimensional Nanoscopy of Colloidal Crystals. *Nano Lett.* 8, 1309–1313.
- Hays, S.L., Firmenich, A.A., Massey, P., Banerjee, R., and Berg, P. (1998). Studies of the interaction between Rad52 protein and the yeast single-stranded DNA binding protein RPA. *Mol. Cell Biol.* 18, 4400–4406.

- He, Z., Henricksen, L.A., Wold, M.S., and Ingles, C.J. (1995). RPA involvement in the damage-recognition and incision steps of nucleotide excision repair. *Nature* **374**, 566–569.
- Heilemann, M., van de Linde, S., Schüttelpel, M., Kasper, R., Seefeldt, B., Mukherjee, A., Tinnefeld, P., and Sauer, M. (2008). Subdiffraction-Resolution Fluorescence Imaging with Conventional Fluorescent Probes. *Angew. Chemie Int. Ed.* **47**, 6172–6176.
- Hell, S., and Stelzer, E.H.K. (1992). Properties of a 4Pi confocal fluorescence microscope. *J. Opt. Soc. Am. A* **9**, 2159.
- Hell, S.W., Dyba, M., and Jakobs, S. (2004). Concepts for nanoscale resolution in fluorescence microscopy. *Curr. Opin. Neurobiol.* **14**, 599–609.
- Hoeijmakers, J.H. (2001). Genome maintenance mechanisms for preventing cancer. *Nature* **411**, 366–374.
- Hong, E.L. (2001). *Saccharomyces cerevisiae* Dmc1 Protein Promotes Renaturation of Single-strand DNA (ssDNA) and Assimilation of ssDNA into Homologous Super-coiled Duplex DNA. *J. Biol. Chem.* **276**, 41906–41912.
- Hong, S., Sung, Y., Yu, M., Lee, M., Kleckner, N., and Kim, K.P.P. (2013). The Logic and Mechanism of Homologous Recombination Partner Choice. *Mol. Cell* **51**, 440–453.
- Houtsmuller, A.B., Rademakers, S., Nigg, A.L., Hoogstraten, D., Hoeijmakers, J.H., and Vermeulen, W. (1999). Action of DNA repair endonuclease ERCC1/XPF in living cells. *Science* **284**, 958–961.
- Huang, B., Wang, W., Bates, M., and Zhuang, X. (2008). Three-dimensional super-resolution imaging by stochastic optical reconstruction microscopy. *Science* **319**, 810–813.
- Huang, B., Bates, M., and Zhuang, X. (2009). Super-Resolution Fluorescence Microscopy. *Annu. Rev. Biochem.* **78**, 993–1016.
- Iaccarino, I., Palombo, F., Drummond, J., Totty, N.F., Hsuan, J.J., Modrich, P., and Jiricny, J. (1996). MSH6, a *Saccharomyces cerevisiae* protein that binds to mismatches as a heterodimer with MSH2. *Curr. Biol.* **6**, 484–486.
- Iacovoni, J.S., Caron, P., Lassadi, I., Nicolas, E., Massip, L., Trouche, D., and Legube, G. (2010). High-resolution profiling of gammaH2AX around DNA double strand breaks in the mammalian genome. *EMBO J.* **29**, 1446–1457.
- Da Ines, O., Degroote, F., Goubely, C., Amiard, S., Gallego, M.E., and White, C.I. (2013). Meiotic Recombination in Arabidopsis Is Catalysed by DMCI, with RAD51 Playing a Supporting Role. *PLoS Genet.* **9**, e1003787.
- de Jager, M., van Noort, J., van Gent, D.C., Dekker, C., Kanaar, R., and Wyman, C. (2001). Human Rad50/Mre11 Is a Flexible Complex that Can Tether DNA Ends. *Mol. Cell* **8**, 1129–1135.
- Jensen, R.B., Ozes, A., Kim, T., Estep, A., and Kowalczykowski, S.C. (2013). BRCA2 is epistatic to the RAD51 paralogs in response to DNA damage. *DNA Repair (Amst.)* **12**, 306–311.
- Joyce, E.F., Paul, A., Chen, K.E., Tanneti, N., and McKim, K.S. (2012). Multiple Barriers to Nonhomologous DNA End Joining During Meiosis in *Drosophila*. *Genetics* **191**, 739–746.
- Juillerat, A., Gronemeyer, T., Keppler, A., Gendreizig, S., Pick, H., Vogel, H., and Johnsson, K. (2003). Directed Evolution of O6-Alkylguanine-DNA Alkyltransferase for Efficient Labeling of Fusion Proteins with Small Molecules In Vivo. *Chem. Biol.* **10**, 313–317.
- Kanaar, R., Hoeijmakers, J.H., and van Gent, D.C. (1998). Molecular mechanisms of DNA double-strand break repair. *Trends Cell Biol.* **8**, 483–489.
- Keeney, S., Giroux, C.N., and Kleckner, N. (1997). Meiosis-specific DNA double-strand breaks are catalyzed by Spo11, a member of a widely conserved protein family. *Cell* **88**, 375–384.
- King, M.-C. (2003). Breast and Ovarian Cancer Risks Due to Inherited Mutations in BRCA1 and BRCA2. *Science* **302**, 643–646.
- Klar, T.A., and Hell, S.W. (1999). Subdiffraction resolution in far-field fluorescence microscopy. *Opt. Lett.* **24**, 954.
- Kolodner, R.D., and Marsischky, G.T. (1999). Eukaryotic DNA mismatch repair. *Curr. Opin. Genet. Dev.* **9**, 89–96.
- Krawczyk, P.M., Eppink, B., Essers, J., Stap, J., Rodermond, H., Odijk, H., Zelensky, A., van Bree, C., Stalpers, L.J., Buist, M.R., et al. (2011). Mild hyperthermia inhibits homologous recombination, induces BRCA2 degradation, and sensitizes cancer cells to poly (ADP-ribose) polymerase-1 inhibition. *Proc. Natl. Acad. Sci. U. S. A.* **108**, 9851–9856.
- Krokan, H.E., Standal, R., and Slupphaug, G. (1997). DNA glycosylases in the base excision repair of DNA. *Biochem. J.* **325** ( Pt 1), 1–16.
- Kuraoka, I. (2000). Repair of an Interstrand DNA Cross-link Initiated by ERCC1-XPF Repair/Recombination Nuclease. *J. Biol. Chem.* **275**, 26632–26636.
- Kurzbauer, M.-T.T., Uanschou, C., Chen, D., Schlögelhofer, P., and Schlegelhofer, P. (2012). The recombinases DMC1 and RAD51 are functionally and spatially separated during meiosis in Arabidopsis. *Plant Cell* **24**, 2058–2070.
- de Laat, W.L. (1998). DNA Structural Elements Required for ERCC1-XPF Endonuclease Activity. *J. Biol. Chem.* **273**, 7835–7842.
- Lahue, R.S., Su, S.S., and Modrich, P. (1987). Requirement for d(GATC) sequences in *Escherichia coli* mutHLS mismatch correction. *Proc. Natl. Acad. Sci. U. S. A.* **84**, 1482–1486.
- Lee, J.-H. (2004). Direct Activation of the ATM Protein Kinase by the Mre11/Rad50/Nbs1 Complex. *Science* **304**, 93–96.
- Lee, J.-H. (2005). ATM Activation by DNA Double-Strand Breaks Through the Mre11-Rad50-Nbs1 Complex. *Science* **308**, 551–554.
- Lee, J.Y., Terakawa, T., Qi, Z., Steinfeld, J.B., Redding, S., Kwon, Y., Gaines, W.A., Zhao, W., Sung, P., and Greene, E.C. (2015). Base triplet stepping by the Rad51/RecA family of recombinases. *Science* **349**, 977–981.
- Lindahl, T. (1974). An N-glycosidase from *Escherichia coli* that releases free uracil from DNA containing deaminated cytosine residues. *Proc. Natl. Acad. Sci. U. S. A.* **71**, 3649–3653.
- van de Linde, S., Löscherberger, A., Klein, T., Heidbreder, M., Wolter, S., Heilemann, M., and Sauer, M. (2011). Direct stochastic optical reconstruction microscopy with standard fluorescent probes. *Nat. Protoc.* **6**, 991–1009.
- Long, D.T., Raschle, M., Joukov, V., and Walter, J.C. (2011). Mechanism of RAD51-Dependent DNA Interstrand Cross-Link Repair. *Science* **333**, 84–87.
- Los, G. V., Encell, L.P., McDougall, M.G., Hartzell, D.D., Karassina, N., Zimprich, C., Wood, M.G., Learish, R., Ohana, R.F., Urh, M., et al. (2008). HaloTag: A Novel Protein Labeling Technology for Cell Imaging and Protein Analysis. *ACS Chem. Biol.* **3**, 373–382.

- Luckow, B., Bunz, F., Stillman, B., Lichter, P., and Schütz, G. (1994). Cloning, expression, and chromosomal localization of the 140-kilodalton subunit of replication factor C from mice and humans. *Mol. Cell. Biol.* **14**, 1626–1634.
- Lukinavičius, G., Umezawa, K., Olivier, N., Honigsmann, A., Yang, G., Plass, T., Mueller, V., Raymond, L., Corréa, I.R., Luo, Z.-G., et al. (2013). A near-infrared fluorophore for live-cell super-resolution microscopy of cellular proteins. *Nat. Chem.* **5**, 132–139.
- Manley, S., Gillette, J.M., Patterson, G.H., Shroff, H., Hess, H.F., Betzig, E., and Lippincott-Schwartz, J. (2008). High-density mapping of single-molecule trajectories with photoactivated localization microscopy. *Nat. Methods* **5**, 155–157.
- Mason, J.M., Dusad, K., Wright, W.D., Grubb, J., Budke, B., Heyer, W.-D., Connell, P.P., Weichselbaum, R.R., and Bishop, D.K. (2015). RAD54 family translocases counter genotoxic effects of RAD51 in human tumor cells. *Nucleic Acids Res.* **43**, 3180–3196.
- Masson, J.Y., Tarsounas, M.C., Stasiak, a. Z., Stasiak, a., Shah, R., McIlwraith, M.J., Benson, F.E., and West, S.C. (2001). Identification and purification of two distinct complexes containing the five RAD51 paralogs. *EMBO J.* **20**, 3296–3307.
- Masutani, C., Sugawara, K., Yanagisawa, J., Sonoyama, T., Ui, M., Enomoto, T., Takio, K., Tanaka, K., van der Spek, P.J., and Bootsma, D. (1994). Purification and cloning of a nucleotide excision repair complex involving the xeroderma pigmentosum group C protein and a human homologue of yeast RAD23. *EMBO J.* **13**, 1831–1843.
- Matos, J., and West, S.C. (2014). Holliday junction resolution: Regulation in space and time. *DNA Repair (Amst)*. **19**, 176–181.
- Matsumoto, Y., Kim, K., and Bogenhagen, D.F. (1994). Proliferating cell nuclear antigen-dependent abasic site repair in *Xenopus laevis* oocytes: an alternative pathway of base excision DNA repair. *Mol. Cell. Biol.* **14**, 6187–6197.
- Matulova, P., Marini, V., Burgess, R.C., Sisakova, A., Kwon, Y., Rothstein, R., Sung, P., and Krejci, L. (2009). Cooperativity of Mus81-Mms4 with Rad54 in the Resolution of Recombination and Replication Intermediates. *J. Biol. Chem.* **284**, 7733–7745.
- Mazin, A. V., Bornarth, C.J., Solinger, J.A., Heyer, W.D., and Kowalczykowski, S.C. (2000). Rad54 protein is targeted to pairing loci by the Rad51 nucleoprotein filament. *Mol. Cell* **6**, 583–592.
- Mazin, A. V., Alexeev, A.A., and Kowalczykowski, S.C. (2003). A novel function of Rad54 protein. Stabilization of the Rad51 nucleoprotein filament. *J. Biol. Chem.* **278**, 14029–14036.
- Medhurst, A.L. (2006). Evidence for subcomplexes in the Fanconi anemia pathway. *Blood* **108**, 2072–2080.
- Mellon, I., Spivak, G., and Hanawalt, P.C. (1987). Selective removal of transcription-blocking DNA damage from the transcribed strand of the mammalian DHFR gene. *Cell* **51**, 241–249.
- Moerner, W.E. (1996). High-Resolution Optical Spectroscopy of Single Molecules in Solids. *Acc. Chem. Res.* **29**, 563–571.
- Mok, M.T.S., and Henderson, B.R. (2012). The in vivo dynamic interplay of MDC1 and 53BP1 at DNA damage-induced nuclear foci. *Int. J. Biochem. Cell Biol.* **44**, 1398–1409.
- Moser, J., Volker, M., Kool, H., Alekseev, S., Vrieling, H., Yasui, A., van Zeeland, A.A., and Mullenders, L.H.F. (2005). The UV-damaged DNA binding protein mediates efficient targeting of the nucleotide excision repair complex to UV-induced photo lesions. *DNA Repair (Amst)*. **4**, 571–582.
- Moser, J., Kool, H., Giakzidis, I., Caldecott, K., Mullenders, L.H.F., and Fouteri, M.I. (2007). Sealing of Chromosomal DNA Nicks during Nucleotide Excision Repair Requires XRCC1 and DNA Ligase III $\alpha$  in a Cell-Cycle-Specific Manner. *Mol. Cell* **27**, 311–323.
- Muniandy, P.A., Liu, J., Majumdar, A., Liu, S., and Seidman, M.M. (2010). DNA interstrand crosslink repair in mammalian cells: step by step. *Crit. Rev. Biochem. Mol. Biol.* **45**, 23–49.
- Nakazawa, Y., Sasaki, K., Mitsutake, N., Matsuse, M., Shimada, M., Nardo, T., Takahashi, Y., Ohyama, K., Ito, K., Mishima, H., et al. (2012). Mutations in UVS-SA cause UV-sensitive syndrome and impair RNA polymerase II processing in transcription-coupled nucleotide-excision repair. *Nat. Genet.* **44**, 586–592.
- Nick McElhinny, S.A., Kissling, G.E., and Kunkel, T.A. (2010). Differential correction of lagging-strand replication errors made by DNA polymerases  $\alpha$  and  $\delta$ . *Proc. Natl. Acad. Sci.* **107**, 21070–21075.
- Nimonkar, A. V., Genschel, J., Kinoshita, E., Polaczek, P., Campbell, J.L., Wyman, C., Modrich, P., and Kowalczykowski, S.C. (2011). BLM-DNA2-RPA-MRN and EXO1-BLM-RPA-MRN constitute two DNA end resection machineries for human DNA break repair. *Genes Dev.* **25**, 350–362.
- Nishi, R., Okuda, Y., Watanabe, E., Mori, T., Iwai, S., Masutani, C., Sugawara, K., and Hanaoka, F. (2005). Centrin 2 Stimulates Nucleotide Excision Repair by Interacting with Xeroderma Pigmentosum Group C Protein. *Mol. Cell. Biol.* **25**, 5664–5674.
- Nussenzweig, A., Chen, C., da Costa Soares, V., Sanchez, M., Sokol, K., Nussenzweig, M.C., and Li, G.C. (1996). Requirement for Ku80 in growth and immunoglobulin V(D)J recombination. *Nature* **382**, 551–555.
- Ochs, F., Somyajit, K., Altmeyer, M., Rask, M.-B., Lukas, J., and Lukas, C. (2016). 53BP1 fosters fidelity of homology-directed DNA repair. *Nat. Struct. Mol. Biol.*
- Oliver, A.W., Swift, S., Lord, C.J., Ashworth, A., and Pearl, L.H. (2009). Structural basis for recruitment of BRCA2 by PALB2. *EMBO Rep.* **10**, 990–996.
- Patterson, G.H., and Lippincott-Schwartz, J. (2002). A photoactivatable GFP for selective photolabeling of proteins and cells. *Science* **297**, 1873–1877.
- Petes, T.D. (2001). Meiotic recombination hot spots and cold spots. *Nat. Rev. Genet.* **2**, 360–369.
- Petukhova, G., Stratton, S., and Sung, P. (1998). Catalysis of homologous DNA pairing by yeast Rad51 and Rad54 proteins. *Nature* **393**, 91–94.
- Plans, V., Scheper, J., Soler, M., Loukili, N., Okano, Y., and Thomson, T.M. (2006). The RING finger protein RNF8 recruits UBC13 for lysine 63-based self polyubiquitylation. *J. Cell. Biochem.* **97**, 572–582.
- Qiao, H., Chen, J.K., Reynolds, A., Höög, C., Paddy, M., and Hunter, N. (2012). Interplay between synaptonemal complex, homologous recombination, and centromeres during mammalian meiosis. *PLoS Genet.* **8**, e1002790.
- Qin, J., Richardson, L.L., Jasin, M., Handel, M.A., and Arnheim, N. (2004). Mouse Strains with an Active H2-Ea Meiotic Recombination Hot Spot Exhibit Increased Levels of H2-Ea-Specific DNA Breaks in Testicular Germ Cells. *Mol. Cell. Biol.* **24**, 1655–1666.
- Raderschall, E., Golub, E.I., and Haaf, T. (1999). Nuclear foci of mammalian recombination proteins are located at single-stranded DNA regions formed after DNA damage. *Proc. Natl. Acad. Sci. U. S. A.* **96**, 1921–1926.

- Reid, D. a., Keegan, S., Leo-Macias, A., Watanabe, G., Strande, N.T., Chang, H.H., Oksuz, B.A., Fenyo, D., Lieber, M.R., Ramsden, D. a., et al. (2015). Organization and dynamics of the nonhomologous end-joining machinery during DNA double-strand break repair. *Proc. Natl. Acad. Sci. U. S. A.* *112*, E2575–2584.
- Reuter, M., Zelensky, A., Smal, I., Meijering, E., van Cappellen, W.A., de Gruiter, H.M., van Belle, G.J., van Royen, M.E., Houtsmuller, A.B., Essers, J., et al. (2014). BRCA2 diffuses as oligomeric clusters with RAD51 and changes mobility after DNA damage in live cells. *J. Cell Biol.* *207*, 599–613.
- Rieger, B., and Stallinga, S. (2014). The Lateral and Axial Localization Uncertainty in Super-Resolution Light Microscopy. *ChemPhysChem* *15*, 664–670.
- Rogakou, E.P., Pilch, D.R., Orr, A.H., Ivanova, V.S., and Bonner, W.M. (1998). DNA Double-stranded Breaks Induce Histone H2AX Phosphorylation on Serine 139. *J. Biol. Chem.* *273*, 5858–5868.
- Van Royen, M.E., Zotter, A., Ibrahim, S.M., Geverts, B., and Houtsmuller, A.B. (2011). Nuclear proteins: finding and binding target sites in chromatin. *Chromosome Res.* *19*, 83–98.
- Van Royen, M.E., van Cappellen, W.A., Geverts, B., Schmidt, T., Houtsmuller, A.B., and Schaaf, M.J.M. (2014). Androgen receptor complexes probe DNA for recognition sequences by short random interactions. *J. Cell Sci.* *127*, 1406–1416.
- Rust, M.J., Bates, M., and Zhuang, X. (2006). Sub-diffraction-limit imaging by stochastic optical reconstruction microscopy (STORM). *Nat. Methods* *3*, 793–795.
- Sarkar, S., Davies, A.A., Ulrich, H.D., and McHugh, P.J. (2006). DNA interstrand crosslink repair during G1 involves nucleotide excision repair and DNA polymerase  $\zeta$ . *EMBO J.* *25*, 1285–1294.
- Sartori, A.A., Lukas, C., Coates, J., Mistrik, M., Fu, S., Bartek, J., Baer, R., Lukas, J., and Jackson, S.P. (2007). Human CtIP promotes DNA end resection. *Nature* *450*, 509–514.
- Schaeffer, L., Moncollin, V., Roy, R., Staub, A., Mezzina, M., Sarasin, A., Weeda, G., Hoeijmakers, J.H., and Egly, J.M. (1994). The ERCC2/DNA repair protein is associated with the class II BTF2/TFIIH transcription factor. *EMBO J.* *13*, 2388–2392.
- Schermelleh, L., Heintzmann, R., and Leonhardt, H. (2010). A guide to super-resolution fluorescence microscopy. *J. Cell ...* *190*, 165–175.
- Schlacher, K., Christ, N., Siaud, N., Egashira, A., Wu, H., and Jasin, M. (2011). Double-strand break repair-independent role for BRCA2 in blocking stalled replication fork degradation by MRE11. *Cell* *145*, 529–542.
- Schücker, K., Holm, T., Franke, C., Sauer, M., and Benavente, R. (2015). Elucidation of synaptonemal complex organization by super-resolution imaging with isotropic resolution. *Proc. Natl. Acad. Sci.* *112*, 2029–2033.
- Schwacha, A., and Kleckner, N. (1997). Interhomolog Bias during Meiotic Recombination: Meiotic Functions Promote a Highly Differentiated Interhomolog-Only Pathway. *Cell* *90*, 1123–1135.
- Schwertman, P., Lagarou, A., Dekkers, D.H.W., Raams, A., van der Hoek, A.C., Laffeber, C., Hoeijmakers, J.H.J., Demmers, J. a, Fouteri, M., Vermeulen, W., et al. (2012). UV-sensitive syndrome protein UVSSA recruits USP7 to regulate transcription-coupled repair. *Nat. Genet.* *44*, 598–602.
- Sehorn, M.G., Sigurdsson, S., Bussen, W., Unger, V.M., and Sung, P. (2004). Human meiotic recombinase Dmc1 promotes ATP-dependent homologous DNA strand exchange. *Nature* *429*, 433–437.
- Sengerová, B., Wang, A.T., and McHugh, P.J. (2011). Orchestrating the nucleases involved in DNA interstrand cross-link (ICL) repair. *Cell Cycle* *10*, 3999–4008.
- Shahid, T., Soroka, J., Kong, E.H., Malivert, L., Mcllwraith, M.J., Pape, T., West, S.C., and Zhang, X. (2014). Structure and mechanism of action of the BRCA2 breast cancer tumor suppressor. *Nat. Struct. Mol. Biol.*
- Shaner, N.C., Campbell, R.E., Steinbach, P. a, Giepmans, B.N.G., Palmer, A.E., and Tsien, R.Y. (2004). Improved monomeric red, orange and yellow fluorescent proteins derived from *Discosoma* sp. red fluorescent protein. *Nat. Biotechnol.* *22*, 1567–1572.
- Sharonov, A., and Hochstrasser, R.M. (2006). Wide-field subdiffraction imaging by accumulated binding of diffusing probes. *Proc. Natl. Acad. Sci.* *103*, 18911–18916.
- Sheridan, S.D., Yu, X., Roth, R., Heuser, J.E., Sehorn, M.G., Sung, P., Egelman, E.H., and Bishop, D.K. (2008). A comparative analysis of Dmc1 and Rad51 nucleoprotein filaments. *Nucleic Acids Res.* *36*, 4057–4066.
- Shibata, A., Conrad, S., Birraux, J., Geuting, V., Barton, O., Ismail, A., Kakarougkas, A., Meek, K., Taucher-Scholz, G., Löbrich, M., et al. (2011). Factors determining DNA double-strand break repair pathway choice in G2 phase. *EMBO J.* *30*, 1079–1092.
- Shrivastav, M., De Haro, L.P., and Nickoloff, J.A. (2008). Regulation of DNA double-strand break repair pathway choice. *Cell Res.* *18*, 134–147.
- Shroff, H., Galbraith, C.G., Galbraith, J.A., and Betzig, E. (2008). Live-cell photoactivated localization microscopy of nanoscale adhesion dynamics. *Nat Meth* *5*, 417–423.
- Singleton, M.R., Wentzell, L.M., Liu, Y., West, S.C., and Wigley, D.B. (2002). Structure of the single-strand annealing domain of human RAD52 protein. *Proc. Natl. Acad. Sci.* *99*, 13492–13497.
- Solinger, J.A., Lutz, G., Sugiyama, T., Kowalczykowski, S.C., and Heyer, W.D. (2001). Rad54 protein stimulates heteroduplex DNA formation in the synaptic phase of DNA strand exchange via specific interactions with the presynaptic Rad51 nucleoprotein filament. *J. Mol. Biol.* *307*, 1207–1221.
- Solinger, J. a, Kianitsa, K., and Heyer, W.-D. (2002). Rad54, a Swi2/Snf2-like Recombinational Repair Protein, Disassembles Rad51:dsDNA Filaments. *Mol. Cell* *10*, 1175–1188.
- Spain, B.H., Larson, C.J., Shihabuddin, L.S., Gage, F.H., and Verma, I.M. (1999). Truncated BRCA2 is cytoplasmic: Implications for cancer-linked mutations. *Proc. Natl. Acad. Sci.* *96*, 13920–13925.
- Stap, J., Krawczyk, P.M., Van Oven, C.H., Barendsen, G.W., Essers, J., Kanaar, R., and Aten, J.A. (2008). Induction of linear tracks of DNA double-strand breaks by [alpha]-particle irradiation of cells. *Nat Meth* *5*, 261–266.
- Stasiak, A., and Di Capua, E. (1982). The helicity of DNA in complexes with recA protein. *Nature* *299*, 185–186.
- Stiff, T. (2004). ATM and DNA-PK Function Redundantly to Phosphorylate H2AX after Exposure to Ionizing Radiation. *Cancer Res.* *64*, 2390–2396.
- Stucki, M., Clapperton, J.A., Mohammad, D., Yaffe, M.B., Smerdon, S.J., and Jackson, S.P. (2005). MDC1 Directly Binds Phosphorylated Histone H2AX to Regulate Cellular Responses to DNA Double-Strand Breaks. *Cell* *123*, 1213–1226.
- Subach, F. V, Patterson, G.H., Manley, S., Gillette, J.M., Lippincott-Schwartz, J., and Verkhusa, V. V (2009). Photoactivatable mCherry for high-resolution two-color fluorescence microscopy. *Nat Meth* *6*, 153–159.

- Sung, P., and Klein, H. (2006). Mechanism of homologous recombination: mediators and helicases take on regulatory functions. *Nat. Rev. Mol. Cell Biol.* **7**, 739–750.
- Sung, P., and Roberson, D.L. (1995). DNA strand exchange mediated by a RAD51-ssDNA nucleoprotein filament with polarity opposite to that of RecA. *Cell* **82**, 453–461.
- Suzuki, K., Okada, H., Yamauchi, M., Oka, Y., Kodama, S., and Watanabe, M. (2006). Qualitative and Quantitative Analysis of Phosphorylated ATM Foci Induced by Low-Dose Ionizing Radiation. *Source Radiat. Res.* **165**, 499–504.
- Sy, S.M.H., Huen, M.S.Y., and Chen, J. (2009). PALB2 is an integral component of the BRCA complex required for homologous recombination repair. *Proc. Natl. Acad. Sci. U. S. A.* **106**, 7155–7160.
- Symington, L.S. (2002). Role of RAD52 Epistasis Group Genes in Homologous Recombination and Double-Strand Break Repair. *Microbiol. Mol. Biol. Rev.* **66**, 630–670.
- Taccioli, G., Rathbun, G., Oltz, E., Stamato, T., Jeggo, P., and Alt, F. (1993). Impairment of V(D)J recombination in double-strand break repair mutants. *Science* **260**, 207–210.
- Taylor, M.R.G., Špirék, M., Chaurasiya, K.R., Ward, J.D., Carzaniga, R., Yu, X., Egelman, E.H., Collinson, L.M., Rueda, D., Krejci, L., et al. (2015). Rad51 Paralogs Remodel Pre-synaptic Rad51 Filaments to Stimulate Homologous Recombination. *Cell* **162**, 271–286.
- Thompson, R.E., Larson, D.R., and Webb, W.W. (2002). Precise nanometer localization analysis for individual fluorescent probes. *Biophys. J.* **82**, 2775–2783.
- Thorslund, T., Esashi, F., and West, S.C. (2007). Interactions between human BRCA2 protein and the meiosis-specific recombinase DMC1. *EMBO J.* **26**, 2915–2922.
- Tokunaga, M., Imamoto, N., and Sakata-sogawa, K. (2008). Highly inclined thin illumination enables clear single-molecule imaging in cells. *5*, 159–161.
- van Veelen, L.R., Cervelli, T., van de Rakt, M.W.M.M., Theil, A.F., Essers, J., and Kanaar, R. (2005). Analysis of ionizing radiation-induced foci of DNA damage repair proteins. *Mutat. Res. Mol. Mech. Mutagen.* **574**, 22–33.
- Walker, J.R., Corpina, R.A., and Goldberg, J. (2001). Structure of the Ku heterodimer bound to DNA and its implications for double-strand break repair. *Nature* **412**, 607–614.
- Wang, X., and Haber, J.E. (2004). Role of Saccharomyces Single-Stranded DNA-Binding Protein RPA in the Strand Invasion Step of Double-Strand Break Repair. *PLoS Biol.* **2**, e21.
- Wang, S., Moffitt, J.R., Dempsey, G.T., Xie, X.S., and Zhuang, X. (2014). Characterization and development of photoactivatable fluorescent proteins for single-molecule-based superresolution imaging. *Proc. Natl. Acad. Sci.*
- Wang, S., Zickler, D., Kleckner, N., and Zhang, L. (2015). Meiotic crossover patterns: Obligatory crossover, interference and homeostasis in a single process. *Cell Cycle* **14**, 305–314.
- Wesoly, J., Agarwal, S., Sigurdsson, S., Bussen, W., Komen, S., Van, Qin, J., Steeg, H. Van, Benthem, J. Van, Wassenaar, E., Baarends, W.M., et al. (2006). Differential contributions of mammalian Rad54 paralogs to recombination, DNA damage repair, and meiosis. *Mol. Cell. Biol.* **26**, 976–989.
- Wilson, T.E., Grawunder, U., and Lieber, M.R. (1997). Yeast DNA ligase IV mediates non-homologous DNA end joining. *Nature* **388**, 495–498.
- Wyman, C., and Kanaar, R. (2006). DNA Double-Strand Break Repair: All's Well that Ends Well. *Annu. Rev. Genet.* **40**, 363–383.
- Xue, L., Karpenko, I.A., Hiblot, J., and Johnsson, K. (2015). Imaging and manipulating proteins in live cells through covalent labeling. *Nat. Chem. Biol.* **11**, 1–7.
- Yonetani, Y. (2005). Differential and collaborative actions of Rad51 paralog proteins in cellular response to DNA damage. *Nucleic Acids Res.* **33**, 4544–4552.
- Yuan, S.S., Lee, S.Y., Chen, G., Song, M., Tomlinson, G.E., and Lee, E.Y. (1999). BRCA2 is required for ionizing radiation-induced assembly of Rad51 complex in vivo. *Cancer Res.* **59**, 3547–3551.
- Zelensky, A., Kanaar, R., and Wyman, C. (2014). Mediators of homologous DNA pairing. *Cold Spring Harb. Perspect. Biol.* **6**, a016451.
- Zhang, M., Chang, H., Zhang, Y., Yu, J., Wu, L., Ji, W., Chen, J., Liu, B., Lu, J., Liu, Y., et al. (2012). Rational design of true monomeric and bright photoactivatable fluorescent proteins. *Nat. Methods* **9**, 727–729.
- Zhou, Y., Caron, P., Legube, G., and Paull, T.T. (2013). Quantitation of DNA double-strand break resection intermediates in human cells. *Nucleic Acids Res.* **1–11**.
- Zierhut, C., and Diffley, J.F.X. (2008). Break dosage, cell cycle stage and DNA replication influence DNA double strand break response. *EMBO J.* **27**, 1875–1885.





## Chapter II

# Single Molecule Localization in R (SMoLR), a versatile software package for visualization and analysis of single molecule localization data in R

Maarten W. Paul<sup>\*1,2</sup>, Johan A. Slotman<sup>\*1</sup>, Martijn de Groot<sup>1</sup>, Zhanmin Lin<sup>3</sup>,  
Adriaan B. Houtsmuller<sup>1,2</sup>


<sup>1</sup>Optical Imaging Centre, <sup>2</sup>Department of Pathology, and <sup>3</sup>Department of Neurosciences, Erasmus University Medical Center, 3000 CA Rotterdam, The Netherlands

\*Contributed equally

*Manuscript in preparation*



## Abstract



Localization-based super resolution microscopy enables determination of the localization of proteins at high accuracy. Extracting quantitative information from super resolution images is essential for biological interpretation of the data. For this purpose, we developed a flexible framework that enables exploration and analysis of single-molecule localization data within the R programming environment in a package which we named *SMoLR* (Single Molecule Localization in R). The package includes methods for visualization and quantification of large localization data sets consisting of multiple images. The package can be applied to visualize and analyze nanoscale subcellular structures, and obtain statistics about distribution and localization of molecules within them. Using image feature-based particle averaging we describe a method to combine single molecule data and to identify common features in nanoscale subcellular structures. We applied the developed methods to address biological questions on the organizations of proteins in foci during DNA Double Strand Break Repair and the localization of scaffolding proteins in neuronal synapses.

## Introduction

The development of super resolution microscopy techniques makes it possible to study subcellular structures at nanoscale using fluorescence microscopy. Among those super resolution techniques, single molecule localization microscopy (SMLM) provides the highest spatial resolution as the localization of individual molecules can be determined at accuracies ranging from 5 to 20 nm dependent on the brightness of the fluorophore (Schermelleh et al., 2010). SMLM relies on detecting the signal of single fluorescent emitters, by separating in time the fluorescence of spatially overlapping signals, either by induced stochastic blinking of fluorophores (dSTORM) (Rust et al., 2006), photo activation (PALM) (Betzig et al., 2006) or transient binding of fluorophores (PAINT) (Sharonov and Hochstrasser, 2006). In living cells this same principle can also be applied for single particle tracking (sptPALM) (Manley et al., 2008). This facilitates the detection of the position of fluorescent molecules in densely labeled biological samples with high accuracy, resulting in an image with a resolution far below the diffraction limit where, dependent on photon yield, a localization accuracy of approximately 10 nm can be achieved (Betzig et al., 2006; Nieuwenhuizen et al., 2013).

Reconstruction, visualization and analysis of single molecule localization data requires dedicated software. The first step of the analysis is the reconstruction of super resolution images by detecting and fitting a Gaussian distribution reflecting point spread functions (PSFs) to signals of individual fluorophores in the image. For this goal many methods and corresponding software packages have previously been developed (Sage et al., 2015), which are available either as stand-alone packages (open source) on the internet or are included in commercial microscope setups for real-time analysis of the data. In addition, software has been described in literature that is dedicated to visualization of localization data, of which examples are PALMSiever (Pengo et al., 2014) and for 3D localization data, ViSP (El Beheiry and Dahan, 2013). However publicly available software that enables researchers to perform in-depth quantitative and statistical analysis of PALM/STORM data, and fits to the

specific needs of these researchers is still lacking.

In many biological samples a multitude of macromolecular assemblies and protein complexes within one cell can be observed, such as double strand break (DSB) foci (Reid et al., 2015), nuclear pores (Szymborska et al., 2013), focal adhesions (Rossier et al., 2012), virus particles (Laine et al., 2015) or neuronal spines (Dani et al., 2010). Super resolution microscopy is well suited to study those assemblies, since the increased resolution permits to investigate, at the single molecule level, the internal composition and protein distribution of these nanoscale assemblies, which have typical diameters ranging from 100 nm up to 2  $\mu$ m. Several publications have shown that analysis of sufficient numbers of super resolved cellular structures can provide a better understanding of the organization of protein assemblies, relate this to their function, and to infer molecular mechanisms by which they exert their biological functions (Van Engelenburg et al., 2014; Reid et al., 2015; Szymborska et al., 2013).

Since many microscopic images include entire cells from which the subcellular structures will be analyzed, an important first step is the selection of individual regions of interest (ROIs) from the overall image. The ROI images can be analyzed using image analysis software such as the widely used open source software ImageJ or FIJI. However, localization data obtained by SMLM consists of Cartesian coordinates representing the localization estimate of individual fluorophores, labeling the protein (or other biomolecule), whereas the standard digital image format that image analysis packages use consists of equally spaced binned intensities (pixels or voxels). The pointillist nature of the data gives possibilities for alternative types of analysis of the data, for which the resourceful possibilities of R can be of great value. In R, data sets containing hundreds to thousands of ROIs with localization data can be analyzed in parallel.

Here, we present a versatile software package, named SMoLR (Single Molecule Localization in R), that enables biologists to analyze single molecule localization data in a quantitative way.

## Description of the software

R is a data analysis environment which is frequently used in the biological community especially for high-throughput genomic data (Huber et al., 2015). The possibilities of R for high-throughput data analysis, provides an excellent base for analysis of localization data, as the numbers of individual structures to analyze, such as DSB foci or neuronal synapses, are generally high. This type of data can be defined as spatial point patterns describing the underlying spatial organization of proteins. Other scientific fields where spatial data is analyzed, such as ecology and geography, also frequently use R and its dedicated packages (CRAN Task View: Analysis of Spatial Data, sd). Additional advantages of using R for analysis of SMLM data is the free/open source availability of the software as well as the large online active community. Using R, it is also relatively easy to analyze data sets with a large number of images or sets of ROI's from images. Moreover, with the powerful statistics available in R it is possible to explore the localization data and readily visualize results

using the plotting and statistics packages present in R (Baddeley et al., 2016).

SMoLR is developed in R (R Core Team, 2016) using Rstudio (RStudio Team, 2015). The software package requires basic experience with R. Therefore, we also implemented a data browser, which enables to explore the basic functionalities of the package for researchers unfamiliar with R. The functions in the software package can be applied to a single image (in R this is a *data.frame* with localizations) or alternatively to a large number of protein assemblies in parallel (organized in R as a *list* data type) (Table 1). This enables straightforward extraction of quantitative parameters regarding, shape, size, protein distribution and cluster localization from all these objects.

### Input data

The input data for the package is localization data, typically a table of Cartesian coordinates, which can be obtained using software for detecting single molecule localizations from raw data. The data processing steps that should be

Importing data	Input	Description	Depends on
SMOLR_IMPORT()	folder of localizations files	Import localizations files into R data structures	
SMOLR_LOAD()	folder of localizations files	Loads R data which was imported using SMOLR_IMPORT()	
RImageROI()	ImageJ ROImanager (.roi/.zip)	Imports ROIs defined in ImageJ to R	RImageROI[1]
<b>Visualization</b>			
SMOLR()	localizations (vectors,data.frame,list)	Visualization of localizations by Precision-based Gaussian Plotting	
SMOLR_KDE()	localizations (vectors,data.frame,list)	Visualization by 2D Kernel density estimation, intensity normalized by localization density/nm <sup>2</sup>	KernSmooth[2], EBImage[3]
SMOLR_PLOT()	localizations (vectors,data.frame,list)	Visualization of all localizations by scatterplot with options to adjust size or color of individual localizations	
<b>Quantification</b>			
SMOLR_DBSCAN()	localizations (vectors,data.frame,list)	Density based Clustering by counting the number of localizations (MinPts) in a certain radius (eps)	dbscan[4]
SMOLR_TO_PPP()	localizations (vectors,data.frame,list)	Facilitates analysis of localization data using spatstat, an extensive library for spatial analysis.	spatstat[5]
SMOLR_FEATURES()	SMOLR_KDE	Feature extration from images	EBImage[3]
SMOLR_POINT_FEATURES()	SMOLR_KDE,SMOLR_DBSCAN	Point based features, e.g. cluster area, elongation, number of localizations	
SMOLR_ROTATE()	localizations	Rotate and translate localization data based on defined angle	
SMOLR_PARAMETER()	localizations	Calculate basic statistics from localizations (x,y, precision)	

[1] <https://cran.r-project.org/web/packages/RImageROI/index.html>

[2] <https://cran.r-project.org/web/packages/KernSmooth/index.html>

[3] <https://bioconductor.org/packages/release/bioc/html/EBImage.html>

[4] <https://cran.r-project.org/web/packages/dbscan/index.html>

[5] <https://cran.r-project.org/web/packages/spatstat/index.html>

**Table 1** Description of the main functions that are available in SMoLR. These functions require different input and for most of the functions different types of input are possible. Using R function definitions, the correct function is applied depending on the class of the input data. Some of the functions are dependent on existing R packages which can be found at the indicated webpages.

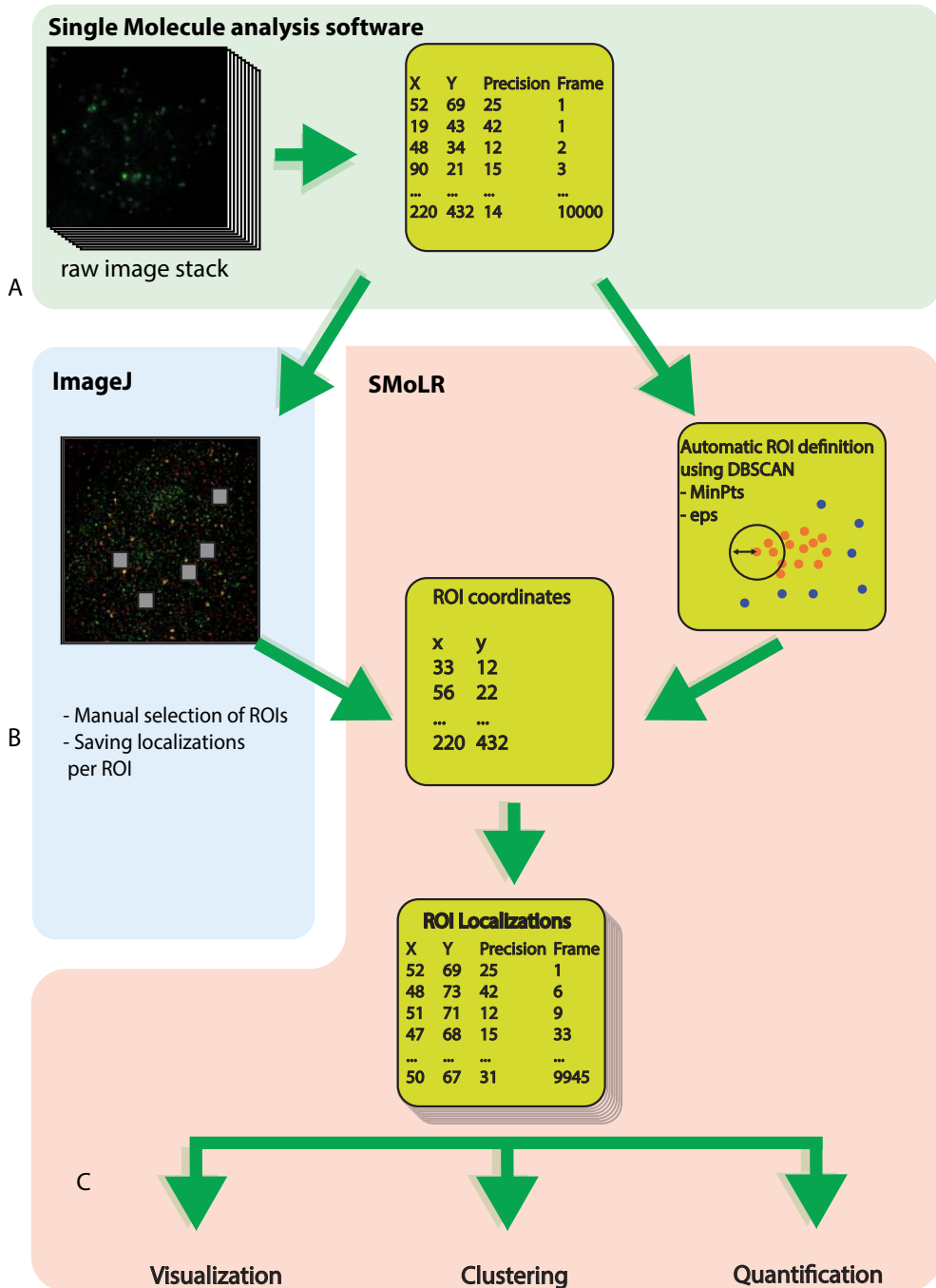


**Figure 1 Workflow of the SMoLR package** **A)** Super resolution images along with the table of localization data are obtained by Single Molecule Localization Microscopy using single molecule localization software **B)** The single molecule localization data (coordinates) are imported in R using the `SMoLR_IMPORT()` function (see Table 1). The localization data can be present in separate text files for all the ROIs but ROIs can also be calculated in R using DBSCAN clustering. The localization data is organized in a list. These data structures can serve as input for the several functions available in the package. **C)** In SMoLR different types of functions are available which can be divided in Visualization, Clustering and Quantification. An overview of all functions can be found in Table 1 and Figure 2.

*SMOLR\_IMPORT* function the localizations are well organized which makes it easy for further data analysis in the package (Figure 1B, Table 1). Besides selection of the ROIs in a different software package it is also possible to automatically acquire the ROIs by using one of the clustering algorithms provided in SMoLR. The individual clusters can be converted to ROIs for further analysis (Figure 1C). The data organized in lists can be used as input for the other functions in SMoLR or loaded in data browser as described below.

## Visualization

Single molecule localization data can be visualized in many different ways (Baddeley et al., 2010). Currently one of the most frequently used approaches is to plot Gaussian distributions for all localizations with standard deviations corresponding to the estimated localization accuracy (*SMOLR()*, Table 1, Figure 2A). This method is visually attractive but it is difficult to define a threshold, since the intensity does not only depend on the number of localizations present at a certain position but also on localization precision of the individual localizations. As an alternative, we implemented a 2D-kernel density estimation (KDE) approach, in which the density of detected molecules per area is normalized to the total number of localizations in the image (*SMOLR\_KDE()*, Table 1, Figure 2). The intensity of the individual pixels (default is 5x5 nm pixels) is therefore a direct measure of the density of localizations at that position. Subsequently a threshold can be set at a specific density of localizations to define localizations that belong together in a cluster. These defined clusters can then be used for quantification of the super resolution structures, by serving as the input for SMoLR functions which enable measurement of parameters such as size, intensity and length of the clusters.

As a second visualization approach, we developed an adapted scatter plot function (*SMOLR\_PLOT()*, Table 1, Figure 3) based on the R graphics modules, which include additional options to plot size and color of the localizations using additional parameters relevant for localization microscopy, such as the time frame

in which a molecule was detected (Figure 3A-C) and its localization precision (Figure 3D). This enables the user to visually inspect the localization data to eliminate artefacts occurring during extraction of localization analysis from raw data. Frequently occurring artefacts are drift during image acquisition, but also incorrect grouping of detections. The function can also be used to color based on any other parameter, for example after clustering of the data, the cluster it belongs to (Figure 3E). Finally, it is also possible to filter the data in the plot for example to only show the localized molecules with a high localization precision (Figure 3F). The plot can also be used to visualize features of ROIs or clusters in an overlay with a microscopy image. As an example, we visualized the cluster configurations of RAD51 and DMC1 in meiotic DSB foci, which are discussed in depth in Chapter 3 of this thesis. The cluster configurations are defined as the number of clusters of both DMC1 and RAD51 (Figure 4).

Finally, more types of visualization are implemented in SMoLR by using the *spatstat* package with the *SMOLR\_to\_ppp()* function (Table 1). For example, it is possible to plot a Voronoi triangulation (Figure 2C). The area of the individual tiles relates with the local labelling density, because the denser the localizations at a certain position the smaller the tiles will be. Therefore this visualization method can also be used to perform clustering as recently described (Levet et al., 2015).

## Clustering and quantification

Clustering of single molecule data is comparable to segmentation in conventional image analysis and in the same way as with segmented objects, features can be extracted from the clusters. As a first option a binary KDE image can be used to quantify the number of clusters per ROI. To calculate several image features per cluster we incorporated functions of an image analysis package in R: *EBimage* (Pau et al., 2010) (Figure 2). Additionally, several descriptive statistics are calculated, for example the number of localizations, mean position of the cluster and the mean localization precision. All these parameters can be used for exploration of the

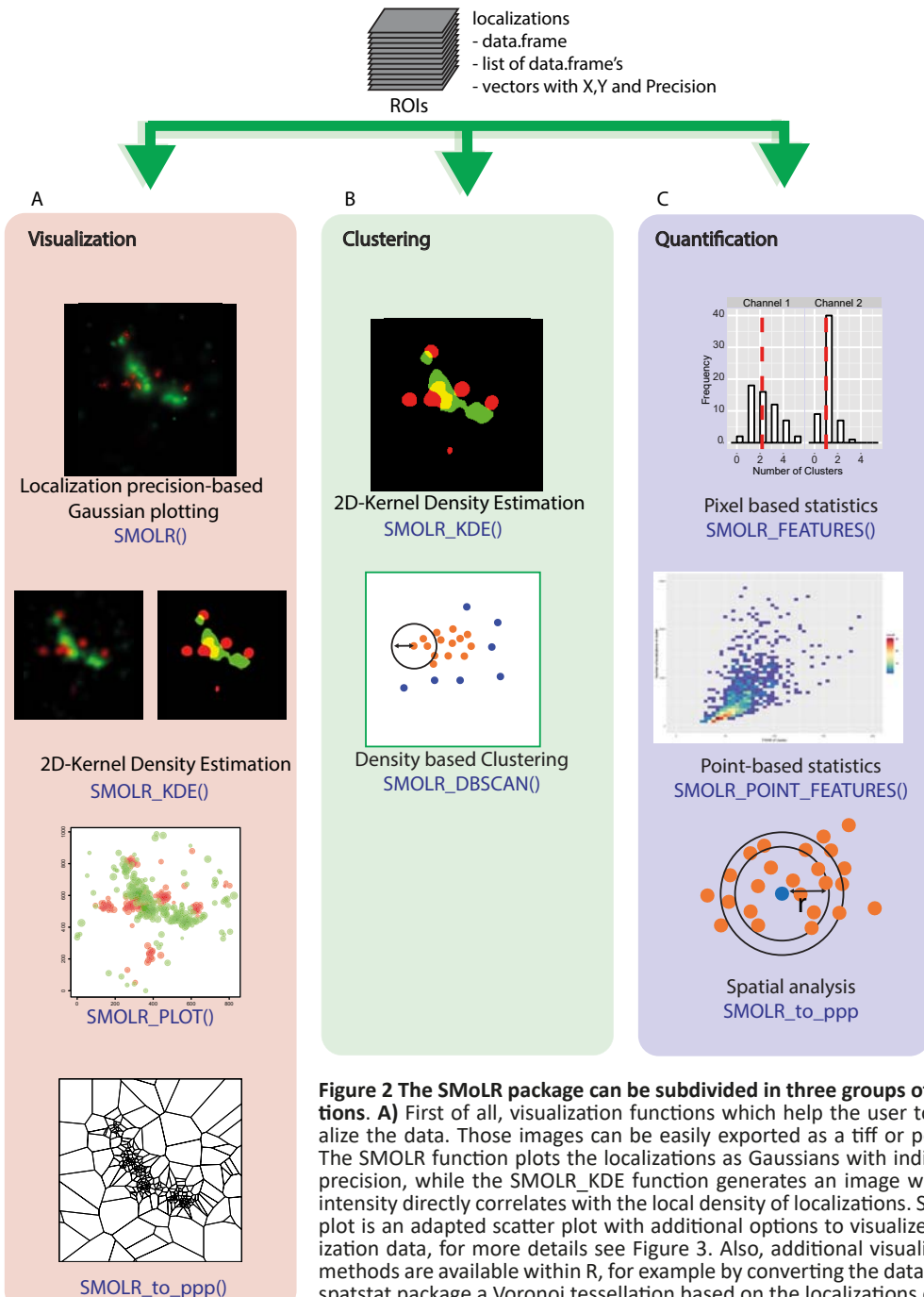


**Figure 2** The SMoLR package can be subdivided in three groups of functions. **A)** First of all, visualization functions which help the user to visualize the data. Those images can be easily exported as a tiff or pdf file. The SMoLR function plots the localizations as Gaussians with individual precision, while the `SMOLR_KDE` function generates an image wherein intensity directly correlates with the local density of localizations. `SMOLR_PLOT` is an adapted scatter plot with additional options to visualize localization data, for more details see Figure 3. Also, additional visualization methods are available within R, for example by converting the data to the `spatstat` package a Voronoi tessellation based on the localizations can be calculated and plotted. **B)** Secondly there are clustering functions, which helps the user to cluster their data what is required for the third step, the quantification of the data. `DBSCAN` is a localization-based clustering algorithm which estimates for every localization the number of localizations within a user-defined radius and assigns the localization to a cluster when sufficient nearby localizations are present. The thresholded `SMOLR_KDE` defines clusters based on a user-defined localization density threshold. **C)** Quantification of the data can be done using feature extraction of the binary Kernel Density Estimation, using `DBSCAN` clustering or spatial analysis can be performed using the `spatstat` package. For details about the in- and output of the different functions see Table 1.

done before starting to use SMoLR are for example: grouping of localizations from the same molecule, drift correction and channel alignment. SMoLR provides a stepwise approach to import these experimental data sets containing localization data from different proteins or different conditions (Figure 1A).

The localization data should contain the Cartesian coordinates of the localizations along with other values that are obtained during the localization analysis including localization precision, standard deviation of the Gaussian fit and the time frame in which the molecule was detected. Most of the functions were developed based on 2D-localization data, however for some of the functions 3D information can

be included in the analysis (e.g. *SMOLR\_PLOT*, *SMOLR\_DBSCAN*).

SMoLR is optimally used by defining multiple structures (ROIs) in the original super resolution images. The imported data can be either text files containing the localizations of the several ROIs or localization data sets of complete images along with the positions of the ROIs in the images (Figure 1B). One of the options is to select the ROIs in ImageJ and the localizations of the ROIs can be stored in text files using the ImageJ macro language (a macro provided as Supplemental Software). Alternatively using the *RimageROI()* function in SMoLR, the coordinates of ROIs stored with the ROI Manager in ImageJ can also be loaded into R (Table 1). Using the

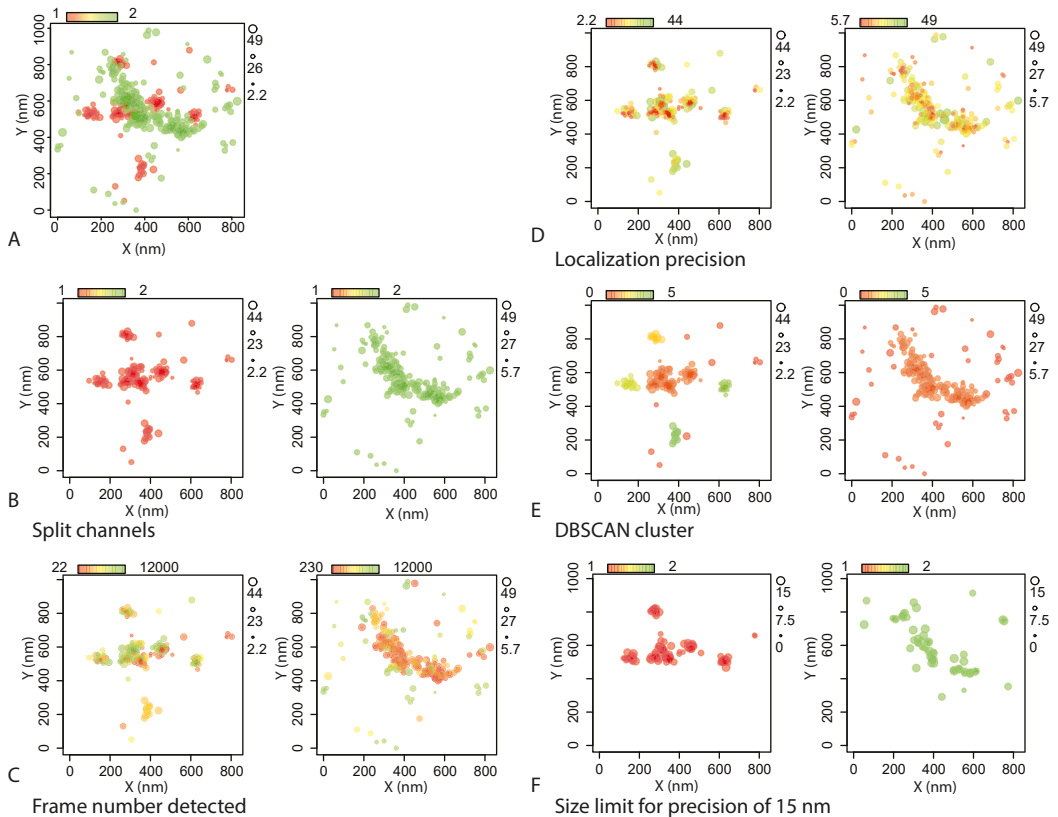


**Figure 3** Examples of the possibilities of the SMOLR plot with localization data. In all the plots the relation between the color and scale used can be found in the legend above the plot, while at the side of the plot the relation between the size of the points and the scale is shown. **A)** Dual color images can be plotted within one plot, **B)** but also next to each other. The size of the points is related to the localization precision, in those examples the color is represented by the channel, **C)** the first frame the localization was detected and **D)** localization precision. **E)** The color can also be used to visualize the clustering by DBSCAN. **F)** Furthermore, it is possible to filter data based on a defined range in color and size of the individual localizations plotted.

dataset and comparison between different conditions, either manually or by multivariate analysis, for example principal component analysis.

In addition to the density estimation we implemented a widely used clustering algorithm for localization data: the DBSCAN clustering method (Ester et al., 1996) (Figure 2B). The DBSCAN algorithm used here is from the recently released `dbscan` package (Hahsler, 2015), which is applicable for DBSCAN on large localization data sets. The DBSCAN method identifies clusters of localizations by linking localizations within a defined threshold distance. At the same time a certain number of localizations has to be within this distance of a localization to be assigned to a cluster. When not enough localizations are within this distance the localization is assigned as noise. By varying both thresholds, based on visual inspection, the algorithm can subsequently be applied to large data sets to obtain statistics about the shape of the calculated clusters.

The datasets processed in our package can be also used in the `spatstat` package in R (Baddeley and Turner, 2005) (using the

`SMoLR_to_spatstat()` function). `Spatstat` is an extensive library that enables the user to perform different types of spatial analysis on the localizations data. This type of analysis has been shown useful to study to clustering of membrane proteins (Owen et al., 2010; Sengupta et al., 2011) and clustering of RNA polymerase II in the nucleus (Cisse et al., 2013), and can be used to study organization of proteins in other cases. For exploratory analysis several functions within the `spatstat` package are available (Ripley-K function, the linearized L-function and pair-correlation functions). The `spatstat` functions can also be used to study the correlation between two different proteins, using marked point patterns together with functions which estimate the cross function (K-cross) (Figure 2).

### Single molecule localization image averaging

Resolving ultrastructure by single molecule localization of the nuclear pore complex (Szymborska et al., 2013), synaptonemal complex (Schücker et al., 2015) or viral particles (Van Engelenburg et al., 2014), showed the power of

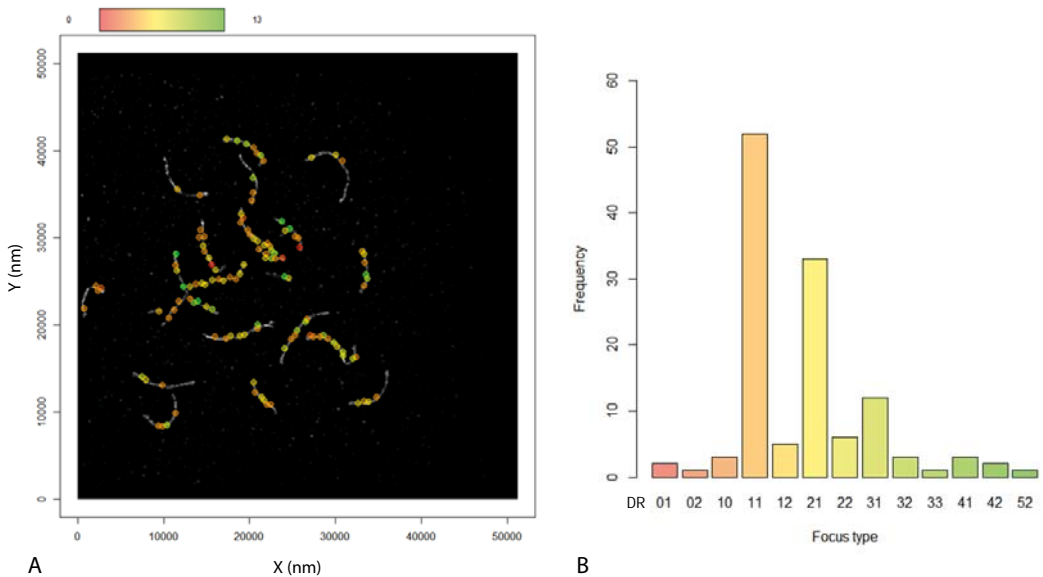


**Figure 4 SMoLR plot with overlay** **A)** Visualization of image features projected on the microscopy image. Meiotic DMC1-RAD51 foci in a spread meiotic mouse cell were characterized based on the number of clusters of respectively DMC1 and RAD51 at every focus (DR). This feature was plotted on top of a Structured Illumination microscopy image visualizing SYCP3, a protein present at the lateral elements of the synaptonemal complex. **B)** The absolute frequencies of the different cluster configurations (DR=DMC1/RAD51) as shown in A. The colors in the bar plot correspond to the colors in the plot in A.



combining a large number of individual SMLM images to obtain a generalized structure (particle averaging). However, particle averaging is a computationally demanding procedure, especially when no template is available to which the individual images can be matched (Broeken et al., 2015). Furthermore compared to reconstruction of protein structure by cryo-EM, the number of acquired structures is frequently much lower (Boekema et al., 2009). Particle averaging also assumes that individual structures represent identical or at least highly similar structures. However, for some biological structures there might be quite some variation in the organization of the individual structures, although they can have certain features in common. We therefore implemented a rotation algorithm, as will be described below, based on extracted features from the individual images, which can be very informative to observe common features from the imaged structures.

### **Image feature based rotational alignment**

Features that can be extracted with the SMoLR package (using EBImage or localization based features) can be used for alignment. For example, the center of mass of clusters can be used to center structures. In some cases, the clusters may have specific shapes that enable to rotate and overlay the individual ROIs. For example, elongated structures can be aligned using the major axis of the structure (Figure 5A). The presence of multiple clusters within individual ROIs that can be distinguished from each other (for instance on the basis of shape, size or distance to the center of mass), provides another possibility to align structures by rotating the similar clusters towards the same point (Figure 5B). This can be two clusters that are present in two different channels of the super resolution image, or clusters with distinct areas (i.e. a small and a large cluster) (Figure 5B). The alignments can be averaged or overlaid, and subsequently used to visualize and extract common features from the individual images and to compare the averaged images when acquired from images recorded under different biological conditions, time points during a specific process

or from different proteins (see Chapters 3 and 4 for examples of this type of analysis).

### **2-D projection of 3-D single molecule structures**

Even without actual 3-D data it is possible to obtain some 3-D information, since the image analyzed is a 2-D projection of a 3-D structure. The observed patterns from the aligned and averaged images can, in combination with prior knowledge, be used to postulate an underlying 3-D structure or shape. This generalized structure can then be imported into dedicated simulation software with which the outcome of a single molecule imaging experiment, i.e. a generalized image derived from 2-D projections of randomly oriented 3-D structures, can be predicted (see Chapter 3 for an example). This result can then be compared with the experimental 2-D data that is obtained in the actual SMLM experiment. In addition, the simulation software can also be useful to get insight in the effect of 2-D projection while imaging a 3-D structure (Figure 5C-H). Examples of features that can be used to compare the 2-D projections are the distribution of major axis length and the eccentricity, which is a measure of elongation. In 2-D projections of a simulated, elongated structure the major axis will always be shorter than the original structure, but the average length one would obtain when measuring large numbers of 2-D projections is still very close to the real length of the structure (Figure 5C-E). This effect is also illustrated in the elongation ratio which is still near maximum number for most structures of the rotated structures, showing that nonetheless most 2D projected structures will also be elongated although they are rotated in 3D (Figure 5F).

The feature based rotational analysis can then be applied to our simulated data set to create a summed image. This can be useful to test hypotheses about the organization of proteins in SMLM data sets. Our simulation data can be analyzed by the same rotation algorithm which in this case results in a projection image with an elongated green structure with two red spots on the end of the green signal (Figure 5G). If we also take the position of the red signal into

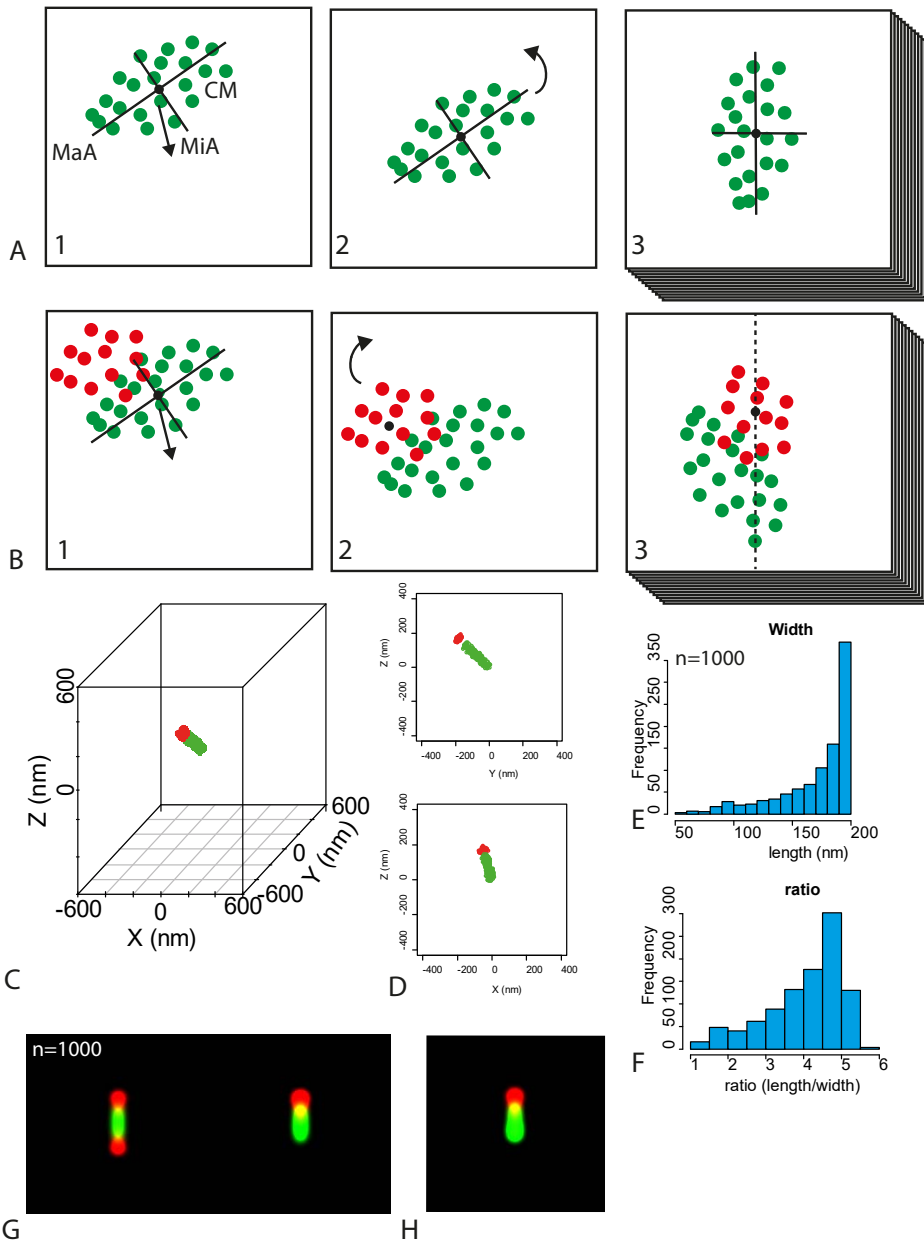


**Figure 5 Image features-based particle averaging.** Using features extracted from the super resolution images, rotations can be applied. **A)** This can be done using the center of mass of structure together with their major axis (MaA=Major Axis, MiA=minor axis, CM=Center of Mass) or **B)** by using the center of mass of different clusters in the images. **C,D)** A randomly rotated simulated elongated structure (green: 200 nm in length, 200 localizations, red: 20nm diameter sphere, 100 localizations) has a different appearance from different side views. **E)** The length of the projection an elongated structure (length: 300 nm) at the x-y plane, rotated away with a defined angle from the x-y plane. **F)** A large number of those random rotated structures can be used to analyze, for example, the spread in the distribution of the 2D projected length and eccentricity. **G)** Random rotated structures can be aligned based on the center of mass and elongation of the cluster in one of the channels (green) and shows the summed projections from all ( $n=1000$ ) structures. Using an extra restraint to keep most of the red signal to the top can be helpful to further align the structures. **H)** Alternatively, if simulating an asymmetric structure with most green signal opposite of the red spot can be used to rotate the green channel and subsequently keep most of the green signal to the bottom side.

account it is also to get all red signal at one side of the green signal. In the same way, instead of using the red signal to further align the images we can also use asymmetry in the green signal. A structure can be simulated where the green structure is asymmetric with more localizations at the end away from the red signal. When aligning those structures, putting the highest green signal downwards, in the projection we are also able to position the red signal at one side of the green signal (Figure 5H). This analysis shows that when certain spatial organization patterns are found in cells this algorithm can be used to try to reveal the underlying structure.

## Web-based image browser

For exploration of single molecule data and for people unfamiliar with R we developed an interactive webpage image browser using the Shiny software package (Chang et al., 2015). The image browser runs as a local web server

and can therefore also be used to share results with other people. Localization datasets, which can be Rdata files or Excel sheets, can be loaded into the webpage. The above described visualizations are presented on the webpage for the individual ROIs (Figure 6). By labelling the individual ROIs with a certain condition it is also possible to compare the statistics of distinct groups within the data set. On the first page, several analysis parameters are shown, which can be changed by the user, after which all results will be recalculated based on the new settings (Figure 6A). In the second tab the several visualization methods (described above in the SMO LR package) are shown (Figure 6B and C). Additionally, for the KDE function the calculated image features are indicated for every image in the thresholded binary image (Figure 6C). On a separate page of the image browser it is also possible to compare the features of a dataset with multiple channels and groups (Figure 6D).

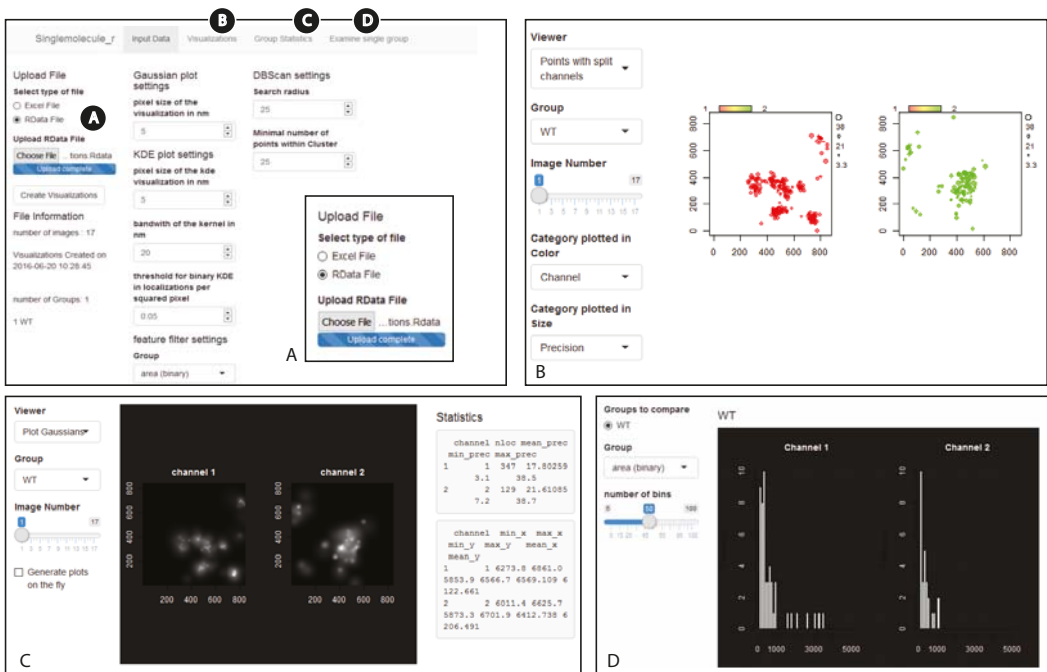


**Figure 6 Data browser based using the shiny package.** The software can be run from every computer with Rstudio and it is possible to access the application using a web browser. **A)** Data can be loaded which is previously imported in R (.Rdata), alternatively an Excel file containing the localization data can be used. In the tabs, basic options of the several SMO LR functions are available. It is possible to adapt the different parameters on the first tab page. **B)** While at the second tab the different types of visualization can be found. Also, some general setting about the image are shown. **C)** In the next tab it is possible to explore the extracted features which are visualized in histograms. **D)** In the last tab, if different datasets are available, the features different conditions can be compared.

## Experimental Results

We used SMoLR in the research described in Chapters 3, 4 and 5. Here we show two other examples of the use of SmoLR to address the following research questions: the organization of protein clusters in synaptic membranes in neurons as well as the dynamic distribution of different repair proteins within foci formed during DNA double strand break repair.

### SMoLR analysis of protein clusters in neuronal synapses

Shank2 is a protein present in the spines of neuronal dendrites. Spines are protrusions of dendrites involved in transmitting electric stimuli between the neurons. Spines contain numerous proteins that either support their structure or that are involved in biomolecular transport to and from spine and dendrite. Shank2 is an adapter protein that connects postsynaptic membrane receptors to the cytoskeleton. Shank2 forms clusters near the postsynaptic membrane, which are too small to determine quantitative parameters like size and shape using conventional fluorescence microscopy. Therefore, we performed dSTORM on primary neuron cultures, which matches well with the same image we obtained with confocal microscopy (Figure 7A-B) and used the SMoLR package to analyze the resulting super resolution localization data. We used additional confocal images to check whether the clusters we detect in dSTORM images match with the spines. Several dSTORM images were imported as localization data using the SMoLR\_IMPORT function. To automatically detect clusters of Shank2 from the STORM image we used our SMoLR\_DBSCAN function (Table 1). Subsequently we used the package to calculate several localization-based features of these clusters, using the SMoLR\_POINT\_FEATURES function. Note that these features are calculated based on the localizations and not by converting the localizations to an image. The `SMoLR_POINT_FEATURES()` function returns a list of all detected clusters and morphological and other quantitative features describing these structures. This enables us to get a detailed view on the shape and organization of the protein clusters. Using the SMoLR\_PLOT

function we plotted statistics of the clusters, for example, the measured size of the clusters in color projected on top of the super resolution image. This provides information on whether there is any general spatial organization of clusters that have specific features in common, in this case cluster size (Figure 7C). We can for example see that there are only a few larger clusters while there are many more small clusters, which are spread homogeneously through the neuron.

We also observe a clear elongation (length vs. width ratio) of these structures (Figure 7D,E,F), corroborating previous results for several scaffold proteins in neuronal spines by super resolution microscopy (Dani et al., 2010).

### SMoLR analysis of the spatial organization of DNA repair proteins in DSB foci

In a second study, we used SMoLR to analyze the localization of DNA Double Strand Break Repair proteins inside repair foci induced by ionizing radiation. During one of the pathways of DSB Repair, homologous recombination (HR), the resected ssDNA ends are coated with the ssDNA binding protein RPA. Subsequently RPA is replaced by RAD51 mediated by BRCA2 (Jensen et al., 2010). The formation of RAD51 filaments around the ssDNA plays an essential role in the search for homologous DNA templates in the sister chromatid to repair the broken DNA strand in an error-free manner. Among others, these proteins assemble at the sites of damage into DSB foci, which can be visualized by (immuno-)fluorescence microscopy (see also Chapter 1, 4 and 5).

We were interested whether we could obtain structural information from cells stained with RAD51. After ionizing radiation DSB foci appear which by super resolution microscopy clearly show an elongated pattern (Figure 8A-D). To obtain ROIs containing individual foci we used DBSCAN (Table 1 and Figure 8B) to detect clusters. Although it is challenging to determine the number of protein in clusters, it is possible to compare the relative number of localizations per cluster in the data set. We observe for RAD51 that longer clusters do contain more

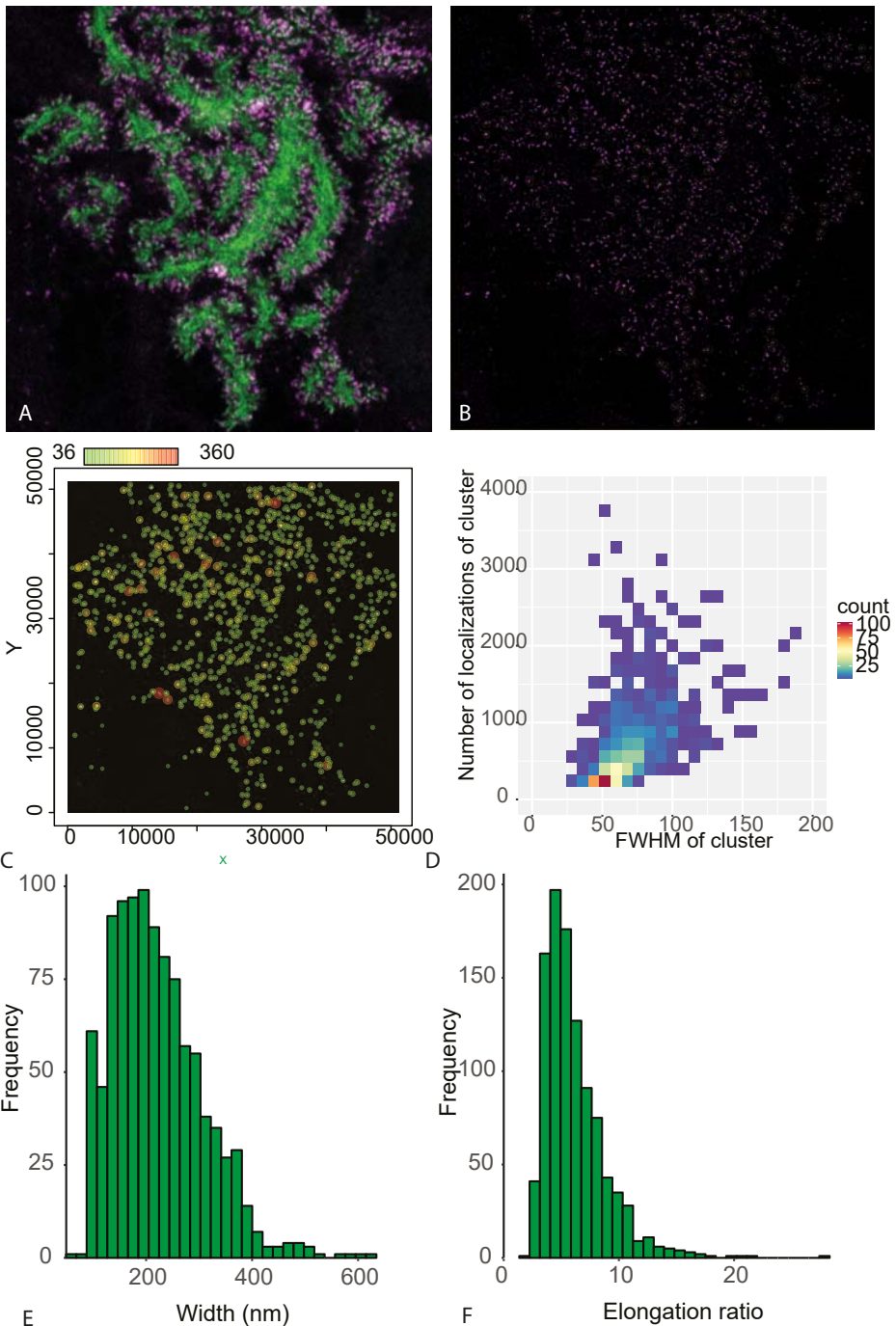


**Figure 7 Super resolution analysis of the Post Synaptic Density protein Shank2 in cultured mouse neurons.**

**A)** Two-color confocal image of a Purkinje cell stained for Calbindin (green) to visualize the entire neuron and Shank2 (magenta) localizing in the postsynaptic density. **B)** the corresponding dSTORM image of Shank2. **C)** The detected clusters of Shank2 are projected on to the super resolution image. The color and size of the clusters indicate the size of the cluster (green to red; small to large). **D)** Using a color coded 2D histogram the distribution of numbers of localizations and the size of the clusters is displayed. **E,F)** Histograms showing the width (measured as the length of the cluster along the major axis) and the length ratio (major divided by minor axis) of the protein clusters.

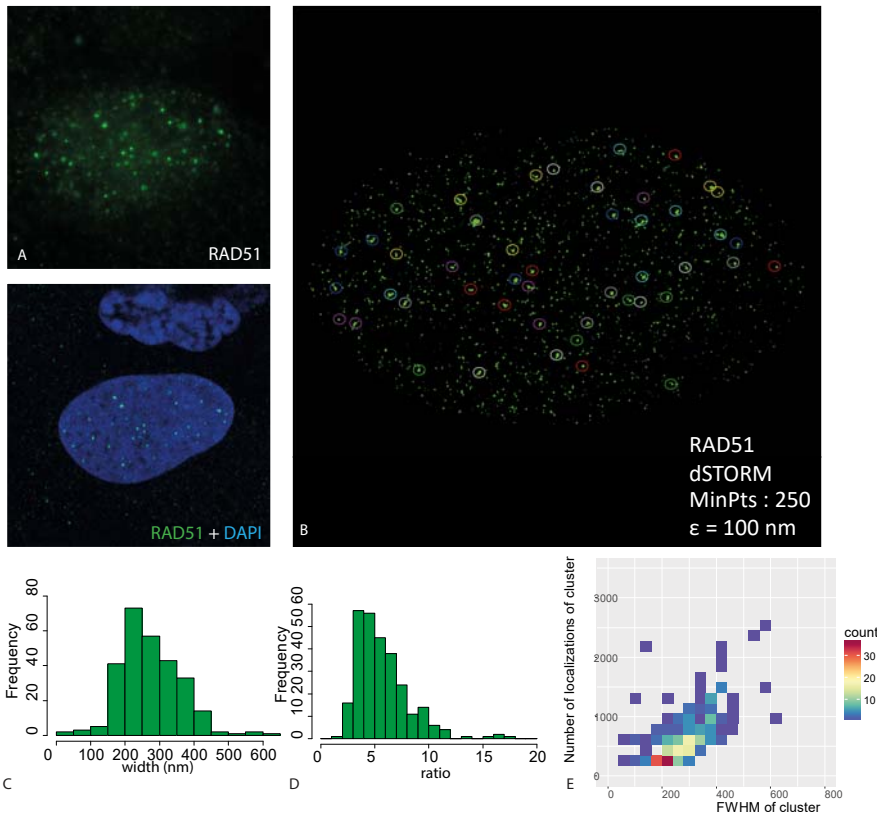



**Figure 8 Nanoscale quantification of IR induced RAD51 foci.** **A)** Confocal image of an U2OS cell treated with 6 Grey of ionizing radiation stained for anti-RAD51 (secondary antibody conjugated with Alexa 647) and the DNA stained with DAPI. **B)** The same cell was imaged by dSTORM and the DBSCAN algorithm was used to detect the DSB foci inside the cell nucleus using a mask based on the DAPI signal. **C)** The length of the RAD51 foci along the major axis. **D)** The ratio of the major vs the minor axis showing the elongated nature of the RAD51 foci. **E)** The number of localizations of the clusters plotted in a 2D histogram with the size of the cluster on the other axis.

localizations, showing that elongated RAD51 foci are not longer because the localized proteins are less densely distributed, but because more protein is present. To visualize this, we used a two-dimensional histogram to show the correlation between cluster size and the number of localizations per cluster (Figure 8E).

When visualized using wide field microscopy DSB proteins seem to co-localize in foci. However, super resolution microscopy allows to investigate the internal distribution of these foci and already has revealed individual spatially separated or partially overlapping domains within the repair foci (Brown et al., 2015; Chapman et al., 2012; Reid et al., 2015) and this thesis chapter 3 and 4). In this study, we manually selected over a hundred DSB foci from several dual color dSTORM images which were immunostained for RAD51 and either BRCA2 or RPA and imported

these as regions of interest (ROIs) into Rstudio (Figure 9). Using the *SMOLR\_POINT\_FEATURES()* function we determined features of the shape of the clusters within the foci (Figure 9A-B). As with RAD51 we analyzed the size of the clusters using a 2D histogram (Figure 9A, B).

For both RPA and BRCA2 we observe that at half an hour after damage induction most clusters are relatively small compared to later time points (2 and 6 hours). For BRCA2 we observed increase in the size of the clusters together with an increase in the number of localizations (Figure 9A). Interestingly, some of the RPA clusters over time show increased numbers of localizations, but no increase in size, suggesting that proteins in those clusters get more concentrated during the life time of a DSB focus (Figure 9B).



Furthermore, we investigated to what extent clusters of the two proteins are overlapping. For this, we took the center of mass of the RAD51 localizations and counted the number of localizations in rings going outwards from the center of mass of the RAD51 signal. This can be plotted as a histogram with the frequency of localizations with the distance from the center of mass (Figure 9C-D). This shows that for both BRCA2 and RPA at the early time points there is more protein away from the center of the focus, which is not overlapping with the RAD51 signal while at the later time points the signals of BRCA2/RPA and RAD51 show much more overlap.

We then used rotational analysis (see above) to get more insight in the spatial distribution of protein clusters inside foci. All images of foci were aligned and rotated based on the elongated RAD51 signal, so that the longest axis is oriented vertically and the side with highest RAD51 signal is rotated to the top. The BRCA2 or RPA localizations in the same image were aligned and rotated together with RAD51. The localizations of all images were then projected on top of each other using the SMoLR function to reconstruct a generalized map with both channel together (Figure 9E-F) or by separating the two channels and indicating the center of the image, which allows easier comparison between the images (Figure 9G-H). We see a similar trend for both BRCA2 and RPA where a 0.5 hour after damage induction the signal of both BRCA2 and RPA seems to be more spread out and become more condensed after 2 hours. However, when looking at the images of 0.5 hour after IR we see that largest amount BRCA2 is below the horizontal dashed line while for RPA the highest intensity is found just above the dashed line. We then see at 2 hours after IR for BRCA2 that the signal is still below the dashed line while the signal expands at the 6-hour time point. For RPA, we see at 2 hours after IR that the signal is quite spherical and at the center of the RAD51 signal while after 6 hours also, just as in the BRCA2 images the signal becomes more expanded and elongated along the vertical axis.

An additional possibility with this data set when using rotational alignment is to combine the alignment of two sets of images which are

stained for one common protein and two different proteins, on top of each other. In this case, we used images of both RPA and BRCA2 which were both aligned on basis of the corresponding RAD51 signal. We overlaid the summed images of both protein in one image (Figure 9I). In both situations cells were treated and prepared in the same way. However, doing a 3 color STORM experiment would be very challenging and further more would pose problems due the secondary antibody cross-reactivity due to the species of the antibodies.

## Discussion

Quantitative analysis of localization data requires tailor-made software and the possibility to design scripts dedicated to the specific needs of the biological system studied. An easily accessible, simple Graphical User Interface facilitates the use of software accessible by other researchers, but does not allow to fully access all features present in localization data. Therefore, the presented SMoLR package is not only useful for researchers with basic experience in programming in R to explore their localization data in R, but can also be used as a toolbox with functions to be applied in more advanced scripts dedicated to specific data sets (Figure 6 and 7). The data browser we developed can be used by researchers that only require browsing through the data and want to identify interesting features that require further analysis in R. This fits very well in an iterative approach where observations in the individual images can be visualized and subsequently quantified and tested on the whole data set. The approach might lead to new hypotheses which can then again be investigated on basis of the individual images and quantified for all data.

For analysis of macromolecular assemblies in cells using super-resolution microscopy it is important to include sufficient data. This means that it is important to summarize the data of several images together. Using our package, it is straight-forward to combine the data of multiple cells in a single data set. Our package also makes it easy to compare images taken under different conditions or at different time points

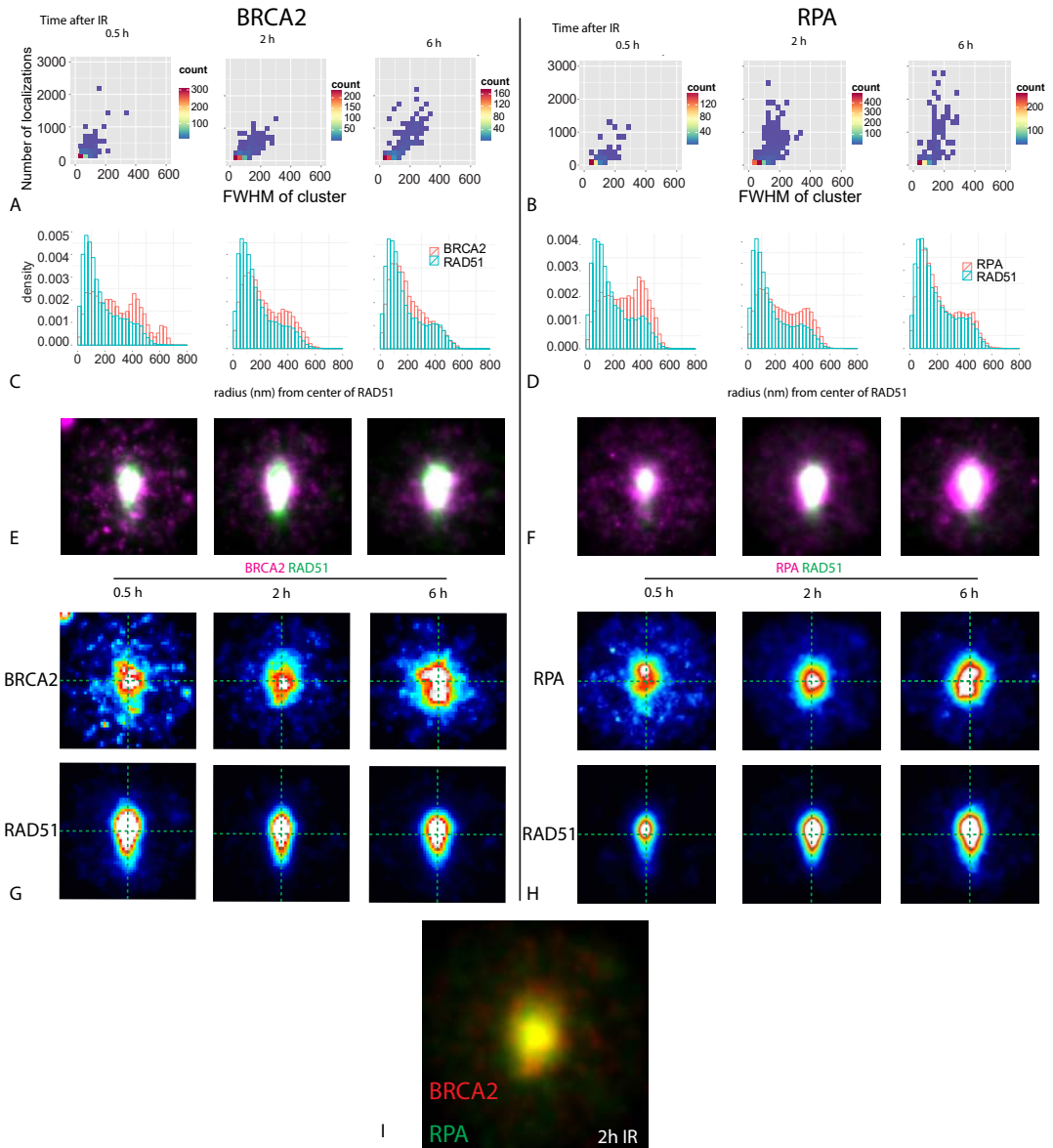


**Figure 9 Quantitative analysis of super resolution imaging of DNA Double Strand Break foci.** U2oS cells treated with 6Gy or ionizing radiation and fixed at the indicated time points were stained using antibodies against RAD51 and either BRCA2 or RPA. **A,B**) Clusters of BRCA2 and RPA were identified using DBSCAN clustering. The 2D histograms show the size and number of localizations of the clusters. **C,D**) The number of localizations from all foci of that condition within the radius indicated by the bins in the histograms from the center of the RAD51 signal. **E,F**) Summed images of feature based rotation. The foci are aligned rotating the elongated structure of RAD51 (magenta) along the vertical axis. Subsequently all foci are rotated in such a way that most RAD51 signal is at the top. The BRCA2 or RPA signal (RPA) is rotated in the same way. **G,H**) The same images as in E,F but plotted with a different look up table and showing the center of the image at the intersection of the dashed lines. **I**) Overlay image of the rotated images of BRCA2 and RPA with RAD51 aligned. ( $n$  is respectively 157,186,150 foci for BRCA2/RAD51 0.5,2 and 6 hours after IR, while for RPA/RAD51  $n$  is respectively 154,198,115 for the three time points).



and to include proper controls to assure the detected organizational patterns are significant and relevant. In R, combining our package with the spatstat package for spatial analysis it is also straight-forward to average the spatial distribution (Ripley's K, Pair Correlation Function) of several ROIs in one plot.

The analysis of protein clusters in neurons can be useful to correlate phenotype and behavior directly to the spatial organization of synapse proteins. The above described example shows that with SMoLR it is possible to obtain statistical relevant descriptions of the protein clusters at high resolution.

The analysis of DSB foci shows that additional information about the relative spatial organization can be obtained by extensive quantitative analysis of single molecule localization data by SMoLR. We for instance observed that RPA at the later time points shows increasingly dense clusters that do not increase in size. It can be hypothesized that the resected DNA to which RPA is bound condenses during repair or preparation for repair while the DNA which is displaced by BRCA2 and loaded with RAD51 needs to be more opened up to facilitate homology search and strand invasion. The rotational analysis also shows that at half an hour after IR RPA and BRCA2 are localized at a different position relative to the RAD51 signal (Figure 9). While RPA is localized closer to the higher intensity RAD51, BRCA2 is positioned more at the other side where in general less RAD51 is present. In future experiments this could be analyzed in more detail to investigate whether these different localizations relate to the mechanisms whereby BRCA2 loads RAD51 on the DNA. We observed for both BRCA2 and RPA that from half an hour until 2h after irradiation, the clusters are localized closer to the intense RAD51 signal. After six hours, the clusters are spread out along the RAD51 filament. It has been suggested before (Agarwal et al., 2011) that the number of RAD51 foci is at maximum at about 2 hours and therefore at 6 hours after IR it is possible that only the most persistent foci are left. It might be that during these 6 hours, resection of the DNA is continuously progressing leading to DSBs with long strands of ssDNA and loading of RPA even 6

hours after DSB induction. The presence of both RPA and BRCA2 at all the different time points suggests a very dynamic regulation of loading and dissociation of RAD51 during the time the DSB is being repaired.

## Conclusion

The nature of Single Molecule Localization data, essentially a table with coordinates, makes it very attractive to perform different types of quantification besides the common image analysis methods. It is therefore a powerful technique to extract quantitative information about the (relative) localization of proteins at high resolution. In many situations, multiple similar structures are present within a cell and the recorded super resolution image. By combining the presented methods and workflow to extract relevant features from the localization data, together with the powerful statistics available in R, it is possible to explore the variation in structures, determine common features describing the structures while at the same time comparing different conditions or proteins. Using feature-based alignment and rotational analysis these observed structural organizations can be verified, visualized and combined with rotational simulations to get more insight. The complete workflow for single molecule localization microscopy presented here, enables biologists to explore (super resolution) microscopy data to the full extent.

## Acknowledgements

We thank Pim van Bersselaar, Martin van Royen, Gert van Cappellen and Gert-Jan Kremers for critical feedback and testing of the software.

## References

- Agarwal, S., van Cappellen, W.A., Guenole, A., Eppink, B., Linsen, S.E. V., Meijering, E., Houtsmuller, A., Kanaar, R., and Essers, J. (2011). ATP-dependent and independent functions of Rad54 in genome maintenance. *J. Cell Biol.* *192*, 735–750.
- Baddeley, A., and Turner, R. (2005). spatstat : An R Package for Analyzing Spatial Point Patterns. *J. Stat. Softw.* *12*.

- Baddeley, A., Rubak, E., and Turner, R. (2016). *Spatial Point Patterns: Methodology and Applications with R* (CHAPMAN & HALL CRC).
- Baddeley, D., Cannell, M.B., and Soeller, C. (2010). Visualization of localization microscopy data. *Microsc. ...* 16, 64–72.
- El Beheiry, M., and Dahan, M. (2013). ViSP: representing single-particle localizations in three dimensions. *Nat. Methods* 10, 689–690.
- Betzig, E., Patterson, G.H., Sougrat, R., Lindwasser, O.W., Olenych, S., Bonifacino, J.S., Davidson, M.W., Lippincott-Schwartz, J., and Hess, H.F. (2006). Imaging Intracellular Fluorescent Proteins at Nanometer Resolution. *Science* 313, 1642–1645.
- Boekema, E.J., Folea, M., and Kouřil, R. (2009). Single particle electron microscopy. *Photosynth. Res.* 102, 189–196.
- Broeken, J., Johnson, H., Lidke, D.S., Liu, S., Nieuwenhuizen, R.P.J., Stallinga, S., Lidke, K.A., and Rieger, B. (2015). Resolution improvement by 3D particle averaging in localization microscopy. *Methods Appl. Fluoresc.* 3, 14003.
- Brown, M.S., Grubb, J., Zhang, A., Rust, M.J., and Bishop, D.K. (2015). Small Rad51 and Dmc1 Complexes Often Co-occupy Both Ends of a Meiotic DNA Double Strand Break. *PLOS Genet.* 11, e1005653.
- Chang, W., Cheng, J., Allaire, J., Xie, Y., and McPherson, J. (2015). shiny: Web Application Framework for R. R package version 0.12.2.
- Chapman, J.R., Sossick, A.J., Boulton, S.J., and Jackson, S.P. (2012). BRCA1-associated exclusion of 53BP1 from DNA damage sites underlies temporal control of DNA repair. *J. Cell Sci.* 125, 3529–3534.
- Cisse, I.I., Izeddin, I., Causse, S.Z., Boudarene, L., Senecal, A., Muresan, L., Dugast-Darzacq, C., Hajj, B., Dahan, M., and Darzacq, X. (2013). Real-time dynamics of RNA polymerase II clustering in live human cells. *Science* 341, 664–667.
- Dani, A., Huang, B., Bergan, J., Dulac, C., and Zhuang, X. (2010). Superresolution Imaging of Chemical Synapses in the Brain. *Neuron* 68, 843–856.
- Van Engelenburg, S.B., Shtengel, G., Sengupta, P., Waki, K., Jarnik, M., Ablan, S.D., Freed, E.O., Hess, H.F., and Lippincott-Schwartz, J. (2014). Distribution of ESCRT machinery at HIV assembly sites reveals virus scaffolding of ESCRT subunits. *Science* 343, 653–656.
- Ester, M., Kriegel, H.P., Sander, J., and Xu, X. (1996). A Density-Based Algorithm for Discovering Clusters in Large Spatial Databases with Noise. *Second Int. Conf. Knowl. Discov. Data Min.* 226–231.
- Hahsler, M. (2015). dbscan: Density Based Clustering of Applications with Noise (DBSCAN) and Related Algorithms.
- Huber, W., Carey, V.J., Gentleman, R., Anders, S., Carlson, M., Carvalho, B.S., Bravo, H.C., Davis, S., Gatto, L., Girke, T., et al. (2015). Orchestrating high-throughput genomic analysis with Bioconductor. *Nat. Methods* 12, 115–121.
- Jensen, R.B., Carreira, A., and Kowalczykowski, S.C. (2010). Purified human BRCA2 stimulates RAD51-mediated recombination. *Nature* 467, 678–683.
- Laine, R.F., Albecka, A., van de Linde, S., Rees, E.J., Crump, C.M., and Kaminski, C.F. (2015). Structural analysis of herpes simplex virus by optical super-resolution imaging. *Nat. Commun.* 6, 5980.
- Levet, F., Hosy, E., Kechkar, A., Butler, C., Beghin, A., Choquet, D., and Sibarita, J.-B. (2015). SR-Tesseler: a method to segment and quantify localization-based super-resolution microscopy data. *Nat. Methods* 12, 1065–1071.
- Manley, S., Gillette, J.M., Patterson, G.H., Shroff, H., Hess, H.F., Betzig, E., and Lippincott-Schwartz, J. (2008). High-density mapping of single-molecule trajectories with photoactivated localization microscopy. *Nat. Methods* 5, 155–157.
- Nieuwenhuizen, R.P.J., Lidke, K.A., Bates, M., Puig, D.L., Grünwald, D., Stallinga, S., and Rieger, B. (2013). Measuring image resolution in optical nanoscopy. *Nat. Methods* 10, 557–562.
- Owen, D.M., Rentero, C., Rossy, J., Magenau, A., Williamson, D., Rodriguez, M., and Gaus, K. (2010). PALM imaging and cluster analysis of protein heterogeneity at the cell surface. *J. Biophotonics* 3, 446–454.
- Pau, G., Fuchs, F., Sklyar, O., Boutros, M., and Huber, W. (2010). EBImage—an R package for image processing with applications to cellular phenotypes. *Bioinformatics* 26, 979–981.
- Pengo, T., Holden, S.J., and Manley, S. (2014). PALMsiever: a tool to turn raw data into results for single-molecule localization microscopy. *Bioinformatics* 31, 797–798.
- R Core Team (2016). *R: A Language and Environment for Statistical Computing*.
- Reid, D. a., Keegan, S., Leo-Macias, A., Watanabe, G., Strande, N.T., Chang, H.H., Oksuz, B.A., Fenyo, D., Lieber, M.R., Ramsden, D. a., et al. (2015). Organization and dynamics of the nonhomologous end-joining machinery during DNA double-strand break repair. *Proc. Natl. Acad. Sci. U. S. A.* 112, E2575–2584.
- Rossier, O., Oceau, V., Sibarita, J.-B., Leduc, C., Tessier, B., Nair, D., Gatterdam, V., Destaing, O., Albiges-Rizo, C., Tampé, R., et al. (2012). Integrins  $\beta$ 1 and  $\beta$ 3 exhibit distinct dynamic nanoscale organizations inside focal adhesions. *Nat. Cell Biol.* 14, 1057–1067.
- RStudio Team (2015). *RStudio: Integrated Development Environment for R*.
- Rust, M.J., Bates, M., and Zhuang, X. (2006). Sub-diffraction-limit imaging by stochastic optical reconstruction microscopy (STORM). *Nat. Methods* 3, 793–795.
- Sage, D., Kirshner, H., Pengo, T., Stuurman, N., Min, J., Manley, S., and Unser, M. (2015). Quantitative evaluation of software packages for single-molecule localization microscopy. *Nat. Methods* 12.
- Schermelleh, L., Heintzmann, R., and Leonhardt, H. (2010). A guide to super-resolution fluorescence microscopy. *J. Cell ...* 190, 165–175.
- Schücker, K., Holm, T., Franke, C., Sauer, M., and Benavente, R. (2015). Elucidation of synaptonemal complex organization by super-resolution imaging with isotropic resolution. *Proc. Natl. Acad. Sci.* 112, 2029–2033.
- Sengupta, P., Jovanovic-Talisman, T., Skoko, D., Renz, M., Veatch, S.L., and Lippincott-Schwartz, J. (2011). Probing protein heterogeneity in the plasma membrane using PALM and pair correlation analysis. *Nat Meth advance on*, 969–975.
- Sharonov, A., and Hochstrasser, R.M. (2006). Wide-field subdiffraction imaging by accumulated binding of diffusing probes. *Proc. Natl. Acad. Sci.* 103, 18911–18916.
- Szymborska, A., de Marco, A., Daigle, N., Cordes, V.C., Briggs, J.A.G., and Ellenberg, J. (2013). Nuclear Pore Scaffold Structure Analyzed by Super-Resolution Microscopy and Particle Averaging. *Science* 341, 655–658.

## Supplemental file: R Vignette of the SMoLR package

# Introduction to Single Molecule Localization in R (SMoLR)

Maarten Paul (*m.w.paul@erasmusmc.nl*) and Johan Slotman (*j.slotman@erasmusmc.nl*)

2017

The SMoLR package consists of a set of functions dedicated to quantitative analysis of Single Molecule Localization data in R.

- Importing and organizing large single molecule localization data sets
- Visualize super resolution localization data
- High-throughput analysis of large data sets

### Import of localization data

Using `SMOLR_IMPORT`, different types of data can be imported into R from a folder. The localizations from different ROIs or images are sorted in a list of `data.frame`'s. Different profiles are available to load different types of data.

```
SMOLR_IMPORT(folder="../loc",profile = "roiloc")
SMOLR_LOAD(folder="../loc")
```

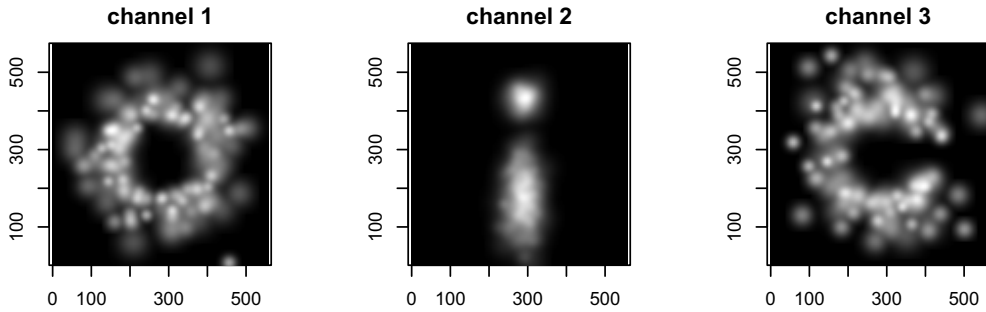
Example of localizations `data.frame`

Index	X	Y	Precision	PSF	First_Frame	N_detections	Photons	Channel
18590	12427	7201	19	178.2	1351	1	494	1
18631	12438	7182	28	178.9	1354	1	342	1
60796	12433	7163	21.3	186.9	4901	1	563	1
99444	12474	7175	20.8	179.4	7950	1	364	1
99482	12451	7156	18.4	185.2	7953	1	563	1
107190	12502	7064	25.4	176.9	8598	1	317	1
108532	12447	7060	21.9	173.9	8704	1	370	1
108626	12442	7112	18.9	183.7	8712	1	450	1
108637	12463	7145	18.2	161.6	8713	1	356	1
108654	12473	7119	21.6	184.7	8714	1	416	1

## Visualization

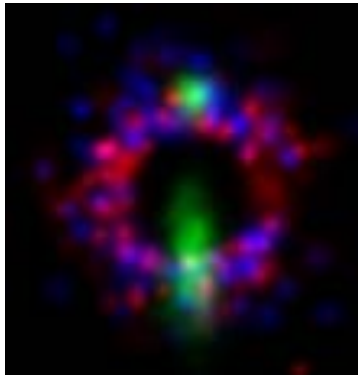
The localizations can be plotted by individual Gaussians using the `SMOLR` function. This can also be applied to a list of `data.frame`'s. This will create an list of super resolution images. In this example a `data.frame` is the input. The plot function can be applied to the `SMOLR_image` object. This will return images of all channels in gray scale.

```
img <- SMOLR(smolrdata)
plot(img)
```



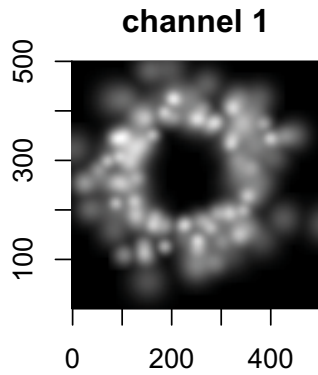
Alternatively an RGB image can be plotted.

```
plot(img,rgb=TRUE)
```



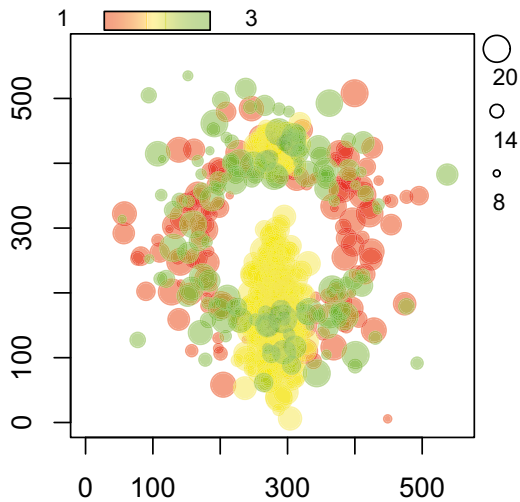
Instead of using the image in R it is also possible to export an image as tiff.

```
plot(SMOLR(subset(smolrdata,Channel==1)))
```



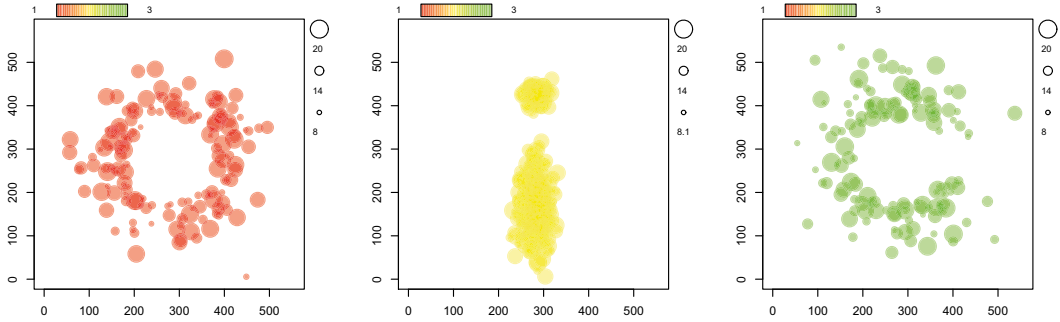
Using the SMOLR\_PLOT function the localizations can be plotted in a scatter plot

```
par(mar=c(2,2,2,2))
SMOLR_PLOT(smolrdata)
```



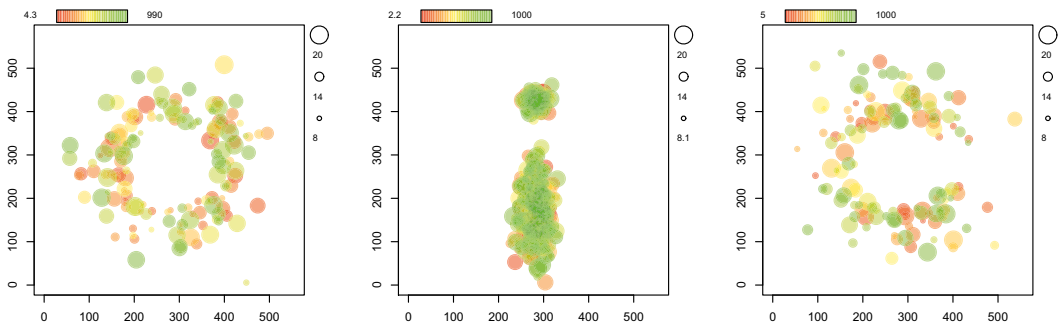
Plotting channels separately

```
par(mar=c(2,2,2,2))
SMOLR_PLOT(smolrdata,split_ch = T)
```



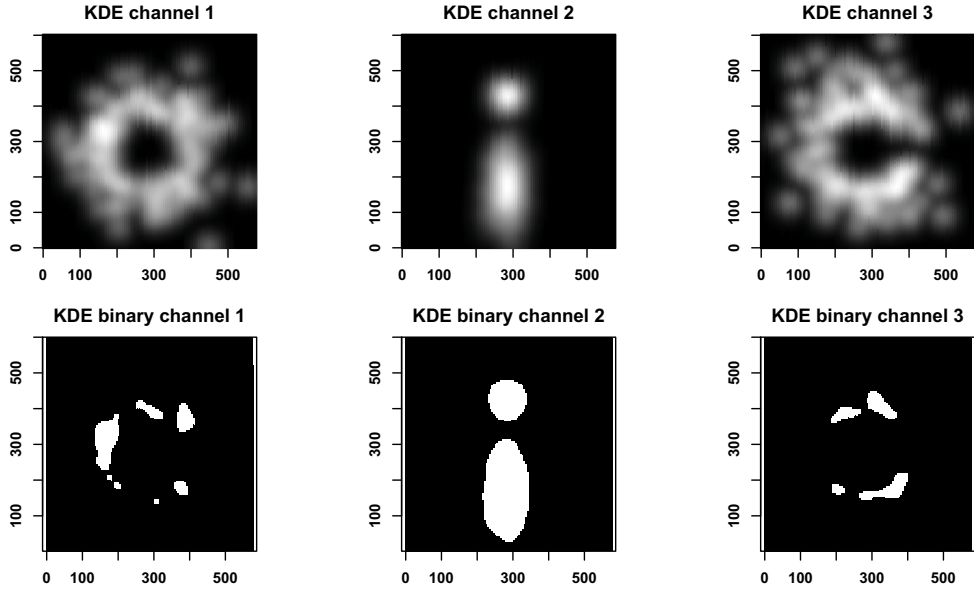
The color and size of the points in the plot can be related to column in the data.frame. In this example the color represents the Frame in which the localization is detected, while the size is by default equal to the localization precision.

```
par(mar=c(2,2,2,2))
SMOLR_PLOT(smolrdata,split_ch = T,color = smolrdata$First_Frame)
```



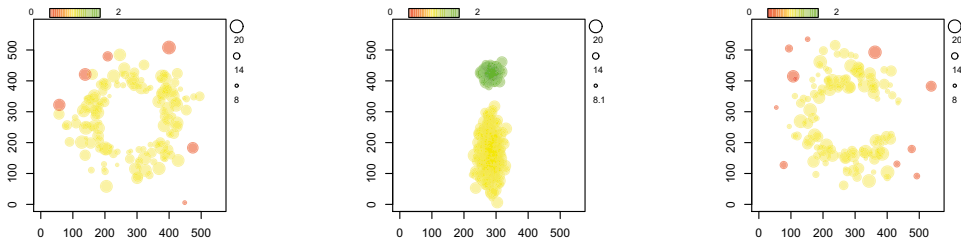
## Clustering

```
plot(SMOLR_KDE(smolrdata))
```



Visualization of DBSCAN clustering. The colors indicate the assigned cluster, while the red localizations are considered background.

```
plot(SMOLR_DBSCAN(smolrdata,eps=50,MinPts=5))
```



## Features

From the data image features can be calculated, using the `SMOLR_FEATURES` function. This function can be applied to a `data.frame`, but also to a list of `data.frame`'s.

```
features <- SMOLR_FEATURES(SMOLR_KDE(smolrdata))
```

Table 2: Table continues below

x.0.m.cx	x.0.m.cy	x.0.m.majoraxis	x.0.m.eccentricity	x.0.m.theta
62	29	3.266	4.13e-07	1.571
75.64	36.55	9.572	0.6783	-0.8246
40.5	37.5	4.781	0.6708	-0.7854
36	42	3.266	0	0
34.12	62.64	30.91	0.9083	1.376
77.92	74.94	16.01	0.787	-1.498
58.23	79.73	18.84	0.9516	-0.5429

x.0.s.area	x.0.s.perimeter	x.0.s.radius.mean	x.0.s.radius.sd
9	8	1.207	0.2071
53	22	3.705	0.4907
14	10	1.689	0.2161
9	8	1.207	0.2071
286	70	10.02	3.314
120	37	5.843	1.232
81	34	5.294	2.1

Alternatively instead of using the image-based features, features based on the localization data can be calculated.

```
point_features <- SMOLR_POINT_FEATURES(SMOLR_DBSCAN(smolrdata,eps=50,MinPts=5))
```

Table 4: Table continues below

Channel	cluster	meanX	meanY	sd	width	area	perimeter
1	1	292.6	300.9	123.5	426	4169	791.4
2	1	298.6	194	73.42	317.7	3348	607.6
2	2	301.2	449	22.79	79.79	724.8	149.8
3	1	290.3	309.6	148.9	453.6	4728	873.1

major_axis	minor_axis
238.4	8.516
138.5	8.373
37.37	8.214
289.6	8.257







## Chapter III

# Super resolution imaging of RAD51 and DMC1 in DNA repair foci reveals dynamic distribution patterns in meiotic prophase

Fabrizia Carofiglio<sup>1#</sup>, Maarten W. Paul<sup>2#</sup>, Johan A. Slotman<sup>2,3#</sup>, H. Martijn de Gruiter<sup>2</sup>, Wiggert A. van Cappellen<sup>2</sup>, Adriaan B. Houtsmuller<sup>2,3&</sup>, Willy M. Baarends<sup>1&\*</sup>

1 Department of Developmental Biology, Erasmus MC - University Medical Center, PO box 2040, 3000CA, Rotterdam, The Netherlands

2 Erasmus Optical Imaging Centre, Department of Pathology, Erasmus MC - University Medical Center, PO box 2040, 3000CA, Rotterdam, The Netherlands

3 Department of Pathology, Erasmus MC - University Medical Center, PO box 2040, 3000CA, Rotterdam, The Netherlands

<sup>#</sup>Co-first authors

<sup>&</sup>Co-senior authors

<sup>\*</sup>Author for correspondence

*Manuscript in preparation*

## Abstract

The recombinase RAD51, and its meiosis-specific paralog DMC1 localise at DNA double-strand break (DSB) repair sites in meiotic prophase nuclei. Using super resolution microscopy on mouse spermatocyte nuclei we show that the majority of meiotic DSB repair foci contain an elongated RAD51 cluster and either one (D1R1 configuration) or two (D2R1 configuration) DMC1 clusters. D2R1 configurations consist of one RAD51 cluster, closely adjacent to a DMC1 cluster, and a separate DMC1 cluster at a distance of around 250nm. As prophase progresses, less D1R1 and more D2R1 foci are observed, while the RAD51 cluster in the D2R1 foci elongates and gradually orients towards the distant DMC1 cluster. The results indicate that although many RAD51 and DMC1 loading patterns may occur, DMC1 accumulation on both ends of the DSB, and RAD51 loaded adjacent to DMC1 on one end only, is most likely the most productive configuration to achieve meiotic recombination repair.

## Introduction

DNA double strand breaks (DSBs) are highly detrimental lesions (Schipler and Iliakis, 2013). Homologous recombination (HR) is an error-free repair process that uses an intact DNA molecule to recover the genetic information that may have been lost upon DSB formation (San Filippo et al., 2008). In HR, the two ends of the break are resected, generating 3'-single-stranded DNA (ssDNA) overhangs of several hundreds of base pairs, which are initially bound by the ssDNA-binding protein replication protein A (RPA) (San Filippo et al., 2008). RPA is then replaced by RAD51, an ATP-driven recombinase that forms a right-handed helical filament on the 3' overhang (presynaptic phase) (Liu et al., 2010). When the formed nucleoprotein filament associates with a homologous DNA sequence, strand invasion occurs (synaptic phase), which is observed as the formation of the displacement loop (D-loop) in *in vitro* assays. In the postsynaptic phase, DNA synthesis is primed by the 3' end of the invading strand, and the genetic content of the damaged DNA molecule is reconstituted from the homologous template.

Mammalian meiotic cells make use of DSBs and homologous recombination in order to pair paternal and maternal homologous chromosomes. At first hundreds of DSBs are actively induced in a regulated fashion by the transesterase SPO11 (Baudat et al., 2000; Keeney et al., 1999; Keeney et al., 1997; Romanienko and Camerini-Otero, 2000). When strand invasion involves the homologous chromosome, the formation of a repair intermediate brings the homologs in close proximity, and thereby contributes to homologous chromosome pairing and formation of the synaptonemal complex (SC) (Baudat et al., 2000; Romanienko and Camerini-Otero, 2000).

In meiotic prophase, RAD51 is partnered by its homolog DMC1, which is not expressed in somatic cells (Bishop, 1994; Gupta et al., 2001; Habu et al., 1996; Shinohara and Shinohara, 2004; Yoshida et al., 1998). Similar to RAD51, DMC1 forms right-handed nucleoprotein filaments that coat the resected ssDNA ends and can drive homology search (Sheridan et al.,

2008). In mouse, accumulation of both recombinases at sites of DSBs can be observed as colocalising protein foci, associated with the chromosomal axes in widefield microscopy (Moens et al., 1997; Tarsounas et al., 1999). In addition, genetic studies in *S. cerevisiae* led to the conclusion that both Rad51 and Dmc1 are necessary for interhomolog recombination in wild type cells (Hong et al., 2013; Lao et al., 2013; Liu et al., 2014). In meiotic recombination in yeast, Rad51 has an accessory role to stimulate interhomolog strand invasion by Dmc1 (Cloud et al., 2012). A similar finding has been reported in plants, where the recombination phenotype of a *AtRad51* knockout strain could be rescued by the expression of a catalytically inactive RAD51-GFP fusion protein (Da Ines et al., 2013). In *A. thaliana*, immunofluorescence analysis of AtRAD51 and AtDMC1 foci by confocal microscopy showed that the two proteins do not fully colocalise within one and the same recombination nodule. It was speculated that DMC1 and RAD51 load at different ends of the break, and that DMC1 drives one end into strand-invasion (Kurzbaue et al., 2012). Recently, these observations were challenged by super resolution analyses of Rad51 and Dmc1 foci in *S. cerevisiae* nuclei (Brown et al., 2015). Results obtained in this analysis indicated that complex loading patterns of Rad51 and Dmc1 may exist, where by the two DSB-ends form paired foci consisting of both recombinases partially covering the resected ends. Here, we applied dual color direct Stochastic Optical Reconstruction Microscopy (dSTORM) and triple color three-dimensional Structured Illumination Microscopy (3D-SIM) to simultaneously visualise the distribution of DMC1 and RAD51 within DSB foci on the chromosomal axes, in relation to the progression of male mouse meiotic prophase. We observed that the localisation events of RAD51 and DMC1 clustered in distinct areas within a single DSB repair focus, where the majority of observed structures contained a single RAD51 cluster, and either one or two DMC1 clusters (further referred to as D1R1 and D2R1). Furthermore, the distances between the clusters were surprisingly consistent in all structures. Finally, during progression of prophase from leptotene,

through zygotene, to pachytene, the frequency of D1R1 foci decreased, accompanied by an increase in the frequency of D2R1 foci. In *Sycp1* knockout spermatocytes, which lack the transverse filaments (TF) of the SC, axial elements of the SC align but do not synapse (de Vries et al., 2005). In this mutant, RAD51 and DMC1 initially formed similar structures but in pachytene-like nuclei, the foci configurations corresponded most to those observed in leptotene nuclei of the wild type. Our super resolution microscopy data together with our modeling experiments, suggest that DMC1 frequently loads at the two opposite ends of the DNA break, and RAD51 associates mainly with only one of the two ends during mouse meiotic prophase. Thus, the super resolution microscopy data presented here provide new insight in the dynamic composition of meiotic DSB repair foci, and demonstrates that this approach provides new opportunities for investigation of recombination intermediates at nanoscale.

## Results

### Composition of meiotic recombination foci revealed by super resolution imaging

DSB foci were visualised in spread meiotic nuclei immunostained for RAD51, DMC1, and SYCP3, using 3D-SIM and dSTORM, (Figure 1A-I). By utilizing a microscope that combines 3D-SIM and dSTORM, we were able to visualise the same field of view applying both techniques with the same objective lens (Figure 1G, I). The 3D-SIM images were used to visualise synaptonemal complexes (SCs), to be able to identify the substage of meiotic prophase and meiotic DSB foci (also in the SIM image), which were further analysed in images acquired by dSTORM. In DMC1 and RAD51 co-staining experiments, the two proteins displayed distinct localisation patterns, indicating that the used antibodies do not cross-react under these conditions (Figure 1G, I).

A total dataset of 2315 manually selected foci was generated by analysis of 18 nuclei in different meiotic substages, imaged in four independent experiments (Figure 1-figure supplement

1A-C). The maximum number of foci per nucleus was observed in early zygotene, corresponding well with what we and others have reported previously (Figure 1-figure supplement1B, C) (Carofiglio et al., 2013; Cole et al., 2012; Tarsounas et al., 1999). We observed that the foci were composed of separate DMC1 and RAD51 clusters (Figure 1F-I). This prompted us to examine the spatial distribution of localisations of DMC1 and RAD51 within DSB repair foci in more detail, to identify possible predominant patterns.

### Two prominent configuration types of RAD51 and DMC1 assemblies

To quantify and categorize the different patterns of RAD51 and DMC1 clusters, we analysed the spatial density of both proteins using a 2D Kernel Density Estimation function (Figure 1J). We defined a threshold of 5 dSTORM localisations per single 25 nm<sup>2</sup> pixel below which the signal was considered to be background. In this way we created a binary image and identified specific clusters with a minimal size of 50 pixels, within the ROIs (600nm diameter circles) that were enriched for either one of the two proteins. We quantified the number of clusters within each ROI and observed that for both RAD51 and DMC1 a single cluster within a ROI was most frequently observed (Figure 2A). Foci with multiple RAD51 or DMC1 clusters were also present, but were more frequent for DMC1 compared to RAD51 (Figure 2A). Using the above described thresholding for clusters, ROIs with low density of localisations of either RAD51 or DMC1 were classified as having 0 clusters of RAD51 or DMC1 respectively, even if some localisations were present. Next, we quantified the different RAD51 and DMC1 clustering combinations in our ROIs dataset in order to assess how the two recombinases relate to each other within each ROI. We observed that ROIs composed of a combination of one or two clusters per protein were the most represented. ROIs composed of more than two clusters of either protein occurred at a frequency of only 26%. In the distribution of cluster combinations, 56 % of the total population of ROIs fell within two specific groups: a single DMC1 cluster with a single

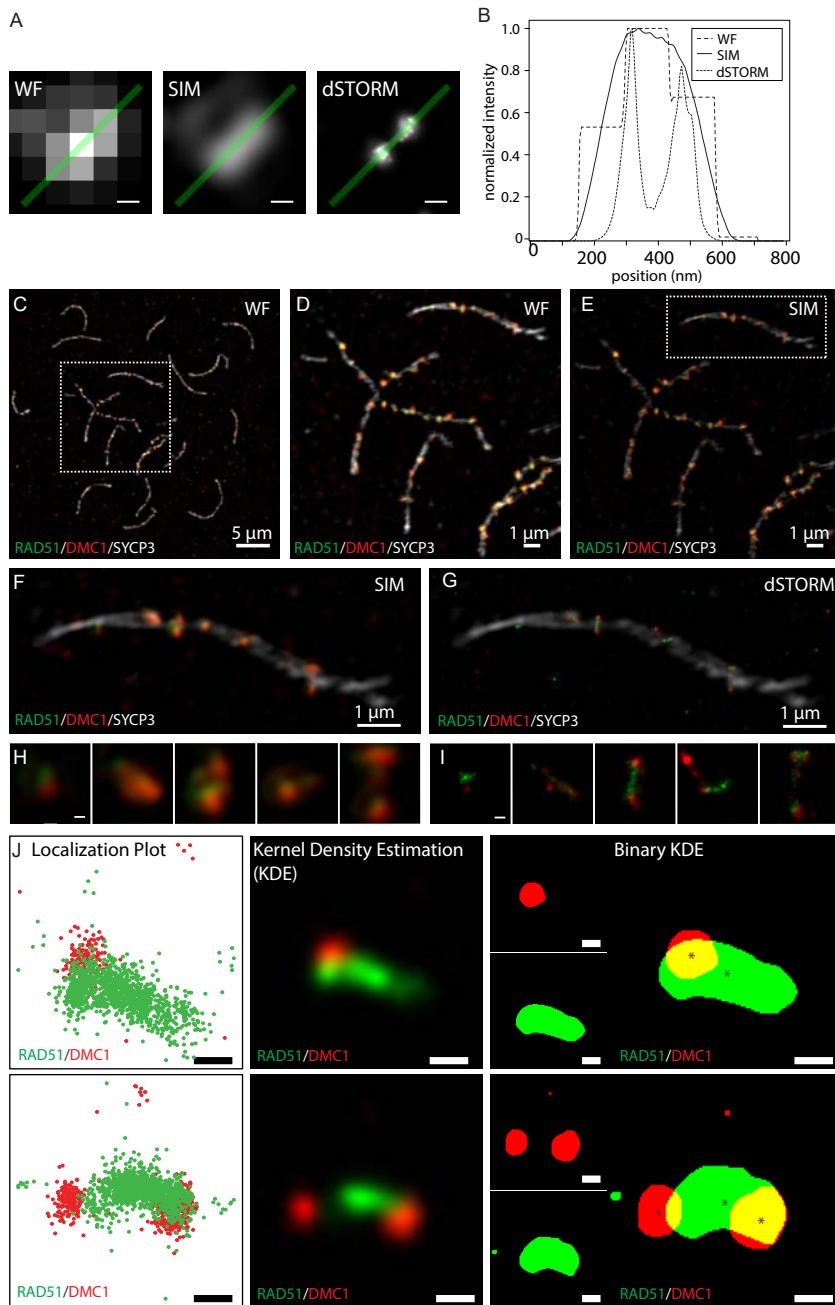


**Figure 1 Meiotic DSB foci in super resolution** **A)** single DMC1 focus imaged in widefield, 3D-SIM, and dSTORM to visualise the difference in resolution between the three imaging techniques. **B)** The intensity profile across the image (green line in **A**). **C-J)** Spread mouse late zygotene nucleus immunostained with primary antibodies for RAD51, DMC1, and SYCP3, and appropriate secondary antibodies conjugated with Alexa-488 (green), Alexa-647 (red), and Alexa-555 (white), respectively. **C)** Widefield image of complete nucleus. **D-E)** Widefield and 3D-SIM of boxed region in **C**. 3D-SIM **F)** and SYCP3 3D-SIM overlaid with RAD51/DMC1 dSTORM images **G)** of boxed region in **C**. Close-up of single DSB foci present on the synaptonemal complex shown in **D** in 3D-SIM **H)** and dSTORM **I)**. **J)** Single DSB foci of two types (upper panels D1R1, lower panels D2R1) represented in 3 different visualisation/analysis methods: scatter plot of localisations, kernel density estimation of localisations, and binary representation of the kernel density estimation. Asterisks indicate centre of mass of DMC1 and RAD51 clusters. Scale bars 100nm.

RAD51 cluster (D1R1), or two DMC1 clusters with a single RAD51 cluster (D2R1) (Figure 2B).

We also analysed a mouse mutant model in which assembly of the synaptonemal complex (SC) is incomplete due to the absence of the central or transverse filament of the SC (*Sycp1*<sup>-/-</sup> 2 animals, two independent experiments, 10 nuclei, 2042 manually selected foci, Figure 2-figure supplement 1) (de Vries et al., 2005). In spermatocytes from these mice, homologous chromosomes show pairing but no synapsis, and the distances between paired axial elements are larger than between lateral elements in synapsed SCs in the wild type (around 80 nm in wild type and 200 nm in the knockout) (de Vries et al., 2005). In this mutant, leptotene appears normal, and the number of DSB foci observed at this stage is similar to the maximum number observed in wild type spermatocytes, but the failure to synapse disturbs subsequent stages, and prevents completion of meiotic DSB repair ((de Vries et al., 2005); (Boateng et al., 2013; Hamer et al., 2006; Hamer et al., 2008; Schramm et al., 2011) and Figure 2-figure supplement 1). All configurations were present in similar frequencies in wild type and *Sycp1*<sup>-/-</sup> nuclei (Figure 2A, B). Given the high relative frequencies of the D1R1 and D2R1 configurations in both wild type and *Sycp1*<sup>-/-</sup> spermatocytes, we investigated these configurations in more detail.

## Temporal analysis of D1R1 and D2R1 configurations during meiotic prophase

We argued that later meiotic prophase sub-stages would be enriched for more advanced recombination intermediates compared to early meiotic prophase nuclei. In both wild type and *Sycp1* knockout nuclei, the D1R1 configuration was the most abundant configuration at leptotene, suggesting that this is an early configuration in which DMC1 and RAD51 form filaments on the resected DSB ends. In the transition to zygotene in the wild type, a significant reduction of the D1R1 configuration frequency was observed, parallel to a 2-fold increase in the relative frequency of D2R1 foci. (Figure 3A). In the *Sycp1*<sup>-/-</sup> spermatocytes, the D1R1 configuration frequency decreased only transiently in zygotene, parallel to an increase in the absolute and relative frequencies of several different complex configuration frequencies involving up to three DMC1 or RAD51 clusters. In contrast, cells that reached a pachytene-like stage displayed D1R1 at a frequency that was similar again to what was observed for leptotene nuclei. The frequency of D2R1 foci remained constant during the different analysed stages of the *Sycp1* knockout (Figure 3B). Surprisingly, we observed no significant difference between frequencies of D1R1 and D2R1 configurations on synapsed versus unsynapsed axes in the wild

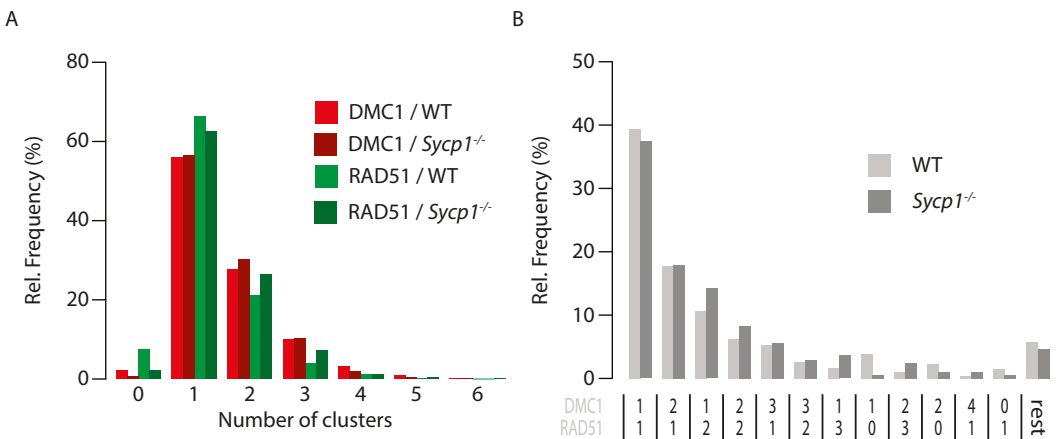


**Figure 2** Abundance of cluster configurations in wild type and *Sycp1*<sup>-/-</sup> spermatocytes **A**) Relative frequency of foci containing indicated number of RAD51 or DMC1 clusters per focus as a percentage of the number of foci per genotype. **B**) Relative frequency of foci containing the indicated combinations of RAD51 and DMC1 clusters per focus as a percentage of the number of foci per genotype.

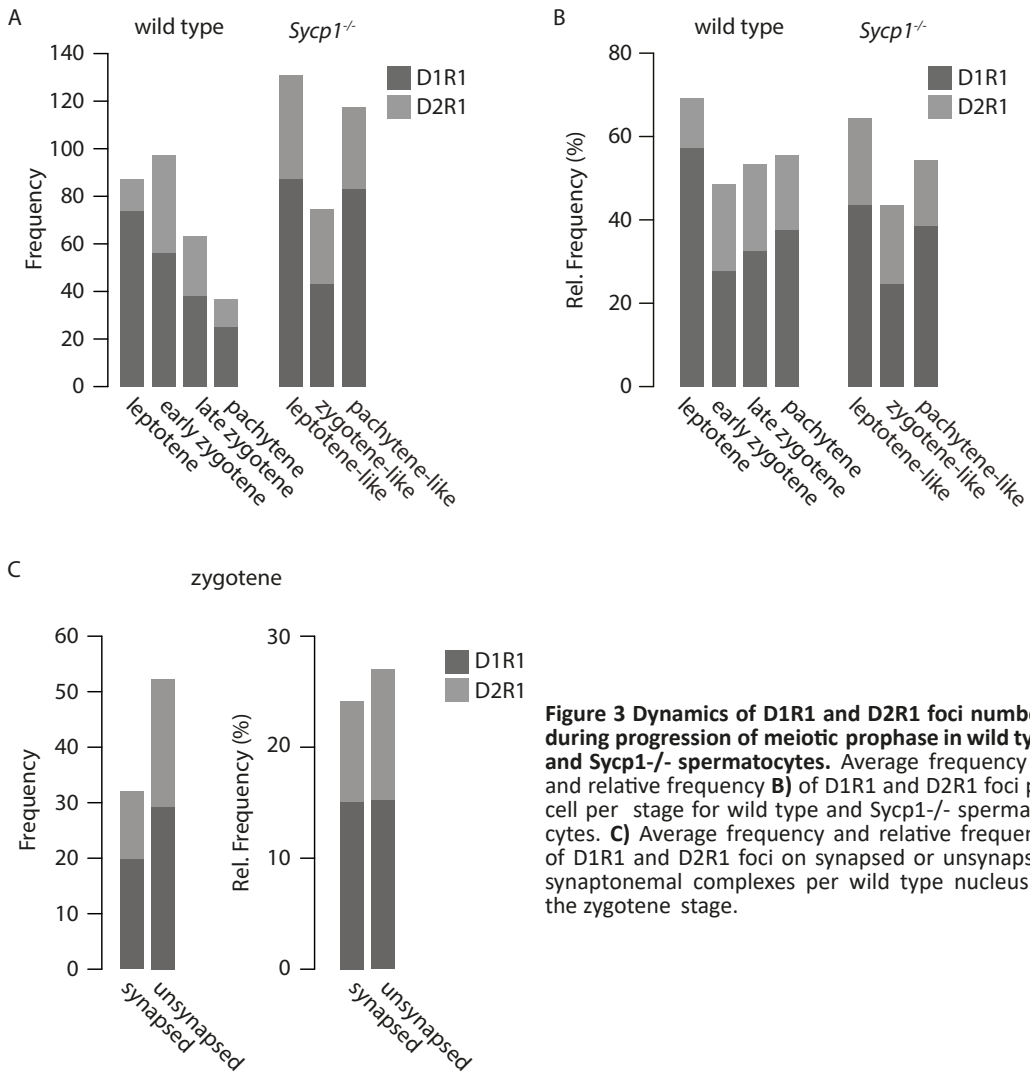


**Figure 3** Dynamics of D1R1 and D2R1 foci numbers during progression of meiotic prophase in wild type and *Sycp1*<sup>-/-</sup> spermatocytes. Average frequency **A**) and relative frequency **B**) of D1R1 and D2R1 foci per cell per stage for wild type and *Sycp1*<sup>-/-</sup> spermatocytes. **C**) Average frequency and relative frequency of D1R1 and D2R1 foci on synapsed or unsynapsed synaptonemal complexes per wild type nucleus at the zygotene stage.

type zygotene nuclei (Figure 3C). We also did not detect any overt specific distribution pattern of the different configurations relative to each other along the axial/lateral elements of the SC (Figure 3-figure supplement 1).

Since we observed clear changes in the D1R1 and D2R1 configurations over time, and between wild type and *Sycp1*<sup>-/-</sup> spermatocytes, we further focused on a better understanding of the molecular characteristics of these two cluster configurations.

### Asymmetrical distribution of RAD51 relative to DMC1

To investigate the spatial organization of

protein clusters in the identified configurations further, we determined the center of mass of every cluster in each ROI and measured the distance between the center of RAD51 cluster(s) and DMC1 cluster(s) (Figure 4A, B). Interestingly, minimum distances coherently clustered at approximately 70 nm (wild type/*Sycp1*<sup>-/-</sup>;  $68.4 \pm 1.2 \text{ sem} / 75.8 \pm 1.1 \text{ sem}$ ) for all analysed foci configurations in wild type and *Sycp1* knockout nuclei. Thus, all foci that contain more than one RAD51 and/or DMC1 cluster, contain at least one RAD51 and one DMC1 cluster that are in close proximity to each other, with an average distance of approximately 70nm (Figure 4A). Since only a single cluster is present for each of



the individual recombinases in the D1R1 group, the distribution of the maximum distance was the same as for the minimum distance. Importantly, it completely overlapped with the first peak of the distribution of maximum distances of all configurations, suggesting that all foci with more than one RAD51 and/or DMC1 cluster, also contain RAD51 and DMC1 clusters that are larger (localisations are more spread) or that are spatially more separated from each other, with an average distance of around 300 nm (wild type/*Sycp1*<sup>-/-</sup>; 287.4±2.7sem/308.6±2.8sem) (Figure 4B).

From these data we inferred that the D2R1 configuration is asymmetrical with respect to the position of the RAD51 cluster relative to the two DMC1 clusters, allowing us to define a close-DMC1 and a far-DMC1 cluster. Subsequently, we could determine that the DMC1 and RAD51 cluster area sizes in the D1R1 foci are very similar to the cluster area sizes of the close-DMC1 and RAD51 cluster in the D2R1 foci, respectively. Moreover, in both D1R1 and D2R1 foci, the (close-)DMC1 cluster became smaller as cells progressed from leptotene to late zygotene. In pachytene, the area of the (close-)DMC1 cluster returns to a size that is similar to what was observed at leptotene (Figure 4C, D). The close-DMC1 cluster, on average occupied a much larger area compared to the far-DMC1 cluster (Figure 4D). The far-DMC1 cluster displayed a small but gradual increase in size as meiotic prophase progressed (Fig. 4D). In *Sycp1*<sup>-/-</sup> spermatocytes, the (close-)DMC1 cluster area appeared larger compared to what was observed in the wild type, and even displayed an increase in DMC1 cluster area size in the zygotene- and pachytene-like D1R1 foci, compared to leptotene-like foci (Fig 4C). In addition, the area of the far-DMC1 was larger in the zygotene-like nuclei compared to the other stages, but the RAD51 and close-DMC1 cluster areas were similar at all *Sycp1*<sup>-/-</sup> stages examined (Figure 4C, D).

### Consensus patterns of the spatial organization in D1R1 and D2R1 foci

Upon visual inspection, the foci that were grouped within a certain DnRn subtype, still

appeared very different from each other (Figure 5-figure supplement 1). This may be caused by the fact that we are representing three-dimensional structures in a two-dimensional image. To obtain more insight in the actual structure of the two main DnRn configurations, we used alignment by rotation to be able to detect possible consensus patterns in D1R1 and D2R1 foci (Figure 5A, B). For the D1R1 group, the DMC1 cluster was used as an anchor point and the RAD51 cluster was used for the rotation. We rotated the structures so that the center of the RAD51 cluster was aligned along the vertical axis above the DMC1 cluster. Then we generated a single fused image of all aligned foci, pooled from the nuclei that were at a specific stage of meiotic prophase. We observed that the RAD51 and DMC1 cluster partially overlap, but that the degree of overlap decreases while meiosis progresses (Fig. 5A). This observation was supported by the results from measurements of the distances between the RAD51 and DMC1 cluster (Figure 5C), showing that the distance between RAD51 and DMC1 is shorter at leptotene compared to the other stages in wild type. In *Sycp1*<sup>-/-</sup> D1R1 foci, the degree of overlap was also reduced at the zygotene-like stage, relative to the leptotene-like stage, but increased again at pachytene (Figure 5B). Accordingly, the RAD51-DMC1 distance increases only transiently at the zygotene-like stage (Figure 5C). We observed no differences in distances between clusters within configurations on synapsed versus asynapsed axes (Figure 5-figure supplement 2).

In the D2R1 group we used the close DMC1 cluster as anchor, and either the RAD51 cluster or the far-DMC1 cluster was rotated until it aligned. The alignment using the RAD51 cluster for rotation provided insight in the location of the far-DMC1 cluster with respect to the two other clusters. The locations of the signals of the far-DMC1 cluster were highly variable at leptotene, but formed a crescent moon-shaped structure around the other two clusters in zygotene and pachytene nuclei (Fig. 5A). Most of the signal appeared on the top, indicating some type of spatial relation between the RAD51 cluster, which is rotated to a position above the

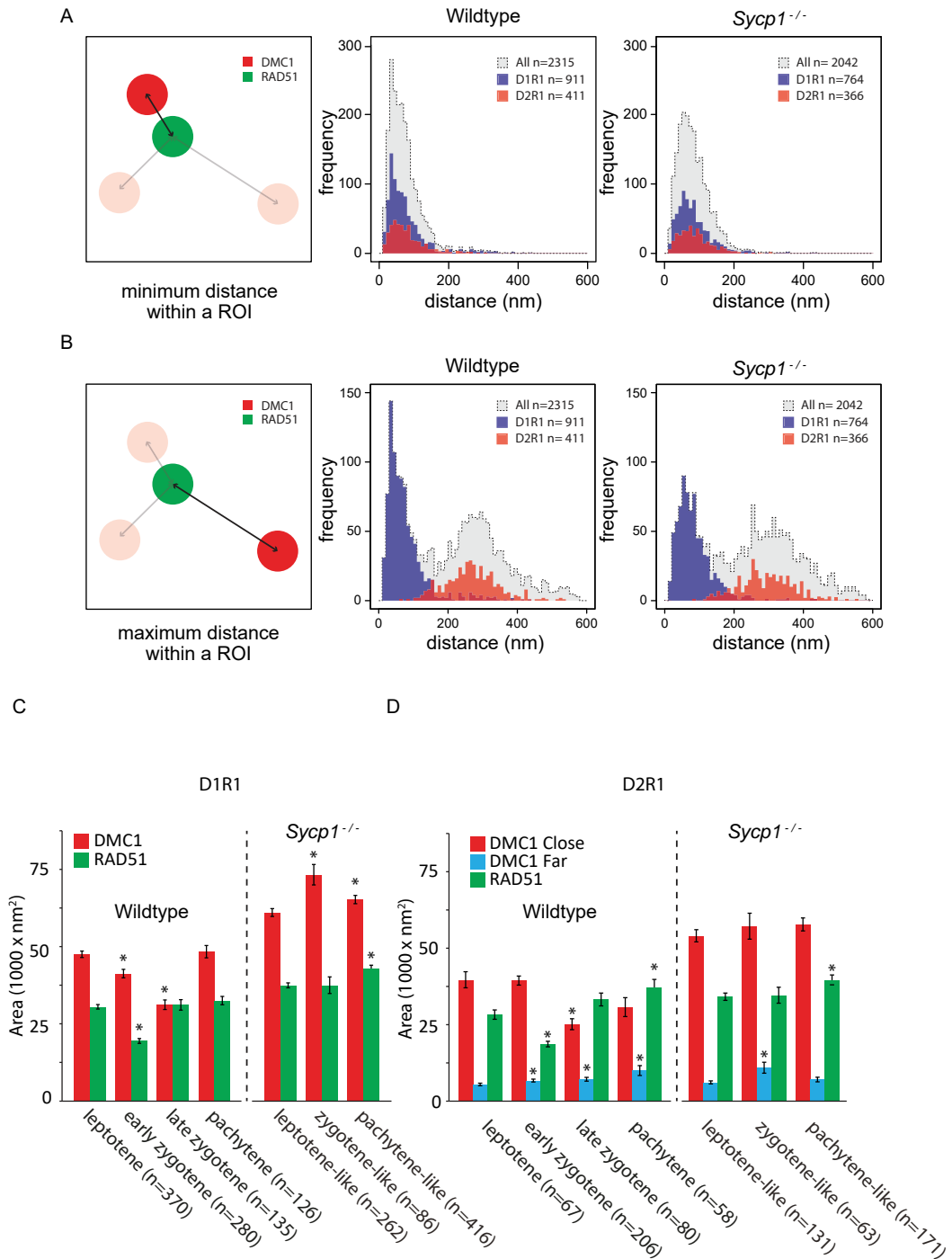


**Figure 4 Distances between DMC1 and RAD51 clusters, and area occupancy.** Distribution of the minimum **A**) and maximum **B**) distances between the center of mass of RAD51 and DMC1 clusters in wild type (middle panel) and *Sycp1*<sup>-/-</sup> (right panel) foci. Dashed lines with grey fill represent all foci, the D1R1 and D2R2 subgroups are depicted in blue and red histograms, respectively. Area of RAD51 and DMC1 close and far clusters in D1R1 subgroup **C**). Area of RAD51 and DMC1 close and far clusters in D2R1 subgroup **D**). Error bars indicate SEM, asterisks indicate significant difference compared to leptotene ( $P < 0.05$ ) based on the number of foci that was analysed (n).

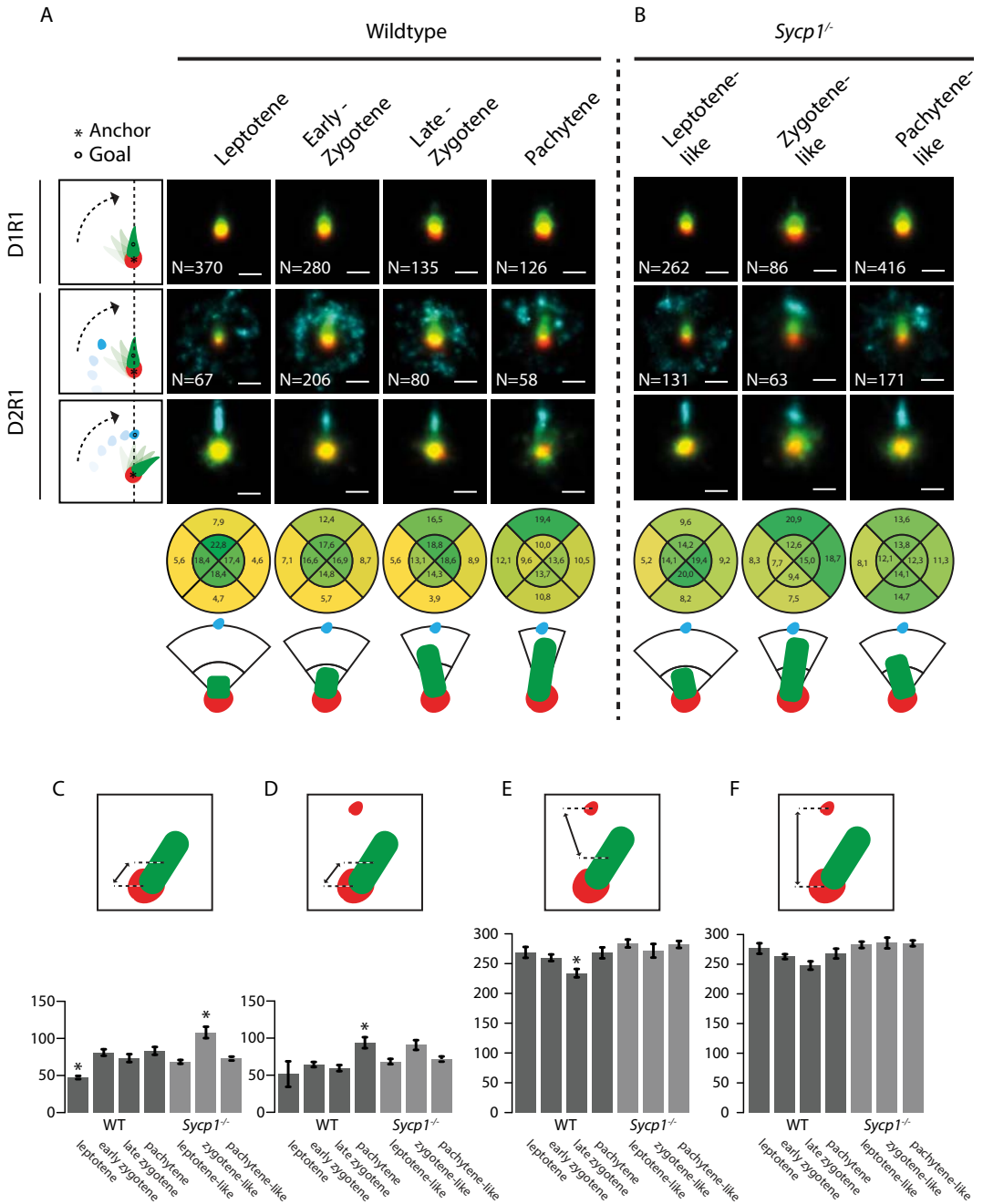


**Figure 5 Consensus patterns of D1R1 and D2R1 through the stages of meiotic prophase I** A-B) Summed images of all rotated patterns and aligned foci within the D1R1 and D2R1 group per stage. Images were rotated as indicated by schematic drawings to the left of each row, whereby the anchor (\*) indicates the cluster that is centered, and the goal (o) the cluster that is rotated until it aligns along the axis. Underneath each column, the percentage of signal for the RAD51 cluster localising in each indicated quadrant is shown for each stage for the rotation whereby the close-DMC1 is used as anchor and the far-DMC1 as goal. A schematic interpretation of the results of the rotations is shown at the bottom. C-F) Mean distances between the indicated clusters per stage in wild type and *Sycp1*<sup>-/-</sup> spermatocytes. Error bars indicate SEM. Asterisks indicate significant difference compared to all other stages (P<0.05). Scale bars represent 100nm.

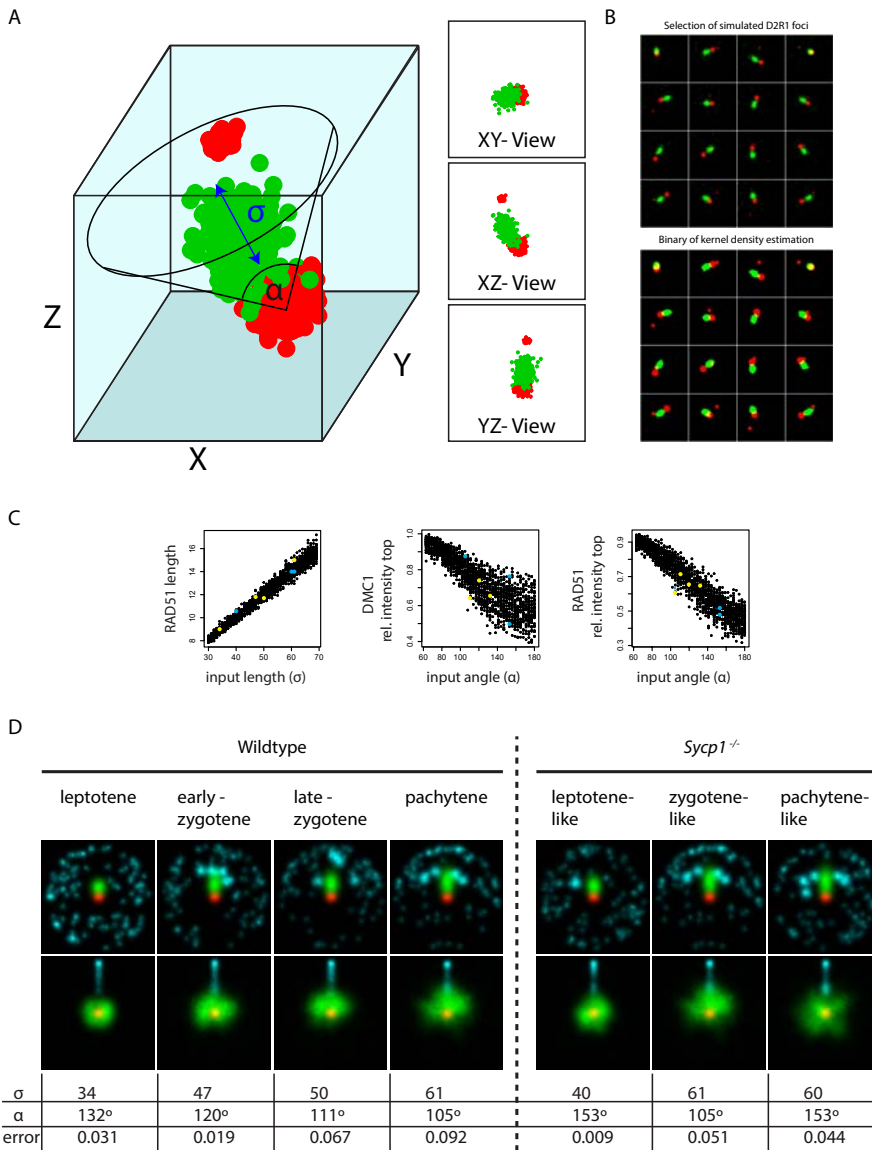


**Figure 6 Simulations of D2R1 rotations** **A)** Model of D2R1 foci in three dimensions. **B)** Selection of simulated foci using one model randomly positioned in space and visualised in two dimensions. **C)** Measured RAD51 length, RAD51 intensity in the top quadrant and DMC1 intensity in the top half for all simulated foci, whereby each point represents an assembly from 200 aligned foci. Coloured points represent measured values from experimental data from both wild type (yellow) and *Sycp1*<sup>-/-</sup> (blue) nuclei at the stages analysed. **D)** Summed images of simulations that fit best to experimental data, length (full width half maximum:  $2.355\sigma$ ), angle and error are indicated.

close-DMC1 cluster, and the far-DMC1 cluster that then also ends up mostly above the RAD51 and close-DMC1 clusters. As meiotic prophase progresses, the far-DMC1 cluster became more and more localised in a smaller region above the close-DMC1 cluster and the RAD51 cluster, showing that a relatively large fraction of the D2R1 foci has a DMC1-RAD51-DMC1 type

of structure. When we aligned the two DMC1 clusters we assessed the RAD51 location relative to the two DMC1 clusters by quantifying the relative number of RAD51 localisations present in four quarters (above, below, left and right) of the image, relative to the close-DMC1 cluster. As expected, based on the results of the rotation with the far-DMC1 cluster, the highest

percentage of the RAD51 signal was observed between the two DMC1 clusters, and more signal accumulated in the upper part of that quadrant as prophase progressed (Fig. 5A). In agreement with this observation, the center of mass of the RAD51 cluster seemed to be extending away from the closest DMC1 anchor cluster as cells progressed from zygotene to pachytene (Figure 5D). The mean distance between the two DMC1 clusters, and between the RAD51 and the far-DMC1 cluster in the D2R1 decreased as prophase progressed, but increased again in pachytene (Figure 5E-F). Overall, the consensus patterns in *Sycp1*<sup>-/-</sup> spermatocytes were similar, but the configurations were more variable (Fig. 5B-F). For example, the directionality of RAD51 towards the far DMC1 cluster was clear at the zygotene-like stage, but lost at pachytene-like. Furthermore, in the analyses of the distances between the clusters of the D2R1 configurations, the distance between the close-DMC1 cluster and RAD51 initially appeared larger compared to the wild type, and increased more when cells developed from leptotene to zygotene, but in pachytene-like *Sycp1*<sup>-/-</sup> spermatocytes the distance was similar to what was observed at leptotene. The distance of the far-DMC1 cluster to RAD51 or to the close-DMC1 cluster was large at all stages, in contrast to the reduction observed during zygotene in the wild type (Fig. 5B, E-F).

### Three-dimensional simulations of the D2R1 configuration

The chromatin spreads used in these analyses are very thin, avoiding the presence of more than one focus at a certain location, but most likely still retain the three dimensional structure of a single focus. Taking this into account, we used the program R to simulate a 3D model of D2R1 configurations (Figure 6A, Rich media file 1). We analysed the simulated data (discarding the z information) in the same way as the experimental data. Interestingly, around 15% of the simulated D2R1 configurations in a three-dimensional space are represented as D1R1 in the two-dimensional representations, and also a small fraction of D3R1 and D2R2 configurations were observed. This is most likely caused by

situations whereby spurious detections rise just above the background, resulting in detection of an additional cluster. We performed rotation and alignment on the simulated D2R1 configurations in the dataset, using the close-DMC1 cluster as an anchor, and rotating either RAD51 or the far DMC1 cluster to the vertical axis. Strikingly, it can be observed that the simulated data fits best if the degree of freedom for the angle gradually reduces from 132° to 105° and the length of RAD51 gradually increases from 80 to 144 nm going from leptotene to pachytene (Fig. 6C,D). Comparing the simulations to the *Sycp1*<sup>-/-</sup> D2R1 rotations, it appears that the degree of rotation freedom for the close-DMC1-RAD51 cluster combination relative to the DMC1-DMC1 axis is larger than in wild type at the leptotene-like and pachytene-like stages, but actually more restricted in the zygotene-like nuclei, for which a maximal rotation angle of 105 and a length of 144 nm fitted best.

## Discussion

We simultaneously determined the localisation of the recombinases RAD51 and DMC1 at nanoscale resolution in more than 4000 DSB foci in 18 wild type and 10 *Sycp1*<sup>-/-</sup> spermatocytes. Moreover, we distinguished early, intermediate and late stages of meiotic prophase by co-staining of the synaptonemal complex. Together, this allowed us to reconstruct generalised RAD51 and DMC1 distribution patterns within repair foci as they develop during meiotic prophase.

### DMC1 and RAD51 localise in separate clusters within DSB foci

Single molecule localisations of RAD51 and DMC1 were not homogeneously distributed, but formed separable clusters within a single DSB focus. The majority of the investigated DSBs showed one RAD51 cluster and either one or two DMC1 clusters (D1R1 and D2R1). More complex configurations were also observed, but computer simulations indicate that part of these actually represent D2R1 configurations. Therefore, although additional more complex configurations also occur, they are present at lower frequency than observed. These configurations

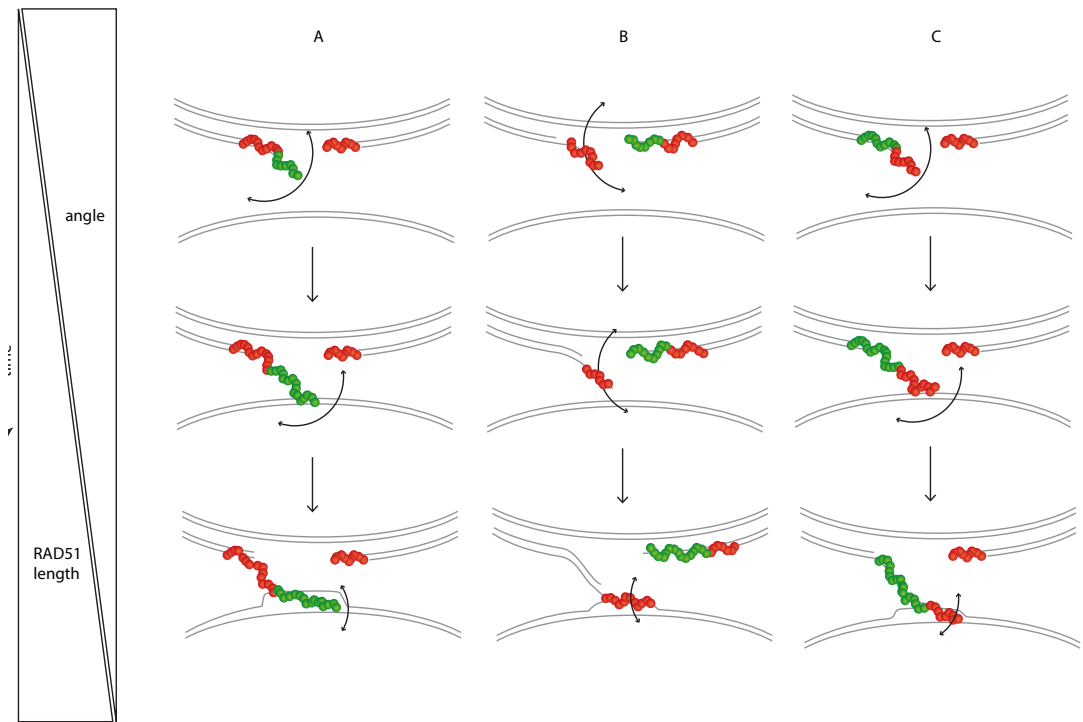


**Figure 7 Schematic model of RAD51 and DMC1 cooperation in meiotic recombination foci.** A speculative model is proposed, for dynamic patterns of RAD51 and DMC1 localisation and organization in recombination intermediates in mouse meiotic prophase in subsequent steps. Initial resection of the 5' strands after DSB formation may occur asymmetrically, as suggested by studies in budding yeast (Neale et al., 2005), allowing some functional differences between the two DSB-ends. Subsequently, the D1R1 configuration, may form as a result of one or more of the depicted accumulation patterns of RAD51 and DMC1, with or without additional presence of RPA-(like) proteins A). When one of the two strands begins homology search B), the two DSB ends will diverge, allowing visualisation of two separate DMC1 clusters (D2R1), or this could be accompanied by additional loading of DMC1. Based on available information from yeast genetics, we favour model 3, in which the RAD51 filament that contains both RAD51 and DMC1 performs the homology search. As time progresses, the RAD51 filament changes shape, and becomes more elongated, in addition, the freedom of movement of the RAD51-DMC1 filament gradually decreases, perhaps signifying more stable interactions with the homolog. Finally RAD51 is most often localised between the two DMC1 clusters, when the highest level of stable structural organization is reached. Further strand exchange, may be associated with subsequent loss of (part) of the DMC1 signal. In *Sycp1*<sup>-/-</sup> spermatocytes homologous recombination may be arrested just prior to the final depicted stage.

may then represent either short-lived transitional structures or, unfavorable and therefore unstable structures that occur due to the stochastic nature of macromolecular complex formation. Since D1R1 frequencies go down and D2R1 frequencies go up during prophase progression, we hypothesize that D1R1 configurations represent an early stage of DSB repair, when the recombinases have recently loaded, whereas D2R1 configurations form later, during homology search and strand invasion.

We estimate the length of the RAD51 cluster to reach a maximum of around 140 nm, which

corresponds to around 100 nm after correction for the antibodies that were used to detect the recombinase. The DMC1 cluster in the D1R1 configuration, and the close DMC1 cluster in the D2R1 configuration are of similar size. An *in vitro* filament of RAD51 with a length of 100 nm covers approximately 200 bp of ssDNA (Ristic et al., 2005). However, we cannot accurately estimate the length of the ssDNA that is covered by the RAD51 and DMC1 clusters in our *in vivo* analyses because we have no information regarding the folding of such filaments in association with other complexes, such as structural

components of the SC. Furthermore, there are no data available regarding the actual length of single-stranded resected DNA of meiotic DSBs in mouse meocytes. Thus, based on what is currently known, it is very well possible that the large DMC1 and RAD51 clusters represent adjacent folded filaments covering all ssDNA on one or two DSB ends.

### **The D1R1 configuration represents an early recombinase structure**

The D1R1 configuration may be formed from any asymmetric loading pattern, but it seems highly unlikely that RAD51 and DMC1 accumulate both at each end of the DSB since we did not observe paired occurrence of D1R1 configurations, and D2R2 configurations, or configurations with an even larger number of clusters, were rare. From the alignment by rotation and the distance measurements it appears that there is a gradual lengthening of the RAD51 moiety of the D1R1 structure. However, we also observed a transient reduction in the overall size of the D1R1 configuration during zygotene. So, although lengthening may suggest additional loading, a decrease in overall size could be caused by removal of RAD51 and DMC1 from the DNA. Combining these two observations would therefore fit best with a gradually more stretched configuration, accompanied by loss of the recombinases. The subsequent increase in area sizes in pachytene could then represent formation of new D1R1 structures, while the smaller D1R1s have evolved into D2R1s.

### **D2R1 represents a DSB intermediate with asymmetric loading of RAD51 and DMC1**

The similarity of the (close) DMC1 and RAD51 clusters in the D2R1 and D1R1 configurations in terms of size and proximity implies that the D1R1 evolves into a D2R1 configuration. The additional DMC1 domain at longer distance from RAD51 in D2R1 could then result from new loading of DMC1, or from splitting of the DMC1 cluster into two independent clusters that stabilize at a distance of 200-250 nm.

The gradual increasing size of the second DMC1 domain supports the idea of new loading

of DMC1, but even its maximum size is more than 10 fold smaller than the areas occupied by the adjacent close DMC1 and RAD51 clusters. So either the far DMC1 cluster may be somehow compacted, or it represents binding of DMC1 to a shorter stretch of ssDNA. The adjacent close DMC1 and RAD51 clusters may represent adjacent filaments, formed in either direction relative to the 3' end of the ssDNA. The fact that the distances of both the close DMC1 cluster, and of the RAD51 cluster, from the far DMC1 cluster are very similar and show similar changes as meiotic prophase progresses (Fig 6F,G) supports the idea that these two clusters are physically coupled.

### **The number and organization of the D1R1 and D2R1 configurations are affected in *Sycp1*<sup>-/-</sup> spermatocytes**

Our high resolution analyses confirm the previously reported increased number of repair foci in the *Sycp1*<sup>-/-</sup> zygotene-like and pachytene-like spermatocytes compared to the corresponding wild type cells that was previously reported (de Vries et al., 2005). Interestingly, we observed an increased frequency of D1R1 configurations in the pachytene-like *Sycp1*<sup>-/-</sup> nuclei compared to zygotene-like nuclei. Recent data indicate that when synapsis is not achieved, feedback mechanisms may act locally to maintain SPO11 activity in unsynapsed regions (Faieta et al., 2015; Gray et al., 2013; Kauppi et al., 2013), which is in agreement with the increased frequency of early recombinase configurations in late-stage *Sycp1*<sup>-/-</sup> spermatocytes. We also observed an increased frequency of D2R1 configurations in leptotene-like nuclei, in comparison to the wild type, which can be attributed to the fact that when a true synapsed structure cannot be formed, initial alignment and pairing will be less stable, and cells that should be in zygotene will still appear as leptotene in the *Sycp1*<sup>-/-</sup> nuclei. Moreover, the observation that both D1R1 as well as D2R1 configurations are larger compared to the same configurations in wild type nuclei fits well with a model where a stable recombination intermediate cannot be formed, leading to increased size of the RAD51/DMC1 clusters due to additional protein loading and

the absence of advancing structures that start to release recombinases as strand invasion is initiated. The longer average distance between the RAD51 and the close DMC1 cluster at the zygotene-like stage compared to the corresponding wild type stage, as well as the absence of a transiently reduced distance between RAD51 and the far DMC1 clusters also indicates a lack of progression to the most advanced type of D2R1 configuration. In the rotation analyses, it appeared that the D2R1 configuration in *Sycp1*<sup>-/-</sup> zygotene-like nuclei was much more clearly organized as a DMC1-RAD51-DMC1 structure compared to wild type nuclei at any stage. Perhaps stalling of repair generates a longer lifetime of this particular configuration, allowing a more organized summed image. Still, in the pachytene-like *Sycp1*<sup>-/-</sup> nuclei, this high level of organization appears to be lost again, and this might be due to increased presence of new, more early, D2R1 configurations, or reflect loss of overall organisation as repair fails. Taken together, the measurements in this mouse model confirm the robustness of our analyses of RAD51/DMC1 foci, and indicate that the increased number of repair foci in *Sycp1*<sup>-/-</sup> zygotene- and pachytene-like spermatocytes is due at least in part to induction of late DSBs, in response to asynapsis. Furthermore, the transition of the D2R1 configuration to a stage whereby the DMC1-DMC1 distance becomes shorter concomitant with a reduction in the area occupied by the close DMC1 cluster does not occur in *Sycp1*<sup>-/-</sup> spermatocytes, indicating that these changes in the D2R1 configuration represent a specific functional transition, which requires the presence of SYCP1.

### Models for early RAD51/DMC1 filament structures

Based on our observations, the four models depicted in Figure 7A for initial formation of the D1R1 configuration are equally likely. Based on the genetic evidence that RAD51 may stimulate DMC1 activity, it would be more likely that DMC1 would be loaded on the 3' end of the ssDNA, to facilitate its strand-invasion activity (Cloud et al., 2012; Lao et al., 2013). Combined with the above described coupled behaviour of

the RAD51 and close DMC1 cluster and their overall resemblance to the clusters in D1R1, we favour models 3 and 4 in Figure 7A.

The two DMC1 clusters of the D2R1 configuration are somehow structurally connected, as shown by the constant distance between their centers of mass. A functional connection is also indicated from the results from the rotation analyses and the simulations thereof indicating that the RAD51 cluster becomes more elongated, and more frequently localised in the direction of the far DMC1 spot, as meiotic prophase progresses. These data are consistent with all three models depicted in Figure 7B. However, starting from models 3 and 4 for D1R1 in Figure 7A, only model 3 in Figure 7B would remain for the D2R1 configuration. This would be consistent with a role for RAD51 in formation of the presynaptic filament only, which would require ATP-binding, but no ATPase activity, and DMC1 (activated by RAD51 on the same strand) functioning in the actual homology recognition and strand exchange reaction.

All foci that we analysed were associated with a SYCP3 axial or lateral filament. However, there was no clear fixed orientation of any of the configurations relative to the SYCP3 filament. Still it may be suggested that the structural association between the DSB repair complex and the developing synaptonemal complex may cause a spatial restriction for the DSB ends coated by RAD51 and/or DMC1.

Recent data indicate that the homology search involves two functionally distinct phases: a first phase during which 8nt regions of microhomology are probed, and a second phase that involves further strand invasion, and D-loop formation (Lee et al., 2015). This fits well to the data presented here, where in the wild type late zygotene and pachytene nuclei, the transient reduction of the DMC1-DMC1 distance, and a concomitant possible loss of DMC1 protein from the close DMC1 cluster (given its reduction in size), may represent the transition from this first phase to the second, more stable situation, that would then possibly depend on the presence of functional SYCP1 protein. At the other end of the DSB, a DMC1 only filament may be the quiescent strand, lacking the (activating) RAD51



component (Figure 7B, model 3), in agreement with a model proposed by Hong et al. (2013), in which only one end of the DSB is performing homology search, branching away from the DSB site (Hong et al., 2013). Further studies will be required to test the model, for instance by super resolution imaging of additional involved proteins in combination with visualisation of DNA. In addition, the experimental combination of meiosis-defective knockout mouse models with super resolution microscopy provides a promising new approach to study the dynamics of mouse meiotic recombination and meiotic defects at the molecular level.

## Materials and Methods

### Animals

Two wild type (5-10 weeks old) and two *Sycp1* knockout (12 weeks old) mice (previously described (de Vries et al., 2005)) were killed. All animal experiments were approved by the local animal experiments committee DEC Consult and animals were maintained under supervision of the Animal Welfare Officer.

### Meiotic spread preparation and immunofluorescence

Spread nuclei for immunocytochemistry were prepared as described (Peters et al., 1997). Cells were spread on 1.5 thickness coverslips ( $170 \pm 5 \mu\text{m}$ ), previously coated with 1% poly L-lysine (Sigma) and stained with antibodies mentioned below in six separate staining experiments for dSTORM and 3D-SIM analyses as follows:

- Four experiments to collect the images of the 18 nuclei presented in Figure 1-figure supplement 1

- Two experiments in which the fluorophores were swapped as described below in the paragraph entitled 3D-SIM and dSTORM imaging, to confirm that this does not alter our main observations

- Two experiments to collect the images of 10 *Sycp1* knockout nuclei nuclei presented in Figure 2-figure supplement 1

Before incubation with antibodies, coverslips were washed in PBS (3x10 min), and

non-specific sites were blocked with 0.5% w/v BSA and 0.5% w/v milk powder in PBS. Primary antibodies were diluted in 10% w/v BSA in PBS, and incubations were overnight at room temperature in a humid chamber. Subsequently, coverslips were washed (3x10 min) in PBS, blocked in 10% v/v normal swine serum (Sigma) in blocking buffer (supernatant of 5% w/v milk powder in PBS centrifuged at 14,000 rpm for 10 min), and incubated with secondary antibodies in 10% normal swine serum in blocking buffer overnight at room temperature. Finally, coverslips were washed (3x10 min) in PBS (in the dark) and immediately used for imaging.

### Antibodies

For primary antibodies, we used goat antibody against SYCP3 (R&D Systems), mouse monoclonal antibody against DMC1 (Abcam ab1837), and a previously generated rabbit polyclonal anti RAD51 (Essers et al., 2002). For secondary antibodies, we used a donkey anti-rabbit IgG Alexa 488/647, donkey anti-mouse Alexa IgG 488/647, and donkey anti-goat Alexa 555 (Molecular Probes).

### Sample preparation

Coverslips immunostained as described above were mounted in an Attofluor Cell Chamber (Life Technologies). For drift correction and channel alignment 100nm Gold nanoparticles (Sigma) were added to the sample. To perform dSTORM imaging, an imaging buffer was prepared containing 40mM MEA (Sigma), 0.5mg/ml Glucose Oxidase (Sigma), 40  $\mu\text{g}/\text{ml}$  Catalase (Sigma) and 10% w/v Glucose in PBS pH 7.4. Samples were incubated in the imaging buffer during the entire imaging session.

### 3D-SIM and dSTORM imaging

Imaging was performed using a Zeiss Elyra PS1 system. Both 3D-SIM and dSTORM data were acquired using a 100x 1.49NA objective. 488, 561, 642 100mW diode lasers were used to excite the fluorophores together with respectively a BP 495-575 + LP 750, BP 570-650 + LP 750 or LP 655 excitation filter. For 3D-SIM imaging a grating was present in the light path. The grating was modulated in 5 phases and 5

rotations, and multiple z-slices were recorded on an Andor iXon DU 885, 1002x1004 EMCCD camera. dSTORM imaging was done using near-TIRF settings while the images were recorded on Andor iXon DU 897, 512x512 EMCCD camera. At least 10 000 images were acquired and frames were subsequently imaged at an interval of 33ms for Alexa 647. For Alexa 488 an interval of 50ms was used to compensate for the lower photon yield of the Alexa 488 dye. We used Alexa 488 and Alexa 647 dyes coupled to secondary antibodies to detect respectively RAD51 and DMC1 or vice versa. Using either fluorophore combination, we consistently detected ~1.5 times more localisation events for RAD51 than DMC1. As expected, we observed more localisations for Alexa 647 compared to Alexa 488, due to the more suitable photochemical properties for dSTORM of the former (van de Linde et al., 2011). We chose the more efficient Alexa 647 dye to detect DMC1, that is either less abundant or less well recognized by the primary antibody compared to RAD51, and the Alexa 488 dye to detect RAD51.

## Image analysis

3D-SIM images were analysed using the algorithm in the ZEN2011 (Carl Zeiss, Jena) software. Channels were aligned based on a reference sample containing 100nm Tetraspeck beads (Life Technologies). For dSTORM, individual fluorescent events were localised in the subsequent frames using a 2D Gauss fitting algorithm in the ZEN2011 (Carl Zeiss, Jena) software. Detections in subsequent frames originating from the same fluorophore were grouped. Drift was corrected using 100nm gold nanoparticles (Sigma). The same fiducials were used to align the two color dSTORM images using an affine alignment. Dual color dSTORM and triple color SIM images were aligned, based on the dSTORM and 3D-SIM Alexa 647 images, using a channel alignment algorithm in the ZEN2011 software. All observed foci were manually selected based on the SIM images, and square regions (side of 600 nm) around the foci were selected using ImageJ within the Fiji platform (Schindelin et al., 2012). For each stage and each genotype, 2-5 nuclei were analysed. Each nucleus can be viewed as

a biological replicate when differences between stages are considered, whereas each focus can be considered a biological replicate when the overall properties of the foci are analysed. Technical replication is not applicable for the types of analyses used here. The single molecule localisations of the individual foci were subsequently imported into R using the RStudio GUI for further analysis (Pau, Oles, Smith, Sklyar and Huber, EBImage: Image processing toolbox for R. v. 2.13 (2013) [http://watson.nci.nih.gov/bioc\\_mirror/packages/2.13/bioc/html/EBImage.html](http://watson.nci.nih.gov/bioc_mirror/packages/2.13/bioc/html/EBImage.html); R Development Core Team, R: A language and environment for statistical computing. R Foundation for Statistical Computing, R Foundation for Statistical Computing, Vienna, Austria, ISBN 3-900051-07-0, <http://www.R-project.org>.)

Selected foci that were spatially overlapping were excluded if the percentage of overlapping localisations was larger than 25%. Also foci containing less than 50 localisations were excluded from further analysis.

## Foci shape analysis

Single molecule localisation data was used to fit a 2D Kernel Density Estimation (KDE) function (Wand, 2013, KernSmooth: Functions for kernel smoothing for Wand & Jones 2.23-10, <http://CRAN.R-project.org/package=KernSmooth>). The KDE function estimates the density of localisations at a certain position in the image. The bandwidth of the density estimation was set to the approximate average localisation precision of our data: 20 nm. The 2D KDE gives a normalized density over the image. Because we are interested to determine the absolute density of localisations, the normalized density is multiplied by the number of localisations in the ROI. After fitting a 2D KDE to the data we are able to define objects by applying a threshold. The threshold is set at 5 localisation/pixel, equal to 0.2 localisations/nm<sup>2</sup>. The resulting binary images were used to determine shape features (center of mass i.e.) (Pau, Oles, Smith, Sklyar and Huber, EBImage: Image processing toolbox for R. v. 2.13 (2013) [http://watson.nci.nih.gov/bioc\\_mirror/packages/2.13/bioc/html/EBImage.html](http://watson.nci.nih.gov/bioc_mirror/packages/2.13/bioc/html/EBImage.html)). Pairwise comparison between

the mean values of image features from individual meiotic stages was performed using an independent two sample Student t-test. A P-value below 0.05 was considered a significant difference between the two samples. For alignment by rotation the center of mass was used to center images on the close DMC1 cluster for alignment by rotation. The subsequent localisations were all rotated so that either the far DMC1 or RAD51 center aligned above the (close DMC1) center. All localisations from indicated stages were pooled and visualised as an image.

## Simulation

We generated a 3D model of a D2R1 focus consisting of three distinct Gaussian distributions of 3d coordinates. The two DMC1 clusters are represented as globular distributions where the standard deviation ( $\sigma$ ) of the Gaussian distribution is equal in x,y and z. RAD51 is represented as an ellipsoid distribution in which the  $\sigma$  of the Gaussian distribution is larger in one dimension. We used the mean number of localisations measured per cluster: 267, 564 and 51 coordinates for RAD51, close DMC1 and far DMC1 respectively. We included 50 randomly distributed background coordinates in the model. The model was organized in such a way that the 'close' DMC1 cluster and the RAD51 cluster are physically connected. The far DMC1 cluster was placed randomly at distance of 400 nm from the close DMC1 and the RAD51 cluster localises at a random angle relative to the DMC1-DMC1 axis in a three-dimensional space. We then varied the length of the main axis of the RAD51 cluster ( $\sigma$ ) and the maximal angle ( $\alpha$ ) at which the 'close' DMC1-RAD51 cluster combination could be positioned relative to the DMC1-DMC1 axis, and generated datasets of 200 configurations for every combination of  $\sigma$  and  $\alpha$ . We fitted the experimental data to the simulations using 3 parameters: the  $\sigma$  of a Gaussian fitted over the RAD51 signal ( $\sigma$ -RAD51), the percentage of DMC1 signal in the top half of the center ( $\alpha$ -DMC1) in the rotation where RAD51 is aligned to the top, and the percentage of RAD51 in the top quadrant ( $\alpha$ -RAD51) in the rotations where the far DMC1 is aligned to the top. These 3 parameters were

measured in both the simulated data and the experimental data (Fig 7B). Using a least mean squares method the simulation which fits the experimental data best was determined.

## Acknowledgements

We would like to thank Prof. Dr. J. Anton Grootegoed (Erasmus MC, Rotterdam) for his valuable comments and suggestions to the manuscript draft.

## Author Contributions

Conceptualization, FC, MWP, JAS, ABH, and WMB; Methodology, FC, MWP, JAS, WavC, MdG, and ABH; Software, MWP, JAS, and MdG; Formal Analyses, MWP and JAS; Investigation, FC, MWP, and JAS; Writing-Original Draft, FC and WMB; Writing-Review & Editing, all authors; Visualisation, FC, MWP, JAS, and WMB; Supervision, ABH, and WMB; Funding Acquisition, ABH and WMB

## References

- Baudat, F., Manova, K., Yuen, J.P., Jasin, M., and Keeney, S. (2000). Chromosome synapsis defects and sexually dimorphic meiotic progression in mice lacking *spo11*. *Mol. Cell* 6, 989-998.
- Bishop, D.K. (1994). RecA homologs Dmc1 and Rad51 interact to form multiple nuclear complexes prior to meiotic chromosome synapsis. *Cell* 79, 1081-1092.
- Boateng, K.A., Bellani, M.A., Gregoretti, I.V., Pratto, F., and Camerini-Otero, R.D. (2013). Homologous Pairing Preceding SPO11-Mediated Double-Strand Breaks in Mice. *Developmental cell* 24, 196-205.
- Brown, M.S., Grubb, J., Zhang, A., Rust, M.J., and Bishop, D.K. (2015). Small Rad51 and Dmc1 Complexes Often Co-occupy Both Ends of a Meiotic DNA Double Strand Break. *PLoS Genet* 11, e1005653.
- Carofoglio, F., Inagaki, A., de Vries, S., Wassenaar, E., Schoenmakers, S., Vermeulen, C., van Cappellen, W.A., Sleddens-Linkels, E., Grootegoed, J.A., Te Riele, H.P., *et al.* (2013). SPO11-independent DNA repair foci and their role in meiotic silencing. *PLoS Genet* 9, e1003538.
- Cloud, V., Chan, Y.L., Grubb, J., Budke, B., and Bishop, D.K. (2012). Rad51 is an accessory factor for Dmc1-mediated joint molecule formation during meiosis. *Science* 337, 1222-1225.
- Cole, F., Kauppi, L., Lange, J., Roig, I., Wang, R., Keeney, S., and Jasin, M. (2012). Homeostatic control of recombination is implemented progressively in mouse meiosis. *Nat Cell Biol* 14, 424-430.

- Da Ines, O., Degroote, F., Goubely, C., Amiard, S., Gallego, M.E., and White, C.I. (2013). Meiotic recombination in Arabidopsis is catalysed by DMC1, with RAD51 playing a supporting role. *PLoS Genet* 9, e1003787.
- de Vries, F.A., de Boer, E., van den Bosch, M., Baarends, W.M., Ooms, M., Yuan, L., Liu, J.G., van Zeeland, A.A., Heyting, C., and Pastink, A. (2005). Mouse Sycp1 functions in synaptonemal complex assembly, meiotic recombination, and XY body formation. *Genes Dev* 19, 1376-1389.
- Essers, J., Hendriks, R.W., Wesoly, J., Beerens, C.E., Smit, B., Hoeijmakers, J.H., Wyman, C., Dronkert, M.L., and Kanaar, R. (2002). Analysis of mouse Rad54 expression and its implications for homologous recombination. *DNA Repair (Amst)* 1, 779-793.
- Faieta, M., Di Cecca, S., de Rooij, D.G., Luchetti, A., Muroccca, M., Di Giacomo, M., Di Siena, S., Pellegrini, M., Rossi, P., and Barchi, M. (2015). A surge of late-occurring meiotic double-strand breaks rescues synapsis abnormalities in spermatocytes of mice with hypomorphic expression of SPO11. *Chromosoma*.
- Gray, S., Allison, R.M., Garcia, V., Goldman, A.S., and Neale, M.J. (2013). Positive regulation of meiotic DNA double-strand break formation by activation of the DNA damage checkpoint kinase Mec1(ATR). *Open biology* 3, 130019.
- Gupta, R.C., Golub, E., Bi, B., and Radding, C.M. (2001). The synaptic activity of HsDmc1, a human recombination protein specific to meiosis. *Proc Natl Acad Sci U S A* 98, 8433-8439.
- Habu, T., Taki, T., West, A., Nishimune, Y., and Morita, T. (1996). The mouse and human homologs of DMC1, the yeast meiosis-specific homologous recombination gene, have a common unique form of exon-skipped transcript in meiosis. *Nucleic Acids Res* 24, 470-477.
- Hamer, G., Gell, K., Kouznetsova, A., Novak, I., Benavente, R., and Hoog, C. (2006). Characterization of a novel meiosis-specific protein within the central element of the synaptonemal complex. *J Cell Sci* 119, 4025-4032.
- Hamer, G., Wang, H., Bolcun-Filas, E., Cooke, H.J., Benavente, R., and Hoog, C. (2008). Progression of meiotic recombination requires structural maturation of the central element of the synaptonemal complex. *J Cell Sci* 121, 2445-2451.
- Hong, S., Sung, Y., Yu, M., Lee, M., Kleckner, N., and Kim, K.P. (2013). The logic and mechanism of homologous recombination partner choice. *Mol Cell* 51, 440-453.
- Kauppi, L., Barchi, M., Lange, J., Baudat, F., Jasin, M., and Keeney, S. (2013). Numerical constraints and feedback control of double-strand breaks in mouse meiosis. *Genes Dev* 27, 873-886.
- Keeney, S., Baudat, F., Angeles, M., Zhou, Z.H., Copeland, N.G., Jenkins, N.A., Manova, K., and Jasin, M. (1999). A mouse homolog of the *Saccharomyces cerevisiae* meiotic recombination DNA transesterase Spo11p. *Genomics* 61, 170-182.
- Keeney, S., Giroux, C.N., and Kleckner, N. (1997). Meiosis-specific DNA double-strand breaks are catalyzed by Spo11, a member of a widely conserved protein family. *Cell* 88, 375-384.
- Kurzbaue, M.T., Uanschou, C., Chen, D., and Schlogelhofer, P. (2012). The recombinases DMC1 and RAD51 are functionally and spatially separated during meiosis in Arabidopsis. *Plant Cell* 24, 2058-2070.
- Lao, J.P., Cloud, V., Huang, C.C., Grubb, J., Thacker, D., Lee, C.Y., Dresser, M.E., Hunter, N., and Bishop, D.K. (2013). Meiotic crossover control by concerted action of Rad51-Dmc1 in homolog template bias and robust homeostatic regulation. *PLoS Genet* 9, e1003978.
- Lee, J.Y., Terakawa, T., Qi, Z., Steinfeld, J.B., Redding, S., Kwon, Y., Gaines, W.A., Zhao, W., Sung, P., and Greene, E.C. (2015). DNA RECOMBINATION. Base triplet stepping by the Rad51/RecA family of recombinases. *Science* 349, 977-981.
- Liu, J., Doty, T., Gibson, B., and Heyer, W.D. (2010). Human BRCA2 protein promotes RAD51 filament formation on RPA-covered single-stranded DNA. *Nat Struct Mol Biol* 17, 1260-1262.
- Liu, Y., Gaines, W.A., Callender, T., Busygina, V., Oke, A., Sung, P., Fung, J.C., and Hollingsworth, N.M. (2014). Down-regulation of Rad51 activity during meiosis in yeast prevents competition with Dmc1 for repair of double-strand breaks. *PLoS Genet* 10, e1004005.
- Moens, P.B., Chen, D.J., Shen, Z., Kolas, N., Tarsounas, M., and Heng, H.H.Q. (1997). Rad51 immunocytology in rat and mouse spermatocytes and oocytes. *Chromosoma* 106, 207-215.
- Peters, A.H., Plug, A.W., van Vugt, M.J., and de Boer, P. (1997). A drying-down technique for the spreading of mammalian meiocytes from the male and female germline. *Chromosome Res* 5, 66-68.
- Ristic, D., Modesti, M., van der Heijden, T., van Noort, J., Dekker, C., Kanaar, R., and Wyman, C. (2005). Human Rad51 filaments on double- and single-stranded DNA: correlating regular and irregular forms with recombination function. *Nucleic Acids Res* 33, 3292-3302.
- Romanienko, P.J., and Camerini-Otero, R.D. (2000). The mouse spo11 gene is required for meiotic chromosome synapsis. *Mol. Cell* 6, 975-987.
- San Filippo, J., Sung, P., and Klein, H. (2008). Mechanism of eukaryotic homologous recombination. *Annu Rev Biochem* 77, 229-257.
- Schindelin, J., Arganda-Carreras, I., Frise, E., Kaynig, V., Longair, M., Pietzsch, T., Preibisch, S., Rueden, C., Saalfeld, S., Schmid, B., et al. (2012). Fiji: an open-source platform for biological-image analysis. *Nat Methods* 9, 676-682.
- Schipler, A., and Iliakis, G. (2013). DNA double-strand-break complexity levels and their possible contributions to the probability for error-prone processing and repair pathway choice. *Nucleic Acids Res* 41, 7589-7605.
- Schramm, S., Fraune, J., Naumann, R., Hernandez-Hernandez, A., Hoog, C., Cooke, H.J., Alsheimer, M., and Benavente, R. (2011). A novel mouse synaptonemal complex protein is essential for loading of central element proteins, recombination, and fertility. *PLoS Genet* 7, e1002088.
- Sheridan, S.D., Yu, X., Roth, R., Heuser, J.E., Sehorn, M.G., Sung, P., Egelman, E.H., and Bishop, D.K. (2008). A comparative analysis of Dmc1 and Rad51 nucleoprotein filaments. *Nucleic Acids Res* 36, 4057-4066.
- Shinohara, A., and Shinohara, M. (2004). Roles of RecA homologues Rad51 and Dmc1 during meiotic recombination. *Cytogenetic and genome research* 107, 201-207.
- Tarsounas, M., Morita, T., Pearlman, R.E., and Moens, P.B. (1999). RAD51 and DMC1 form mixed complexes associated with mouse meiotic chromosome cores and synaptonemal complexes. *J. Cell. Biol.* 147, 207-220.
- van de Linde, S., Loschberger, A., Klein, T., Heidbreder, M., Wolter, S., Heilemann, M., and Sauer, M. (2011). Direct stochastic optical reconstruction microscopy with standard fluorescent probes. *Nat Protoc* 6, 991-1009.
- Yoshida, K., Kondoh, G., Matsuda, Y., Habu, T., Nishimune, Y., and Morita, T. (1998). The mouse RecA-like gene Dmc1 is required for homologous chromosome synapsis during meiosis. *Mol. Cell* 1, 707-718.

## Supplementary Figures

A

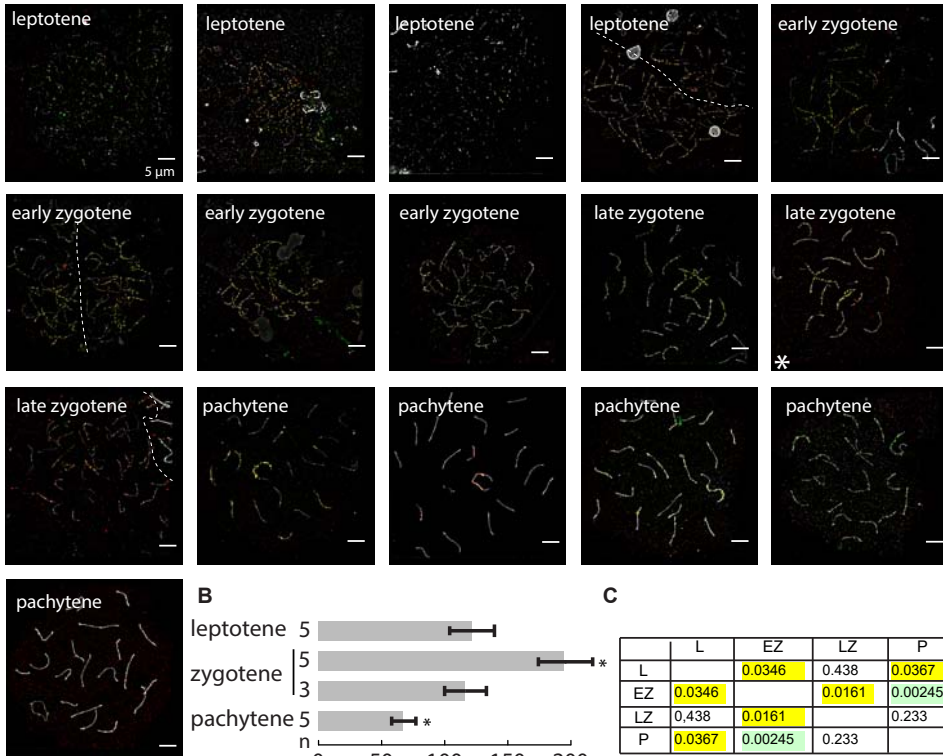


**Figure 1-figure supplement 1 Analysed wild type nuclei. A)** 3D-SIM images of the wild type nuclei analysed per stage. Nuclei were immunostained for RAD51 (green), DMC1 (red), and SYCP3 (white). In cases where two nuclei were imaged in the same field of view they are separated by a dashed line. Scale bars represent 5  $\mu$ m. **B)** Bar graph showing the average number of foci from wild type spermatocyte nuclei that were analysed in dSTORM per stage (leptotene, early-late zygotene, pachytene). The number of analysed nuclei per stage is indicated to the left of each bar. Error bars indicate SEM, asterisk indicate significant difference to all other stages ( $p < 0.05$ ). **C)** P-values for foci number comparisons between stages (yellow background;  $p < 0.05$ , green background  $p < 0.005$ )

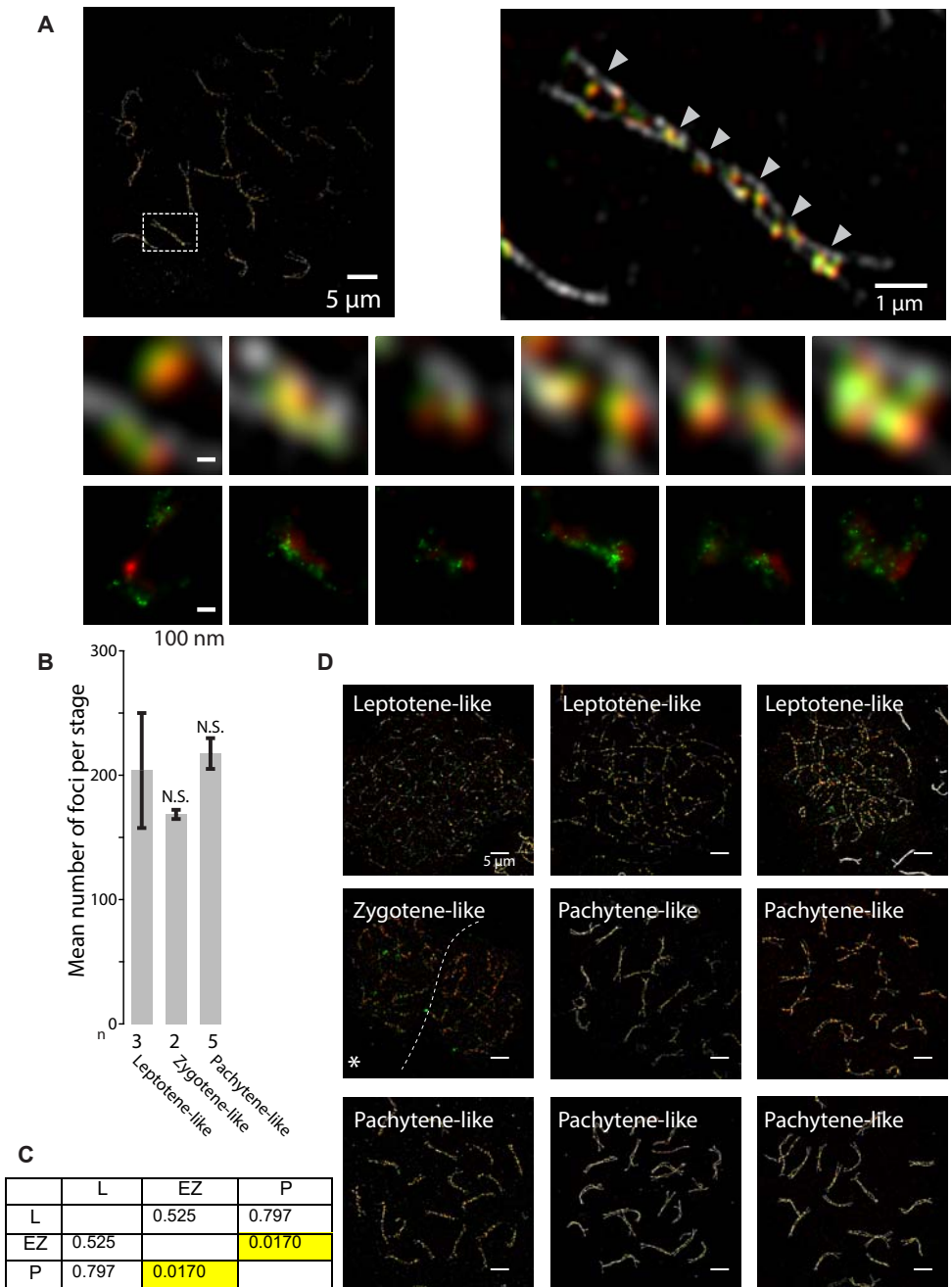


**Figure 2-figure supplement 1: Analysed *Sycp1*<sup>-/-</sup> nuclei.** **A)** 3D-SIM image of microspread pachytene-like meiotic nucleus from *Sycp1*<sup>-/-</sup> mouse immunostained with primary antibodies for RAD51, DMC1, and SYCP3, and appropriate secondary antibodies labelled with Alexa-488 (green), Alexa-647 (red), and Alexa-555 (white), respectively. The boxed region is shown to the right and the arrowheads mark regions shown in below. **B)** Bar graph showing the average number of foci from wild type spermatocyte nuclei that were analysed in dSTORM per stage (lepto- tene, early -late zygotene, pachytene). The number of analysed nuclei per stage is indicated underneath each bar. Error bars indicate SEM values. **C)** P-values for foci number comparisons between stages (yellow background; p<0.05, green background p<0.005). **D)** 3D-SIM images of the *Sycp1*<sup>-/-</sup> nuclei analysed per stage. Nuclei were immunostained for RAD51 (green), DMC1 (red), and SYCP3 (white).

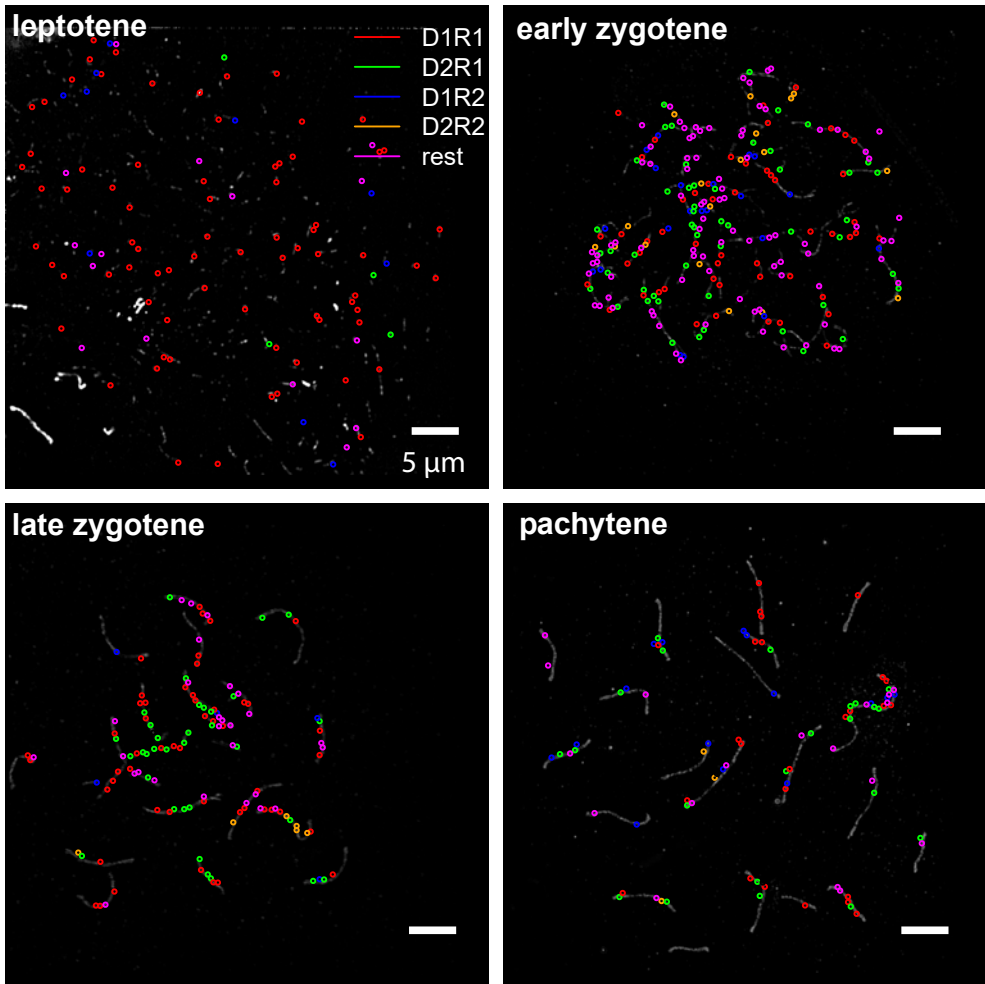


**Figure 3-figure supplement 1 Distribution of different DnRn configurations along the chromosomes of wild typespermatocytes.** The ROIs defined for a wild type leptotene, early zygotene, late zygotene and pachytene nucleus immunostained for RAD51, DMC1 and SYCP3 are superimposed on the SYCP3 SIM image (white). Red ROIs correspond to D1R1, green ROIs correspond to D2R1, blue ROIs to D1R2, yellow ROIs to D2R2 and magenta ROIs to the rest group of configurations. Scale bars indicate 5 μm.

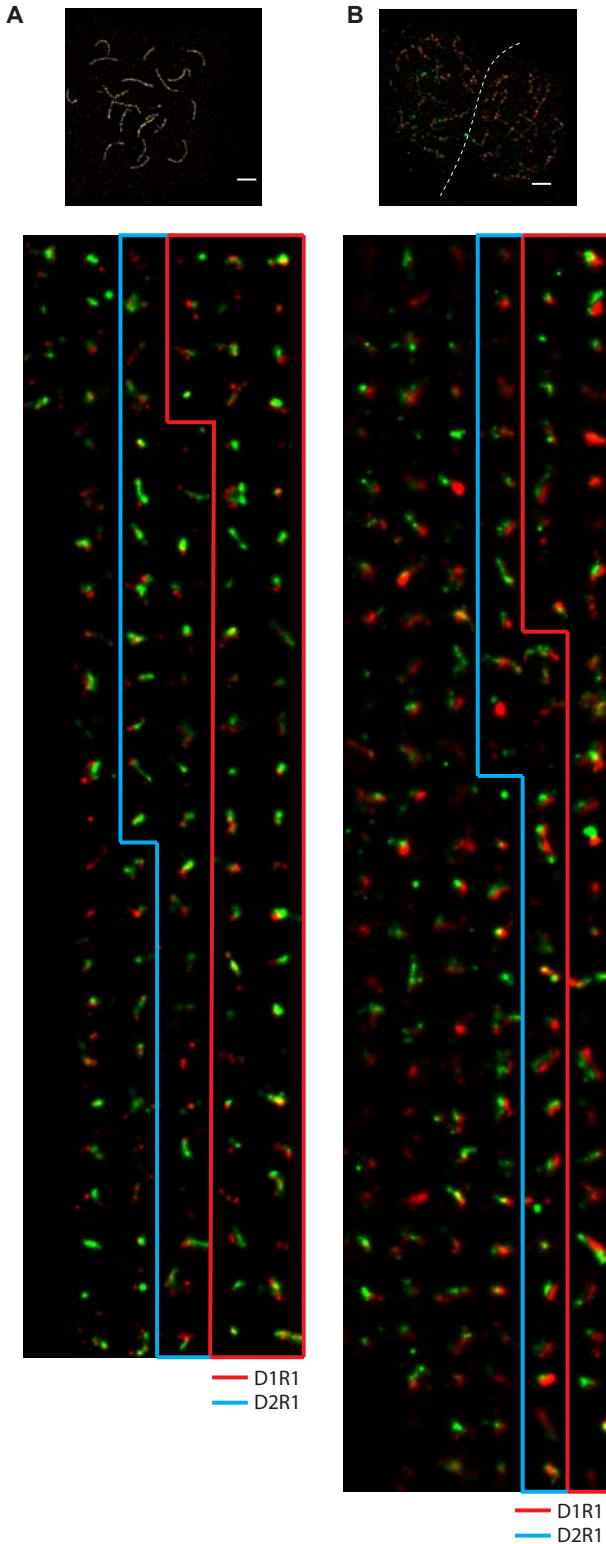


**Figure 5-figure supplement 1 Differential visual appearance of DnRn foci. A)** Wild type late zygotene nucleus and immunostained for RAD51 (green), DMC1 (red) and SYCP3 (white) with a compilation of all ROIs shown below. ROIs are sorted by their DnRn configuration, from most frequent to rare configuration. The boxes indicated the ROIs belonging to the D1R1 (red) and D2R1 (blue) configurations. The images are reconstructed with plotted Gaussian distributions proportional to the precision of the individual localisations. **B)** Two *Sycp1*<sup>-/-</sup> zygotene-like nuclei immunostained as indicated in (A) and a compilation of all ROIs of the left nucleus is shown below, as described for the wild type nucleus in (A).



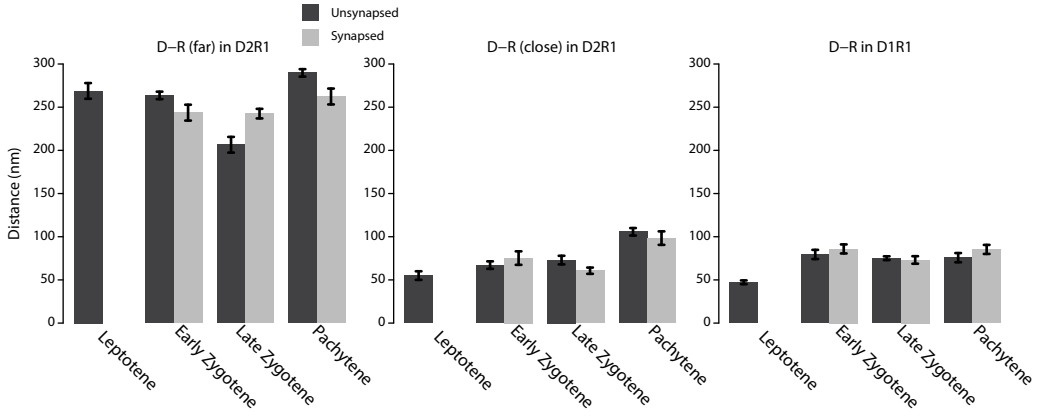


**Figure 5-figure supplement 2 Distances between DMC1 and RAD51 clusters per stage on synapsed and unsynapsed axes** Mean distances between the DMC1 and RAD51 clusters in D1R1 and D2R1 configurations per stage in wild type spermatocytes, distributed over synapsed or unsynapsed axes. Error bars indicate SEM.







## Chapter IV

# Architectural plasticity of human BRCA2-RAD51 complexes in DNA break repair

Humberto Sánchez<sup>1</sup>, Maarten W. Paul<sup>2,3</sup>, Małgorzata Grosbart<sup>1</sup>, Sarah E. van Rossum-Fikkert<sup>1,4</sup>, Joyce H. G. Lebbink<sup>1,4</sup>, Roland Kanaar<sup>1,4</sup>, Adriaan B. Houtsmuller<sup>2,3</sup>, and Claire Wyman<sup>1,4</sup>

<sup>1</sup> Department of Molecular Genetics, Cancer Genomics Center Netherlands, Erasmus University Medical Center, 3000 CA Rotterdam, The Netherlands

<sup>2</sup> Erasmus Optical Imaging Centre, Erasmus University Medical Center, 3000 CA Rotterdam, The Netherlands

<sup>3</sup> Department of Pathology, Erasmus University Medical Center, 3000 CA Rotterdam, The Netherlands

<sup>4</sup> Department of Radiation Oncology, Erasmus University Medical Center, 3000 CA Rotterdam, The Netherlands

*Published in Nucleic Acids Res. 2017*

## Abstract

The tumor suppressor BRCA2 is a large multi-functional protein mutated in 50-60 % of familial breast cancers. BRCA2 interacts with many partners and includes multiple regions with potentially disordered structure. In homology directed DNA repair BRCA2 delivers RAD51 to DNA resulting in removal of RPA and assembly of a RAD51 nucleoprotein filament. Dynamic rearrangements of BRCA2 likely drive this molecular hand-off initiating DNA strand exchange. We show human BRCA2 forms oligomers which can have an extended shape. Scanning force microscopy and quantitative single molecule fluorescence define the variety of BRCA2 complexes, reveal dramatic rearrangements upon RAD51 binding and the loading of RAD51 patches on single strand DNA. At sites of repair in cell nuclei, super-resolution microscopy shows BRCA2 and RAD51 arranged in largely separate locations. We identified dynamic structural transitions in BRCA2 complexes suggested to facilitate loading of RAD51 onto RPA coated single strand DNA and subsequent release of BRCA2.



## Introduction

Many proteins with regulatory roles, such as tumor suppressors like BRCA2, have regions of undefined structure sometimes described as intrinsically disordered. Not surprisingly due to its size and potentially disordered regions, the structure of the BRCA2 protein has been challenging researchers for more than two decades. Structural models obtained by X-ray crystallography have been determined for isolated parts of BRCA2. The DNA binding domain co-purified with the DSS1 (deleted in split-hand/split foot syndrome) protein and the BRC4 repeat fused with RAD51 show details of the interfaces between parts of BRCA2 and elements of the DNA recombination machinery (Pellegrini et al., 2002; Yang et al., 2002). Full length BRCA2 interacts with 5-6 RAD51 molecules (Jensen et al., 2010) and facilitates formation of RAD51 filaments on DNA to catalyze the strand exchange step of homologous recombination (HR) (Jensen et al., 2010; Liu et al., 2010; Thorslund et al., 2010). The arrangement of BRCA2 dimers associated with RAD51 and single stranded DNA (ssDNA) has been determined from electron microscopy (EM) image reconstruction (Shahid et al., 2014). BRCA2 associates with several additional partners including PALB2 that mediates interaction with BRCA1 (Siaud et al., 2011; Sy et al., 2009). BRCA2 function will require dynamic rearrangement of these molecular complexes facilitating partner exchange throughout the process of HR.

Here we investigate the global arrangement of BRCA2, changes upon RAD51 binding and loading on DNA using single-molecule visualization techniques *in vivo* and *in vitro*. Scanning force microscopy (SFM) reveals three-dimensional structures of biomolecules *in vitro* in conditions compatible with biochemical activity. Combining SFM with total internal reflection fluorescence microscopy (TIRF-SFM) (Sanchez et al., 2013) allows the identification and quantification of proteins in heterogeneous mixtures like the BRCA2-RAD51 complexes addressed here. In cells BRCA2 moves in the nucleus as oligomeric clusters together with RAD51 (Reuter et al., 2014). Using single molecule localization by direct stochastic optical reconstruction

microscopy (dSTORM) (Heilemann et al., 2008), we determined the arrangement of BRCA2, RAD51, and RPA in microscopically discernable structures (foci) formed in the cell nucleus after DNA damage induction. Although diffusing together, as reported previously (Reuter et al., 2014), BRCA2 and RAD51 were largely separated at sites of DNA repair, in patterns that changed over time. These results reveal biological functions of the BRCA2 protein machinery manifest as the structural transitions and dynamic interactions observed by single molecule imaging of biochemical samples and super resolution in cells.

## Results

### Human BRCA2 associates as oligomers

To study the architectural arrangements of BRCA2 protein, we purified full-length human BRCA2 protein fused with two maltose binding proteins (MBP) as described (Jensen et al., 2010). Visualization by SFM reveals the ensemble of BRCA2 complexes and their structural variation at nm resolution after deposition in conditions compatible with biochemical activity (10 mM HEPES [pH 8.2], 112 mM NaCl) and in the absence of fixation agents. A variety of BRCA2 oligomers were evident in SFM images, as previously observed EM images, from which prominent dimers were compiled for structure building (Shahid et al., 2014). BRCA2 complexes appeared as a heterogeneous population of branched elongated structures (Fig. 1A). SFM imaging provides an accurate representation of protein association in solution and distribution of multimeric states. (Janicijevic et al., 2003; Ratcliff and Erie, 2001) The volume and the skeleton length of individual BRCA2 protein complexes were used to estimate the number of monomers by a semi-automatic analysis routine (Sanchez and Wyman, 2015). The distribution of BRCA2 complexes (Fig. 1B), based on volume and skeleton length, had two main populations containing dimers, the most prominent, ( $1.6 \pm 0.4$  [SD] subunits) and likely tetramers or pentamers ( $4.6 \pm 2.8$  [SD]) with a skeleton length of  $179 \pm 114$  (SD) and  $403 \pm 132$  (SD)

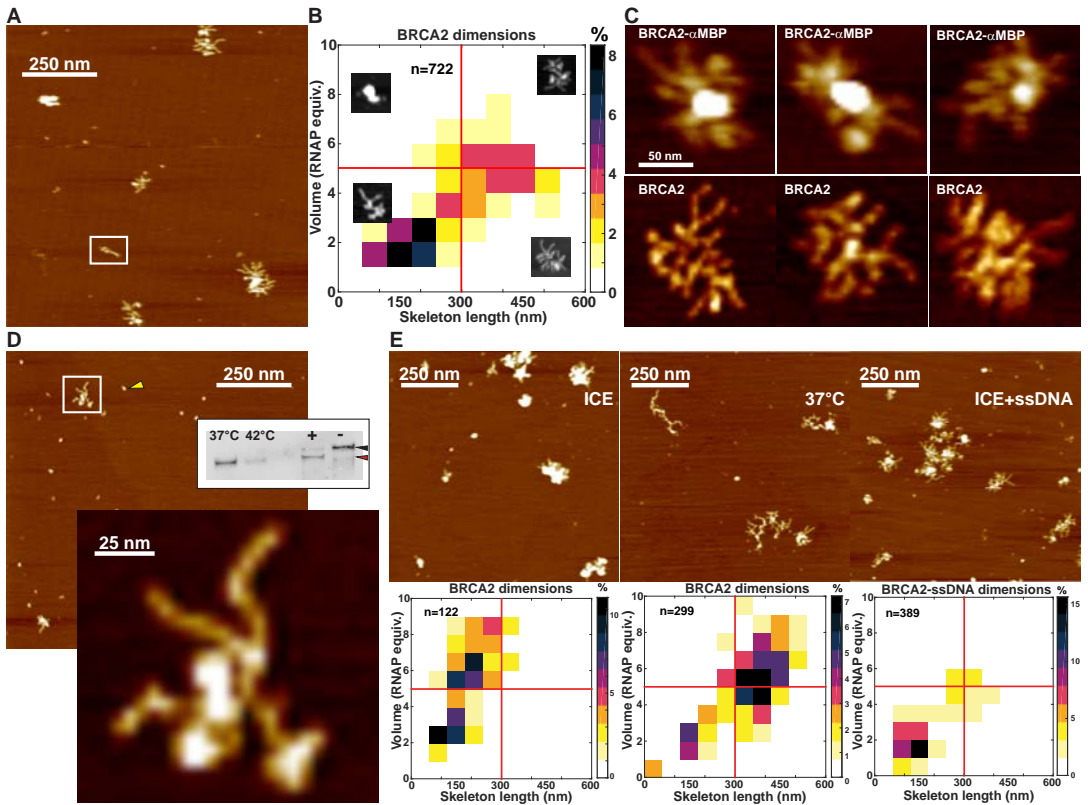


**Figure 1 Human BRCA2 associates in high-order oligomers that are temperature sensitive.** **A)** Representative SFM image of 2xMBP-BRCA2. Several complexes from monomers (example boxed) to higher order oligomers showing a characteristic V-shape. Image size 1 x 1  $\mu\text{m}$ . **B)** Distribution of complexes based on volume and length. All individual complexes from images similar to those shown in panel A were measured and their distribution plotted in a two dimensional histogram with bin size 60 nm x 1 RNAP equiv. One RNAP ( $\sim 450$  kDa) equals approximately one 2xMBP-BRCA2 (470 kDa). Color indicates percentage of total complexes analyzed as shown in the scale bar. Red lines are guides to view bins. Inset images are zoomed examples (shown at different scales) representative of complexes in quadrants defined by the red lines. **C)** SFM images of BRCA2 incubated with MBP antibody (upper row) compared to BRCA2 alone (bottom row). **D)** The MBP tag does not influence BRCA2 oligomeric structure. SFM image of BRCA2 (white square and zoomed view below) after cleavage of the MBP tags by incubation with PreScission protease. The small round particles (yellow arrowhead) in the background are either protease or cleaved tag. Inset shows Western blot verification of tag cleavage. Samples are: lane "+" after and "-" before protease incubation. Western blot control and size comparison are: lane "37°C" extracts from human BRO-derived melanoma cells showing endogenous BRCA2 which is as expected degraded as shown in lane "42°C". Black arrowhead: MBP tagged BRCA2; red arrowhead: untagged BRCA2. Color intensity indicates height (from 0 to 1.5 nm, dark to light). **E)** SFM images of BRCA2 and quantification of size distribution, in conditions as labeled; incubation on ice, *in situ* warming to 37°C, or incubation with 66 nt ssDNA.

nm, respectively. Isolated monomers of BRCA2 were up to 100 nm in length (example boxed in Fig. 1A). Inspection of the oligomeric complexes revealed an intriguing, recurrent protruding V-shape domain. One arm of the V was significantly shorter than the other ( $35 \pm 5$  [SD] nm vs  $44 \pm 6$  [SD] nm from 235 analyzed complexes,  $p < 0.05$  two-sample t-test). This arrangement could result from folding one BRCA2 monomer near the middle of the molecule, or an

association between two different monomers in parallel or antiparallel orientation with a small offset. Antibodies recognizing the MBP tags increased the volume in the center of the complex but not to the protruding ends of the elongated structures (Fig. 1C). This suggests that some of the C-terminal DNA binding domains could be protruding (see discussion). The association of BRCA2 into multimers and the arrangement of the elongated domains was independent of

MBP as the shape or distribution of forms was unchanged after removal of the tags (Fig. 1D).

The oligomeric and elongated appearance of BRCA2 suggested structural variability characteristic of proteins with intrinsically disordered regions. The structure of proteins with intrinsically disordered regions can vary dramatically due to relatively subtle change in conditions (Uversky, 2016). We tested the effect of incubation at different temperatures and addition ssDNA on BRCA2 complex architecture. Notably, the protein complexes assumed a largely globular shape if the sample was deposited from incubation on ice (Fig. 1E). This transition was readily reversible as *in situ* warming to 37°C of the sample on mica, or incubation on ice with linear ssDNA oligonucleotides before deposition for imaging, exposed the branched structures. This suggests that self-association among BRCA2 domains, resulting in globular or extended structures, is readily reversible and dynamically inconsistent with the behavior of intrinsically disordered regions.

### Structural plasticity of Human BRCA2

Primary sequence analysis predicts the frequent occurrence of segments along the BRCA2 amino acid sequence that can be described

as intrinsic disordered regions (IDRs) (Cortese et al., 2008; Oldfield and Dunker, 2014) (Fig. S1A-C). IDRs are often characteristic of flexible linkers involved in the assembly of macromolecular complexes (Oldfield and Dunker, 2014; Wright and Dyson, 2015). We compared the dimensions of the BRCA2 elongated structures with double-stranded DNA (dsDNA) and the coiled-coils of the RAD50 component of the human MRN complex (de Jager et al., 2001) visualized by SFM. Full width at high maximum (FWHM) of extended BRCA2 was similar to dsDNA or RAD50 coiled coils indicating a true width of 2 or 3 nm after accounting for SFM tip distortions (Bustamante et al., 1993). The apparent persistence length (PL) of elongated BRCA2 ( $17 \pm 1$  [SD] nm) was less than dsDNA ( $56 \pm 6$  [SD] nm) or RAD50 coiled coils (30 nm (van Noort et al., 2003)), showing the flexibility of BRCA2 as a polymer (Fig. S1D-E).

### BRCA2-RAD51 complexes are regular elongated structures

BRCA2 functions in HR associated with RAD51. To describe the arrangement and variation in BRCA2-RAD51 complexes we used TIRF-SFM (Sanchez et al., 2013) and compared fluorescent RAD51, hereafter RAD51, (Candelli et

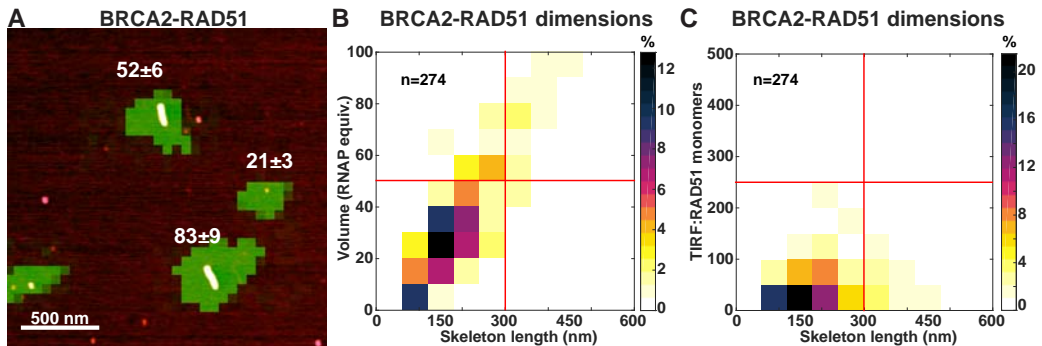


**Figure 2 BRCA2-RAD51 complexes organize into filament-like structures** **A)** RAD51-BRCA2 complexes visualized by combined SFM and fluorescence microscopy (TIRF-SFM). SFM scan overlaid with fluorescence image (green) of BRCA2 incubated with fluorescent RAD51 and cross-linked with glutaraldehyde. Numbers indicate RAD51 monomers  $\pm$  SD for the complexes shown. **B)** Volume and length of all complexes were measured and their distribution plotted in a two dimensional histogram with bin size 60 nm  $\times$  10 RNAP equiv. Color indicates percentage of total of complexes analyzed (n=274) as shown in the scale bar. **C)** Distribution of RAD51-BRCA2 complexes based on number of fluorophores (RAD51) and length. All complexes were measured and their distribution plotted in a two dimensional histogram with bin size 60 nm  $\times$  50 RAD51 monomers. Color indicates percentage of total complexes analyzed (n=274) as shown in the scale bar.



al., 2014; Modesti et al., 2007; van Mameren et al., 2009) (Fig. S2A), BRCA2 and a mixture of the two, in the absence of DNA and nucleotide cofactor. BRCA2-RAD51 complexes were formed at a molar ratio of 1:24 and visualized by TIRF-SFM, after fixation with glutaraldehyde (Fig. 2A). In the absence of fixation limited BRCA2-RAD51 complexes were observed by SFM, indicating interactions that are dynamic or transient in these conditions. The co-incubation resulted in protein complexes with an unanticipated filament-like appearance not apparent for either RAD51 or BRCA2 separately prepared with the same fixation protocol (Fig. S3). Analysis of TIRF-SFM images revealed filament like structures ranging from 30 nm to more than 500 nm long, and a main population with a volume equivalent to 20-30 RNAP equiv., including 50-100 RAD51 monomers based on fluorescence (Fig. 2B-C). The number of RAD51 monomers based on fluorescence intensity in BRCA2-RAD51 complexes was lower than in RAD51-DNA complexes with the same volume (see Materials and Methods and Fig. S2B for details of the quantification). The extra volume in the BRCA2-RAD51 complexes in the main population was equivalent to 12 to 26 BRCA2 monomers. Similar structures were observed using unlabeled RAD51 protein indicating that the regular elongated forms are not due to the fluorescent label (Fig. S4A). The elongated structures had an interrupted height profile repeating with  $51 \pm 67$  (SD) nm periodicity along their contour, indicating the end-to-end association of smaller complexes. For comparison dimeric BRCA2-RAD51 complexes reconstructed from EM images are roughly oval at 26.5 nm X 16.5 nm (Shahid et al., 2014). Additionally, BRCA2-RAD51 complexes were wider (FWHM =  $17.8 \pm 6$  [SD] nm) and stiffer (PL =  $698 \pm 338$  [SD] nm) than RAD51-dsDNA (FWHM =  $8.75 \pm 3.1$  [SD] nm, PL =  $91 \pm 11$  [SD] nm) filaments (Fig. S1D). Together the volume and fluorescence analysis of complexes observed by SFM indicated they consist of 4-5 RAD51 per BRCA2, similar to the stoichiometry of on average 4.5 to maximal 6 RAD51 per BRCA2 determined by biochemical methods (Jensen et al., 2010). The elongated structures indicated specific interactions, captured during fixation, resulting

regular, ordered multimers with a unit length of about 50 nm.

### Multiple patches of BRCA2-RAD51 load on ssDNA

The organization of RAD51 by BRCA2, in the absence of DNA, into higher order structures larger than those previously described (Shahid et al., 2014), suggested the possibility that RAD51 is loaded onto ssDNA in a manner distinct from the nucleation and growth mechanism commonly described (Candelli et al., 2014; Holloman, 2011; Shahid et al., 2014; van der Heijden et al., 2007; van Mameren et al., 2009). To observe the effect of BRCA2 on RAD51-DNA loading, we incubated ssDNA ( $\Phi$ X174 Virion) with fluorescent RAD51 alone (Fig. 3A) or with BRCA2-RAD51 (Fig. 3B) in the presence of ATP and  $Mg^{2+}$ , necessary cofactors for dynamic filament assembly. We used sub-saturating concentrations of RAD51 (1 monomer per 4 nt) to highlight the possible mediator effect of BRCA2. DNA-protein complexes with fluorescent RAD51 were visualized by TIRF-SFM after fixation with glutaraldehyde (Fig. 3A) and analyzed for volume and fluorescence intensity (Fig. S4B). In these conditions, RAD51 alone did not stably bind to ssDNA and the DNA appeared mainly free of protein (31 out of 37 DNA molecules, Fig. 3Ai) with unbound RAD51 in the background. Incubation of BRCA2 with RAD51 resulted in multiple RAD51 patches on all ssDNA molecules (Fig. 3Aii, iii). The amount of fluorescent RAD51 in these DNA-protein complexes was determined by TIRF-SFM (Fig. S4B). Volume analysis indicated that BRCA2 was included, in addition to RAD51 detected by fluorescence, in the DNA bound structures. For example, in the population with a volume equivalent to 30-40 BRCA2 monomers. and  $143 \pm 101$  (n=17) RAD51 monomers detected by fluorescence would include additional volume equivalent to 18-28 BRCA2 monomers. Both RAD51 and BRCA2 can bind ssDNA and either or both proteins could be bound in the complexes observed here. This striking association of RAD51 with DNA only in the presence of BRCA2 reflects the importance of the BRCA2-RAD51 complex for initiating DNA strand exchange.

The DNA-protein complexes observed by SFM, including RAD51 and BRCA2, had patches with regular features (Fig. 3Aiii). The average length of the patches, delineated by a decrease in the cross-section height or a kink in the contour was  $71 \pm 24$  (SD) nm (from 405 patches in 79 DNA-protein complexes). The dimensions of the DNA bound complexes (FWHM=  $13.9 \pm 6.7$  [SD] nm, height=  $3.8 \pm 1.5$  [SD] nm) were different from both the RAD51-dsDNA filaments (FWHM=  $8.75 \pm 3$  [SD] nm, height=  $2.5 \pm 0.6$  [SD] nm,  $n= 101$ ) and the BRCA2-RAD51 complexes (FWHM=  $17.8 \pm 6$  [SD] nm, height=  $2.4 \pm 0.9$  [SD] nm,  $n=123$ ). These dimensions, together with volume measurements and number of

RAD51 estimated from fluorescence, indicate that BRCA2 not only facilitates RAD51 loading on ssDNA but that interaction with ssDNA also induced partial release of BRCA2.

The apparent release of BRCA2 was more evident when the DNA protein complexes were visualized in the absence of fixation (Fig. 3B). Pre-incubation of the ssDNA with RPA (visualized in Fig. 3B without fixation) resulted in limited loading of RAD51 in the absence of BRCA2 (Fig. 3Bii, iii and Fig. S4E-F). Interestingly DNA electrophoretic mobility shift experiments suggest that BRCA2 could rearrange RPA on DNA (Fig. S4D, compare lanes 2 and 6). As expected, BRCA2 enhanced RAD51 loading onto RPA

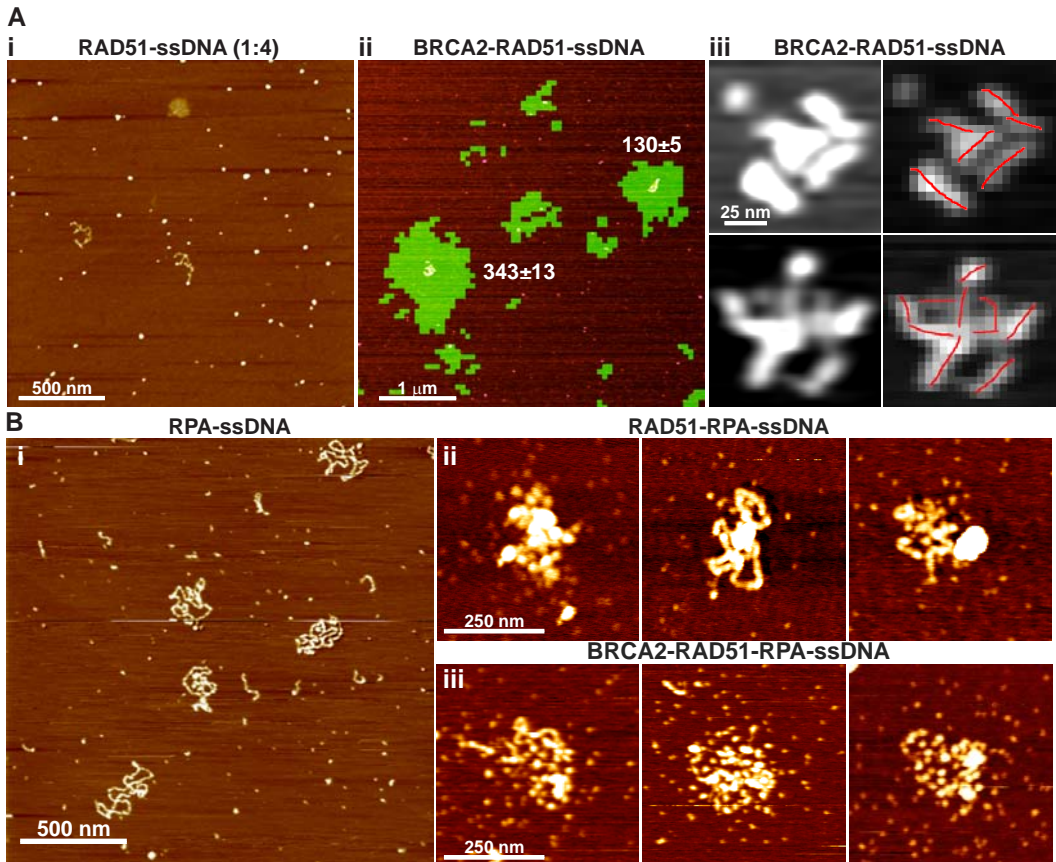


**Figure 3 BRCA2 oligomers mediate RAD51 hand-off to DNA. A)** Loading of RAD51 on DNA **(i)** SFM image of ΦX174 Virion ssDNA incubated with RAD51 and cross-linked with glutaraldehyde. Color intensity indicates height (from 0 to 3 nm). **(ii)** TIRF-SFM image of ΦX174 Virion ssDNA incubated with BRCA2-RAD51 and cross-linked with glutaraldehyde. **(iii)** Examples of multiple BRCA2-RAD51 complexes bound to ΦX174 Virion ssDNA from images similar to panel B. The patch length (red line) was analyzed with ‘SFMetrics’ **B)** Loading of RAD51 on RPA coated ssDNA **(i)** SFM image of ΦX174 Virion ssDNA incubated with RPA, visualized without fixation. **(ii)** RAD51-RPA-ssDNA complexes visualized by SFM without fixation. **(iii)** BRCA2-RAD51-RPA-ssDNA complexes visualized by SFM without fixation.

coated ssDNA (Fig. 3B and Fig. S4E-H). About 2 fold more RAD51 was loaded onto ssDNA pre-incubated with RPA in the presence of BRCA2,  $137 \pm 42$  (SD) vs  $69 \pm 42$  (SD) RAD51 monomers per DNA molecule (Fig. S3F, H). The resulting protein DNA complexes also appeared very different from those formed on ssDNA alone. BRCA2 loaded RAD51 was more evenly distributed loaded onto RPA-ssDNA, not in defined patches (compare Fig. 3Aiii to Fig. 3Biii). In addition, based on fluorescence intensity estimates of RAD51 monomers and volume, BRCA2 was largely absent from these complexes (Fig. 3B). The architectural rearrangements and molecular hand-off of RAD51 from BRCA2 to DNA was apparently enhanced by interaction with RPA.

### Distinct arrangements of BRCA2 and RAD51 at DNA damage sites in the cell nucleus

With conventional microscopy resolution RAD51 and BRCA2 are reported to co-localize at sites of DNA damage (Bekker-Jensen et al., 2006; Krawczyk et al., 2011; Reuter et al., 2014). However our *in vitro* results suggest that BRCA2 and RAD51 may separate once RAD51 is loaded onto DNA. To determine the arrangement of BRCA2, RAD51 and RPA in the nucleus of U2OS cells after DNA double-strand break induction, we used single molecule localization microscopy (dSTORM). This provides localization accuracy relevant to molecular dimensions. Typical accumulations of RAD51, often referred to as DNA repair foci, were clearly visible by fluorescence confocal microscopy (Fig. S5A and S6A). Localization of individual molecules by dSTORM revealed that RAD51 focal accumulations were frequently elongated some more than 400 nm long (Figure 4A-C). Subsequent two-color dSTORM imaging revealed that BRCA2 localizations were relatively diffuse with several clusters around the elongated RAD51 accumulations (Fig. 4C). As expected from their relative nuclear concentration (Reuter et al., 2014) and likely interaction stoichiometry (Jensen et al., 2010) most BRCA2 clusters were smaller than RAD51 clusters, including fewer localizations.

The relative location of BRCA2 and RAD51 was analyzed quantitatively (Fig. 4C-E, S5). Each

RAD51 focus was oriented with its long axis vertical with the most intense signal up and an overlay of all foci was compiled (Fig. 4E, see also Fig. S5E). BRCA2 localizations (magenta) were not concentrated in the center but clearly spread around the central RAD51 cluster. The spatial overlap between two different protein species in single molecule localization microscopy can be studied by quantifying the abundance of localizations of the one protein near localizations of the other (Rossy et al., 2014). Here the fraction of RAD51 localizations that overlapped with the BRCA2 was quantified by counting the number of BRCA2 localizations within a radius of 50 nm from every RAD51 localization (Fig. S5C-D). From this a fraction of overlapping RAD51 localizations can be calculated for every DSB focus. For each time point after DNA damage induction by ionizing irradiation (IR) we classified foci based on the fraction of overlapping BRCA2 and RAD51 they included and plotted their distribution in histograms (Fig. 4D). As can be seen at all 3 time points after IR (0.5, 2 and 6 hours) most foci included at least some RAD51 signal that was not overlapping with the BRCA2 signal (cumulative total of all histogram bars except fraction overlapping = 1.0). At 0.5 hr after inducing breaks, with 6 Gy ionizing irradiation, the most frequent class of foci had no overlap in BRCA2 and RAD51 (30%). This pattern changed in time after irradiation. The proportion of foci with most BRCA2 and RAD51 overlapping (histogram bin at 0.8 to 1.0 fraction overlapping) increased at 2 and 6 hours. In comparison similar two-color dSTORM imaging for RPA and RAD51 showed a different distribution within foci with varying overlap (Fig. 4F, S6C-D). As a control for our imaging, analysis methods and comparison of the histogram presentations, we stained RAD51 with a mixture of secondary antibody labeled with two different dyes which showed almost complete overlap in signal, as expected (Fig. 4G). We have reliably quantified the relative distribution of different proteins in DNA damage include foci, where BRCA2 and RPA were often separated from RAD51. Changes in these patterns can be correlated to dynamic interactions during the DNA repair process and used to test biological function.

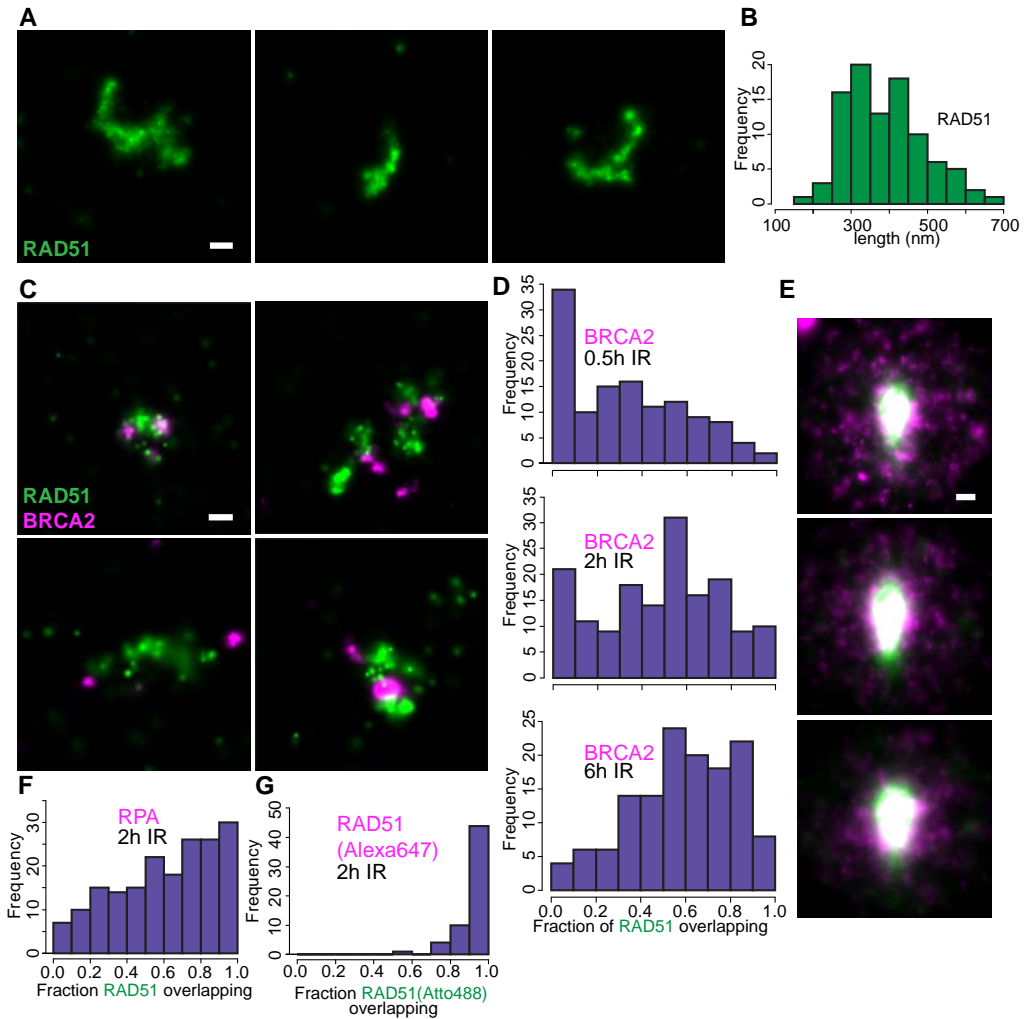


**Figure 4** BRCA2 and RAD51 have differential localization patterns in ionizing radiation induced foci. **A)** Super resolution (dSTORM) images of RAD51 foci detected by immunofluorescence in U2OS cells fixed 2 hours after treated with 6 Gy of ionizing radiation (IR). **B)** Distribution of the RAD51 structures based on length of the major axis. **C)** Examples of repair foci RAD51 (green, Atto488 conjugated secondary antibody) and BRCA2 (magenta, Alexa647 conjugated secondary antibody) acquired with dSTORM. **D)** RAD51 localizations that overlap with BRCA2 were determined for every ROI (focus) and the distribution of foci based on fraction overlapping signals plotted in a histogram (Fig.S4D). ( $n = 15, 11, 11$  cells respectively). **E)** Summed projections of dSTORM images of repair foci aligned and rotated based on the RAD51 (green) signal, show the BRCA2 (magenta) signal spread around RAD51. Images represent the same time points as in D. **F)** The distribution of foci based on fraction of overlapping signals for RAD51 and RPA. **G)** As a control cells were stained for RAD51 and two different secondary antibodies showing, as expected, all foci with near complete overlap of signals in this analysis. Scale bars indicate 100 nm.

## Discussion

We have determined the relative arrangement of essential DNA break repair proteins, BRCA2, RAD51 and RPA, in complexes on DNA from purified components and in the cell nucleus. These data identify steps in the molecular choreography of assembling functional repair

machinery where it is needed. BRCA2 alone displays variable structures, depending on mild changes in conditions and to binding partners, features characteristic of proteins including intrinsically disordered regions. Binding to RAD51 induces dramatic reorganization into a regular complex capable of multimerization and active

in loading RAD51 onto ssDNA. We observe at least partially release of RAD51 from BRCA2 to DNA in the presence of RPA. Super-resolution imaging in cell nuclei also indicated that BRCA2 and RAD51 separate at the sites of DNA damage. BRCA2 however remained in the area of the DNA damage, as also observed in foci with standard microscopy, possibly indicating a role late in DNA break repair.

BRCA2 is responsible for delivering RAD51 to sites of DNA breaks in the nucleus. As such it has to scan nuclear volume for sites where its action is needed. At an approximate concentration of 10 nM, in the range estimated for BRCA2 and several other DNA repair proteins in the cell nucleus (Essers et al., 2002a; Ghaemmaghani et al., 2003; Reuter et al., 2014), each protein would have to search volumes equivalent to a sphere with radius of about 300 nm. Our direct SFM visualization shows that BRCA2 oligomers can adopt an extended configuration spanning up to several hundred nanometers. BRCA2 oligomers in this conformation effectively tether multiple C-terminal DNA binding domains. In addition association with multiple RAD51 monomers effectively provides additional DNA binding domains tethered in close proximity. These features would facilitate an effective search for DNA damage sites in the nucleus via frequent non-specific interactions (Reuter et al., 2014). BRCA2 regions characterized as intrinsically disordered could allow fluctuating inter- and intra-molecular associations with low entropy cost promoting conformational flexibility and functional exchange of binding partners (Shoemaker et al., 2000). Intrinsically disordered regions of BRCA2 may also facilitate its accumulation via interaction with poly(ADP-ribose) which has been suggested to seed the accumulation of intrinsically disordered proteins at the sites of DNA breaks (Altmeyer et al., 2015).

*In vitro* single-molecule experiments have extensively studied the DNA binding behavior of RAD51 (Candelli et al., 2014; Hilario et al., 2009; van der Heijden et al., 2007; van Mameren et al., 2009) where filament formation is described as a two-steps process involving nucleation and growth. Our previous live cell imaging data (Reuter et al., 2014) indicated that most,

if not all, nuclear RAD51 is traveling in complex with BRCA2 suggested that filament formation *in vivo* may be dominated by these complexes and not free RAD51. We show here that BRCA2 transforms RAD51 into a stiff multimeric DNA binding complex offering potential mechanistic advantages. The BRCA2-RAD51 complex is essentially a multimeric DNA binding complex that would facilitate loading of RAD51 onto ssDNA in competition with proteins like RPA (Jensen et al., 2010; Liu et al., 2010; Thorslund et al., 2010). Although RAD51 *in vitro* can displace RPA on ssDNA, we note that *in vivo* the relative concentrations of these proteins likely make this ineffective. Modification of RAD51 by phosphorylation mitigates the need for mediators to replace RPA *in vitro* (Subramanyam et al., 2016). However if post-translational modification not occur effectively after filament formation, additional help to replace RPA initiating filament formation would be needed. Even a single BRCA2 comprising three OB folds and multiple RAD51s forms a multimeric ssDNA binding complex that we suggest could effectively compete away ssDNA-bound RPA without the need of direct interaction between BRCA2 and RPA (Sing et al., 2014). The complete dependence on BRCA2 for loading RAD51 on ssDNA in the absence of RPA, observed here with limited RAD51 (Fig. 3), possibly suggests an additional role for this complex unfolding ssDNA secondary structures. In combination BRCA2-RAD51 complexes serve a series of functions: catching RPA-ssDNA, using the BRCA2 DNA-binding domains to promote replacement of RPA for RAD51, and delivering multiple RAD51 molecules for efficient filament formation (Fig. S4G). We anticipate that the intrinsically disordered regions of BRCA2 are essential for dynamic structural rearrangements that catalyze molecular hand-off events in the cell nucleus.

Although all detectable RAD51 diffuses in the cell nucleus in complex with BRCA2 (Reuter et al., 2014) release to load RAD51 onto DNA at break sites is expected *in vivo*. The accumulation of DNA break repair proteins at sites of damage in the cell nucleus has been extensively studied by fluorescence microscopy. After DNA breaks are induced, proteins needed to perform

DNA strand exchange in HR reorganize by rapidly associating in clusters, or repair foci, in a BRCA2 dependent manner (Tarsounas et al., 2003). The limited resolution of standard light microscopy is unable to resolve the relative arrangement of RAD51, BRCA2, and other repair proteins in foci that all appear as (overlapping) spherical clusters. The increased resolution of dSTORM, acquired by separating the fluorescence signal of individual molecules, enables accurate localization of single molecules in densely labeled samples. We present here super resolution images of RAD51, BRCA2 and RPA detected by immuno-fluorescence in DNA damage induced foci. We observe RAD51 arranged in an elongated patterns, up to several 100 nm long. Though there is no independent evidence that these structures are RAD51-DNA filaments, this elongated appearance is expected for a protein that coats DNA, in a filament. The length of the elongated RAD51 structures is reasonable given that 450 nm (approximate median of the distribution Fig. 4B) is equivalent to a perfect RAD51-DNA filament including 900 nt of DNA and 300 RAD51 molecules (note number of localizations does not equal number of molecules in our super-resolution methods employing indirect immunofluorescence staining and detection of fluorophore blinking).

Our immunofluorescence experiments show distinct patterns of BRCA2, RAD51 and RPA in DNA damage induced foci. The RAD51 primary antibody used is polyclonal and will recognize many epitopes or presentations of RAD51. The monoclonal BRCA2 antibody recognizes one of the RAD51 binding BRC repeats. It is possible this epitope is not as efficiently recognized if RAD51 is bound to some of the BRC repeats in BRCA2. Even if all BRCA2 is not detected all RAD51 should be detected whereby the distinct pattern of RAD51 and BRCA2 reveal different dynamic arrangements at DNA breaks sites. At the earliest times analyzed after damage (0.5 hr) BRCA2 is in small clusters separated from most of an elongated, much larger RAD51 cluster (Fig. 4D-E) consistent with a molecular hand-off upon loading RAD51 onto DNA. However, hand-off does not lead to BRCA2 absence from the foci, as BRCA2 clusters are observed

also at later stages (2 and 6 hours after damage induction). This suggests a role for BRCA2 beyond delivering RAD51 and that BRCA2 and RAD51 may re-associate before leaving the site of DNA damage.

In our super resolution images the RPA signal is also largely separated from RAD51 as expected if RAD51 replaces RPA bound to DNA (Fig. 4F and S6C). Interestingly we observe both BRCA2 and RPA are present at the RAD51 damage induced foci at all three time points after damage induction. The retention of RPA at DSBs has been observed in yeast by CHIP, both at the DNA break site and at repair donor locus (Wang and Haber, 2004). We observe RPA in dense clusters, with large number of localizations, in contrast to RAD51, which is present in an extended pattern. As is the case for the DNA repair foci observed with conventional microscopy, there is no proof that the foci presented here with dSTORM represent DNA bound proteins; however their patterns are consistent with the different roles of these proteins and the structures they are expected to form on DNA.

The relative patterns of BRCA2 and RAD51 change over time after DNA damage (Essers et al., 2002b). Here we observe specifically that localization of BRCA2 and RAD51 within 50 nm of each other is more common at later times, 2 and 6 hr after damage induction. At the dose of DNA damage inflicted, some of the damage is irreparable and some cells will eventually die. Thus the later time points may represent repeated attempts to repair or stalled repair. The increased association of BRCA2 and RAD51 in time may represent additional BRCA2 functions, stabilizing RAD51 association with broken DNA or more intriguingly an active role in removal of RAD51 after repair. Distinguishing these possibilities awaits further analysis and the ability to follow a repair event over time. However the ability to define and quantify relative protein arrangements demonstrates the power of our analysis to determine function in cells during the DNA repair process. We propose that the malleable nature of BRCA2, including multiple intrinsically disordered domains, facilitate its functions to locate break sites in nuclear space, exchange RPA for RAD51 on ssDNA and deliver

RAD51 as multimeric complexes for efficient assembly of strand exchange machinery.

## Materials and Methods

### Proteins, DNAs, and bulk assays

BRCA2 tagged with two tandem repeats of the maltose binding protein (MBP) at the N-terminus was purified after transient transfection of human embryonic kidney 293T cells with pCMV1 plasmid containing the full length BRCA2 gene (kindly provided by S. Kowalczykowski) as described (Jensen et al., 2010). Aliquots of BRCA2 with concentration range 50-100 ng/ml (as estimated using extinction coefficient at 280 nm of  $365,160 \text{ M}^{-1} \text{ cm}^{-1}$ ) were stored at  $-80^\circ\text{C}$  in elution buffer from the final purification column (50 mM HEPES [pH 8.2], 10% glycerol, 450 mM NaCl, 1 mM DTT, 0.5 mM EDTA). Protein identity was confirmed by mass spectrometry (ErasmusMC Proteomics) and Western blotting (see below). BRCA2 protein was purified by three different persons in the laboratory producing four distinct stocks used for the SFM characterization. Prediction of intrinsic disordered regions in primary sequence was done using two different prediction web tools: IUPred (<http://iupred.enzim.hu>) (Dosztanyi et al., 2005; Fukuchi et al., 2011) and DisEMBLTM (<http://dis.embl.de>).

Human RAD51 and RPA were expressed in *Escherichia coli* and purified as described (Henricksen et al., 1994; Modesti et al., 2007). RAD51 with a single cysteine exposed to the solvent was Alexa Fluor 488 (Invitrogen) labeled (degree of labeling 1.3) using maleimide chemistry and checked for biochemical activities (ATPase and D-loop formation) as described (Candelli et al., 2014; Modesti et al., 2007).

*E. coli* RNA polymerase (Boehringer Mannheim) was used as SFM size calibration standard.

Linear ssDNA (1000 bases) molecules were generated by PCR amplification of pBluescript DNA and degradation of one strand with lambda exonuclease I as described (Sanchez et al., 2013). Circular ssDNA (5386 bases)  $\Phi\text{X174}$  Virion DNA was purchased from New England Biolabs. Oligonucleotide sequence of the 66-mer

was as described (van der Linden et al., 2009).

Electrophoretic mobility shift assays (EMSA) were done by mixing Cy5-labeled 90 nt ssDNA (Mazin et al., 2000) (90 nM in nt) with or without RPA (60 nM) in reaction buffer (50 mM Tris-HCl [pH 7.5], 1 mM DTT, 60 mM KCl, 2 mM  $\text{CaCl}_2$ , and 1 mM ATP) for 10 min at  $37^\circ\text{C}$  in a final volume of 10  $\mu\text{l}$ . Then RAD51 (300 nM), BRCA2 (20 nM), a mixture of both, or protein storage buffer was added and incubation continued for additional 20 min. The reactions products were separated on a 5% non-denaturing polyacrylamide gel running in  $0.5\times$  TB buffer at  $4^\circ\text{C}$ . Gels were analyzed using a Typhoon Trio scanner exciting the dye-coupled DNA.

### MBP cleavage, and immunodetection of BRCA2

Purified 2xMBP-BRCA2 aliquots ( $\sim 1 \text{ mg}$ ) were incubated with 2 units of PreScission protease (GE Healthcare) or with protease storage buffer for 1 hr at  $4^\circ\text{C}$ . Reaction mixture was split for immunodetection and SFM imaging. Samples were run on a 3-8% NuPAGE Tris-Acetate gel (LifeTechnologies), which was blotted on PVDF membrane (Immobilon) for 2 hrs at  $4^\circ\text{C}$  at 300 mA. After 1 hr blocking with 5% milk, the membrane was incubated with the primary antibody Anti-BRCA2 OP95, Calbiochem, 1:2000 dilution in 1% milk and 0.1% PBS buffer) overnight at  $4^\circ\text{C}$ . The secondary antibody (Anti-mouse HRP, Abcam, 1:2000 dilution in 1% milk and 0.1% PBS buffer) was incubated for 2 hrs at room temperature. The membrane was exposed with ECL (Pierce) and imaged with an Uvitec Alliance 2.7 instrument (Cambridge, UK). Cellular extracts from human BRO-derived melanoma cells treated for hyperthermia (a gift from H. Odijk) were used as molecular weight markers for endogenous BRCA2 identification (Krawczyk et al., 2011). The protease reaction mixture was diluted ten times in BRCA2 storage buffer for SFM visualization in order to reduce background from protease molecules.

### SFM microscopic analysis of protein, and protein-DNA complexes

Samples were imaged in air at room temperature by tapping mode SFM using a Nanoscope

III or Nanoscope IV (Digital Instruments). Silicon Pointprobe tips were type NHC-W, resonance frequency 310-372 kHz, from Nanosensors supplied by Veeco Instruments, Europe. Images were collected at 2  $\mu\text{m}$  x 2  $\mu\text{m}$ , 512 X 512 pixels, and processed only by flattening to remove background slope.

BRCA2 protein was diluted four times from the frozen stock with HEPES buffer (final composition: 10-25 ng BRCA2, 22 mM HEPES [pH 8.2], 2.5% glycerol, 112 mM NaCl, 0.25 mM DTT, 0.12 mM EDTA). After incubation at 37°C or on ice, as described in the text, 50  $\mu\text{M}$  spermidine was added as binding agent and the protein deposited on freshly cleaved mica for 1 min, washed 3 times with MilliQ water and dried with filtered air.

The volume, length, and contour profile (width and height) measurements were done using 'SFMetrics' software tool as described (Sanchez and Wyman, 2015). Measurements are reported together with associated standard deviations. The volume of each complex was normalized to *E. coli* RNA polymerase (RNAP) with a known molecular weight of 450 kDa that appeared in SFM as regular round objects. In order to characterize the shape of the complex the minimum length occupied by each complex, defined as skeleton length, was measured. The contours of V-shape domains of BRCA2 oligomers were traced manually.

Purified 2xMBP-BRCA2 protein (~1  $\mu\text{g}$ ) was incubated with Anti-Maltose Binding Protein antibody ( $\alpha$ -MBP ab9084, Abcam) (250 ng) for 50 min at 37°C. Unbound antibody was removed by size exclusion chromatography (Sephacrose CL-4B, Sigma). Fractions containing BRCA2- $\alpha$ -MBP complexes were visualized by SFM.

Apparent persistence length ( $P_l$ ) was obtained assuming a worm-like chain model for semi-flexible polymers. In two dimensions (2D), the mean square of the end-to-end distance ( $R$ ) can be written as a function of the contour length ( $C_i$ ) and  $P_l$ :

$$\langle R^2 \rangle_{2D} = 4P_l C_i \left( 1 - \frac{2P_l}{C_i} \left( 1 - e^{-\frac{C_i}{2P_l}} \right) \right)$$

L measurements and P calculation were performed using 'Easyworm' software tool (Lamour

et al., 2014) from more than 100 complexes in each case.

Automatic peak-to-peak analysis was performed using 'peakfinder.m' MATLAB script (by Nathanael C. Yoder) and returned peaks at local maxima that were at least a half standard deviation of the sample above surrounding data and larger than the mean of the sample.

For in situ warming of BRCA2, mica containing the sample was placed on a Dry Block Thermostat UBD (Grant Instruments) at 37°C for 30 min.

Interactions between protein and DNA were performed in solution at the indicated concentrations before the sample was deposited on mica. When indicated sample was cross-linked with glutaraldehyde (0.12 %) for 5 min at 37°C, quenched with 50 mM Tris-HCl [pH 7.5], and deposited in the presence of 10 mM  $\text{Mg}^{2+}$ . BRCA2-RAD51 elongated complex were selected based on eccentricity above 0.7 (ratio of the distance between the foci of the ellipse modelling the protein complex and its major axis length).

### Sample preparation for TIRF-SFM visualization

Nucleoprotein filaments were formed by incubating linear ssDNA (1000 bases, 1.5  $\mu\text{M}$ ) molecules with RAD51 (1  $\mu\text{M}$ ) in binding buffer (10 mM HEPES [pH 8.2], 60 mM KCl, 2 mM  $\text{CaCl}_2$ , 1 mM DTT, and 1 mM ATP) (Modesti et al., 2007; Sanchez et al., 2013). BRCA2-RAD51 complexes were formed by incubating an excess of RAD51 (0.6  $\mu\text{M}$ ) with BRCA2 (0.025  $\mu\text{M}$ ) in buffer containing 12.5 mM HEPES [pH 8.2], 4 mM Tris-HCl [pH 7.5], 3.25% glycerol, 125 mM NaCl, 65 mM KCl, 0.4 mM DTT, 0.17 mM EDTA, taking into account contributions from all protein storage buffers. This reaction buffer composition was kept constant in all subsequent incubations unless noted. After 30 min at 37°C, glutaraldehyde was added to a final concentration of 0.12%, followed by additional 5 min incubation, and quenched by adding Tris-HCl to a final concentration of 50 mM [pH 7.5]. The sample was diluted (from 1:20 to 1:200 in order to reduce fluorescent signal due to free RAD51) in deposition buffer (10 mM HEPES-KCl [pH 8.2], 10 mM  $\text{Mg}_2\text{Cl}$ ) and deposited with 3



pM TransFluospheres on cleaved mica mounted on glass cover slips, as previously described (Ristic et al., 2011; Sanchez et al., 2010; Sanchez et al., 2013). After one minute the mica surface was rinsed with MilliQ water and dried with filtered air. RAD51 loading onto DNA was also analyzed in ATP hydrolysis conditions by supplementing the filament formation reaction described above with 1 mM ATP and 2 mM Mg<sub>2</sub>Cl (ATPase-Buffer). Circular ssDNA ΦX174 Virion DNA (2.4 μM in nt) was incubated with RPA (0.1 μM). When indicated RPA-DNA complexes were incubated with preassembled BRCA2 (0.025 μM)-RAD51 (0.6 μM) in ATPase-Buffer. Glutaraldehyde was added as indicated. Concentrations indicate final amount in the reactions. Samples were deposited for TIRF-SFM as described above and observed with a Nikon TE 2000U microscope as described (Sanchez et al., 2013). Scanning force microscopy was done with a NanoWizard®II scanner (JPK instruments) mounted on the fluorescence microscope (Ristic et al., 2011; Sanchez et al., 2010; Sanchez et al., 2013). Correlation of fluorescence and topographic images was done with the JPK DirectOverlay™ software tool. Data analysis was performed with custom-made software written in MATLAB and available in <http://cluster15.erasmusmc.nl/TIRF-SFM-scripts>.

### Quantification of fluorescent RAD51 monomers

The number of RAD51 monomers per complex was determined by quantification of fluorescence intensity by using the stepwise photobleaching of single fluorophores. In order to compensate for intensity variations due to differences in sample thickness, or constrains in the degrees of freedom of the fluorophore because of sample deposition on mica, a global estimation approach was used. Intensity of one fluorophore was defined per each field of view (FOV) after averaging the intensity steps in every region of interest (ROI) as follows; sequential frames (exposure time of 300 ms) from the same FOV were acquired until photobleaching of almost all fluorophores. This stack of images was used to make a maximum intensity projection (Figure S2Ai) that creates an output image

where each pixel contains the maximum value over all images in the stack at the particular pixel location (Figure S2Aii). From each ROI the intensity trace over time was extracted from a sequence of 300 frames where only a few fluorophores remained blinking until complete bleaching. Intensity variations were estimated by a step fitting algorithm (Kerssemakers et al., 2006; Sanchez et al., 2013; van Mameren et al., 2009) (Figure S2Aiii, iv). Step sizes smaller than background and bigger than two times the median value were discarded from the analysis. The reported number of fluorophores is the maximum intensity in the ROI divided by the mean of average step sizes for each ROI (Figure S2Av, vi).

Stable nucleoprotein filaments with defined components were formed with RAD51 and 1000 nt ssDNA in the presence of ATP-Ca<sup>2+</sup> (Fig. S2Bi). A perfectly formed RAD51 filament on this length DNA would consist of a maximum of 333 monomers (one RAD51 per 3 nucleotides) with a maximum length of 400 nm. Two-dimensional histograms in Fig. S2Bii and iii show the varied population of filaments formed in these conditions (partially covered, fully covered, and association of more than one filament) as previously observed (Modesti et al., 2007; Ristic et al., 2005; Sanchez et al., 2013). For example, in the filaments grouped between 360 and 420 nm length, the main population (5 % of the total) had a volume of 30 to 40 RNAP equiv., representing 365 to 489 RAD51 monomers, and 200 to 300 fluorophores as estimated by optical microscopy. Taking into account that volume can be overestimated due to tip distortions (Bustamante et al., 1993), and fluorescence intensity underestimated because of surface-fluorophore interaction (Sanchez et al., 2013), our data is in reasonable agreement with the expected 333 RAD51 monomers per fully covered DNA molecule showing the consistency of our TIRF-SFM approach for protein quantification.

### Cell culture (for super resolution microscopy)

U2OS cells were cultured in phenol-red free DMEM (Lonza) medium supplemented with 10% FCS, L-glutamine and Pen-Strep. For

microscopy experiments cells were cultured on 24 mm round coverslips of 1.5 thickness (170 ± 5 µm). Cells were irradiated the next day with 6 Gy of ionizing radiation using a <sup>137</sup>Cs source.

### Immunostaining and sample preparation

After washing with PBS cells were fixed at the indicated time points with 2% PFA in PBS (Lonza) for 20 minutes, permeabilized with PBS with 0.1% Triton and blocked with PBS+ (0.5% BSA and 0.15% glycine). Primary antibodies were incubated at room temperature for two hours in PBS+. Primary antibodies used for those experiments were: anti-RAD51 (rabbit polyclonal) (van Veelen et al., 2005), mouse monoclonal anti-BRCA2 (OP95, Calbiochem) and mouse monoclonal anti-RPA32 (ab2175, Abcam). For single color dSTORM experiments RAD51 antibody was directly conjugated with Alexa647 using APEX Antibody Labeling Kit (Molecular Probes, Thermo Scientific). For dual color dSTORM experiments secondary antibodies were used.

After multiple washing steps with PBS with 0.1% Triton coverslips were incubated for 1 hour with secondary antibodies recognizing either rabbit or mouse immunoglobulin conjugated with fluorescent dyes, Alexa647 (Thermo Scientific) or Atto488 (Rockland). To avoid background of free antibodies, the samples were postfixed for 20 min with 2% PFA in PBS. 100nm Tetraspeck beads (Life Technologies) were added to the fixed cells for channel alignment and drift correction. To perform dSTORM imaging coverslips were mounted in a coverslip holder and incubated in imaging buffer containing 25mM MEA (Sigma), 0.5mg/ml Glucose Oxidase (Sigma), 40 µg/ml Catalase (Sigma), and 10% w/v Glucose in Tris-HCl pH 8.0.

### dSTORM imaging

Confocal and dSTORM data were acquired on a Zeiss Elyra PS1 system using a 100x 1.49NA α Plan Apochromat objective. Confocal images were acquired using an Argon laser and 633nm diode laser. For dSTORM 488 and 642 100mW diode lasers were used to excite the fluorophores together with, respectively, a BP 495-575 + LP 750 or LP 655 excitation filter.

Additionally a 20mW 405 laser was used to increase blinking during dSTORM imaging. Imaging was performed using HiLo illumination and the data was acquired using a 512 x 512 pixel Andor iXon DU 897 EMCCD camera. Per super resolution image 10 000-15 000 images were acquired with an acquisition time of 33 ms. Two color imaging was performed sequentially, first Alexa647 followed by Atto488.

### dSTORM data analysis

A 2D Gaussian fitting algorithm (ZEN 2011, Carl Zeiss, Jena) was used to detect and localize the fluorescent events in the individual frames of the dSTORM movies. Overlapping fluorescent detections were discarded. Detections within a distance of 20 nm and 5 subsequent frames were assumed to originate from the same fluorophore and grouped together. Tetraspeck beads (100 nm) deposited on the cells before the experiment were used to correct for drift. To align the two color dSTORM images the positions of the same fiducials were used for an affine alignment. RAD51 dSTORM images were aligned, with the corresponding confocal image using a channel alignment algorithm in the ZEN2011 software. The confocal images were used to manually select the foci. Circular Regions of Interests with a 1 µm diameter around the foci were selected using Fiji/ImageJ. The localizations of these ROIs were exported using an ImageJ macro as text files and imported into R using the RStudio for further analysis (R Development Core Team, 2008). Localizations were clustered using a DBSCAN algorithm (Michael Hahsler (2015). dbscan: Density Based Clustering of Applications with Noise (DBSCAN) and Related Algorithms. R package version 0.9-6. (<http://CRAN.R-project.org/package=dbscan>). For a more detailed description of the methods see Figure S5.

### Acknowledgements

We thank I. Vidic for assistance in RPA protein purification, A. Kertokallio and R. v. Zuidam for technical assistance, and D. Ristic and A. Zelensky for critical discussions and comments on the manuscript.

## Funding

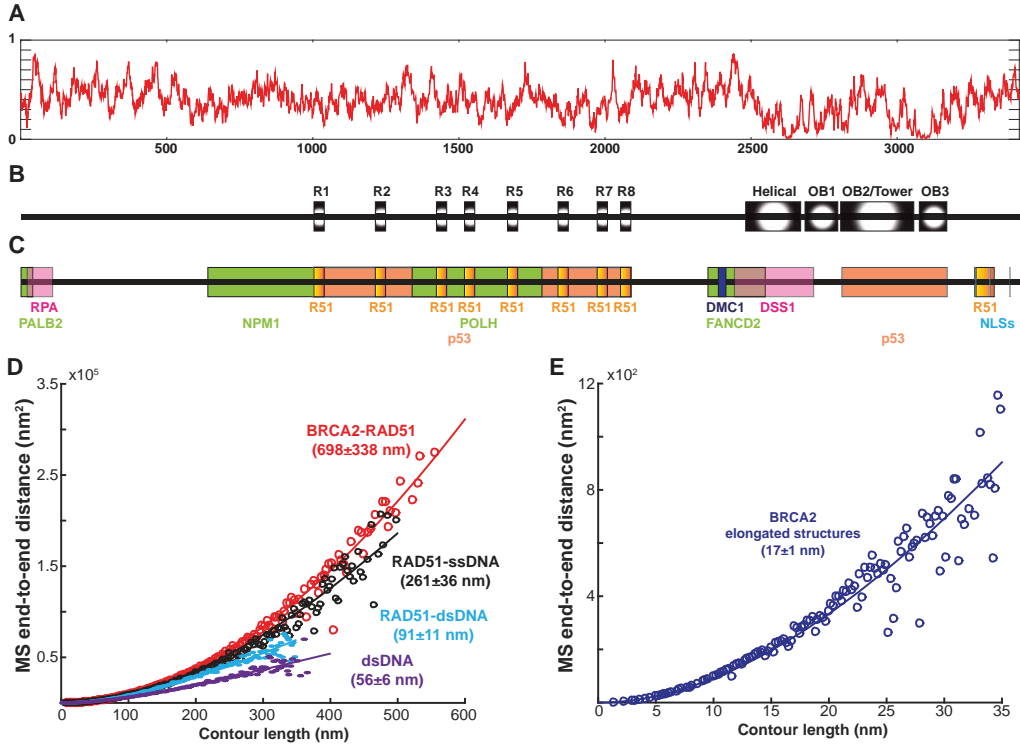
Our work is supported by grants from the Dutch Technology Foundation (STW) project (NWO nano11425 to C.W.), Cancer Genomics Netherlands (NWO gravitation), Marie Curie Reintegration Grant (FP7-276898) to H.S. This work is supported by NanoNextNL, a micro and nanotechnology consortium of the Government of the Netherlands and 130 partners.

## References

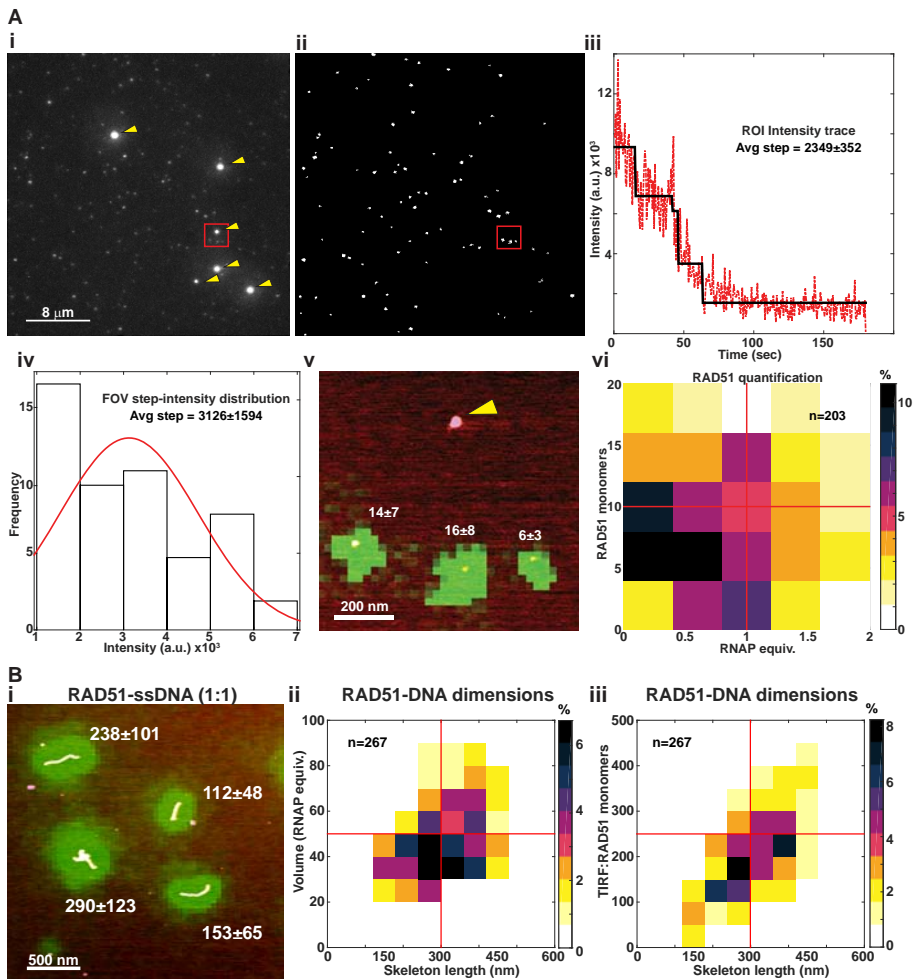
- Altmeyer, M., Neelsen, K.J., Teloni, F., Pozdnyakova, I., Pellegrino, S., Grofte, M., Rask, M.B.D., Streicher, W., Jungmichel, S., Nielsen, M.L., *et al.* (2015). Liquid demixing of intrinsically disordered proteins is seeded by poly(ADP-ribose). *Nat Commun* 6.
- Bekker-Jensen, S., Lukas, C., Kitagawa, R., Melander, F., Kastan, M.B., Bartek, J., and Lukas, J. (2006). Spatial organization of the mammalian genome surveillance machinery in response to DNA strand breaks. *J Cell Biol* 173, 195-206.
- Buisson, R., Niraj, J., Pauty, J., Maity, R., Zhao, W.X., Coulombe, Y., Sung, P., and Masson, J.Y. (2014). Breast Cancer Proteins PALB2 and BRCA2 Stimulate Polymerase  $\eta$  in Recombination-Associated DNA Synthesis at Blocked Replication Forks. *Cell Rep* 6, 553-564.
- Bustamante, C., Keller, D., and Yang, G.L. (1993). Scanning Force Microscopy of Nucleic-Acids and Nucleo-protein Assemblies. *Curr Opin Struct Biol* 3, 363-372.
- Candelli, A., Holthausen, J.T., Depken, M., Brouwer, I., Franker, M.A., Marchetti, M., Heller, I., Bernard, S., Garcin, E.B., Modesti, M., *et al.* (2014). Visualization and quantification of nascent RAD51 filament formation at single-monomer resolution. *Proc Natl Acad Sci U S A* 111, 15090-15095.
- Chen, P.L., Chen, C.F., Chen, Y.M., Xiao, J., Sharp, Z.D., and Lee, W.H. (1998). The BRC repeats in BRCA2 are critical for RAD51 binding and resistance to methyl methanesulfonate treatment. *P Natl Acad Sci USA* 95, 5287-5292.
- Cortese, M.S., Uversky, V.N., and Dunker, A.K. (2008). Intrinsic disorder in scaffold proteins: getting more from less. *Prog Biophys Mol Biol* 98, 85-106.
- Davies, O.R., and Pellegrini, L. (2007). Interaction with the BRCA2 C terminus protects RAD51-DNA filaments from disassembly by BRC repeats. *Nat Struct Mol Biol* 14, 475-483.
- de Jager, M., van Noort, J., van Gent, D.C., Dekker, C., Kanaar, R., and Wyman, C. (2001). Human Rad50/Mre11 is a flexible complex that can tether DNA ends. *Mol Cell* 8, 1129-1135.
- Dosztanyi, Z., Csizmok, V., Tompa, P., and Simon, I. (2005). IUPred: web server for the prediction of intrinsically unstructured regions of proteins based on estimated energy content. *Bioinformatics* 21, 3433-3434.
- Essers, J., Hendriks, R.W., Wesoly, J., Beerens, C.E., Smit, B., Hoeijmakers, J.H., Wyman, C., Dronkert, M.L., and Kanaar, R. (2002a). Analysis of mouse Rad54 expression and its implications for homologous recombination. *DNA Repair (Amst)* 1, 779-793.
- Essers, J., Houtsmuller, A.B., van Veelen, L., Paulusma, C., Nigg, A.L., Pastink, A., Vermeulen, W., Hoeijmakers, J.H.J., and Kanaar, R. (2002b). Nuclear dynamics of RAD52 group homologous recombination proteins in response to DNA damage. *EMBO Journal* 21, 2030-2037.
- Fukuchi, S., Hosoda, K., Homma, K., Gojbori, T., and Nishikawa, K. (2011). Binary classification of protein molecules into intrinsically disordered and ordered segments. *Bmc Struct Biol* 11.
- Ghaemmaghami, S., Huh, W.K., Bower, K., Howson, R.W., Belle, A., Dephoure, N., O'Shea, E.K., and Weissman, J.S. (2003). Global analysis of protein expression in yeast. *Nature* 425, 737-741.
- Heilemann, M., van de Linde, S., Schuttelpel, M., Kasper, R., Seefeldt, B., Mukherjee, A., Tinnefeld, P., and Sauer, M. (2008). Subdiffraction-resolution fluorescence imaging with conventional fluorescent probes. *Angew Chem Int Ed Engl* 47, 6172-6176.
- Henricksen, L.A., Umbricht, C.B., and Wold, M.S. (1994). Recombinant replication protein A: expression, complex formation, and functional characterization. *J Biol Chem* 269, 11121-11132.
- Hilario, J., Amitani, I., Baskin, R.J., and Kowalczykowski, S.C. (2009). Direct imaging of human Rad51 nucleoprotein dynamics on individual DNA molecules. *Proc Natl Acad Sci U S A* 106, 361-368.
- Holloman, W.K. (2011). Unraveling the mechanism of BRCA2 in homologous recombination. *Nat Struct Mol Biol* 18, 748-754.
- Janicijevic, A., Ristic, D., and Wyman, C. (2003). The molecular machines of DNA repair: scanning force microscopy analysis of their architecture. *J Microsc* 212, 264-272.
- Jensen, R.B., Carreira, A., and Kowalczykowski, S.C. (2010). Purified human BRCA2 stimulates RAD51-mediated recombination. *Nature* 467, 678-662.
- Kerssemakers, J.W., Munteanu, E.L., Laan, L., Noetzel, T.L., Janson, M.E., and Dogterom, M. (2006). Assembly dynamics of microtubules at molecular resolution. *Nature* 442, 709-712.
- Krawczyk, P.M., Eppink, B., Essers, J., Stap, J., Rodermond, H., Odijk, H., Zelensky, A., van Bree, C., Stalpers, L.J., Buist, M.R., *et al.* (2011). Mild hyperthermia inhibits homologous recombination, induces BRCA2 degradation, and sensitizes cancer cells to poly(ADP-ribose) polymerase-1 inhibition. *Proc Natl Acad Sci U S A* 108, 9851-9856.
- Lamour, G., Kirkegaard, J.B., Li, H., Knowles, T.P., and Gsponer, J. (2014). Easyworm: an open-source software tool to determine the mechanical properties of worm-like chains. *Source Code Biol Med* 9, 16.
- Liu, J., Doty, T., Gibson, B., and Heyer, W.D. (2010). Human BRCA2 protein promotes RAD51 filament formation on RPA-covered single-stranded DNA. *Nat Struct Mol Biol* 17, 1260-1262.
- Mazin, A.V., Zaitseva, E., Sung, P., and Kowalczykowski, S.C. (2000). Tailed duplex DNA is the preferred substrate for Rad51 protein-mediated homologous pairing. *EMBO Journal* 19, 1148-1156.
- Modesti, M., Ristic, D., van der Heijden, T., Dekker, C., van Mameren, J., Peterman, E.J.G., Wuite, G.J.L., Kanaar, R., and Wyman, C. (2007). Fluorescent human RAD51 reveals multiple nucleation sites and filament segments tightly associated along a single DNA molecule. *Structure* 15, 599-609.
- Oldfield, C.J., and Dunker, A.K. (2014). Intrinsically disordered proteins and intrinsically disordered protein regions. *Annu Rev Biochem* 83, 553-584.

- Pellegrini, L., Yu, D.S., Lo, T., Anand, S., Lee, M., Blundell, T.L., and Venkiteswaran, A.R. (2002). Insights into DNA recombination from the structure of a RAD51-BRCA2 complex. *Nature* 420, 287-293.
- Rajagopalan, S., Andreeva, A., Rutherford, T.J., and Fersht, A.R. (2010). Mapping the physical and functional interactions between the tumor suppressors p53 and BRCA2. *P Natl Acad Sci USA* 107, 8587-8592.
- Ratcliff, G.C., and Erie, D.A. (2001). A novel single-molecule study to determine protein-protein association constants. *J Am Chem Soc* 123, 5632-5635.
- Reuter, M., Zelensky, A., Smal, I., Meijering, E., van Cappellen, W.A., de Gruiter, H.M., van Belle, G.J., van Royen, M.E., Houtsmuller, A.B., Essers, J., et al. (2014). BRCA2 diffuses as oligomeric clusters with RAD51 and changes mobility after DNA damage in live cells. *J Cell Biol* 207, 599-613.
- Ristic, D., Modesti, M., van der Heijden, T., van Noort, J., Dekker, C., Kanaar, R., and Wyman, C. (2005). Human Rad51 filaments on double- and single-stranded DNA: correlating regular and irregular forms with recombination function. *Nucleic Acids Res* 33, 3292-3302.
- Ristic, D., Sanchez, H., and Wyman, C. (2011). Sample preparation for SFM imaging of DNA, proteins, and DNA-protein complexes. *Methods in molecular biology* 783, 213-231.
- Rossy, J., Cohen, E., Gaus, K., and Owen, D.M. (2014). Method for co-cluster analysis in multichannel single-molecule localisation data. *Histochem Cell Biol* 141, 605-612.
- Sanchez, H., Kanaar, R., and Wyman, C. (2010). Molecular recognition of DNA-protein complexes: A straightforward method combining scanning force and fluorescence microscopy. *Ultramicroscopy* 110, 844-851.
- Sanchez, H., Kertokallio, A., van Rossum-Fikkert, S., Kanaar, R., and Wyman, C. (2013). Combined optical and topographic imaging reveals different arrangements of human RAD51 with presynaptic and post-synaptic RAD51-DNA filaments. *P Natl Acad Sci USA* 110, 11385-11390.
- Sanchez, H., and Wyman, C. (2015). SFMetrics: an analysis tool for scanning force microscopy images of biomolecules. *BMC Bioinformatics* 16, 27.
- Shahid, T., Soroka, J., Kong, E.H., Malivert, L., McIlwraith, M.J., Pape, T., West, S.C., and Zhang, X. (2014). Structure and mechanism of action of the BRCA2 breast cancer tumor suppressor. *Nat Struct Mol Biol* 21, 962-968.
- Shoemaker, B.A., Portman, J.J., and Wolynes, P.G. (2000). Speeding molecular recognition by using the folding funnel: the fly-casting mechanism. *Proc Natl Acad Sci U S A* 97, 8868-8873.
- Siaud, N., Barbera, M.A., Egashira, A., Lam, I., Christ, N., Schlacher, K., Xia, B., and Jasin, M. (2011). Plasticity of BRCA2 Function in Homologous Recombination: Genetic Interactions of the PALB2 and DNA Binding Domains. *Plos Genetics* 7.
- Sing, C.E., Olvera de la Cruz, M., and Marko, J.F. (2014). Multiple-binding-site mechanism explains concentration-dependent unbinding rates of DNA-binding proteins. *Nucleic acids research* 42, 3783-3791.
- Spain, B.H., Larson, C.J., Shihabuddin, L.S., Gage, F.H., and Verma, I.M. (1999). Truncated BRCA2 is cytoplasmic: Implications for cancer-linked mutations. *P Natl Acad Sci USA* 96, 13920-13925.
- Subramanyam, S., Ismail, M., Bhattacharya, I., and Spies, M. (2016). Tyrosine phosphorylation stimulates activity of human RAD51 recombinase through altered nucleoprotein filament dynamics. *Proc Natl Acad Sci U S A* 113, E6045-E6054.
- Sy, S.M.H., Huen, M.S.Y., and Chen, J.J. (2009). PALB2 is an integral component of the BRCA complex required for homologous recombination repair. *P Natl Acad Sci USA* 106, 7155-7160.
- Tarsounas, M., Davies, D., and West, S.C. (2003). BRCA2-dependent and independent formation of RAD51 nuclear foci. *Oncogene* 22, 1115-1123.
- Thorslund, T., Esashi, F., and West, S.C. (2007). Interactions between human BRCA2 protein and the meiosis-specific recombinase DMIC1. *Embo J* 26, 2915-2922.
- Thorslund, T., McIlwraith, M.J., Compton, S.A., Lekontsev, S., Petronczki, M., Griffith, J.D., and West, S.C. (2010). The breast cancer tumor suppressor BRCA2 promotes the specific targeting of RAD51 to single-stranded DNA. *Nat Struct Mol Biol* 17, 1263-1265.
- Uversky, V.N. (2016). Dancing Protein Clouds: The Strange Biology and Chaotic Physics of Intrinsically Disordered Proteins. *J Biol Chem* 291, 6681-6688.
- van der Heijden, T., Seidel, R., Modesti, M., Kanaar, R., Wyman, C., and Dekker, C. (2007). Real-time assembly and disassembly of human RAD51 filaments on individual DNA molecules. *Nucleic acids research* 35, 5646-5657.
- van der Linden, E., Sanchez, H., Kinoshita, E., Kanaar, R., and Wyman, C. (2009). RAD50 and NBS1 form a stable complex functional in DNA binding and tethering. *Nucleic acids research* 37, 1580-1588.
- van Mameren, J., Modesti, M., Kanaar, R., Wyman, C., Peterman, E.J., and Wuite, G.J. (2009). Counting RAD51 proteins disassembling from nucleoprotein filaments under tension. *Nature* 457, 745-748.
- van Noort, J., van Der Heijden, T., de Jager, M., Wyman, C., Kanaar, R., and Dekker, C. (2003). The coiled-coil of the human Rad50 DNA repair protein contains specific segments of increased flexibility. *Proc Natl Acad Sci U S A* 100, 7581-7586.
- van Veelen, L.R., Cervelli, T., van de Rakt, M.W., Theil, A.F., Essers, J., and Kanaar, R. (2005). Analysis of ionizing radiation-induced foci of DNA damage repair proteins. *Mutat Res* 574, 22-33.
- Wang, H.F., Takenaka, K., Nakanishi, A., and Miki, Y. (2011). BRCA2 and Nucleophosmin Coregulate Centrosome Amplification and Form a Complex with the Rho Effector Kinase ROCK2. *Cancer Research* 71, 68-77.
- Wang, X., and Haber, J.E. (2004). Role of Saccharomyces single-stranded DNA-binding protein RPA in the strand invasion step of double-strand break repair. *PLoS Biol* 2, E21.
- Wang, X.Z., Andreassen, P.R., and D'Andrea, A.D. (2004). Functional interaction of monoubiquitinated FANCD2 and BRCA2/FANCD1 in chromatin. *Mol Cell Biol* 24, 5850-5862.
- Wong, J.M.S., Ionescu, D., and Ingles, C.J. (2003). Interaction between BRCA2 and replication protein A is compromised by a cancer-predisposing mutation in BRCA2. *Oncogene* 22, 28-33.
- Wright, P.E., and Dyson, H.J. (2015). Intrinsically disordered proteins in cellular signalling and regulation. *Nat Rev Mol Cell Bio* 16, 18-29.
- Yang, H.J., Jeffrey, P.D., Miller, J., Kinnucan, E., Sun, Y.T., Thoma, N.H., Zheng, N., Chen, P.L., Lee, W.H., and Pavletich, N.P. (2002). BRCA2 function in DNA binding and recombination from a BRCA2-DSS1-ssDNA structure. *Science* 297, 1837-1848.

## Supplementary Figures



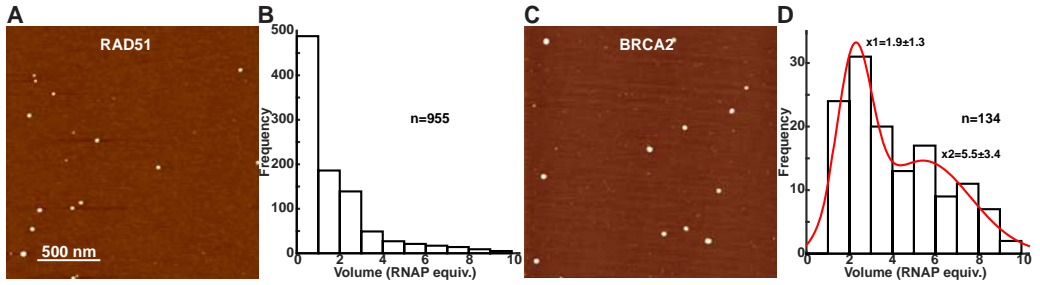
**Supplementary Figure 1 Intrinsic disordered regions span the entire BRCA2 sequence.** **A)** Amino acid sequence of human BRCA2 analysed by IUpred web tool (Dosztanyi et al., 2005). Computed disorder probability (red line) is plotted against residue number. **B)** Folded domains described in BRCA2. R1-R8: BRC repeats; Helical: Helical domain, OB: Oligosaccharide binding domain; Tower: Tower domain. **C)** Interaction regions identified between BRCA2 and PALB2 (Sy et al., 2009), RPA (Wong et al., 2003), nucleophosmin (NPM1) (Wang et al., 2011), RAD51 (R51) (Chen et al., 1998; Davies and Pellegrini, 2007), polymerase eta (Buisson et al., 2014), p53 (Rajagopalan et al., 2010), DMC1 (Thorslund et al., 2007), FANCD2 (Wang et al., 2004), DSS1 (Yang et al., 2002), and the nuclear localization signals (NLSs) (Spain et al., 1999). **D)** BRCA2 is a flexible polymer that produces rigid rods upon RAD51 interaction. Mean square (MS) end-to-end distances plotted as a function of the contour length (circles) of RAD51-BRCA2 complexes (n=123), dsDNA (n=107), RAD51-dsDNA filaments (n=101), and RAD51-ssDNA (n=105) filaments in nanometers (nm). Lines are fits (with coefficient of determination, indicating goodness of the fit, >0.9) of the worm-like chain model to the data. Apparent persistence length for each complex is indicated between brackets  $\pm$  SD. **E)** Similar analysis for the BRCA2 V-shape domains (n=111)



**Supplementary Figure 2 Quantification of RAD51 monomers by fluorescence. A) Analysis of RAD51 protein.**

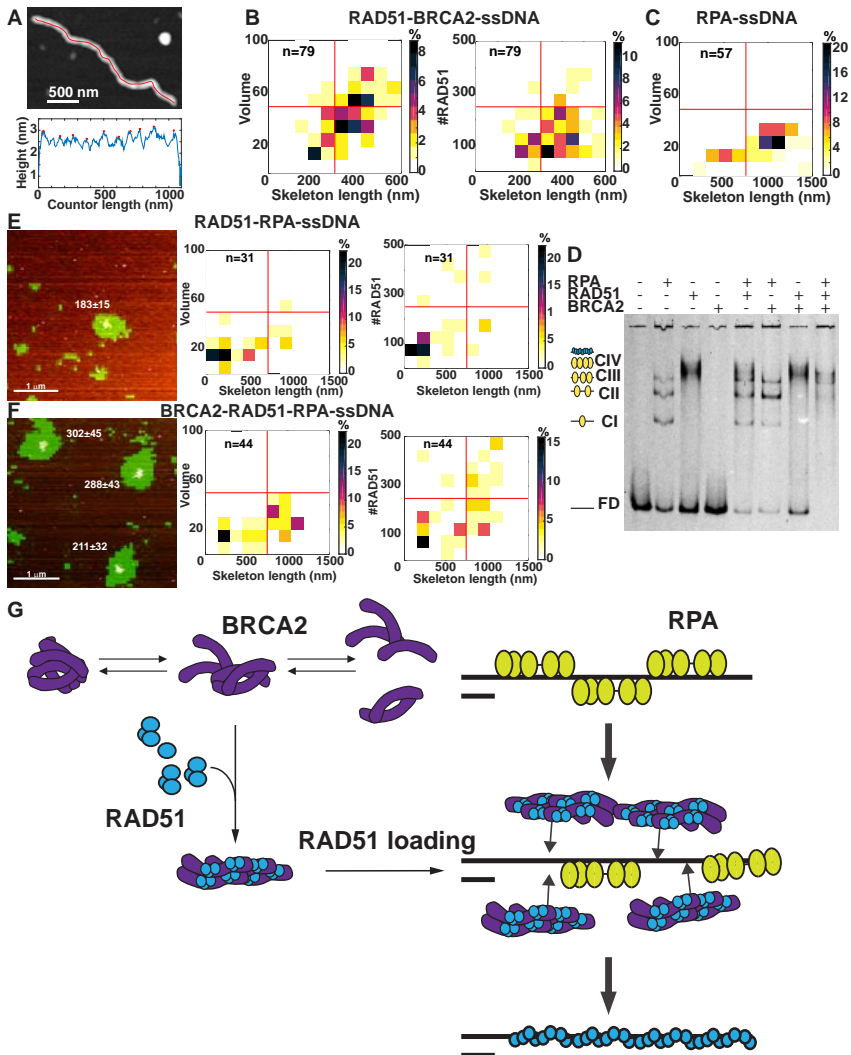
**(i)** TIRF image (maximum intensity projection from a stack of 300 frames) of fluorescent RAD51. Yellow arrowheads indicate fluorescent fiducials. Red box shows the region enlarged in panel v. **(ii)** Binary mask obtained from image in panel A showing selected regions of interest (ROIs) for quantitative analysis. **(iii)** Example intensity trace from one ROI in panel ii. Number of fluorophores were determined based on intensity steps from bleaching and blinking of single AF488 dyes. **(iv)** Distribution of step intensities from all ROIs in panel ii presented as histogram with bin size of 1000 intensity arbitrary units (a.u.). FOV: Field of view. **(v)** RAD51 proteins visualized by TIRF-SFM. SFM scan overlaid with fluorescence image (green) from boxed area in panels i and ii. Numbers indicate RAD51 monomers  $\pm$  SD per ROI. Yellow arrowhead indicates a fluorescent fiducial. **(vi)** Distribution of RAD51 protein with respect to volume and number of fluorophores. Individual complexes from images similar to panel (v) were measured and their distribution plotted in a two dimensional histogram with bin size 0.4 RNAP equiv.  $\times$  4 fluorophores. Color indicates percentage of total ROIs analyzed ( $n=203$ ) as shown in the color bar. Red lines are guides to view bins.

**B) Analysis of RAD51-ssDNA complexes. (i)** Calibration of TIRF-SFM set-up for quantification of fluorescent RAD51. SFM scan overlaid with fluorescence image (green) of ssDNA incubated with RAD51 and cross-linked with glutaraldehyde. Numbers indicate the amount of RAD51 monomers  $\pm$  SD per protein complex. **(ii)** Volume and length of individual complexes from images similar to panel (i) were measured and their distribution plotted in a two dimensional histogram with bin size 60 nm  $\times$  10 RNAP equiv. Color indicates percentage of total complexes analyzed ( $n=267$ ) as shown in the color bar. **(iii)** Distribution of RAD51-ssDNA complexes based on number of fluorophores (RAD51) and length. Bin size 60 nm  $\times$  50 RAD51 monomers.



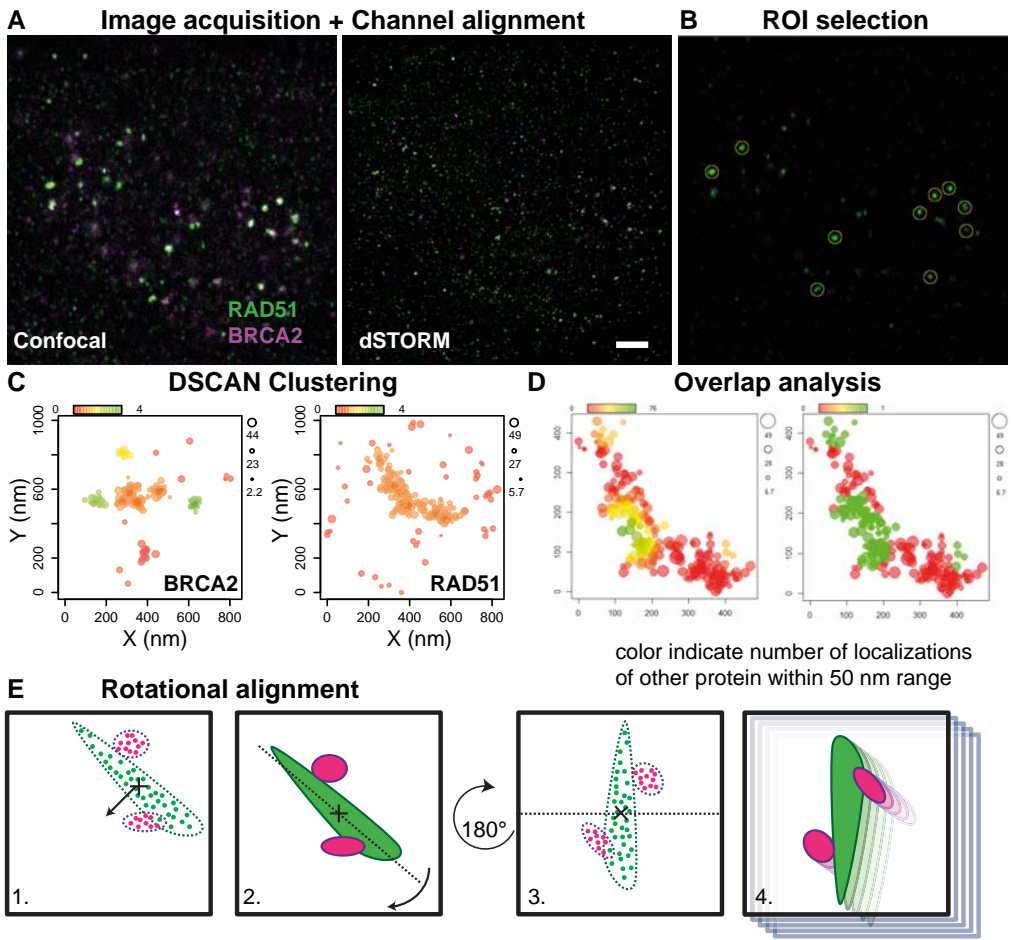
**Supplementary Figure 3 RAD51 and BRCA2 alone do not make elongated structures.** **A)** Representative SFM image of RAD51 incubated with glutaraldehyde. Image size 2 x 2 mm. **B)** Measurements (n=955) of RAD51 volume from images such as **A)** presented as distribution in a histogram with bin size of 1 RNAP equiv. **C)** Representative SFM image of BRCA2 incubated with glutaraldehyde. Image size 2 x 2 mm. **D)** Measurements (n=134) of BRCA2 volume from images such as **C)** presented as distribution in a histogram with bin size of 1 RNAP equiv. Red line is the Gaussian fit with two populations centered around 1.9 and 5.5 RNAP equiv., respectively.

IV

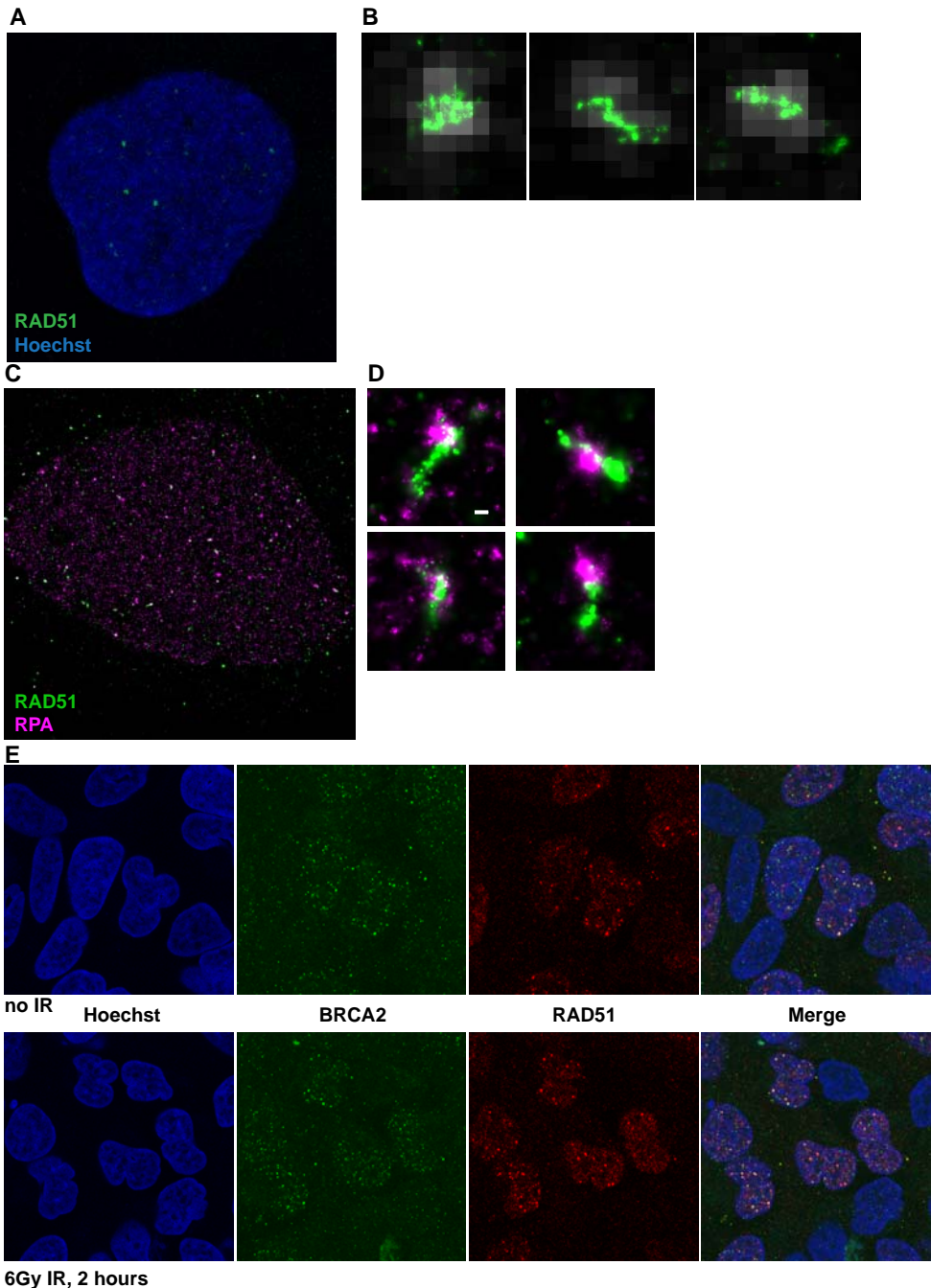


**Supplementary Figure 4 A)** Example of elongated BRCA2-RAD51 (unlabeled) complex with the central contour line indicated in red. Height profile along the red contour line is shown in the graph below with automated peak detections indicated by red circles. **B)** Distribution of RAD51-BRCA2-ssDNA complexes based on volume, length, and number of fluorophores. All complexes from images similar to panel (ii) and (iii) in Figure 3A of the main text were measured and their distribution plotted in a two dimensional histogram with bin size 60 nm x 10 RNAP equiv. (left) and 60 nm x 50 RAD51 monomers (right). **C)** Distribution of RPA-ssDNA of complexes based on volume and length. RPA-ssDNA complexes had an average volume of  $21 \pm 14$  (SD) RNAP equiv. **D)** BRCA2 remodels RPA and helps RAD51 loading on ssDNA. DNA mobility shift assays after incubation with (+) or without (-) proteins; RPA, RAD51 and BRCA2. RPA binds to the fluorescence oligonucleotide with one (CI), two (CII), three (CIII), or four (CIV) monomers (lane 2). In the presence of BRCA2 the amount of CI and free DNA (FD) was reduced with a concomitant increase in CII, indicating a reorganization of the proteins bound to the DNA (lane 6). RAD51 in molar excess shifted more than 50% of the DNA (lane 3), however DNA pre-incubation with RPA inhibited drastically the binding of RAD51 (lane 5). Addition of pre-incubated BRCA2-RAD51 to the reaction recovered the loading of RAD51 on RPA bound DNA (lane 8). Yellow ellipses represent RPA monomers and blue ellipses RAD51 monomers. **E)** Effect of BRCA2 on RAD51 loading on RPA covered ssDNA. RAD51-RPA-ssDNA complexes visualized by TIRF-SFM without fixation. and distribution of RAD51-RPA-ssDNA complexes based on volume and length, or number of fluorophores (RAD51) and length. **F)** BRCA2-RAD51-RPA-ssDNA complexes visualized by TIRF-SFM without fixation and . distribution of BRCA2-RAD51-RPA-ssDNA as above. Numbers in white indicate RAD51 monomers  $\pm$  SD for the DNA-protein complexes shown. **G)** Cartoon illustrating ideas for the dynamic structural rearrangement of oligomeric BRCA2 leading to RAD51 loading on DNA covered by RPA.





**Supplementary Figure 5 Analysis of dSTORM super resolution data.** **A)** Two color confocal images and dSTORM images were acquired using the same microscope and objective lens. dSTORM images were acquired as describe in the Material and Methods section. **B)** Using a channel alignment algorithm within the Zeiss ZEN software, one of both channels of the confocal images was aligned with the dSTORM image. Subsequently ROIs were manually selected from confocal images of the RAD51 staining. The single molecule localizations of these ROIs were analyzed in R-Studio. **C)** The localization data from the ROIs was clustered using a Density Based Clustering Algorithm with Noise (DBSCAN) algorithm. In this algorithm localizations are clustered together based on the local density of localizations with a defined radius, epsilon, and minimum number of points within that radius. The clustering was used to quantify the size and shape of the clusters. Furthermore localizations outside of any cluster were filtered out for further analysis. The plots show the dSTORM localizations of a BRCA2/RAD51 focus. The colors indicate the identified cluster by DSCAN. Localizations with a cluster number 0 (red) are considered background. **D)** To assess the overlap between RAD51 and respectively BRCA2 or RPA; from every RAD51 localization the number of localizations of the other species was measured within a 50 nm radius, this can be visualized by a gradient scatter plot, showing regions with much overlap between both proteins and regions without overlap. A threshold was set on the number of localizations within 50 nm of every RAD51 localization at 1% of all localizations of either BRCA2 or RAD51. This results in a scatter plot with either overlapping (green) or not overlapping (red) localizations. For every ROI the fraction of localizations of RAD51 that overlapped was quantified. **E)** Individual images of DSB foci were aligned by rotation and visualized as one image. For every individual image the following algorithm was performed: 1) The center of mass of the RAD51 signal was determined and the localizations translated accordingly to have the center of mass in the middle of the image. 2) The major axis of the RAD51 signal was determined and the angle of this major axis with respect with the vertical axis was used to rotate the localization with the center of mass as rotation point. 3) For RAD51 the number of localizations above and below the horizontal axis was measured. If the amount of localizations above the horizontal axis was smaller than below the axis the image was rotated for another 180 degrees. 4) Finally the coordinates of the rotated dSTORM images were merged and visualized as a single super resolution image.



**Supplementary Figure 6** **A)** Confocal image of a U2OS cell nucleus treated with 6Gy IR, fixed after 2 hours and stained with RAD51 antibody. The DNA is visualized with Hoechst. **B)** Examples of repair foci imaged both with confocal (grey) and dSTORM (green). Showing the large increase in resolution of dSTORM compared to confocal. **C)** A two-color dSTORM image of RAD51 with RPA treated with 6Gy IR and fixed after two hours. **D)** Examples of DSB foci showing the localization of RAD51 and RPA together. Scale bar is 100 nm. **E)** Confocal images of cells immunostained for BRCA2 and RAD51 of cells treated without and with ionizing radiation (IR). Showing co-localization of BRCA2 and RAD51 in DSB foci. The DNA is visualized by Hoechst.





## Chapter V

# Nanoscale organization of RAD54 revealed by super resolution microscopy

Maarten W. Paul<sup>1,2</sup>, Alex Zelensky<sup>3</sup>, Pim van den Bersselaar<sup>2</sup>, H. Martijn de Gruiter<sup>1</sup>, Humberto Sanchez<sup>3</sup>, Ihor Smal<sup>4</sup>, Claire Wyman<sup>3</sup>, Roland Kanaar<sup>3</sup>, Jeroen Essers<sup>3</sup>, Adriaan B. Houtsmuller<sup>1,2</sup>

<sup>1</sup>Optical Imaging Centre, <sup>2</sup>Department of Pathology, and <sup>3</sup>Department of Molecular Genetics, Biomedical Imaging Group Rotterdam<sup>4</sup>, Erasmus University Medical Center, 3000 CA Rotterdam, The Netherlands

*Manuscript in preparation*

## Abstract

RAD54 is a dynamic ATP-dependent chromatin remodeling protein which is important in repair of DNA Double Strand Breaks through Homologous recombination due to its interaction with the recombinase RAD51. In this study we generated mouse embryonic stem cells expressing RAD54 with fluorescent tags suitable for super resolution microscopy. This permitted us to investigate the localization and dynamics of RAD54 in fixed and live cells at the single molecule level. Using single molecule localization microscopy, we show nanoscale localization of RAD54 and RAD51 within DSB foci. In cells expressing solely RAD54<sup>K189A</sup>, this ATPase deficient mutant protein localizes together with RAD51 in very elongated foci of up to more than a micrometer long, in which RAD54 is localized in multiple clusters along the RAD51 focus. Single molecule tracking of the wild type and mutant RAD54 confirmed the previously reported immobilization of RAD54<sup>K189A</sup> and in addition showed that no increased stable immobilization of the wild type protein occurs even after ionizing radiation. Finally, we used a novel assay in which we used local photoswitching of mMapple3 tagged wildtype RAD54 and RAD54<sup>K189A</sup> to study specifically the localization of immobile RAD54 molecules within foci in wild type and ATPase deficient cells. This showed the very dynamic morphology of the RAD54 DSB foci in chromatin and more specifically showed extensive movement of immobilized RAD54 molecule clusters within the DSB focus.

## Introduction

Stability of the genome is dependent on faithful repair of DNA damage. Homologous recombination (HR) is an essential pathway for repair of DNA Double Strand Breaks (DSBs). Instead of end-to-end ligation, by Non-homologous end joining (NHEJ), HR uses a homologous intact DNA template to repair the break, which in late S and G2 phase can be found at the sister chromatid. The mechanisms required for the broken DSB end to engage with the homologous DNA requires sophisticated protein machinery. Prior to repair a number of essential factors remodel and prepare the DNA molecule for repair. The central and most intensively studied protein in these reactions is the recombinase RAD51. Resection of the broken DSB ends into ssDNA, which is coated with RPA, enables loading of RAD51 on the ssDNA mediated by BRCA2 (Davies et al., 2001; Yuan et al., 1999). These ssDNA-RAD51 filaments enable the probing of homologous sequence along the genome. However RAD51 function is regulated by many proteins for example the RAD51 paralogs (Zelensky et al., 2014) and the DNA-dependent ATPase RAD54.

RAD54 is highly conserved among eukaryotes and is part of the SWI2/SNF2 helicase family, but RAD54 lacks true helicase activity (Petukhova et al., 1998; Swagemakers et al., 1998). However, RAD54 has been shown to be important for homologous recombination to proceed. RAD54 directly interacts with RAD51, but dynamic studies in cells suggest that the interaction of RAD54 with RAD51 is specific to RAD51 bound to DNA (Essers et al., 2002; Tan et al., 1999). The interaction between RAD51 and RAD54 is important for the function of both proteins. While RAD51 stimulates RAD54 branch migration activity, RAD54 is found to be involved in several steps of RAD51 action. For example, RAD54 is involved in promotion of filament formation and stabilizing RAD51 filaments on ssDNA (Mazin et al., 2003). Furthermore it stimulates homology search and strand exchange (Mazina and Mazin, 2004; Renkawitz et al., 2013). This happens through its function as chromatin remodeler, facilitating the displacement histones from chromatin (Alexiadis and Kadonaga, 2002).

Chromatin remodelers, like RAD54, are also important for strand invasion by RAD51 in the complex context of cellular chromatin which is highly challenging compared to strand invasion in naked DNA (Alexeev et al., 2003).

In later steps of HR RAD54 regulates disassembly of RAD51 nucleoprotein filaments. Along with these functions it also has been shown that RAD54 plays a role in preventing RAD51 from loading to dsDNA (Solinger et al., 2002). Biochemical experiments recently showed that human RAD54 can also disassemble RAD51 dsDNA filaments (Mason et al., 2015). Compared to its bacterial homolog RecA, RAD51 has a much weaker ATP activity and therefore probably requires other proteins with their ATPase activity to dissociate from the DNA (Chi et al., 2006; Ristic, 2005). Finally, RAD54 also has RAD51 independent functions concerning DNA remodeling during DSB Repair. It is implicated to be involved in branch migration after strand invasion and it has an important interaction with the Mus81-Eme1 endonuclease, a protein involved in resolving double holiday junctions (Bugreev et al., 2006).

Experiments using purified protein shed light on the localization of RAD54 at RAD51 nucleoprotein filaments. Reconstituted RAD51-RAD54-DNA complexes visualized by electron microscopy showed interesting organization of RAD54 binding at the end of RAD51 dsDNA RAD51 filaments (Kiiianitsa et al., 2006), in line with the function of RAD54 to disassemble RAD51 filaments after joint molecule formation. With a combination of Scanning Force Microscopy and single fluorophore localization it was shown that in a subset of RAD51 ssDNA structures, RAD54 molecules were dispersed in the RAD51 filament (Sanchez et al., 2013). In vitro experiments also shed some light on the dynamics of RAD54, by showing that RAD54 can translocate along dsDNA for thousands of base pairs (AmiTani et al., 2006) and high speed AFM showed short scanning and hopping on the DNA (Sanchez et al., 2011).

In living cells, FRAP experiments have revealed that RAD54 dynamics are very different compared to RAD51, Rad52 or BRCA2. While, for example, RAD51 is stably associated with

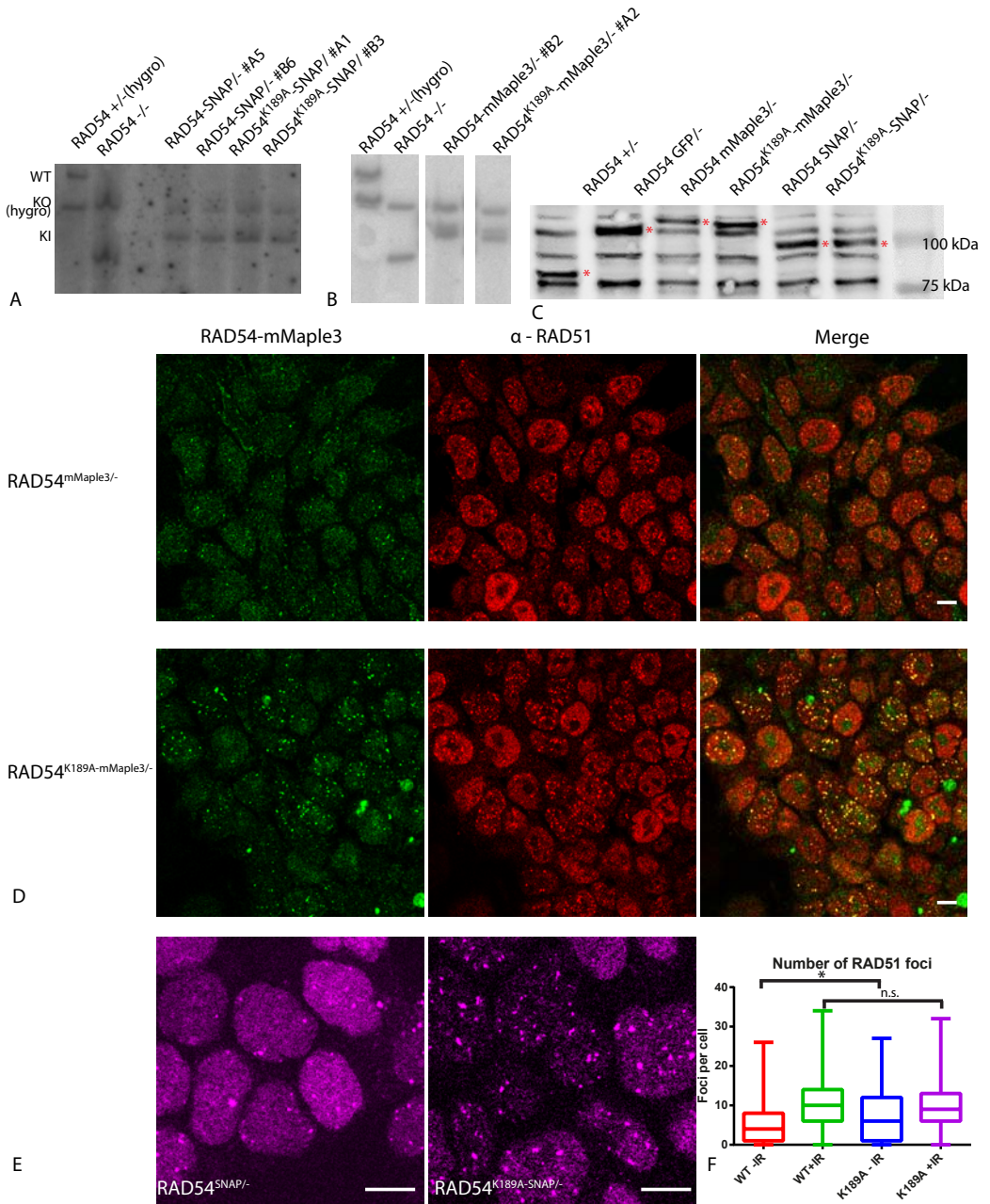


**Figure 1** Characterization of RAD54 mMaple3/SNAPtag knock-in mouse ES cells. **A-B**) Southern blots of the different clones of the RAD54 mMaple3/SNAPtag knock-in mouse ES cells used in this study, showing the disappearance of the wildtype RAD54 allele (WT) and the appearance of an extra band at the expected size (KI). The wildtype allele was targeted while the knock out allele already present in the RAD54<sup>w<sup>t</sup>/-(hygro)</sup> cells was still present. **C**) Expression of the tagged proteins was validated by Western blot using a RAD54 antibody. Wildtype RAD54 is 84 kDa while GFP an mMaple3 should result in a protein of about 111 kDa in size, while SNAPtag tagged RAD54 is 103 kDa in size. **D**) Cells expressing RAD54 fused with photo convertible protein mMaple3 show co-localization in nuclear foci with RAD51 by immunostaining in untreated cells. **E**) Localization of RAD54-SNAPtag labelled with SNAP-SiR substrate in untreated cells. **F**) Quantification of numbers of RAD51 foci in cells expressing SNAP tag tagged wildtype and RAD54(K189A) mutant protein. Cells were treated with 6 Gy of ionizing radiation and fixed two hours later. Foci of more than 100 nuclei per condition were automatically counted. Scale bars, 10 μm.

DSB foci, RAD54 is highly mobile with only very brief interactions with DSB foci (Agarwal et al., 2011; Essers et al., 2006; Reuter et al., 2014). Nonetheless, RAD54 visually accumulates in DSB foci in relatively high numbers (tens to hundreds), suggesting exceptionally high on- and off-rates to and from foci. Interestingly, a previous study has shown that the ATPase activity of RAD54 is required for this dynamic behavior, especially for rapid release from foci (Agarwal et al., 2011). Mutant RAD54<sup>K189A</sup> and RAD54<sup>K189R</sup> cells display increased numbers of spontaneous foci and prolonged presence of DSB foci after damage induction.

In order to further elucidate the mechanisms by which RAD54 regulates homologous recombination we applied super resolution microscopy methods to cells expressing fluorescently tagged RAD54 proteins from the endogenous locus. We show close association of RAD51 and RAD54 at DSB foci by super resolution and were able to identify morphological differences of the RAD51 foci in cells expressing RAD54<sup>K189A</sup>. Furthermore, we were able to track individual RAD54 molecules inside living cells. Giving us a single-molecule view on the behavior of RAD54. We expanded this by applying novel methods that enable to follow localization of the stably bound RAD54 molecules at the DSB focus.

## Results

### Generation of cell lines expressing RAD54 suited for super resolution microscopy

To study endogenously expressed RAD54 we used mouse embryonic cells which express RAD54 tagged with either the photoswitchable protein mMaple3 or a SNAP-tag. mMaple3 is a photo-switchable fluorescent protein of which upon near-UV laser illumination (e.g. 405 nm) the fluorescence spectrum changes, from a spectrum similar to GFP to a spectrum comparable to RFP (Wang et al., 2014). This tag can be used for Photoactivation Assisted Localization Microscopy (PALM) (Betzig et al., 2006) or can be used to apply local photoswitching of subcellular or subnuclear regions (Fuchs et al., 2010). The SNAP tag is a 19 kDa tag, based on the

human AGT protein, which forms a covalent interaction with O6-benzylguanine residues (Keppler et al., 2004). Organic fluorophores synthesized with these residues can form a covalent bond with the SNAP-tag fusions in living cells.

To tag RAD54 protein from the endogenous locus we made use of a targeting construct aiming to replace the sequence of the last few exons of the RAD54 locus with the in-frame coding sequence of RAD54 along with the coding sequence of the protein tag of choice. The replacement of the last exons also allowed to introduce a point mutation in the Walker A ATPase domain (K189A) in the RAD54 protein sequence, which abolishes the ATPase activity of RAD54 (Agarwal et al., 2011). We used cells expressing wildtype RAD54 only from one allele, which made it possible to obtain cells homozygous for the protein fusion, by replacing the intact copy of RAD54 (Essers et al., 1997). Proper integration of the targeting construct was validated by Southern Blot (Figure 1A and B). Using western blot, we also confirmed that in targeted cells all detectable RAD54 protein was tagged (Figure 1C). We further validated the cells by confocal microscopy whereby we observed for both RAD54<sup>WT-mMaple3/-</sup> and RAD54<sup>K189A-mMaple3/-</sup> localization of the protein to nucleus and the formation of foci co-localizing with RAD51 (Figure 1D). We also labelled RAD54<sup>WT-SNAP/-</sup> and RAD54<sup>K189A-SNAP/-</sup> with the SNAPtag-SiR ligand which also showed the correct localization of RAD54 (Figure 1E). In line with earlier observations cells expressing RAD54(K189A) we also observed an increased number of RAD51 foci in untreated cells, compared to what was observed in cells expressing wild type RAD54 (Figure 1F).

### Super resolution microscopy reveals differences in RAD51 foci in cells lacking RAD54 ATPase activity

The observation that RAD54<sup>K189A</sup> cells have elevated numbers of DSB foci in untreated cells, invoked the question whether foci in the mutant also have different shapes or internal organization. However, using confocal microscopy addressing this question is difficult, since spatial resolution is limited (~200nm) and DSB foci are relatively small (0.5 - 1 μm). Super



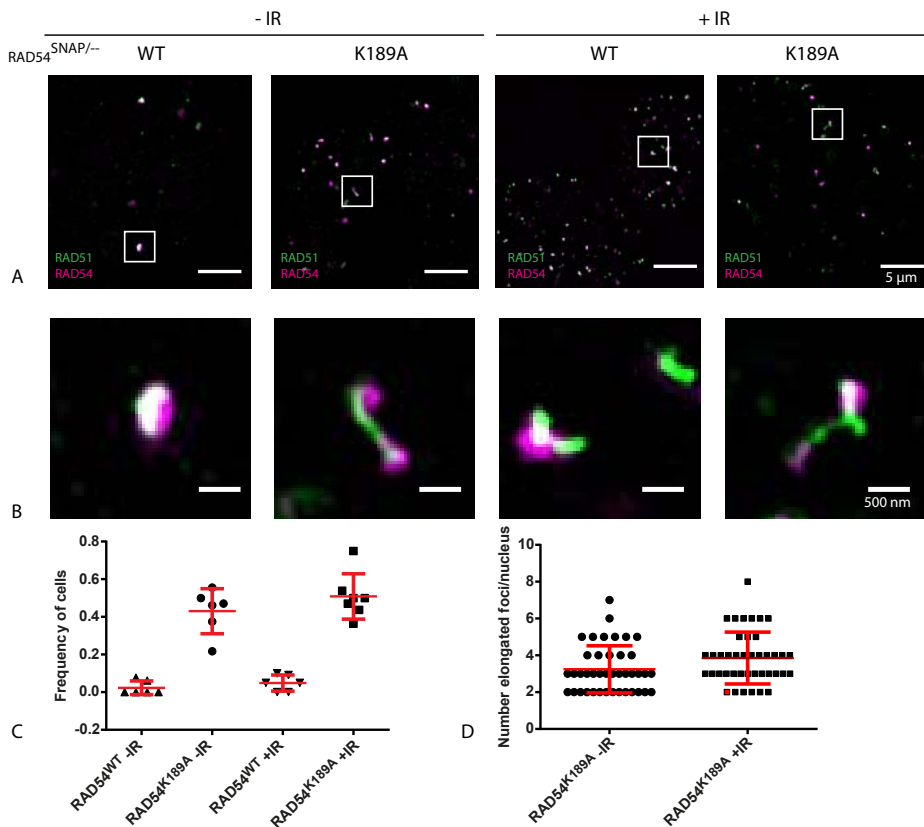


**Figure 2 Super resolution imaging and quantification of RAD51/RAD54.** A) SIM super resolution localization of RAD54 and RAD51 in RAD54<sup>SNAP/-</sup> and RAD54<sup>K189A SNAP/-</sup> cells. RAD54 was stained using SNAP ligand labelled with SNAP-SiR (magenta) before fixation while RAD51 is visualized using RAD51 polyclonal antibody and secondary antibody labelled with Atto488. Cells were pre-extracted as described in the methods section. In the top row, representative nuclei are shown either without ionizing radiation or after 6Gy of ionizing radiation followed by two-hour incubation before fixation. B) Examples of foci from the top row images C) Quantification of the frequency of cells with extended RAD51 foci (minimal 2 per nucleus) as detected by Structured Illumination Microscopy. Minimum 50 cells were counted, every data point represents one field of view with several cells. D) From the RAD54<sup>K189A SNAP/-</sup> cells that had elongated foci the number of elongated foci per nucleus was counted. Every dot in the plot represents one nucleus.

resolution microscopy provides the opportunity to investigate the internal distribution of RAD54 and RAD51 in foci in more detail. Therefore, we used Structured Illumination Microscopy (SIM) which makes it possible to obtain super resolution 3D images using standard fluorophores. We performed immunostainings for RAD51, while RAD54 was labelled with SNAP-SiR in both RAD54<sup>WT-SNAP/-</sup> and RAD54<sup>K189A-SNAP/-</sup> cells (Figure 2A-B). We observed the presence of long RAD51 structures in a large fraction (43%) of the cells expressing only mutant RAD54, while for wild type cells these structures were not observed (Figure 2C). Interestingly, we did not observe a significant increase (43% to 50%)

of elongated structures two hours after ionizing radiation (Figure 2C). Per cell nucleus for the elongated structures we detect on average about 3 of these long RAD51 structures, which does not increase significantly two hours after ionizing radiation (Figure 2D). We observed the presence of these elongated foci consistently in both cell lines of RAD54<sup>K189A</sup> tagged with SNAP-tag and mMaple3. Heterozygous RAD54<sup>WT/K189A-mMaple3</sup> cells did not show these elongated foci (data now shown). This data suggests that abolishing RAD54 ATPase activity alone is sufficient for the formation of the observed elongated structures. The elongated RAD51 foci are already present before damage induction and

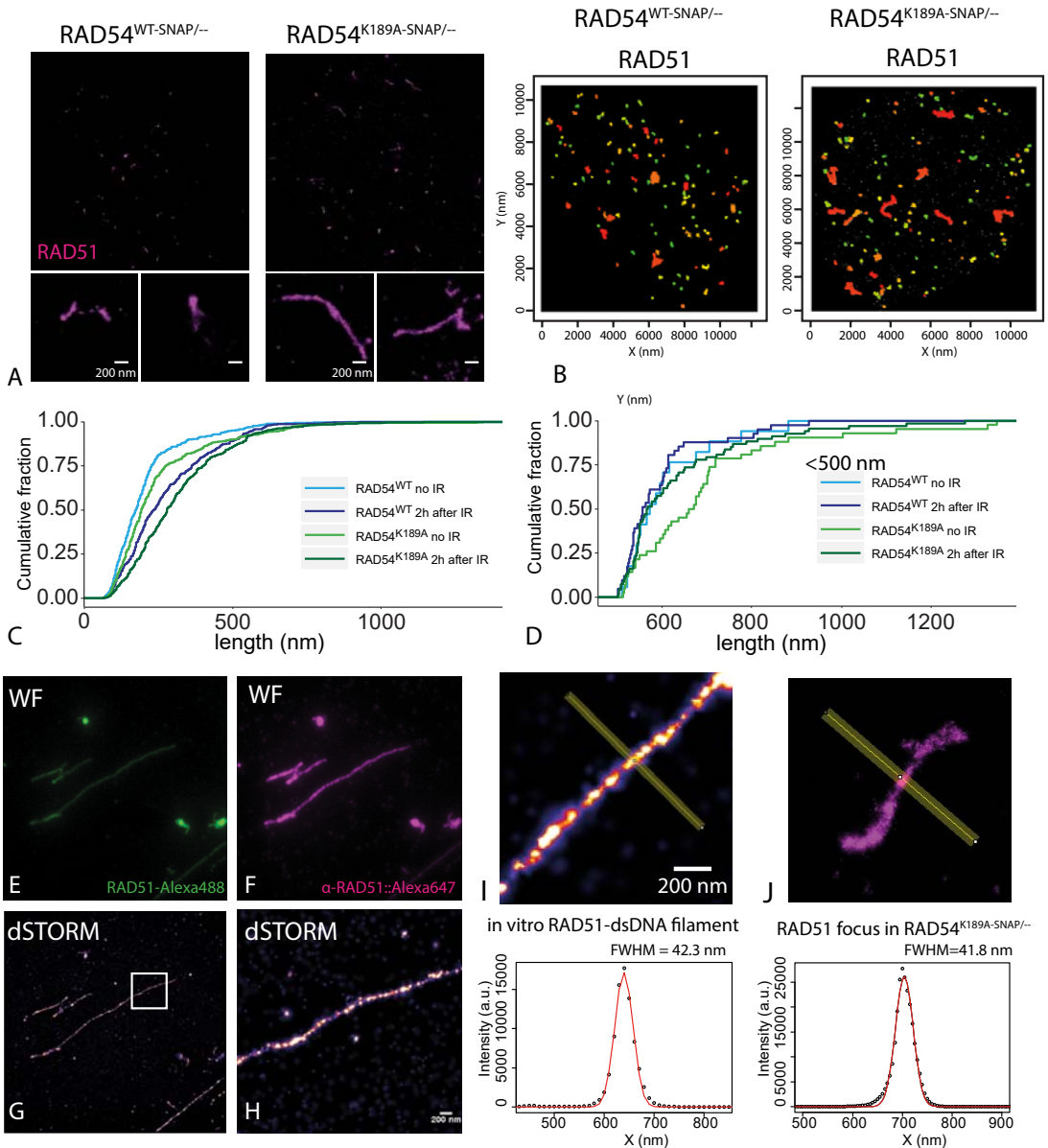


**Figure 3** Single molecule imaging of RAD51 foci in RAD54<sup>WT/-</sup> and RAD54<sup>K189A/-</sup> cells **A**) dSTORM imaging of RAD51 immunostaining in wildtype and RAD54-K189A cells. Cells were treated with 6 Gy of IR and fixed 2 hours later. **B**) Density based (DBSCAN) clustering of RAD51 localizations in respectively a wildtype and RAD54-K189A cell **C**) Quantification of the RAD51 clusters detected using DBSCAN. The estimated length of the RAD51 foci is plotted as a cumulative fraction. **D**) Subset of foci longer than 500 nm. **E**) Purified human RAD51 labelled with Alexa488 was mixed with dsDNA lambda and deposited on a clean coverslip in a buffer containing 2mM Ca<sup>2+</sup> and 1mM ATP. **F**) After crosslinking by 4 % formaldehyde the sample was stained with RAD51 antibody, washed and stained with secondary antibody conjugated with Alexa647 and visualized by widefield microscopy. **G**) dSTORM imaging of the same field-of-view. **H**) Inset of the image in G. **I**) Image of an in vitro RAD51 dsDNA filament. The line profile with the intensity profile in the plot below. **J**) The same as in I) but for an elongated RAD51 focus in a cell expressing RAD54<sup>K189A</sup>.

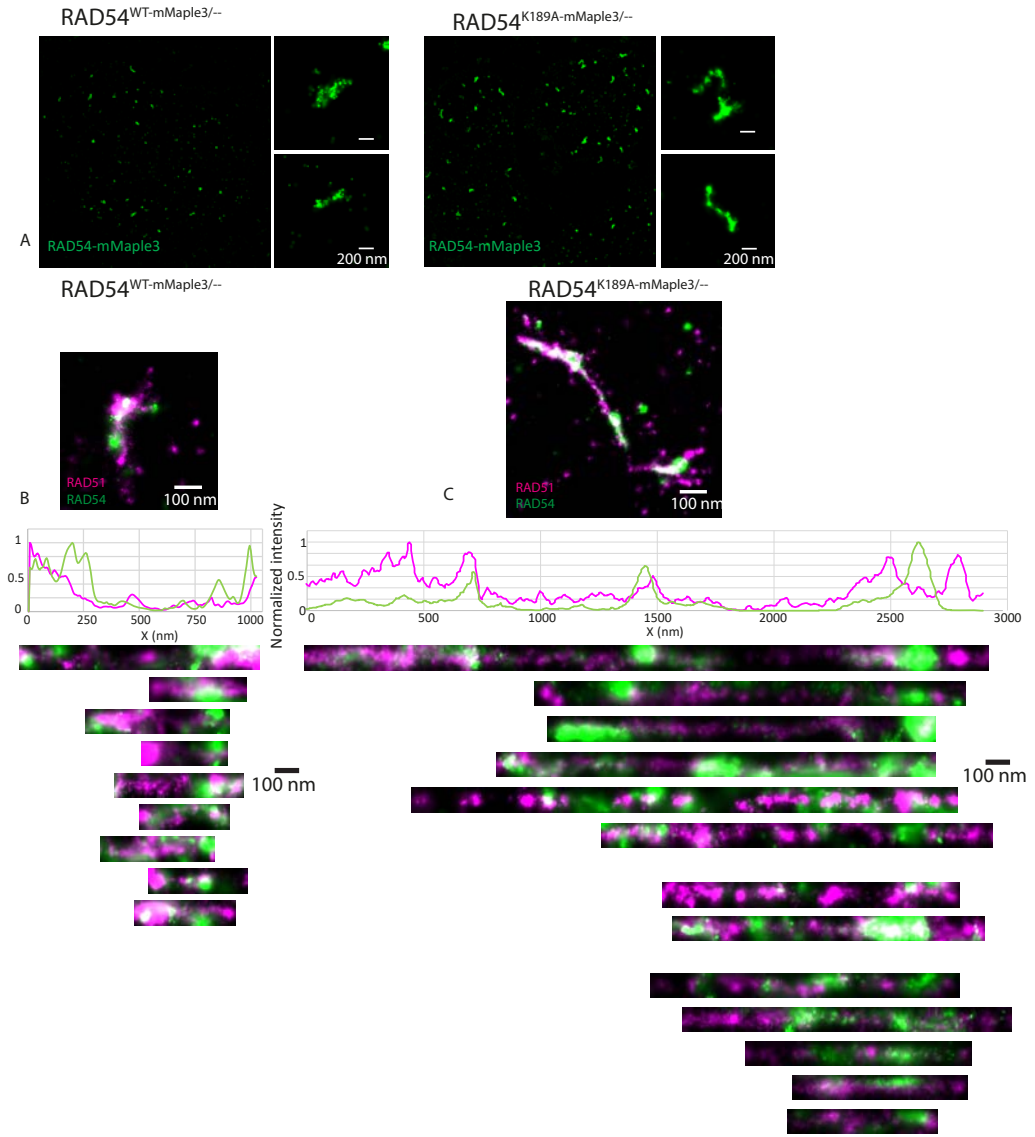


**Figure 4 Localization of RAD54 along RAD51 foci** **A)** PALM imaging of RAD54-mMaple3 in both wildtype and  $RAD54^{K189A}$  cells. Cells were treated with 6 Gy of IR and fixed 2 hours later. SMLM images of RAD54-mMaple3 of  $RAD54^{WT-mMaple3/-}$  and  $RAD54^{K189A-mMaple3/-}$  cells. Showing zoom in on single foci below. **B)** Examples of foci from dual color SMLM images of  $RAD54^{WT-mMaple3/-}$  cells and antibodies against RAD51 (secondary a.b. conjugated with Alexa647). A focus of a  $RAD54^{WT-mMaple3/-}$  cell which was straightened with the intensity profile for both RAD51 and RAD54 below. Examples of straightened foci from different cells are shown. **C)** The same as in C) but from  $RAD54^{K189A-mMaple3/-}$  cells.

the numbers do not increase directly after IR, however as will be discussed later there are indications that elongated foci might be formed much later after IR.

### Nanoscale organization of elongated RAD51 structures

We then used single molecule localization

microscopy to image cells stained for RAD51 and quantified different parameters describing the shape of the foci. The improved resolution of dSTORM indeed even more clearly reveals the elongated RAD51 foci in the  $RAD54^{K189A}$  mutant, while also the wildtype foci appear elongated, although to a lesser extent (Figure 3A). Using an automatic clustering algorithm based

on the single molecule localizations (DBSCAN, see Chapter 2) we were able to automatically detect the foci in several nuclei (Figure 3B).

Comparing the size of the RAD51 foci in cells before and after IR in both wildtype as RAD54<sup>K189A</sup> cells a relative increase in foci up to 500 nm was observed, indicating focus formation after IR (Figure 3C). However, in the RAD54<sup>K189A</sup> cells there is always a small fraction of foci that are longer than 500 nm which is not detected in the wildtype cells (Figure 3C). We then analyzed the foci that are longer than 500 nm and these were again plotted as a cumulative distribution (Figure 3D). This plot shows that after IR there are more “smaller” foci in the K189A mutant indicating the formation of normal DSB foci, while for K189A before IR there is a larger fraction of very long foci present.

To validate the antibody staining we compared the in vivo localization of RAD51 in foci with in vitro RAD51 filaments formed around dsDNA and stabilized in presence of ATP and Ca<sup>2+</sup> (Figure 3E). Part of the purified RAD51 was labelled with Alexa488 which enabled to compare the signals from the labelled RAD51 with the indirect immunostaining of anti-RAD51 antibodies. The widefield images from both channels looked very similar (Figure 3E-G). Subsequently we applied dSTORM using secondary antibodies conjugated with Alexa647, which is the same dye and antibody combination we used for cell imaging. In vitro formed RAD51 dsDNA filaments imaged by dSTORM showed a FWHM of about 40 nm (Figure 3I), while by electron microscopy the diameter of the filaments was determined to be about 10 nm (Sheridan et al., 2008). This difference can be explained by the use of secondary antibodies, which reduce the effective resolution of the dSTORM images due to the distance between the epitope and the secondary antibody with the dye. Previously it was shown that the use of secondary antibodies leads to overestimation of the diameter of filamentous structures up to 40 nm, which would explain the measured filament thickness in dSTORM in our samples (Mikhaylova et al., 2015). Also, the elongated foci which were detected in RAD54<sup>K189A</sup> cells showed similar thickness as in vitro RAD51 filaments (Figure 3J).

These results show that it is possible to detect RAD51 filaments in vitro using antibodies and that the observed elongated RAD51 structures have similar size and morphology as the in vitro formed dsDNA RAD51 filaments, suggesting that in cells the observed elongated structures represent RAD51-DNA filaments.

### **RAD54 localizes in patches along the RAD51 foci**

We were also interested in how RAD54 is localized along the RAD51 foci. Using confocal microscopy RAD51 and RAD54 foci overlap to a very high extent (Figure 1D). Using cells expressing RAD54-mMaple3 we were able to obtain super resolution images of the localization of endogenous expressed RAD54-mMaple3. In those images, we observed a similar pattern of elongated foci in RAD54<sup>K189A</sup> cells (Figure 4A). We then investigated the relative localization of wild type and mutant RAD54 along the RAD51 elongated foci by acquiring dual color single molecule localization microscopy images of RAD51 and RAD54 together (Figure 4B). In order to be able to visually compare different foci from different cells we used an ImageJ plugin, to straighten elongated and curved wildtype and K189A foci (Figure 4B and C). This enabled to visualize the relative localization of RAD51 and RAD54 along the elongated focus. We observe RAD54 localized along the entire RAD51 focus, but we frequently observed multiple bright RAD54 clusters. This was also the case for the wildtype RAD51/RAD54 foci where often one bright RAD54 cluster was observed. Some of these peaks coincide with high intensity RAD51 signal while others occur between two peaks of RAD51 signal (Figure 4C).

### **Elongated RAD51 foci in cells expressing RAD54(K189A) localize with several DSB repair factors**

In order to see whether these elongated RAD51 structures co-localize with other DSB factors we co-stained for H2AX phosphorylated at Ser139 ( $\gamma$ H2AX) and RPA. While  $\gamma$ H2AX is a generic marker for the DSB Repair response, RPA visualizes the presence of ssDNA, which is formed by DNA end resection during

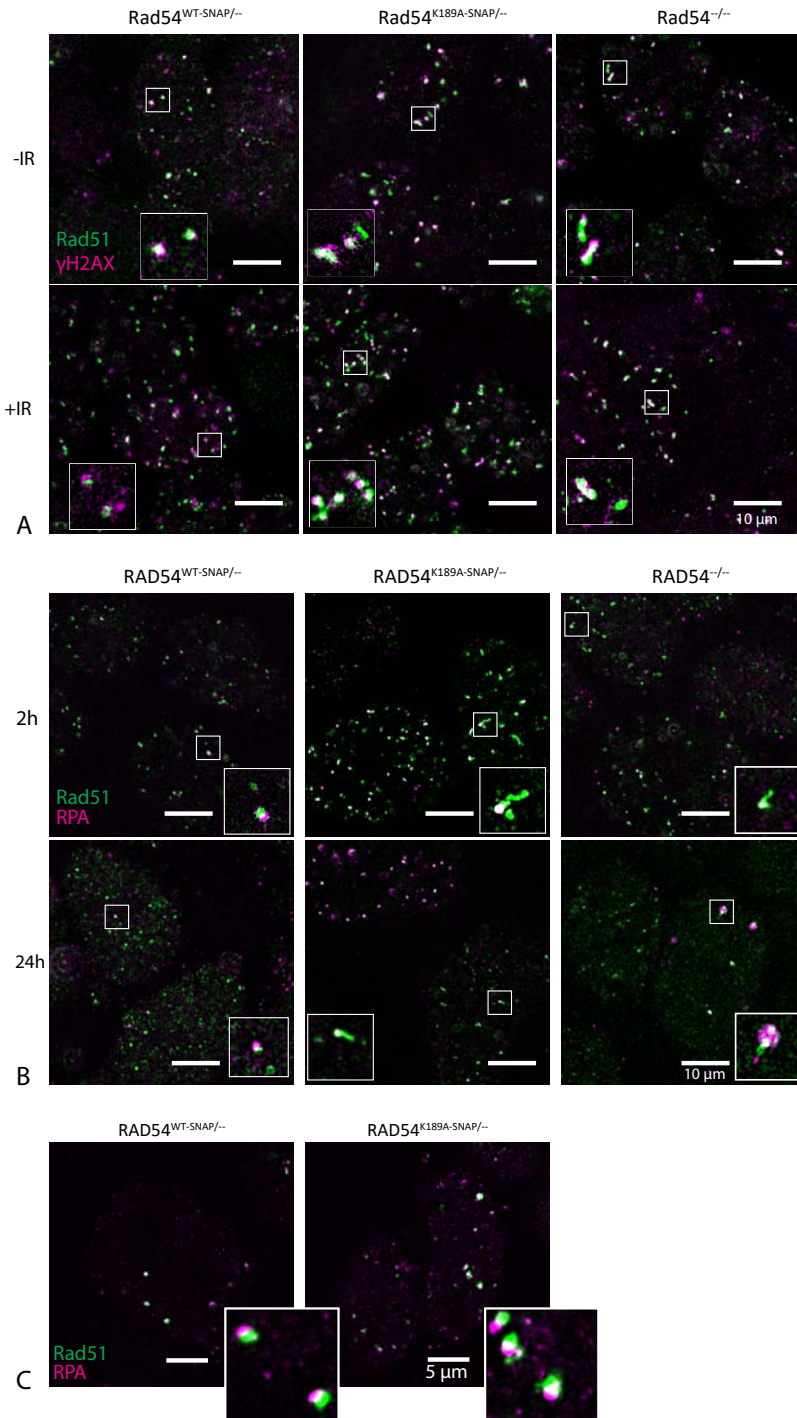


**Figure 5 Localization of different DNA Repair factors at RAD51 foci.** **A)** *RAD54*<sup>WT-SNAP-/-</sup>, *RAD54*<sup>K189A-SNAP</sup> and *RAD54*<sup>-/-</sup> cells were stained for RAD51 and  $\gamma$ H2AX without or with treatment with 6Gy of IR followed by incubation period of 2 hours before the cells were fixed. Representative SIM images are shown. **B)** *RAD54*<sup>WT-SNAP-/-</sup>, *RAD54*<sup>K189A-SNAP</sup> and *RAD54*<sup>-/-</sup> cells were stained with antibodies against RAD51 and RPA after treatment with 6Gy of IR followed by incubation period of either 2 or 24 hours before the cells were fixed. Representative SIM images are shown. **C)** Examples of cell nuclei irradiated with alpha particles forming localized tracks of foci and cells were fixed after 2 hours. Cells were stained with antibodies against RAD51 and RPA. Representative SIM images are shown.

homologous recombination. For  $\gamma$ H2AX we observed that in both wildtype cells as well as in cells that lack functional RAD54, a large number of RAD51 foci colocalize with  $\gamma$ H2AX, however we do clearly observe that  $\gamma$ H2AX does not follow the same elongated pattern as the RAD51 foci (Figure 5A). Also for RPA we did not observe localization along the entire elongated focus but instead we frequently observed a focus of RPA near the very elongated foci (Figure 5B). Two hours after treatment with ionizing radiation we observed RPA foci in both wild type and mutant cells, however after 24 hours in wild-type cells the numbers of RAD51 and RPA foci appear to decrease again, while in the mutant and RAD54 knock out cells we still observe elongated RAD51 foci and also many cells with RPA foci, which suggests that DSB repair is indeed impaired in these mutants.

Additionally, we induced DSBs by irradiation with alpha particles, and observed, in both WT and cells with mutant RAD54, accumulation of RAD51 and RPA after 2 hours, the foci along the alpha track are similar in both the wild type and mutant cells (Figure 5C). This shows that RAD54<sup>K189A</sup> cells are able to form RAD51/RAD54 foci upon induction of damage. However, the observed elongated RAD51 foci appear to not form right after induction of DNA damage, but might appear at later time points.

### **Foci formed in cells expressing RAD54(K189A) are sensitive to hyperthermia**

In order to further understand the nature of the elongated RAD51 foci in the mutant cells, we investigated whether RAD51 foci disappear after treatment with mild hyperthermia. It was previously shown that hyperthermia inhibits the formation of RAD51 foci, which is suggested to be caused by the degradation of BRCA2, the protein which is loading RAD51 on the ssDNA ends of the DSB (Krawczyk et al., 2011). Interestingly, we observe that not only the formation of RAD51 foci is inhibited by hyperthermia, but also RAD51 foci which are already formed after treating cells with IR disappear after hyperthermia treatment. In these experiments, we first used ionizing radiation to induce DNA damage

in the cells followed by a two-hour incubation of the cells to allow RAD51 focus formation, subsequently the cells were exposed to 1.5 hour of mild hyperthermia at 42 °C after which we fixed the cells (Figure 6A). For the wild type RAD54-mMaple3 cells we do observe a complete disappearance of the foci after 1.5 hour of hyperthermia, while the cells treated at 37 degrees do show normal focus formation (Figure 6B). This is also the case for the cells expressing RAD54<sup>K189A</sup>, where both spontaneous as well as irradiation-induced RAD51 foci are not detectable after hyperthermia. To see whether RAD54 itself is degraded upon hyperthermia we quantified the summed intensity of the nuclear RAD54 of multiple nuclei using RAD54-GFP cells (Figure 6C). The photo stability of GFP is still better than photoswitchable proteins which made this a more reliable analysis. We indeed observe a decrease in the total RAD54 signal in the nuclei after hyperthermia and observe just like with the mMaple3 cells the complete disappearance of the foci. The degradation of RAD54 protein could have the effect of RAD51 being released from the DNA. However, since in the RAD54 knock out cells we still observe RAD51 foci this would be an unlikely explanation.

### **RAD54 exhibits different dynamic states**

To understand how the localization of RAD54 at elongated foci relates to the dynamic behavior of individual RAD54 molecules we applied single-particle tracking. The fast diffusing properties and relatively high concentration of RAD54 protein in the cell nucleus makes it a challenge to track individual RAD54 proteins using GFP knock-in cells (Reuter et al., 2014). Therefore, we used the SNAP-tag which allows to limit the number of labelled proteins, by adjusting the concentration of the SNAP-tag substrate. The high brightness, stability and cell permeability of the recently developed SiR dye (Lukinavičius et al., 2013) coupled to the SNAP binding molecule made it possible to acquire data at an interval of 20 milliseconds and to follow individual molecules for several subsequent frames.

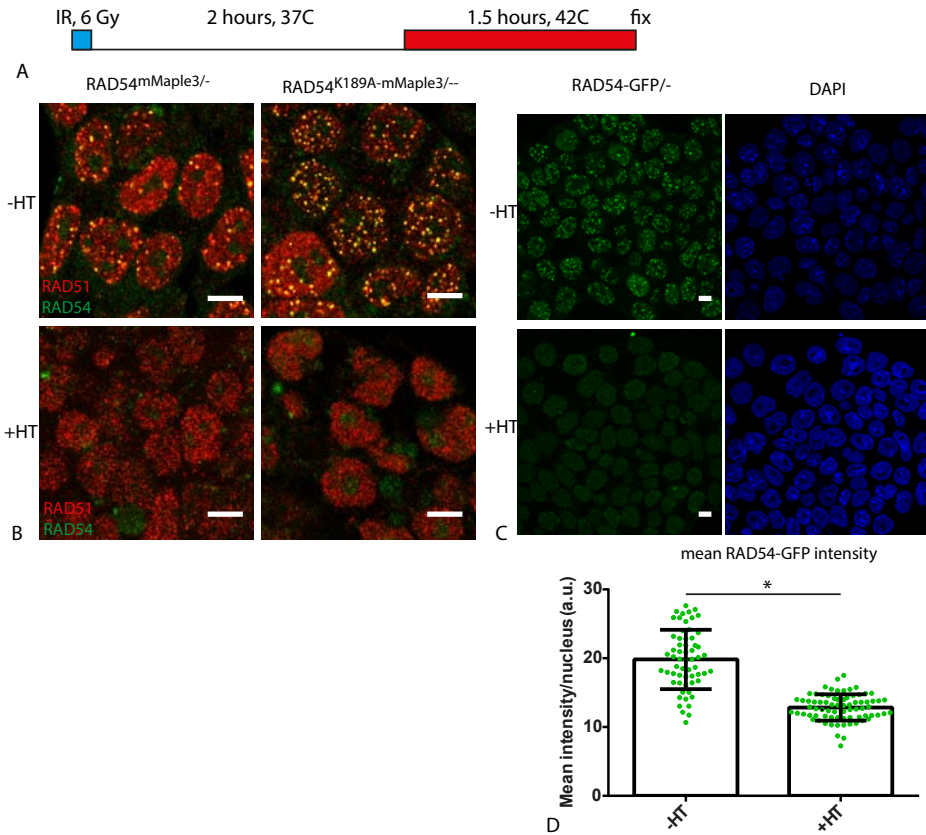


**Figure 6** RAD51 foci are sensitive to mild hyperthermia. **A)** Experimental timing of the hyperthermia experiment, cells were treated with 6Gy of ionizing radiation and incubated for 2 hours at 37C, subsequently they were subjected to 1.5 hours of hyperthermia at 42C and afterwards fixed directly. **B)** RAD54-mMaple3, wildtype and K189A, cells were treated by hyperthermia, showing the complete disappearance of both RAD51 and RAD54 foci. **C)** RAD54<sup>GFP/-</sup> cells treated with hyperthermia according to the described protocol. Cells were fixed and stained for DAPI. The summed intensity per nucleus was quantified in **D)**.

Analysis of the apparent diffusion coefficient of single RAD54 tracks showed two clearly separated populations; an immobile fraction that peaks at  $0.01 \mu\text{m}^2/\text{s}$  while the mobile fraction peaks at about  $3.5 \mu\text{m}^2/\text{s}$ . FRAP experiments on RAD54 already showed that RAD54 is a very mobile protein and we indeed observe the same in single particle tracking (Figure 7A, B). The detected immobile molecules appear to quite well overlap with foci that can be seen in the single frame image that was acquired before particle tracking (Figure 7C). However, thermal drift and movement of the cell and foci during acquisition can result in some differences between snapshot and tracking movie. We do not observe a large difference between in the dynamics of RAD54 in wildtype cells treated without or with

ionizing radiation. While for RAD54<sup>K189A/-</sup> cells the fraction of immobile tracks clearly increased after radiation (Figure 7B). Interestingly, the apparent diffusion constants for the mobile molecules in both the wild type and mutant cells is very similar. This is to be expected, since this is the diffusive behavior of the protein, which apparently is not affected in the mutant. In line with the observation of increased numbers of foci in the mutant either the  $k_{\text{off}}$  of the protein is different or the number of binding sites is increased, which then will result in a larger bound fraction.

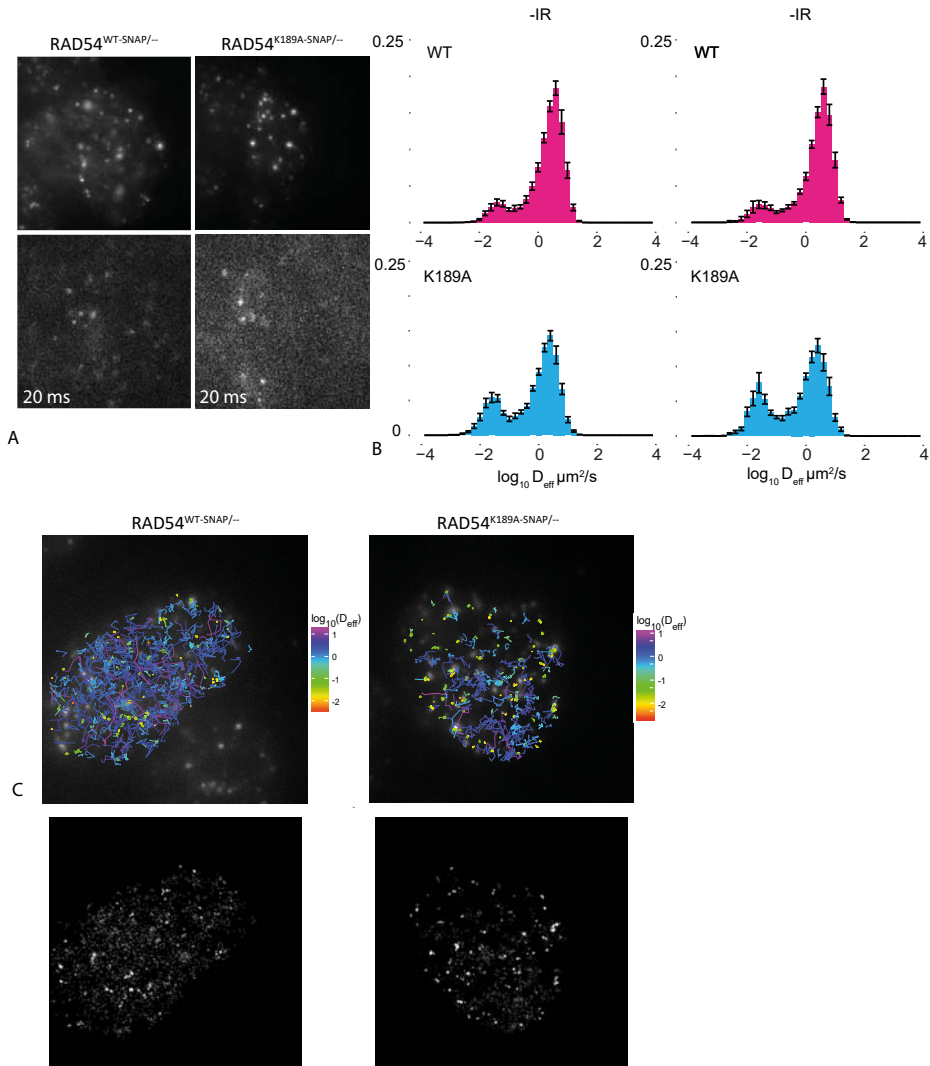


**Figure 7 Dynamics of RAD54 revealed by single particle tracking.** **A)** Example images of RAD54-SNAP cells labelled with SiR dye. On the top a widefield snapshot was taken while in the bottom images single frames from single molecule tracking videos are shown. **B)** The distribution of effective diffusion coefficient was calculated for the different indicated conditions by tracking of single molecules. At least 10 cells were imaged per condition. **C)** Examples of cells that were used in the analysis showing the individual tracks color colored with the estimated effective diffusion coefficient. Below a super resolution reconstruction was made based on the detected signals by single particle tracking.

### Visualization of immobile RAD54 molecules in the focus

To correlate the fixed cell imaging with the particle tracking we aimed to visualize the localization of RAD54 in living cells using RAD54-mMaple3 ES cells. We can observe that although a large fraction is rapidly exchanging in both WT and K189A cells some of the RAD54 proteins are retained at the focus especially in the mutant. We therefore used local photo

switching to visualize the immobilized RAD54 molecules at the foci. When molecules are photoconverted inside the focus, the mobile and short interacting molecules will rapidly diffuse out of the focus while the immobile proteins will retain at the focus. In this way, we can specifically visualize the localization of the immobilized molecules. To locally photo switch the RAD54 molecules a confocal laser scanning setup was used, which enables us to



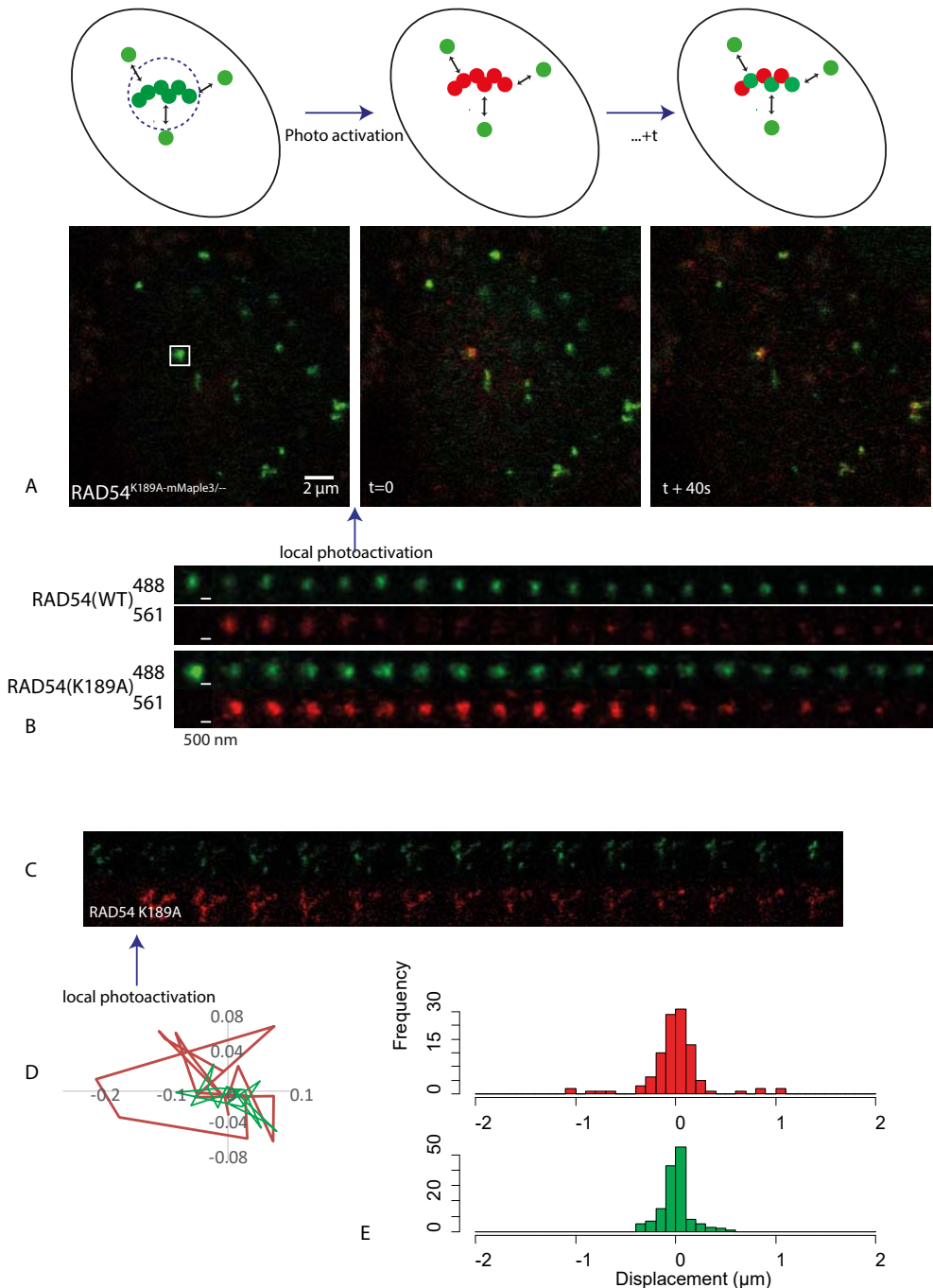


**Figure 8 Local photoconversion visualizes the dynamics of the bound RAD54 protein fraction.** **A)** Using a squared ROI a single focus is photoconverted in a cell nucleus and followed in time. As indicated in the cartoon above during the recording mobile and short interacting molecules will be exchanged (green), while the immobile molecules will remain (red). **B)** Typical examples of a photoswitch experiment with a RAD54 wildtype and K189A focus. **C)** Example of a K189A focus which shows different patches of mobile (green) and immobile (red) at the focus. **D)** The displacement of K189A mutant foci was analyzed. Here an example is shown of the displacement over time for both the mobile (green) and immobile (red) fraction. **E)** The distribution of displacements taken from several foci ( $n=20$ ) for both mobile (green) and immobile (red) fraction.

photo convert RAD54-mMaple3 proteins in a predefined region (Figure 8A). Subsequently we followed the cell in time for about 2 minutes. In line with the particle tracking data and with previous FRAP experiments we observe for the wild type RAD54-mMaple3 cells that the red photo switched molecules are rapidly exchanged by green molecules, while for RAD54-K189A cells a fraction of red molecules (remaining in the foci) is detected for a much longer time, allowing to determine where within DSB foci these mutant proteins are immobilized (Figure 8B). For both wildtype and mutant cells, foci were selected that were relatively small and spherical in size to be able to compare the wildtype and mutant foci. Especially in the mutant cells we can follow the immobile fraction for tens of seconds across multiple frames and see how their localization and clustering within the foci changes in time. Interestingly, we observed highly dynamic movement of the cluster immobile of molecules (Figure 8C). We could follow the relative position of the green (constantly exchanging) region and red (immobile) spot and measure their frame by frame displacement. This analysis shows that the immobile cluster of RAD54 molecules is very dynamic within the foci. This movement is also different when comparing the regions in the focus where rapid exchange takes place (Figure 8D, E).

## Discussion

In this study, we used several advanced fluorescence microscopy techniques to analyze the dynamics and localization of RAD54 and RAD51 in mouse embryonic stem cells. Using single molecule microscopy we could follow and localize individual RAD54 proteins in intact cells and further investigate the previously studied ATPase-dead K189A mutant of RAD54 (Agarwal et al., 2011). We used knock-in cell lines, which enabled us to exclude the potential effects of aberrant protein expression and the presence of untagged wild type protein on the localization and dynamics of the proteins.

Mouse ES cells are known to have higher numbers of spontaneous DSB foci compared to differentiated cells, likely because these cells

are highly dependent on homologous recombination. In cells lacking the ATPase activity of RAD54, however, there is an even higher number of spontaneous foci. Agarwal et al. have shown that the increase in foci numbers does not directly correlate with higher levels of DNA damage, measured by the relative amount of H2AX S139 phosphorylation. However, it was observed that in cells lacking RAD54 ATP activity there was no decrease in foci numbers several hours after induction of DSBs and foci did not redistribute to the cell periphery as was observed in wild type cells (Agarwal et al., 2011). All together, these observations suggest that loss of RAD54 ATPase activity results in a defect HR, after RAD51 is already localized at the site of damage.

### Loss of RAD54 ATPase activity results in the formation of elongated RAD51 foci

Besides elevated foci numbers in RAD54<sup>K189A</sup> cells we observed very elongated RAD51/RAD54 foci present in about 45% of the RAD54<sup>K189A</sup> cells before and two hours after damage (43 and 50%, respectively), but we did not observe them in wildtype or heterozygous cells. The fact that the elongated foci are present already before induction of damage suggests that these elongated foci are not formed immediately at the onset of DNA repair. Previous studies have shown that RAD51 overexpression can cause the formation of worm-like structures in the cell nucleus (Raderschall et al., 2002). In our cell lines, we did not observe clear intensity differences of the total amount of nuclear RAD51 in the nuclei between wildtype and mutant cells. Also, the elongated RAD51/RAD54 structures we observed in the K189A cells do not extend to a full network of filamentous RAD51, but just form a couple of long structures per cell nucleus. Recently it was shown that in cells in which both RAD54 and RAD54B expression is suppressed the formation of RAD51 in wormlike structures can also take place without overexpression of RAD51 (Mason et al., 2015). This is supported by the *in vitro* observation that both yeast and human RAD54 are able and required to displace RAD51 from dsDNA (Mason et al., 2015). However, there is

a clear difference between these RAD51 over-expressing patterns (in which most probably RAD51 is not present in filaments on either ssDNA or dsDNA) and the elongated foci we detected, which are supposedly regulated by RAD54 and its ATPase activity.

In search for the origin and nature of these elongated foci we observed that also RAD54 is present at the elongated foci, but other DSB factors (RPA,  $\gamma$ H2AX) did not localize clearly along the structures. Interestingly, we observed that RPA forms small spherical foci at the end of these elongated foci, which suggest the presence of resected DNA at those foci. After hyperthermia we observed a complete disappearance of all RAD51 foci, which is thought to be caused by the degradation of BRCA2 (Krawczyk et al., 2011). The fact that the elongated foci disappear after hyperthermia could be an indication that they still exhibit some characteristics of genuine DSB foci formed after induction of DNA damage. Since the structures are also visible in the RAD54 knock out cells this observation cannot be solely explained by the degradation of RAD54, which suggests a role for BRCA2 in the disappearance of the foci.

### **Elongated RAD51 foci could be long lasting DSBs**

However, there are hints that the elongated structures are the remainders of previously formed DSBs. In our data, there are indications that 24 hours after irradiation more cells contain the elongated foci, something that needs to be further explored in the future. In meiotic cells elongated RAD51 structures were previously observed in cells which do not express RAD54, and the elongated structures especially accumulate at the later stages of meiosis (pachytene, diplotene) (Wesoly et al., 2006). The accumulation of these structures in later meiotic stages suggests that indeed these long structures are leftovers of RAD51 filaments formed during DSB repair. Furthermore a different study showed that cells that lack functional RAD54 have higher level of chromosomal aberrations and anaphase bridges (Mason et al., 2015), which could be the result of persistent DSBs or other repair intermediates. Recently it

was also shown that phosphorylation of RAD54 at residues near the ATPase domain is responsible for removal of RAD51 at replication forks at the right moment (Spies et al., 2016). Also, cells lacking RAD54 can be further sensitized for DNA damage by knocking-out other DSB factors, for example Mus81 (Ghamrasni et al., 2016; Matulova et al., 2009). This suggests that when RAD54 is not present, repair of the DSB could be directed to a RAD54 independent repair pathway, however in some cases when repair fails this then may lead to persistent immobilization of RAD51.

### **RAD54<sup>K189A</sup> is localized in regularly spaced patches along elongated RAD51 foci**

DSB Repair foci are a very useful read out to study mechanisms of DSB Repair. However, the internal organization of DSB Repair foci in vivo is still an unresolved question. It is clear from microscopy images that some repair factors are more spread around the chromatin (gH2AX, 53BP1), while other factors form more confined foci (Bekker-Jensen et al., 2006). However, the resolution limit does not allow analysis of the localization of proteins within the foci. When studying the relative localization of RAD51 and RAD54 in detail we observed heterogeneous distributions of RAD54 along the RAD51 focus, with several bright clusters. Possibly, In vivo RAD51 is not always present in continuous filaments, which could be beneficial for strand invasion and joint molecule formation (Van Komen et al., 2002). It has recently been suggested that RAD54 preferentially binds at the gaps of RAD51 filaments (Wright and Heyer, 2014), which could explain our observations of discontinuous patches of RAD54 along the RAD51 foci. The next question is whether we would be able to detect RAD51 filaments in intact (fixed) cells. Electron microscopy and SFM are not really suited to address this question. Assuming that in some cases resection of the ends can take place multiple kilo bases away from the break, this would lead to a filament of around 340 nm per 1 kb of RAD51 filament. Differently stated a RAD51 filament of 1  $\mu$ m long will contain about 3kb of DNA. These dimensions are within

reach to be resolved with dSTORM. We could show that these elongated foci are very thin structures with similar dimensions as in vitro formed dsDNA RAD51 nucleoprotein filaments, suggesting the structures observed in cells, represent RAD51 filaments on DNA.

### **Immobilization of RAD54 after ionizing radiation is only detectable in the K189A mutant**

Using single particle tracking we are able to investigate the dynamics of individual RAD54 proteins. We observed for wildtype RAD54 that it exhibits very dynamic mobility with only a small immobile fraction. In line with previous FRAP experiments of RAD54 the single particle tracking showed that the RAD54 interactions at the foci are only very short lived in the sub second range. In that perspective, it is also interesting that we do not observe an increase in the number of immobile molecules after IR in wildtype cells. In the mutant, we observe an increased immobilization after irradiation, which could be caused by the increase in binding sites for RAD54 since more RAD51 is present in filaments, while for wildtype we cannot detect an increased immobilization after IR. However, the residence times of wild type RAD54 molecules are very short, while for mutant molecules the residence times are much longer which we are able to detect by an increased immobilization after ionizing radiation. In the mutant cells, we observe a fraction of the RAD54 molecules that is immobile, nonetheless we observe a sub-population of mutant RAD54 which is still diffusing around, this could relate to the relative concentrations of RAD51 and RAD54 proteins in the nucleus. Previous single molecule tracking experiments have shown that RAD51 compared to RAD54 has a relatively slow mobility, since it is travelling together with BRCA2 throughout the nucleus (Reuter et al., 2014). The fast mobility of RAD54 compared to RAD51 suggests the specific interaction between the proteins is at RAD51 protein bound to the DNA. This is supported by our super resolution images which showed in the mutant many RAD54 proteins bound to the elongated RAD51 structures.

### **Clusters of immobile RAD54 are highly dynamic within DSB foci**

There are several hundred RAD54 molecules present at the focus, of which in the RAD54<sup>K189A</sup> mutant a fraction is immobile. Using local photo conversion of foci, we were able to specifically visualize the immobile RAD54<sup>K189A</sup> molecules and study their dynamics relative to the rapidly exchanging molecules. What we see is a very dynamic movement of the immobilized molecule clusters relative to the regions where RAD54 molecules exchange at a high rate, and interestingly, even when using confocal microscopy, it is possible to see that the signals of dynamic and immobile fractions are not simply overlapping. The very dynamic movement but also the internal dynamics of DSB foci which we observe could be a mechanism in the homologous recombination pathway to facilitate homology search. The dual color super resolution imaging showed that the RAD54 molecules are closely associated with RAD51. In the ATPase mutant, this suggests that RAD54 is stuck at the immobilized RAD51. We could therefore, for the first time, although indirectly, image the dynamics of immobile RAD51. For the future, it would be very interesting to see whether proteins specifically can interact with RAD51 filaments which brings the possibility to follow the repair process in real-time. Further exploration of methods to follow the localization of the immobile molecules from the bulk would be highly enlightening to not only study the internal structure but also internal dynamics of DSB foci. A detailed analysis of the internal dynamics of DSB foci will give useful insight about how the biochemically well-studied processes essential for DSB repair, like resection, homology search and strand invasion are regulated inside the cell nucleus in the complex context of chromatin.

## Materials and Methods

### Cell culture

IB10 mES cell lines were cultured in DMEM supplemented with BRL conditioned medium, L-glutamine, Pen Strap and 10% FCS and grown on dishes coated with 0.1% Porcine gelatin. For live cell imaging cell medium was replaced by Fluorobrite medium (Life Technologies) supplemented with LIF, L-Glutamine and 10% FCS.

### Generation of gene targeting constructs

Constructs for gene targeting were based on the original targeting construct with GFP (Agarwal et al., 2011). The GFP was replaced by a cassette containing a kanamycin selection cassette using Lambda Red recombineering in *E. coli*. Subsequently the constructs were digested by MluI and using Gibson Assembly the sequences of mMaple3 and SNAPtag were integrated into the construct.

### Generation, selection and validation of the ES cell lines

To obtain cells homozygous recombinant RAD54 from the right allele, RAD54<sup>+/-</sup> cells were used, with a hygromycin selection marker on the RAD54 knock-out allele (Tan et al., 1999). The targeting constructs were digested by PvuI and electroporated in RAD54<sup>+/-</sup> IB10 cells. Using the selection marker present on the target sequence cells were selected by puromycin. Subsequently cells were also selected by hygromycin. To obtain homozygous clones, clones were picked from plates under selection of both puromycin and hygromycin. After expanding these colonies genomic DNA was obtained by phenol extraction and clones were screened using a genotyping PCR on the genomic DNA. Multiple positive clones were further validated by Southern blot. Genomic DNA was digested using StuI restriction enzyme and ran over night on a 0.5% agarose gel. The DNA was blotted on a membrane and hybridized with a P<sup>32</sup> labelled DNA probe ranging exon 7 and 8.

Expression of the protein was validated by western blot. Protein samples were obtained from lysed cells. Protein concentration was determined using Lowry assay and 50 µg of protein

was loaded per sample on the gel. Protein was run on an 8% SDS-PAGE gel and subsequently blotted on a nitrocellulose membrane. RAD54 was detected using a goat polyclonal RAD54 (D-18, Santa Cruz) antibody followed by incubation with secondary anti-goat IgG HRP antibody.

### Sample preparation for microscopy

Cells were plated on glass that was coated with a drop of 25 µg/ml Laminin (from mouse Engelbreth-Holm-Swarm (EHS) sarcoma, Roche) solution for 1 hour at room temperature. For fixed cell experiments the cells were cultured on 18mm round coverslips (thickness 1.5H, 170 ± 5 µm). Cells expressing SNAPtag were labelled with SNAP-Cell 647-SiR (New England Biolabs) at the recommended concentration of 3 µM for half an hour followed with 3 times washing with medium.

For live cell imaging cells were grown in µ-Slide 8 Well Glass Bottom (Ibidi) coated with laminin (Roche). For single particle tracking cells were labelled with medium with 3 nM SNAP-Cell 647-SiR (New England Biolabs), followed by 3 washing steps of 10 minutes with medium. During imaging cells were kept at 37 °C and 5% CO<sub>2</sub> using a Tokai Hit stage incubator.

When indicated, cells were irradiated the day after plating using a <sup>137</sup>Cs source with 6 Gy of ionizing radiation.

### Immunofluorescence

Cells were washed with PBS. When indicated, cells were pre-extracted at 4°C for 1 minute using Triton buffer for RAD51 (0.5% Triton X-100, 20 mM Hepes-KOH (pH 7.9), 50 mM NaCl, 3 mM MgCl<sub>2</sub>, 300 mM sucrose). Cells were fixed in 2% PFA in PBS for 20 minutes. After fixation, the cells were washed and permeabilized using PBS with 0.1% Triton. The cells were blocked with PBS+ (0.5% BSA/Glycine in PBS) for 20 minutes. Cells were incubated with primary antibody in PBS+ for 2 hours, washed with 0.1% Triton. Subsequently the samples were incubated for one hour with secondary antibody conjugated with either Alexa 647 (Life Technologies) or Atto488 (Rockland). Primary antibodies used in this study are: rabbit anti-RAD51 (van Veelen et al., 2005), mouse anti-γH2AX (Millipore) and

mouse anti-RPA32 (Abcam).

## Microscopy and super resolution imaging

All imaging was done using a Zeiss Elyra PS1 setup equipped with modules for confocal, SIM and SMLM imaging. For SIM the images were acquired using a 63x objective. Z-stacks were acquired with 5 rotations and 5 translations of the SIM grid. Images were reconstructed using the provided algorithm from Zeiss with the automatic settings. For SMLM with Alexa 647 coverslips with cells were mounted in a coverslip ring and incubated in a dSTORM buffer containing 25 mM MEA (Sigma), Glucose Oxidase (Sigma), Catalase (Sigma) and 10% Glucose in Tris HCl pH 8.0. If only mMaple3 was used for super resolution imaging the sample was mounted in PBS pH 7.4. For every channel 5 000-20 000 frames were acquired. Drift was corrected using 100nm Tetraspeck beads (Molecular Probes) or single color data the channels were aligned using an image correlation-based algorithm (ZEN, Zeiss).

## Quantification of SMLM data

Single molecule localization files were loaded in R using the in house developed SMoLR package. The package was also used for the automatic detection of RAD51 foci using a DBSCAN algorithm (Hahsler, 2015). From the defined clusters features were extracted based on the localizations. The length of the clusters was defined as distance between the extremities along the major axis of the cluster, which is estimated by using a principal component analysis of the x,y coordinates (Levet et al., 2015).

For linearization of RAD54/RAD51 foci the Straighten plugin in ImageJ (Kocsis et al., 1991) was used. A manual definition of a line through the RAD51 focus was used followed by automatic refinement of the nodes to improve straightening. Subsequently the RAD54 signal was straightened by applying the same straightening to the RAD54 signal.

## Particle tracking analysis

Single molecules were localized from the recorded movies by Gaussian fitting using SOS

plugin (Reuter et al., 2014) in ImageJ. Using the SOS plugin nearest neighbor-linking was used to obtain tracked molecules. Particles within a 900 nm radius were linked, with a maximum time gap of one frame. Tracks with a length of 10 frames or longer were included in the analysis. Further analysis was done using R (R Core Team, 2016). The Mean Square Displacement (MSD) was calculated for the individual tracks and fitted using linear regression with a fixed offset equal to the experimentally determined localization precision. The localization precision was determined (31 nm) by SNAP-SiR dyes deposited on glass. The average MSD of multiple videos at  $t=20$  ms was used to determine the localization precision (Van Royen et al., 2014).

## Local photo switching dynamics

RAD54 wildtype and K189A mutant cells were imaged using the Zeiss Elyra confocal modality. A region of was selected Next an 30x30 pixel area (1.3x1.3 $\mu$ m) containing the focus was illuminated with 5% 405nm laser (20 mW) for 50 iterations. Images were recorded for 20 frames with a 5s interval using a GaAsP (Gallium Arsenide Phosphide) detector. Image analysis was done using Fiji (Schindelin et al., 2012). First of all, the photo converted focus was using the center of mass of the summed intensity of the red and green signal together the focus was centered in every frame in the time lapse and saved as a new stack. Within the stack the relative position of the green, red and summed images was calculated.

## Acknowledgments

We thank Hanny Odijk for help with western blotting, Johan Slotman for advice and discussion of the SIM and STORM analysis and Marcel Reuter for support in single molecule tracking analysis.

## References

- Agarwal, S., van Cappellen, W.A., Guenole, A., Eppink, B., Linsen, S.E.V., Meijering, E., Houtsmuller, A., Kanaar, R., and Essers, J. (2011). ATP-dependent and independent functions of RAD54 in genome maintenance. *J. Cell Biol.* *192*, 735–750.
- Alexeev, A., Mazin, A., and Kowalczykowski, S.C. (2003). RAD54 protein possesses chromatin-remodeling activity stimulated by the RAD51-ssDNA nucleoprotein filament. *Nat. Struct. Biol.* *10*, 182–186.
- Alexiadis, V., and Kadonaga, J.T. (2002). Strand pairing by RAD54 and RAD51 is enhanced by chromatin. *Genes Dev.* *16*, 2767–2771.
- Amitani, I., Baskin, R.J., and Kowalczykowski, S.C. (2006). Visualization of RAD54, a Chromatin Remodeling Protein, Translocating on Single DNA Molecules. *Mol. Cell* *23*, 143–148.
- Bekker-Jensen, S., Lukas, C., Kitagawa, R., Melander, F., Kastan, M.B., Bartek, J., and Lukas, J. (2006). Spatial organization of the mammalian genome surveillance machinery in response to DNA strand breaks. *J. Cell Biol.* *173*, 195–206.
- Betzig, E., Patterson, G.H., Sougrat, R., Lindwasser, O.W., Olenych, S., Bonifacino, J.S., Davidson, M.W., Lippincott-Schwartz, J., and Hess, H.F. (2006). Imaging Intracellular Fluorescent Proteins at Nanometer Resolution. *Science* *313*, 1642–1645.
- Bugreev, D. V., Mazina, O.M., and Mazin, A. V. (2006). RAD54 protein promotes branch migration of Holliday junctions. *Nature* *442*, 590–593.
- Chi, P., Van Komen, S., Sehorn, M.G., Sigurdsson, S., and Sung, P. (2006). Roles of ATP binding and ATP hydrolysis in human RAD51 recombinase function. *DNA Repair (Amst.)* *5*, 381–391.
- Davies, A.A., Masson, J.-Y., McIlwraith, M.J., Stasiak, A.Z., Stasiak, A., Venkitesan, A.R., and West, S.C. (2001). Role of BRCA2 in Control of the RAD51 Recombination and DNA Repair Protein. *Mol. Cell* *7*, 273–282.
- Essers, J., Hendriks, R.W., Swagemakers, S.M., Troelstra, C., de Wit, J., Bootsma, D., Hoeijmakers, J.H., and Kanaar, R. (1997). Disruption of mouse RAD54 reduces ionizing radiation resistance and homologous recombination. *Cell* *89*, 195–204.
- Essers, J., Houtsmuller, A.B., Veelen, L. van, Paulusma, C., Nigg, A.L., Pastink, A., Vermeulen, W., Hoeijmakers, J.H.J., and Kanaar, R. (2002). Nuclear dynamics of RAD52 group homologous recombination proteins in response to DNA damage. *EMBO J.* *21*, 2030–2037.
- Essers, J., Houtsmuller, A.B., and Kanaar, R. (2006). Analysis of DNA recombination and repair proteins in living cells by photobleaching microscopy. *Methods Enzymol.* *408*, 463–485.
- Fuchs, J., Böhme, S., Oswald, F., Hedde, P.N., Krause, M., Wiedenmann, J., and Nienhaus, G.U. (2010). A photoactivatable marker protein for pulse-chase imaging with superresolution. *Nat. Methods* *7*, 627–630.
- Ghamrasni, S. El, Cardoso, R., Li, L., Guturi, K.K.N., Bjerregaard, V.A., Liu, Y., Venkatesan, S., Hande, M.P., Henderson, J.T., Sanchez, O., et al. (2016). RAD54 and Mus81 cooperation promotes DNA damage repair and restrains chromosome missegregation. *Oncogene* *1–10*.
- Hahsler, M. (2015). dbSCAN: Density Based Clustering of Applications with Noise (DBSCAN) and Related Algorithms.
- Keppler, A., Pick, H., Arrivoli, C., Vogel, H., and Johnsson, K. (2004). Labeling of fusion proteins with synthetic fluorophores in live cells. *Proc. Natl. Acad. Sci. U. S. A.* *101*, 9955–9959.
- Kianitsa, K., Solinger, J. a, and Heyer, W.-D. (2006). Terminal association of RAD54 protein with the RAD51-dsDNA filament. *Proc. Natl. Acad. Sci. U. S. A.* *103*, 9767–9772.
- Kocsis, E., Trus, B.L., Steer, C.J., Bisher, M.E., and Steven, A.C. (1991). Image averaging of flexible fibrous macromolecules: the clathrin triskelion has an elastic proximal segment. *J. Struct. Biol.* *107*, 6–14.
- Van Komen, S., Petukhova, G., Sigurdsson, S., and Sung, P. (2002). Functional cross-talk among RAD51, RAD54, and replication protein A in heteroduplex DNA joint formation. *J. Biol. Chem.* *277*, 43578–43587.
- Krawczyk, P.M., Eppink, B., Essers, J., Stap, J., Rodermond, H., Odijk, H., Zelensky, A., van Bree, C., Stalpers, L.J., Buist, M.R., et al. (2011). Mild hyperthermia inhibits homologous recombination, induces BRCA2 degradation, and sensitizes cancer cells to poly (ADP-ribose) polymerase-1 inhibition. *Proc. Natl. Acad. Sci. U. S. A.* *108*, 9851–9856.
- Levet, F., Hosy, E., Kechkar, A., Butler, C., Beghin, A., Choquet, D., and Sibarita, J.-B. (2015). SR-Tesseler: a method to segment and quantify localization-based super-resolution microscopy data. *Nat. Methods* *12*, 1065–1071.
- Lukinavičius, G., Umezawa, K., Olivier, N., Honigsmann, A., Yang, G., Plass, T., Mueller, V., Reymond, L., Corrêa, I.R., Luo, Z.-G., et al. (2013). A near-infrared fluorophore for live-cell super-resolution microscopy of cellular proteins. *Nat. Chem.* *5*, 132–139.
- Mason, J.M., Dusad, K., Wright, W.D., Grubb, J., Budke, B., Heyer, W.-D., Connell, P.P., Weichselbaum, R.R., and Bishop, D.K. (2015). RAD54 family translocases counter genotoxic effects of RAD51 in human tumor cells. *Nucleic Acids Res.* *43*, 3180–3196.
- Matulova, P., Marini, V., Burgess, R.C., Sisakova, A., Kwon, Y., Rothstein, R., Sung, P., and Krejci, L. (2009). Cooperativity of Mus81-Mms4 with RAD54 in the Resolution of Recombination and Replication Intermediates. *J. Biol. Chem.* *284*, 7733–7745.
- Mazin, A. V., Alexeev, A.A., and Kowalczykowski, S.C. (2003). A novel function of RAD54 protein. Stabilization of the RAD51 nucleoprotein filament. *J. Biol. Chem.* *278*, 14029–14036.
- Mazina, O.M., and Mazin, A. V (2004). Human RAD54 protein stimulates DNA strand exchange activity of hRAD51 protein in the presence of Ca<sup>2+</sup>. *J. Biol. Chem.* *279*, 52042–52051.
- Mikhaylova, M., Cloin, B.M.C., Finan, K., van den Berg, R., Teeuw, J., Kijanka, M.M., Sokolowski, M., Katrukha, E. a., Maidorn, M., Opazo, F., et al. (2015). Resolving bundled microtubules using anti-tubulin nanobodies. *Nat. Commun.* *6*, 7933.
- Petukhova, G., Stratton, S., and Sung, P. (1998). Catalysis of homologous DNA pairing by yeast RAD51 and RAD54 proteins. *Nature* *393*, 91–94.
- R Core Team (2016). R: A Language and Environment for Statistical Computing.
- Raderschall, E., Bazarov, A., Cao, J., Lurz, R., Smith, A., Mann, W., Ropers, H., Sedivy, J.M., Golub, E.I., Fritz, E., et al. (2002). Formation of higher-order nuclear RAD51 structures is functionally linked to p21 expression and protection from DNA damage-induced apoptosis. *J. Cell Sci.* *115*, 153–164.
- Renkawitz, J., Lademann, C.A., Kalocsay, M., and Jentsch, S. (2013). Monitoring Homology Search during DNA Double-Strand Break Repair In Vivo. *Mol. Cell* *1–12*.

- Reuter, M., Zelensky, A., Smal, I., Meijering, E., van Cappellen, W.A., de Gruiter, H.M., van Belle, G.J., van Royen, M.E., Houtsmuller, A.B., Essers, J., et al. (2014). BRCA2 diffuses as oligomeric clusters with RAD51 and changes mobility after DNA damage in live cells. *J. Cell Biol.* 207, 599–613.
- Ristic, D. (2005). Human RAD51 filaments on double- and single-stranded DNA: correlating regular and irregular forms with recombination function. *Nucleic Acids Res.* 33, 3292–3302.
- Van Royen, M.E., van Cappellen, W.A., Geverts, B., Schmidt, T., Houtsmuller, A.B., and Schaaf, M.J.M. (2014). Androgen receptor complexes probe DNA for recognition sequences by short random interactions. *J. Cell Sci.* 127, 1406–1416.
- Sanchez, H., Suzuki, Y., Yokokawa, M., Takeyasu, K., and Wyman, C. (2011). Protein–DNA interactions in high speed AFM: single molecule diffusion analysis of human RAD54. *Integr. Biol.* 3, 1127.
- Sanchez, H., Kertokallio, A., van Rossum-Fikkert, S., Kanaar, R., and Wyman, C. (2013). Combined optical and topographic imaging reveals different arrangements of human RAD54 with presynaptic and post-synaptic RAD51-DNA filaments. *Proc. Natl. Acad. Sci. U. S. A.* 110, 11385–11390.
- Schindelin, J., Arganda-Carreras, I., Frise, E., Kaynig, V., Longair, M., Pietzsch, T., Preibisch, S., Rueden, C., Saalfeld, S., Schmid, B., et al. (2012). Fiji: an open-source platform for biological-image analysis. *Nat. Methods* 9, 676–682.
- Sheridan, S.D., Yu, X., Roth, R., Heuser, J.E., Sehorn, M.G., Sung, P., Egelman, E.H., and Bishop, D.K. (2008). A comparative analysis of Dmc1 and RAD51 nucleoprotein filaments. *Nucleic Acids Res.* 36, 4057–4066.
- Solinger, J. a, Kianitsa, K., and Heyer, W.-D. (2002). RAD54, a Swi2/Snf2-like Recombinational Repair Protein, Disassembles RAD51:dsDNA Filaments. *Mol. Cell* 10, 1175–1188.
- Spies, J., Waizenegger, A., Barton, O., Sürder, M., Wright, W.D.D., Heyer, W.-D.D., and Löbrich, M. (2016). Nek1 Regulates RAD54 to Orchestrate Homologous Recombination and Replication Fork Stability. *Mol. Cell* 62, 1–15.
- Swagemakers, S.M., Essers, J., de Wit, J., Hoeijmakers, J.H., and Kanaar, R. (1998). The human RAD54 recombinational DNA repair protein is a double-stranded DNA-dependent ATPase. *J. Biol. Chem.* 273, 28292–28297.
- Tan, T.L., Essers, J., Citterio, E., Swagemakers, S.M., de Wit, J., Benson, F.E., Hoeijmakers, J.H., and Kanaar, R. (1999). Mouse RAD54 affects DNA conformation and DNA-damage-induced RAD51 foci formation. *Curr. Biol.* 9, 325–328.
- van Veelen, L.R., Essers, J., van de Rakt, M.W.M.M., Odijk, H., Pastink, A., Zdzienicka, M.Z.M.Z., Paulusma, C.C., and Kanaar, R. (2005). Ionizing radiation-induced foci formation of mammalian RAD51 and RAD54 depends on the RAD51 paralogs, but not on Rad52. *Mutat. Res.* 574, 34–49.
- Wang, S., Moffitt, J.R., Dempsey, G.T., Xie, X.S., and Zhuang, X. (2014). Characterization and development of photoactivatable fluorescent proteins for single-molecule-based superresolution imaging. *Proc. Natl. Acad. Sci.*
- Wright, W.D.D., and Heyer, W.-D.D. (2014). RAD54 Functions as a Heteroduplex DNA Pump Modulated by Its DNA Substrates and RAD51 during D Loop Formation. *Mol. Cell* 53, 1–13.
- Yuan, S.S., Lee, S.Y., Chen, G., Song, M., Tomlinson, G.E., and Lee, E.Y. (1999). BRCA2 is required for ionizing radiation-induced assembly of RAD51 complex in vivo. *Cancer Res.* 59, 3547–3551.
- Zelensky, A., Kanaar, R., and Wyman, C. (2014). Mediators of homologous DNA pairing. *Cold Spring Harb. Perspect. Biol.* 6, a016451.







## **Appendix**

Summary

Samenvatting

CV

Scientific Publications

PhD Portfolio

Dankwoord

## Summary

The genomic DNA packed into chromatin has to be protected from the accumulation of damage. Consequently, a broad range of DNA repair mechanisms have been evolved to repair specific types of DNA damage. The repair of a DNA lesion requires the localization of a multitude of proteins at the site of damage, to detect the lesion, remodel the DNA and eventually repair the DNA damage. For fundamental understanding of the functioning and malfunctioning of DNA Repair proteins it is important to know the precise localization of these proteins and their relative organization in the cell. During DNA Double Strand Break Repair proteins accumulate at the sites of damage, in so-called repair foci, which are visible under the microscope. Using super resolution fluorescence microscopy, it is possible to study the organization of proteins in these foci at near-molecular resolution, making it possible to get insight in the molecular distribution within the cell.

**Chapter I** gives a general introduction into the topics presented in this thesis. The different pathways of DNA repair are discussed with a focus on the mechanisms of DNA Double Strand Break (DSB) repair. In general DSBs are repaired by either Non-Homologous End Joining or Homologous Recombination. Homologous recombination is an intricate repair mechanism, which by using a homologous DNA template can accurately repair the break. In the second part of the chapter recent advances in (super resolution) microscopy are discussed. Fluorescence microscopy is widely used to study to localization and dynamics of proteins in cells. However, the spatial resolution of a light microscope is limited by the diffraction of the light. In the last decade techniques emerged to circumvent this limit. Two super resolution techniques that are used throughout this thesis Structured Illumination Microscopy and Single Molecule Localization Microscopy, use different approaches to obtain high resolution information by controlling the emission of the fluorophores in the sample.

Quantitative analysis of the super resolution data presented in this thesis requires dedicated software to extract the relevant information. In **Chapter II** a software package, named SMoLR, is described, which we developed in the statistical programming environment R. The software package enables robust analysis of large single molecule localization data sets. It is especially powerful for the quantification of the organization of super resolved macromolecular protein assemblies. These assemblies, for example, DSB foci, nuclear pores or focal adhesions are present in large numbers in cells. SMoLR provides different ways to visualize the localization data along with methods to obtain statistics about the numbers and spatial organization of the proteins in the assemblies. Subsequently, we show examples of showing how the software package can be used to address different biological questions using single molecule localization microscopy.

In **Chapter III** we investigate the organization of RAD51 and DMC1 in DSB foci at several stages of meiotic prophase using super resolution microscopy. Meiosis is a reductional cell division which forms the cells required for sexual reproduction. During meiosis DSBs are induced by the cell to facilitate homology search for pairing of homologous chromosomes, which is required for a faithful segregation of the chromosomes into the daughter cells. These DSBs, induced by the nuclease Spo11, are repaired through homologous recombination. The repair through homologous recombination during meiosis requires the localization of both the recombinase RAD51 and its meiotic paralog DMC1 to the break. RAD51 and DMC1 are structurally very similar, but have supposedly different functions in repair of DSBs during meiosis. We observe differential localization of RAD51 and DMC1 in the meiotic DSB foci, where at early time points of meiosis most foci with a single RAD51 and DMC1 spot, at later time points foci with two DMC1 clusters and one RAD51 cluster are present at increasing frequency. We quantified the size and distances between these spots, which enabled us to identify a structural organization of one DMC1 spot near RAD51 while another spot was much further away. Taken this data together we used simulations to elucidate the underlying 3D organization of DMC1 and RAD51 and how this changed during progression of meiosis. These observations suggest that the two ends of the DSB are differently loaded with RAD51 and DMC1, thereby possibly regulating the homology search and strand invasion process during meiosis.

During homologous recombination in higher eukaryotes RAD51 requires BRCA2 to displace RPA and load itself on to the resected ssDNA. BRCA2 is a large multi-domain protein, which at the BRC domains can bind several RAD51 monomers. In **Chapter IV** we used scanning force microscopy to study the conformation of purified BRCA2 proteins under several conditions in vitro, and used super resolution microscopy to relate the results to the situation in the cell. In vitro, BRCA2 alone forms multimers with V-shaped structures. However, when incubated with RAD51 very elongated structures are observed. This elongated BRCA2-RAD51 complex is able to load RAD51 on ssDNA coated with RPA. Using super resolution microscopy, we then visualized the relative localization of BRCA2 and RAD51 inside DSB foci. We show that RAD51 accumulations form extended structures which can be more than 200 nm long, while BRCA2 seems to form smaller protein clusters near the RAD51 focus. Quantification of the amount of overlap between BRCA2 and RAD51, showed that a large fraction of RAD51 is not associated with BRCA2 while it is thought that BRCA2 and RAD51 are closely associated in the cell nucleus. In time after damage induction we observed that BRCA2 is nonetheless retained at the foci. The structural analysis show how the flexibility of BRCA2 is important for regulating its function, while the super resolution data shows the dynamic regulation of RAD51 at the site of damage by BRCA2.

Repair of DSBs requires many different proteins at the break at the right time and at the right concentration. Essential are proteins that regulate the organization of DNA-protein interactions, for example, by converting energy through hydrolysis of ATP. One of these proteins is the SWI/SNF heli-case protein RAD54, which is important at several steps during the repair of DSBs. It is required for the stabilization of RAD51 filaments and is also important for dissociation of RAD51 filaments from duplex DNA after strand invasion has taken place. In **Chapter V** the nanoscale localization of RAD54 is investigated. An ATPase defective mutant gave us the opportunity to further elucidate the mechanisms by which RAD54 is involved in DSB Repair. In combination with super resolution microscopy this enabled us to detect clear differences in the shape of both RAD51 and RAD54 foci in the ATPase deficient mutant compared to wildtype cells. We observed very long RAD51 structures which could be the cause of homologous recombination defect in the ATPase deficient mutant. Furthermore, we used single molecule tracking to obtain understanding in the dynamics of individual RAD54 molecules. In wildtype cells we detected almost only mobile RAD54 molecules while cells lacking RAD54 ATPase activity show a clear population of immobile RAD54 molecules. Additionally, using a photo convertible fluorescent protein we were able to locally photo convert the RAD54 proteins present at a single focus. By monitoring the focus in time we were able to separately visualize the localization of the immobile versus the mobile molecules in the foci. These experiments showed a highly dynamic internal structure of the immobile RAD54 proteins of the ATPase deficient mutant.

## Samenvatting

Het genomisch DNA dat verpakt zit als chromatine moet beschermd worden voor de ophoping van DNA-schade. Zodoende heeft er zich een breed scala aan DNA-reparatiemechanismen geëvolueerd om verschillende soorten DNA-schade te repareren. Om DNA-schade te repareren lokaliseren veel verschillende eiwitten zich rond de plek van de schade: voor het herkennen, bewerken en repareren van de DNA-lesie. Dit proces is heel duidelijk zichtbaar onder een microscoop, omdat tijdens de DNA-dubbelstrengsbreukreparatie ophopingen van eiwitten worden gevormd, zogenaamde foci. Voor het fundamenteel begrijpen van het functioneren en disfunctioneren van DNA-reparatie eiwitten is het belangrijk om de lokalisatie en de relatieve organisatie van deze eiwitten in de cel te kennen. Het gebruik van superresolutie fluorescentiemicroscopie maakt het nu mogelijk om deze eiwitten op 'bijna moleculaire resolutie' te detecteren.

**Hoofdstuk I** geeft een algemene introductie van de onderwerpen die gepresenteerd worden in dit proefschrift. In het eerste deel van de introductie worden de verschillende DNA-reparatiemechanismen met een focus op de mechanismen van DNA dubbelstrengsbreuk reparatie besproken. Over het algemeen worden dubbelstrengsbreuken (DSB's) gerepareerd via non-homologous end joining (NHEJ) of homologe recombinatie (HR). Homologe recombinatie is een complex reparatiemechanisme, waarbij RAD51 wordt geladen op de gebroken DNA-uiteinden, om vervolgens een homologe DNA-template te vinden wat gebruikt kan worden om de breuk te repareren. In het tweede deel van de introductie worden recente ontwikkelingen in (superresolutie) microscopie besproken. Fluorescentiemicroscopie is een veel gebruikte techniek om de lokalisatie en dynamiek van eiwitten te bestuderen in cellen. De ruimtelijke resolutie van een lichtmicroscoop wordt beperkt door de diffractie van het licht. In het laatste decennium zijn er technieken ontwikkeld die deze beperking kunnen omzeilen. Twee superresolutietechnieken die gebruikt worden in dit proefschrift zijn 'Structured Illumination Microscopy' en 'Single-Molecule Localization Microscopy'. Deze technieken gebruiken verschillende benaderingen om hoge resolutie-informatie uit beelden te halen door het controleren van de emissie van de fluoroforen in het preparaat.

Voor kwantitatieve analyse van superresolutiedata, zoals gepresenteerd in dit proefschrift, is gespecialiseerde software nodig om de essentiële informatie uit de data te verkrijgen. In **hoofdstuk II** wordt een softwarepakket, genaamd SMOlR beschreven wat we hebben ontwikkeld gedurende dit onderzoek. Dit is ontwikkeld in de programmeeromgeving 'R' voor de kwantitatieve analyse van 'Single-Molecule Localization' data. Het softwarepakket maakt het mogelijk om grote datasets met lokalisatiedata te analyseren. Het pakket is vooral goed geschikt voor de kwantificatie van macromoleculaire-eiwitcomplexen. Deze complexen, bijvoorbeeld DSB-foci, celkernporiën of focale adhesies, zijn in grote getale aanwezig in cellen. SMOlR maakt het mogelijk om op verschillende manieren de lokalisatiedata te visualiseren en vervolgens statistieken te verkrijgen over de aantallen en de ruimtelijke organisatie van de individuele moleculen in de eiwitcomplexen. Aan het einde van dit hoofdstuk, worden enkele voorbeelden gegeven van de manier waarop de software toegepast kan worden om verschillende biologische vraagstukken te onderzoeken en beantwoorden met het gebruik van 'Single-Molecule Localization Microscopy'.

In **hoofdstuk III** wordt de organisatie van RAD51 and DMC1 in DSB-foci tijdens de verschillende stadia van de meiotische profase bestudeerd door gebruik te maken van superresolutiemicroscopie. Meiose is een reducerende celdeling die plaats vindt tijdens de formatie van de voortplantingscellen. Om het paren van de homologe chromosomen mogelijk te maken, worden tijdens de meiose DSB's geïnduceerd door de cel. De DSB's, geïnduceerd door de nuclease Spo11, worden gerepareerd door middel van homologe recombinatie. De reparatie via homologe recombinatie vereist de lokalisatie van zowel de recombinase RAD51, alsmede zijn meiotische paraloog DMC1 op de plaats van de breuk. RAD51 en DMC1 hebben een vergelijkbare eiwitstructuur, maar hebben waarschijnlijk verschillende functies in de reparatie van DSB's in meiose. Tijdens de eerste tijdspunten van meiosis bevatten de meeste foci een enkele RAD51- en DMC1-spot, terwijl op

latere tijds punten foci met twee DMC1-clusters en één RAD51-cluster met toenemende frequentie voorkomen. Vervolgens hebben we de grootte van de spots en de afstanden tussen de spots gekwantificeerd, wat het mogelijk maakte om een structurele organisatie te bepalen van één DMC1-spot vlakbij RAD51, terwijl een andere DMC1-spot verder verwijderd was RAD51. We hebben deze data vervolgens gecombineerd met simulaties om de onderliggende 3D-organisatie van DMC1 en RAD51 te bepalen, terwijl deze verandert gedurende de progressie van meiose. Deze observaties suggereren dat de twee uiteinden van de DSB verschillend worden geladen met RAD51 en DMC1. Mogelijk kan op deze manier het vinden van homologe DNA-sequentie en invasie van de DNA-streng gereguleerd worden tijdens meiose.

Tijdens homologe recombinatie in hogere eukaryoten heeft RAD51 een ander eiwit genaamd BRCA2 nodig om zichzelf te laden op het enkelstrengs DNA, dat gevormd wordt tijdens resectie. BRCA2 is een groot multi-domeineiwit, dat door middel van de BRC-domeinen meerdere RAD51-monomers kan binden. In **hoofdstuk IV** beschrijven we hoe we gebruik hebben gemaakt van 'Scanning Force Microscopy' voor het bestuderen van de conformatie van gezuiverde BRCA2-eiwitten onder verschillende condities. Daarnaast hebben we superresolutiemicroscopie gebruikt om deze resultaten te correleren met de situatie in de cel. In vitro vormt BRCA2 V-vormige multimeren. Echter, wanneer BRCA2 samen met RAD51 wordt bestudeerd, worden zeer geëlongeerde structuren gevonden. Dit geëlongeerde RAD51-BRCA2-complex maakt het mogelijk om RAD51 op enkelstrengs DNA te laden wat beschermd wordt door RPA. Door middel van superresolutiemicroscopie hebben we vervolgens de relatieve positie van BRCA2 en RAD51 in DSB-foci in celkernen aangetoond. Allereerst observeerden we dat RAD51 accumuleert in verlengde structuren, terwijl BRCA2 kleinere eiwit clusters vormt rondom de RAD51 focus. Kwantificatie van de hoeveelheid overlap tussen het signaal van BRCA2 en RAD51 toont aan dat een grote fractie van RAD51 niet geassocieerd is met BRCA2, terwijl BRCA2 en RAD51 in de celkern over het algemeen een complex vormen. In de tijd na inductie van de DNA-schade observeren we dat BRCA2 echter wel gelokaliseerd is in de DSB-foci. De structurele analyse geeft aan hoe de flexibiliteit van BRCA2 belangrijk is bij het uitvoeren van zijn functie, terwijl de superresolutiedata laat zien hoe RAD51 dynamisch wordt gereguleerd door BRCA2.

Reparatie van DSB's vereist de lokalisatie van verschillende eiwitten op de plek van de breuk op het juiste moment en met de juiste concentratie. Daarbij zijn eiwitten die de organisatie van DNA-eiwitinteracties reguleren belangrijk, dit kunnen zij doen door energie om te zetten doormiddel van ATP hydrolyse. Eén van deze eiwitten is de SWI/SNF helicase RAD54, die belangrijk is bij verschillende stappen in het reparatieproces van DSB's. Het is belangrijk voor de stabilisatie van RAD51-filamenten, maar ook belangrijk voor de dissociatie van RAD51-filamenten van dubbelstrengs DNA nadat invasie van de DNA-streng heeft plaatsgevonden. In **hoofdstuk V** wordt de lokalisatie op nanoschaal van RAD54 bestudeerd. Een mutant zonder ATPase-functie gaf ons de mogelijkheid om de mechanismen waarbij RAD54 betrokken is bij DSB reparatie te onderzoeken. In combinatie met superresolutiemicroscopie gaf dat de mogelijkheid om duidelijke verschillen te ontdekken in de vorm van zowel RAD51- als RAD54-foci tussen de ATPase deficiënte mutant- en wildtypecellen. Daarbij zijn in de mutant zeer lange RAD51-structuren gevonden die mogelijk het gevolg zijn van defecten in homologe recombinatie in de ATPase deficiënte mutant. Bovendien hebben we single-molecule-tracking gebruikt om informatie te verkrijgen over de dynamiek van individuele RAD54-moleculen. In wildtypecellen zijn bijna alle RAD54-eiwitten mobiel, terwijl cellen die RAD54 ATPase activiteit missen, een duidelijke fractie immobiele RAD54-moleculen bevat. Door vervolgens gebruik te maken van photoconverterende fluorescente eiwitten, konden we lokaal RAD54-eiwitten photoconverteren die zich in een focus bevonden. Door deze focus vervolgens in de tijd te bekijken konden we de lokalisatie van de immobiele versus de mobiele eiwitten apart volgen. Deze experimenten toonden de hoge dynamische interne structuur die de immobiele RAD54 eiwitten vormen in de ATPase deficiënte mutant.

## Curriculum Vitae

Name: Martinus Willem Paul  
Date of birth: 5 November 1987  
Place of birth: Leidschendam, The Netherlands

## Education

- 2011–2015 **PhD-candidate**, Department of Pathology, Erasmus Medical Center, Rotterdam, The Netherlands  
*Nanoscopic Analysis of DNA Double Strand Break Repair Foci*  
Promotor: Prof. Dr. A.B. Houtsmuller
- 2006–2011 **BSc & MSc Molecular Life Sciences**, Wageningen University, Wageningen, The Netherlands  
Specializations: Biological Chemistry/Biological Physics
- 2010 **Master thesis**, Laboratory of Biochemistry, Wageningen University, Wageningen, The Netherlands  
*Exploring a FRET-based biosensor for detecting RLK activation*  
Supervisors: Dr. L.M.C. Nitsch and Dr. J.W. Borst
- 2011 **Master internship**, CNRS Centre Biochimie Structurale, Montpellier, France  
*High-throughput PALM microscopy using automatic cell classification*  
Supervisors: dr. M. Nollmann and dr. J.W. Borst
- 2000–2006 **VWO** (pre-university secondary education), Niftarlake College, Maarsse, The Netherlands

## Scientific publications

Melanie K. Buxa, Johan A. Slotman, Martin E. van Royen, **Maarten W. Paul**, Adriaan B. Houtsmuller, Rainer Renkawitz. *Insulator speckles associated with long-distance chromatin contacts*. *Biol. Open* 5, 1266–1274. 2016

Humberto Sánchez, **Maarten W. Paul**, Małgorzata Grosbart, Sarah E. van Rossum-Fikkert, Joyce H. G. Lebbink, Roland Kanaar, Adriaan B. Houtsmuller, and Claire Wyman (2017). *Architectural plasticity of human BRCA2-RAD51 complexes in DNA break repair*. *Nucleic Acid Res.* 2017

Fabrizia Carofiglio\*, **Maarten W. Paul\***, Johan A. Slotman\*, H. Martijn de Gruiter, Wiggert A. van Cappellen, Adriaan B. Houtsmuller, Willy M. Baarends. *Super resolution imaging of RAD51 and DMC1 in DNA repair foci reveals dynamic distribution patterns in meiotic prophase – Manuscript in preparation* \*Authors contributed equally to the work

**Maarten W. Paul\***, Johan A. Slotman\*, H. Martijn de Gruiter, Adriaan B. Houtsmuller. *Single Molecule Localization in R (SMoLR), a versatile software package for visualization and analysis of single molecule localization data in R – Manuscript in preparation* \*Authors contributed equally to the work

**Maarten W. Paul**, Alex Zelensky, Pim van den Bersselaar, H. Martijn de Gruiter, Humberto Sanchez, Ihor Smal, Claire Wyman, Roland Kanaar, Jeroen Essers, Adriaan B. Houtsmuller. *Nanoscale organization of RAD54 revealed by super resolution microscopy – Manuscript in preparation*





## PhD Portfolio

Summary of PhD training and teaching

Name PhD student: Maarten W. Paul Erasmus MC Department: Pathology Research School: Molmed	PhD period: 2011-2015 Promotor(s): Prof. dr. A.B. Houtsmuller Supervisor: Prof. dr. A.B. Houtsmuller
<b>1. PhD training</b>	
	<b>Year</b>
<b>General courses</b> <ul style="list-style-type: none"> <li>- Indesign CS6 for PhD-students and other researchers</li> <li>- Course on R</li> <li>- Stralingshygiene 5B</li> </ul>	2013  2013 2013
<b>Specific courses (e.g. Research school, Medical Training)</b> <ul style="list-style-type: none"> <li>- Course on Molecular Medicine</li> </ul>	2012
<b>Seminars and workshops</b> <ul style="list-style-type: none"> <li>- JNi Scientific Meetings</li> <li>- Annual Molecular Medicine Day           <ul style="list-style-type: none"> <li>- Selected talk</li> <li>- Poster presentation</li> </ul> </li> </ul>	2011-2015  2013 2011-2014
<b>Presentations</b> <ul style="list-style-type: none"> <li>- TRR81 Winter School "Chromatin Changes and Malignancies", Kleinwalsertal, Austria           <ul style="list-style-type: none"> <li>- Oral presentation</li> </ul> </li> <li>- MGC PhD Workshop Munster           <ul style="list-style-type: none"> <li>- Oral presentation</li> </ul> </li> <li>- Focus on Microscopy, Maastricht           <ul style="list-style-type: none"> <li>- Selected talk</li> </ul> </li> </ul>	2013-2014  2014

A

<p><b>(Inter)national conferences</b></p> <ul style="list-style-type: none"> <li>- DutchBiophysics, Veldhoven               <ul style="list-style-type: none"> <li>- Poster presentation</li> </ul> </li> <li>- European Light Microscopy Initiative Meeting, Leuven, Belgium               <ul style="list-style-type: none"> <li>- Poster presentation</li> </ul> </li> <li>- TRR81 Chromatin Symposium, Egmond aan Zee, The Netherlands               <ul style="list-style-type: none"> <li>- Poster presentation</li> </ul> </li> <li>- Labeling &amp; Nanoscopy, Heidelberg, Germany               <ul style="list-style-type: none"> <li>- Poster presentation</li> </ul> </li> <li>- TRR81 Chromatin Symposium, Marburg, Germany               <ul style="list-style-type: none"> <li>- Poster presentation</li> </ul> </li> <li>- Keystone DNA Replication and Recombination, Whistler, Canada               <ul style="list-style-type: none"> <li>- Poster presentation</li> </ul> </li> </ul>	<p>2011-2013 &amp;2015 2012  2013  2014  2015  2015</p>
<p><b>2. Teaching</b></p>	
<p><b>Lecturing</b></p> <ul style="list-style-type: none"> <li>- OIC Course Functional Imaging and Super Resolution Rotterdam</li> </ul>	<p>2014-2015</p>
<p><b>Supervising practicals and tutoring</b></p> <ul style="list-style-type: none"> <li>- OIC Course Functional Imaging and Super Resolution Rotterdam (4x)</li> <li>- Java Programming for Bachelor Nanobiology students</li> </ul>	<p>2011-2015  2013</p>

## Dankwoord

En dan is het klaar! Na vele uren in het lab, data analyseren en schrijven achter de computer en vooral vaak in het donker achter de microscoop zitten ligt er dan eindelijk een proefschrift. Het schrijven van een proefschrift vraagt veel op het persoonlijk vlak, maar samenwerking en de ondersteuning van vele mensen droegen op zijn minst net zoveel bij aan dit proefschrift.

Allereerst, Adriaan, bedankt voor de mogelijkheid die je mij hebt geboden om dit onderzoek uit te voeren. Nadat ik tijdens mijn master stage de eerste ervaringen met superresolutie microscopie had opgedaan, was dit echt een hele mooie mogelijkheid om tijdens een promotieonderzoek mij hier verder in te verdiepen. Je kennis en ervaring wat betreft microscopie was zeer waardevol. Daarnaast waren je creatieve invalshoeken tijdens de werkbijeenkomsten vaak een mogelijkheid om toch weer anders naar de data te kijken. Het werken in jouw groep waar het werken met microscopen goed samen gaat met het beantwoorden van uitdagende biologische vraagstukken was zeer motiverend.

Vervolgens wil ik de leescommissie en de rest van de commissieleden bedanken voor de moeite die zij hebben gestoken in het lezen van mijn proefschrift.

Dan zijn mijn paranimfen Martijn en Johan aan de beurt. Allereerst bedankt dat jullie mijn paranimfen willen zijn, maar ik wil jullie vooral bedanken voor alle gezelligheid en hulp de afgelopen jaren. Het was een waar genoegen om me samen met jullie bezig te houden met de analyse van de single molecule data. Johan het was fijn om tussen alle experimenten te praten over allerlei zinloze dan wel hele belangrijke wetenschappelijke zaken. Martijn heel erg bedankt voor je toegewijde assistentie bij het draaiend houden van de microscopen. Het was gezellig om de afgelopen jaren met je op de kamer te zitten.

De rest van de Houtsmullergroep natuurlijk ook heel erg bedankt voor alles de afgelopen jaren. Bert-Jaap, heel erg bedankt dat ik als je paranimf alvast een keer een promotie van de andere kant heb mogen ervaren. Het was ook heel fijn dat we de afgelopen jaren onze ervaringen en frustraties van een promotieonderzoek konden delen. Thomas, het was gezellig om ons bureau samen te delen, daarnaast was je vrolijkheid tijdens de lange uurtjes in het donkere Be311 achter de microscoop erg fijn. Karin, ons onderzoek was behoorlijk verschillend, maar op het gebied van de microscopie konden we elkaar toch helpen. Zowel Karin als Thomas, veel succes met het afronden van jullie proefschriften! Tsion, bedankt voor je hulp tijdens de experimenten en natuurlijk voor het organiseren en regelen van alles in het lab. Bart, dank dat ik bij jou terecht kon voor al mijn programmeervragen. Martin jij was het die ooit de single-molecule microscopie in het Erasmus hebt opgezet, het was fijn om hierop verder te bouwen. Ilona, als part-time lid van de houtsmuller-groep wil ik jou ook bedanken voor je input en ook voor de gezelligheid. Daarnaast wil ik ook nog Pim bedanken voor de lastige taak om als student een poging te wagen om te helpen bij de photoconversie experimenten.

Met een proefschrift vol met microscopiedata is de hulp van de mensen van het OIC natuurlijk essentieel. Alex, Gert-Jan en Gert bedankt voor al jullie assistentie bij de microscopen. Gert-Jan, ik wil jou daarnaast ook bedanken dat ik veelvuldig gebruik heb kunnen maken van je grote database met DNA sequenties van fluorescente eiwitten.

Willy, jouw kennis van het meiose veld en onze expertise van de microscopie was een hele goede combinatie om een poging te wagen om te beantwoorden hoe RAD51 en DMC1 georganiseerd in DSB foci in meiotische cellen. De vele discussies over de interpretatie van de data was zeer motiverend. Hopelijk kunnen we het verhaal binnenkort tot een mooi einde brengen.

Fabricia, it was your talk in Kleinwalsertal that inspired us to start looking by super resolution on those beautiful meiotic DSB foci. We did not know what to expect, but it turned out to be very exciting! Thank you for your patience during our long microscopy sessions and for carefully selecting all those foci so we could analyse them further.

I would also like to thank the people from Molecular Genetics at our Tuesday afternoon work discussions. Claire, Roland and Jeroen thank you very much for your feedback and advice during the meetings. It was good to receive your support on the biological side of the project. Alex, it was great receiving your help on molecular cloning and the generation of the RAD54 knock-in cells. Your critical feedback was also very helpful. Marcel, thank you for your advice on the live cell particle tracking and data analysis.

Humberto, Gosia and Sari, it was nice that we could combine our data using very different high resolution microscopy techniques to reveal the organization of BRCA2-RAD51 complexes. It is a relief that the paper is now finally published. Humberto thanks for all your effort to get this done!

I also would like to thank the other people from Molecular Genetics, especially Inger, Cecile, Paula, Nathalie and Hanny for their help during my frequent visits at the 6th floor. As well as for allowing me to borrow so often antibodies or BRL medium.

Zhanmin, it was great working with you. We struggled together to get the STORM imaging working, but in the end it paid off. It was very nice to work with you on the improvement of the analysis of the STORM and tracking data, thank you for your patience testing the numerous versions of my analysis scripts. Good luck with finishing your thesis and I also hope for you the paper will be finished very soon!

Ihor and Erik, thank you that we could use your software for our analysis, and thank you for your suggestions on the image analysis and single particle tracking.

Working on the development of microscopy techniques gave me the opportunity to work with many people behind the microscope. It was inspiring to be involved in such different types of research. Although I already mentioned most of them I would still like to acknowledge Melanie and Fabian.

I also would like to thank all the people in the JNI for their help and support during the last years. Especially the people from the department of Urology and the former Trapman group were very helpful solving many practical issues.

Then I would like to thank all the people I met during the Winterschool in Kleinwalsertal. These meetings were very inspiring from the scientific perspective but it was also really nice to play games together and talk to each other at the ski slope.

I also would like to acknowledge the people involved in the Nanoscopy STW program. Especially Erik Manders, as the leader of the program, for the attempts to bring all the PhD students in the program from the different universities together. It was great to hear during these meetings from the other people working on super resolution microscopy in The Netherlands. Sjoerd and Robert, thank you for the discussions about the analysis of our single molecule data. Erwin and Aravindan, thank you for your contributions in the meetings we had to discuss the progress of our projects.

Serdeczne podziękowania dla całej rodziny i przyjaciół w Krakowie za Wasze wsparcie podczas moich badań naukowych jak również za Wasze zainteresowanie moimi postępami w trakcie doktoratu. Dzięki pobytom w Polsce mogłem odpocząć od ciężkiej pracy i nabrać sił na dalsze wyzwania. Może w końcu, dzięki zakończeniu doktoratu, będę mieć wystarczająco dużo czasu, aby nadgonić zaległości w nauce języka polskiego.

Daarnaast wil ik mijn vrienden en familie bedanken voor alle steun. Het uitvoeren van een promotieonderzoek vraagt veel tijd, ook in de avonden en het weekend en nu het klaar is hoop ik met iedereen weer wat vaker af te kunnen spreken. Mijn ouders wil ik bedanken voor alle kansen die zij mij hebben geboden om hier te komen. Henrieke en Eric, bedankt voor jullie interesse in mijn onderzoek, hopelijk helpt dit proefschrift om het nog iets beter te begrijpen ;).

Agnieszka, jij zorgde ervoor dat ik altijd weer inspiratie en motivatie vond om weer door te gaan, bedankt voor al je ondersteuning. Ik hou van jou! Jasper, je bent er nog maar net, maar de afgelopen maanden was al je vrolijkheid een hele fijne afwisseling tijdens het schrijven. Hopelijk behoud je je interesse in alles wat er om je heen gebeurt bij het ontdekken van deze wereld.